TITANIA, TITANATE, AND FLYASH BASED NANOSTRUCTURES AND NANOCOMPOSITES FOR ORGANIC DYE REMOVAL FROM AQUEOUS SOLUTIONS

Thesis Submitted to AcSIR for the Award of the Degree of
DOCTOR OF PHILOSOPHY
in Chemical Sciences

By
Manu Jose
Registration No: 10CC12J39008

Under the guidance of
Dr. Satyajit Shukla

CSIR-NATIONAL INSTITUTE FOR INTERDISCIPLINARY SCIENCE AND TECHNOLOGY (CSIR-NIIST)
THIRUVANANTHAPURAM-695019, KERALA, INDIA

February, 2017

Dedicated to My Beloved Parents and Teachers…

DECLARATION

I hereby declare that the Ph.D. thesis entitled "**Titania, Titanate, and Flyash Based Nanostructures and Nanocomposites for Organic Dye Removal from Aqueous Solutions**" is an independent work carried out by me at the **Materials Science and Technology Division (MSTD), CSIR-National Institute for Interdisciplinary Science and Technology (CSIR-NIIST), Thiruvananthapuram** under the supervision of **Dr. Satyajit Shukla**, **Senior Scientist** and it has not been submitted anywhere else for any other degree, diploma, or title.

Manu Jose

Thiruvananthapuram

February, 2017

CSIR-NATIONAL INSTITUTE FOR INTERDISCIPLINARY SCIENCE AND TECHNOLOGY (CSIR-NIIST)
Council of Scientific and Industrial Research (CSIR)
GOVERNMENT OF INDIA
Thiruvananthapuram-695019, India

Dr. Satyajit Shukla — **Functional Materials Section**
Senior Scientist — **Materials Science and Technology Division**

CERTIFICATE

This is to certify that the work incorporated in this Ph.D. thesis entitled ***"Titania, Titanate, and Flyash Based Nanostructures and Nanocomposites for Organic Dye Removal from Aqueous Solutions"*** submitted by ***Mr. Manu Jose*** to ***Academy of Scientific and Innovative Research (AcSIR), New Delhi*** in partial fulfilment of the requirements for the award of the ***Degree of Doctor of Philosophy*** in ***Chemical Sciences*** embodies original research work under my guidance. I further certify that this work has not been submitted to any other University or Institution in part or full for the award of any degree or diploma. Research materials obtained from other sources have been duly acknowledged in the thesis. Any text, illustrations, and tables used in the thesis from other sources have also been duly cited and acknowledged.

Manu Jose

Dr. Satyajit Shukla
(Thesis Supervisor)

Thiruvananthapuram
February, 2017

Telephone: +91-471-2515385; **Fax:** +91-471-2491712; **E-Mail:** satyajit_shukla@niist.res.in

ACKNOWLEDGEMENTS

It is my great pleasure to express my deep sense of gratitude to my research supervisor ***Dr. Satyajit Shukla*** *for suggesting the research problem and for his guidance, constant support, and encouragement that led to the successful completion of this work.*

I thank Dr. A. Ajayaghosh, present Director, and former Directors Dr. Suresh Das and Dr. Gangan Prathap of CSIR-NIIST, Thiruvananthapuram for providing me the necessary facilities and infrastructure of the institute for carrying out this work.

My Sincere thanks are also due to:

Dr. Mangalam S. Nair and Dr. Luxmi Varma, former and present AcSIR program coordinators at CSIR-NIIST, for timely help and advice for the academic procedures of AcSIR.

Dr. Prabhakar Rao P., Head, Dr. M.T. Sebastian, and Dr. K.G.K. Warrier, former Head, Materials Sciences and Technology Division, for their support.

Dr. S. Ananthkumar, Dr. U.S. Hareesh, and Dr. M.T. Sebastian (DAC members) for their immense support and valuable suggestions throughout the research period.

Dr. Balagopal N. Nair, Dr. Manoj Raama Varma, Dr. Bhoje Gowd E., Dr. K.P. Surendran, Dr. Saju Pillai, Dr. Vasundhara M., Dr. Nishanth K.G., and Scientists of Functional Materials Section for their encouragement and support.

Mr. A. Peer Mohamed for helping me to conduct all the instrumental facilities at the Functional Materials Section. I am also thankful to Mr. Kiran and Mr. Robert Philip for conducting TEM analysis, Mrs. Lucy Paul and Mr. Chandran for SEM, Mr. Prithviraj for XRD, Mrs. Shaharuba and Ms. Athira for COD, Mr. Arun Gopi for Zeta potential, and Mr. Ajeesh for PPMS measurements.

Dr. Halan Prakash, BITS-PILANI, Goa for sharing the knowledge on persulfate activation chemistry.

Mrs. Harsha, Mr. Hareesh, Mr. Aneesh, Ms. Remya, Dr. Adersh, Dr. Smitha, Dr. Sankar Sasidharan, Dr. Seethalekshmi, Dr. Manjumol, Dr. Jaimy, Dr. Sree Remya, Dr. Arun, Dr. Asha Krishnan for giving me basic ideas of research and immense support.

Mr. Sriram, Mr. Manoj, Mr. Rimesh, Mrs. Mahitha, Ms. Suhailath, Ms. Aswathi, Ms. Anjana for their assistance in conducting some of the experiments reported in this thesis.

Mr. Firoz Khan, Ms. Subha, Mrs. Mega, Ms. Suyana, Ms. Swetha, Ms. Minju, Ms. Shijina, Ms. Sreeja, Mr. Visakh, Mrs. Nimisha, Mr. Sundar, Ms. Faten, Ms. Anusree, Mr. Senguttuvan, Mr. Mathew, Mr. Mahesh, Mrs. Babitha, Mrs. Linsha, Mrs. Soumya, Mrs. Jeen, Ms. Suhailath, Mrs. Sumina, Ms. Dhanya, Mr. Bijoy, and Mr. Jaggaiah for their companionship and great support.

Mr. Baiju T.V., Dr. P K. Sajith, Dr. Jatish Kumar, Mr. Rahul S., Mr. Sujith S., Mr. Vipin, and Mr. Shaiju for their great companionship during my stay in Thiruvananthapuram.

I express my sincere gratitude to Mr. Parameswaran and Mr. Govind, Calicut Integrated Powerloom (Ind.) Co-operative Society Limited (CIPCO), Naduvannur, Calicut, Kerala for the successful completion of my CSIR-800 project.

I am grateful to CSIR and DST New Delhi for the financial assistance.

I would like to extend my sincere thanks to all my friends at CSIR-NIIST.

I take this opportunity to pay respect to my parents, teachers, and friends starting from my school days to those at CSIR-NIIST who motivated and blessed me.

Above all, I bow to Almighty for bestowing his blessings upon me.

Manu Jose

CONTENTS

LIST OF FIGURES

LIST OF TABLES

Chapter 1

Chapter 2

LIST OF SCHEMES

LIST OF ABBREVIATIONS

AC	:	Activated carbon
AOPs	:	Advanced oxidation processes
AP	:	3-Aminophthalate
ATN	:	Anatase TiO_2 nanotubes
BJH	:	Barrett-Joyner-Halenda
BOD	:	Biochemical oxygen demand
BET	:	Brunauer-Emmett-Teller
CNT	:	Carbon nanotubes
CWPO	:	Catalytic wet peroxide oxidation
CTAB	:	Cetyltrimethylammonium bromide
COD	:	Chemical oxygen demand
CIP	:	Ciprofloxacin
CB	:	Conduction band
DR	:	Diffuse reflectance
DO	:	Dissolved oxygen
DKR	:	Dubinin-Kaganer-Radushkevich
EPR	:	Electron paramagnetic resonance
EDX	:	Energy dispersive X-ray
FCC	:	Face centered cubic
FA	:	Flyash
FTIR	:	Fourier transform infrared
GNS	:	Graphene nanosheets
HRTEM	:	High resolution transmission electron microscope
HTNS	:	Hydrogen titanate nanosheets
HTNSF	:	Hydrogen titanate nanosheet-γ-Fe_2O_3
HTN	:	Hydrogen titanate nanotubes

IUPAC	:	International union of pure and applied chemistry
JCPDS	:	Joint committee on powder diffraction standards
LPT	:	Layered protonic titanates
MB	:	Methylene blue
MWCT	:	Multiwall carbon nanotubes
NTPC	:	National thermal power corporation
PL	:	Photoluminescence
PPMS	:	Physical property measurement system
KPS	:	Potassium persulfate
ROS	:	Reactive oxygen species
RhB	:	Rhodamine B
SEM	:	Scanning electron microscope
SAED	:	Selected area electron diffraction
TA	:	Terephthalic acid
TBA	:	Tetrabutylammonium
TEM	:	Transmission electron microscope
UV	:	Ultraviolet
VB	:	Valence band
VSM	:	Vibrating sample magnetometer
XRD	:	X-ray diffraction

PREFACE

Organic synthetic-dyes are recalcitrant compounds that are extensively used in various industries such as the textile, pulp and paper, leather tanning, food, agricultural research, hair colorings, and light-harvesting arrays. Textile industrial effluent contains large quantities of unused organic synthetic-dyes as its major component along with the presence of several other auxiliary chemicals. Their presence in the water bodies reduces the sun-light penetration which affects the photosynthesis activity. They are also harmful to the aquatic life due to their highly toxic nature. For human beings, organic synthetic-dyes severely affect the kidney, central nervous systems, liver, brain, reproductive systems, and other vital body organs. Therefore, the removal of highly stable organic synthetic-dyes from the industry effluents and aqueous solutions is of prime importance. Although various physical, chemical, physico-chemical, and biological processes have been developed for this purpose, photocatalysis, adsorption, and Fenton-like advanced oxidation processes (AOPs) are of greater interest in view of their commercial potential. On the other hand, in the field of nanoscience and nanotechnology, various nanostructures including nanocrystalline particles, nanowires, nanofibers, nanotubes, nanosheets, nanobelts, and nanoribbons have been synthesized and utilized for the variety of industrial applications due to their unusual physical and chemical properties relative to those of bulk-counterparts. However, the precise role of these nanostructures in the removal of organic synthetic-dyes from the aqueous solutions and industry effluents is still under the development stage and far away from realizing their full commercial potential. In the present work, titania, titanate, and flyash based nanostructures and nanocomposites in the powder and coating forms have been developed using the

modified wet-chemical techniques and utilized for the removal of organic synthetic-dyes from the aqueous solutions involving the aforementioned dye-removal mechanisms.

The entire thesis has been divided into seven chapters. The first-chapter describes the significance of removal of organic synthetic-dyes from the aqueous solutions and reviews the recent progress in the development of various nanostructures for this potential industrial application involving different mechanisms such as the photocatalysis, adsorption, and AOPs. The major objectives of the thesis are briefly outlined at the end of the chapter.

The second-chapter deals with the synthesis of nanocrystalline particles of anatase-titania (TiO_2) via conventional and acid-catalyst-modified sol-gel processes. The effect of different acid-catalysts such as nitric acid (HNO_3), acetic acid (CH_3COOH) and phosphoric acid (H_3PO_4) on the morphological, chemical, and structural evolution of nanocrystalline TiO_2 has been analyzed by using different analytic techniques. The samples have been utilized for the removal of cationic methylene blue (MB) dye from the aqueous solutions under the ultraviolet (UV)-radiation exposure. The maximum photocatalytic activity has been exhibited by the sample processed using H_3PO_4 as an acid-catalyst. This has been attributed to higher MB adsorption on its surface due to its maximum specific surface-area and higher negative surface-charge which are the result of strong binding of PO_4^{3-} anions on the surface of nanocrystalline anatase-TiO_2. Interestingly, the same sample possess the lowest crystallinity and lowest concentration of hydroxyl-radicals ($^{\bullet}OH$) produced under the UV-radiation exposure which do not support the maximum photocatalytic activity exhibited by this sample. Nevertheless, the involvement of phosphate anions (PO_4^{3-}) in the degradation of MB dye under the UV-radiation exposure has been confirmed via FTIR analysis. The obtained results, thus,

strongly support the dual-role of PO_4^{3-} anions in enhancing the photocatalytic activity of nanocrystalline anatase-TiO_2 which is comparable with that of commercial Degusa-P25.

The third-chapter illustrates the hydrothermal processing and characterization of highly crystalline nanotubes and nanoplates of undoped and silver (Ag)-doped anatase-TiO_2 (ATN) having high aspect-ratio. The nanocrystalline particles of anatase-TiO_2 synthesized using CH_3COOH modified sol-gel process has been utilized as a precursor during the hydrothermal processing. The formation of nanotubes and nanoplates of undoped and Ag-doped anatase-TiO_2, under the given processing conditions, has been attributed *for the first time* to the operation of double-ion-exchange mechanism. This is in contrast to the conventional single-ion-exchange mechanism responsible for the formation of nanotubes of hydrogen titanate (HTN) generally observed with the use of unmodified sol-gel derived nanocrystalline anatase-TiO_2 as a precursor. This is the first investigation to report the synthesis of ATN processed via hydrothermal method without the involvement of thermal treatment. The as processed pure and Ag-doped ATN have been utilized for the removal of cationic MB dye from the aqueous solutions via adsorption mechanism. Ag-doped ATN having Ag/Ti ratio of 1% exhibit the maximum MB adsorption capacity of 39 mg g^{-1}.

In the fourth-chapter, pure and hydrogen phosphate (HP, HPO_4^{2-}) modified HTN have been synthesized via hydrothermal treatment of sol-gel derived pure and titanyl phosphate (TiP_2O_7) / PO_4^{3-} ions modified nanocrystalline anatase-TiO_2 as precursors respectively. The unmodified HTN have been utilized for the removal of cationic MB dye from the aqueous solutions via adsorption and one-step method of chemically-activated catalytic process conducted in the dark (Fenton-like AOP process). The latter involves the activation of strong oxidizer such as hydrogen peroxide (H_2O_2) using HTN

which decomposes the MB dye in the dark-condition (also known as dark-catalysis) via the generation and attack of radical-ions ($^{\bullet}OH$ and superoxide-ion ($O_2^{\bullet-}$)). The maximum MB degradation rate-capacity (mg g^{-1} h^{-1}) has been measured for the one-step method of dark-catalysis process by varying the initial MB and H_2O_2 concentrations. It has been demonstrated *for the first time* that the obtained data can precisely predict the MB adsorption capacity of HTN. The validity of new method for predicting the dye-adsorption capacity has been confirmed via similar tests conducted using the HP-HTN.

The fifth-chapter provides the synthesis of magnetic nanocomposites (HTNSF) consisting of hydrogen titanate ($H_2Ti_3O_7$) nanosheets (HTNS) and maghemite (γ-Fe_2O_3) nanoparticles by simple mechanical mixing of precursors in an aqueous solution having neutral solution-pH. Sol-gel derived nanocrystalline anatase-TiO_2 coated flyash (FA) particles have been utilized for the hydrothermal processing of HTNS. A new model has been proposed to explain the typical attachment of γ-Fe_2O_3 nanoparticles to the edges of HTNS via an ion-exchange bond formation. The dye-adsorption properties of HTNSF magnetic nanocomposites have been investigated using the cationic MB dye. Interestingly, *for the first time*, the attachment of γ-Fe_2O_3 nanoparticles has been noted to enhance the MB adsorption capacity of HTNS instead of decreasing it. A new model has been proposed which satisfactorily explains the strong dependence dye-adsorption capacity on the pore volume of HTNSF magnetic nanocomposite. The latter shows the effective magnetic separation from an aqueous solution in few minutes using an external magnetic field provided by a bar magnet. The reuse of HTNSF-5 magnetic nanocomposite has been successfully achieved through its regeneration via the activation of persulfate ($S_2O_8^{2-}$) anions in an aqueous solution involving the synergy effect in between thermal activation and that by the constituents of HTNSF magnetic nanocomposite.

In the sixth-chapter, the processing and application of magnetically separable palladium (Pd)-magnetite (Fe_3O_4)-flyash composite particles in the decoloration of aqueous solutions containing the industrial azo reactive dyes such as Corafix Red ME4B and Corazol Black BX have been investigated. The mechanism of degradation of azo reactive dyes involves the synergistic activation of $S_2O_8^{2-}$ involving the catalytic and thermal contributions. In contrast to the activation of H_2O_2, the synergistic activation of $S_2O_8^{2-}$ anions has been noted to significantly reduce the chemical oxygen demand (COD) level almost in a single step which reduces the dependency on the post adsorption treatment of activated carbon (AC). Moreover, the regeneration of AC has also been demonstrated using the synergistic activation of $S_2O_8^{2-}$ anions. As a result, AOP based on the activation of $S_2O_8^{2-}$ anions using the magnetically separable Pd-Fe_3O_4-flyash composite particles appears to be an efficient, cost-effective, and non-hazardous approach for the removal of organic synthetic-dyes from the aqueous solutions.

The summary of entire thesis work has been provided in the seventh-chapter which also includes the scope for the future work.

Chapter 1

Introduction to Nanostructures and Nanocomposites for Dye Removal Application

Graphical Abstract

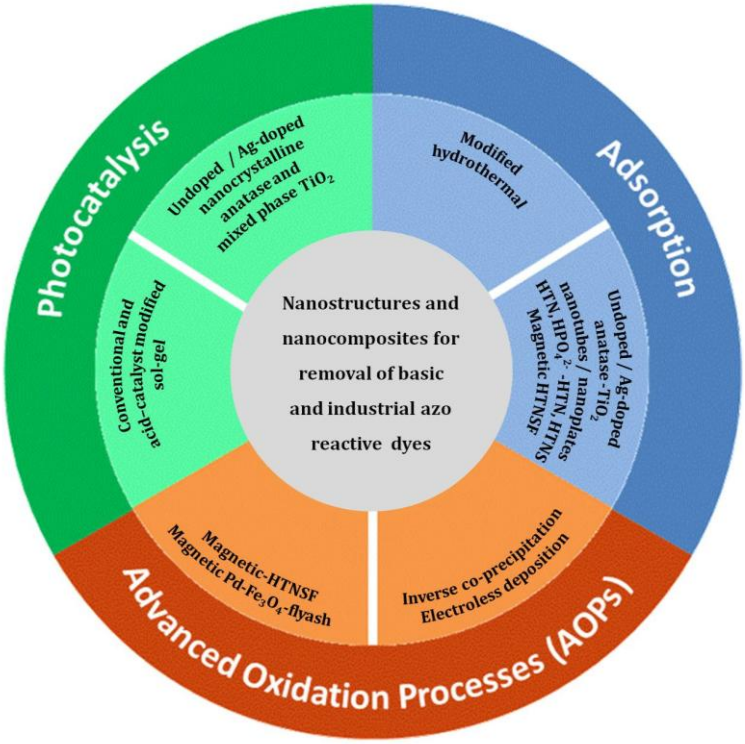

Highlights

- Significance of development of nanomaterials for the removal of organic synthetic-dyes from the aqueous solutions and wastewaters is discussed.
- Principles of three commercially significant dye-removal mechanisms are reviewed.
- Different nanomaterials developed for the removal of organic synthetic-dyes using these mechanisms are summarized.
- Limitations and scope of each dye-removal mechanism are described.
- Motivation and objectives of present thesis work are presented.

1.1. Nanoscience and Nanotechnology

Nanoscience is the study of phenomena and manipulation of materials at atomic, molecular and macromolecular scales, where the properties differ significantly from those at a larger scale; and nanotechnology is the design, characterization, production, and application of structures, devices and systems by controlling shape and size at the nanometer scale.[1] These fields are developed after the brilliant lecture by Richard Feynman in 1960 at a meeting in the American Physical Society entitled as "There's Plenty of Room at the Bottom". He proposed manipulating of individual atoms to make new small structures having very different properties. The importance of nanomaterials arises from its unexpected properties, challenging synthetic procedures, quantum confinement effect, most functional structures in biology, basis of nanoelectronics and photonics.[2] This field deals with the study of objects with smallest dimensions ranging from a few nanometers to less than 100 nanometers.[3] In chemistry, this range of sizes has historically been associated with colloids, micelles, polymer molecules, phase-separated regions in block copolymers, and similar structures—typically, very large molecules, or aggregates of many molecules. More recently, structures such as buckytubes, silicon nanorods, and compound semiconductor quantum dots have emerged as particularly interesting classes of nanostructures. In physics and electrical engineering, nanoscience is most often associated with the quantum behavior of electrons and photons in the nanoscale structures. Biology and biochemistry also have a deep interest in nanostructures as components of the cell; many of the most interesting structures in biology—from DNA and viruses to subcellular organelles and gap junctions can be considered as nanostructures.[2] Metal oxide nanoparticles play a leading role in the development of nanoscience and nanotechnology. Titanium dioxide (TiO_2), zinc oxide

(ZnO), iron oxide (Fe_2O_3), tungsten oxide (WO_3), and manganese oxide (MnO) find a verity of applications from basic pigments to advanced electronic materials.

1.2. Wastewater Remediation

Water is the prime necessity for all the living beings. Industrialization produces considerable amount of polluted water and also cause global warming which results in the depletion of useful surface water. So, the treatment of industrial wastewater, and hence, its reuse have greater significance in the modern world. The different methods for the treatment of wastewater are filtration, sedimentation, gravity separation, flotation, reverse osmosis, electrodialysis, precipitation, oxidation, solvent extraction, ultrafiltration, evaporations, distillation, and adsorption.[4] These conventional wastewater treatment methods are associated with several disadvantages such as the inefficiency for treating large quantities of wastewater, high chemical cost, and sludge formation.[5] There is an urgent need for other alternative techniques which can be used for the effective treatment of wastewater.

The development of nanotechnology leads to considerable amount of study to improve the wastewater treatment processes. At the nanometer scale, the materials possess novel size-dependent properties which differ from those of bulk counterparts and many of the properties find application in the wastewater treatment process. The nanotechnology finds its wide application for treating the polluted water which includes the removal of organic synthetic- dyes, pharmaceuticals, heavy metal-ions, and nuclear wastes. The development of nanotechnology replaces all the conventional wastewater treatment methods and offers a partial solution for the industrial dye removal process. Table 1.1 shows the examples of applications of the different wastewater treatment process which utilizes nanomaterials.

Table 1.1. Examples of potential applications of nanotechnology in water/wastewater treatment.[6]

Applications	Examples of nanomaterials	Some of novel properties
Adsorption	CNTs/nanoscale metal oxide and nanofibers	High specific surface area and assessable adsorption sites, short intraparticle diffusion distance, tunable surface chemistry, and easy reuse.
Disinfection	Nanosilver/titanium dioxide (Ag/TiO_2) and CNTs	Strong antimicrobial activity, low toxicity and cost, high chemical stability, and ease to use.
Photocatalysis	Nano-TiO_2 and Fullerene derivatives	Photocatalytic activity in solar spectrum, low human toxicity, high stability and selectivity, and low cost.
Membranes	Nano-Ag/TiO_2/Zeolites/Magnetite and CNTs	Strong antimicrobial activity, hydrophilicity, low toxicity to humans, high mechanical and chemical stability, high permeability and selectivity, and photocatalytic activity.

1.2.1 Significance of dye removal

Textile industries are the major contributors to dye pollution along with other industries like plastics, rubber, paints, paper, printing and leather. Textile industrial effluent contains large quantities of dyes as its major component along with the presence of many auxiliary chemicals. Worldwide around 100,000 different textile dyes are available and over 700,000 tons are produced annually out of which 2% of dyes are released from the manufacturing industry and 10% are discharged from textile and associated industries.[4] In addition to that the textile factories consume large quantities of water along with other auxiliary chemicals for dyeing process. Dyes are synthetic organic compounds which contain many functional groups associated with them, and they are used to impart color to fabrics, paper, and leathers. Dyes contain at least one chromophore group and a conjugated system, which absorbs in the visible region of the electromagnetic spectrum. Even trace quantities of dyestuff make the solution highly visible due to its very high molar extinction coefficient. Dyes are harmful chemicals because they are found to cause

skin irritation, cancer, allergy, and mutation in human beings.[7] The Table 1.2 below lists some of the commonly used dyes and their general characteristics.

Table 1.2. Commonly used dyes and their general characteristics.[8,9]

Dye type	Examples	Fabric type	Properties	Toxicity
Acid dyes	Acid Red 183, Sunset Yellow, Methyl Orange	Nylon, wool, silk	Water soluble, anionic	Carcinogenic
Basic dyes	Methylene Blue, Janus Green, Basic Green 5	Inks, paper, polyacrylonitrile	Water soluble, releasing colored cations in solution	Carcinogenic
Direct dyes	Congo Red, Direct Red 23, Direct Orange 39	Cotton, regenerated cellulose, paper	Water soluble, anionic, improves wash fastness by chelating with metal salts	Bladder cancer
Dispersive dyes	Disperse Orange 3, Disperse Red	Polyester, nylon, cellulose	Water-insoluble, non-ionic	Allergenic (skin), carcinogenic
Reactive dyes	Reactive Black 5, Reactive Green 19, Reactive Blue 4	Wool, cotton, silk and nylon.	Extremely high wash fastness due to covalent bond formation with fiber	Dermatitis, allergic conjunctivitis
Vat dyes	Vat Blue 4, Vat Green 11, Vat Orange 15	Cellulosic fibers	Use soluble leuco salts after reduction in an alkaline bath	-

Basic dyes are intensely colored and highly visible even at very low concentrations, and most of the dyes are chromium based, which is highly carcinogenic.[10,11] Dye reduces the sun-light penetration, and hence, affects the photosynthesis activity. They are also toxic to aquatic life due to the presence of various harmful chemicals[12] and found to be carcinogenic, mutagenic, or teratogenic to various aquatic species. For human beings, dyes affect kidney, central nervous systems, liver, brain, and reproductive system.[13] Degradation of anthraquinone dyes is most difficult which remain in the solution for quite longer time.[14] Azo dyes contain toxic amine and reactive dyes are water soluble which cause serious trouble to the environment.[15] It is found that mutagenesis, chromosomal fractures, carcinogenesis, and respiratory toxicity are the main negative

effects of the dyes. In addition to that the dyes are found to decrease the dissolved oxygen (DO) which enhances the biochemical oxygen demand (BOD) and chemical oxygen demand (COD) resulting in foul odor.[16] Therefore the removal of toxic dyes from the industry effluent is a challenge to the modern world. The typical characteristics of textile industrial effluents are given in Table 1.3 below.[17]

Table 1.3. Typical characteristics of textile industrial effluent.[17]

Parameter	**Range (mg l^{-1})**
COD	150–12,000
Total suspended solids	2900 and 3100
Total nitrogen	70–80
BOD	80–6000
BOD/COD	0.25

1.2.2. Nanotechnology for dye removal

Since our water bodies are highly contaminated with large amounts of industrial pollutants such as dyes, its purification is one of the main challenges to the modern world. Conventional water treatment technologies including flocculation-coagulation, adsorption by low cost conventional adsorbents (such as coal flyash, peat, and coal), and biological techniques suffers from many disadvantages such as the inefficiency in the complete removal of pollutant, inconvenience in treating large quantities of wastewater, and creation of sludge that becomes a secondary pollutant. The advantage of nanomaterials over conventional materials for the purpose of water decontamination is its high surface area, faster adsorption equilibrium, small diffusion resistance, and enhanced redox as well as photocatalytic properties.[18,19] The advances in the development of nanotechnology are related to photocatalysis, adsorption and advanced oxidation

processes (AOPs), membrane filtration, electrochemical treatment, or the combination of above processes. Another important advantage of nanotechnology is the retention and reuse of nanomaterial which reduces the cost and public health concern. The nanomaterials used for dye removal applications are carbonaceous materials such as the carbon nanotubes (CNT), graphene, graphene oxide, semiconductors which include TiO_2, ZnO, magnesium oxide (MgO), magnetic materials (magnetite (Fe_3O_4)), and biomaterials (nanochitosan).

1.3. Dye-Removal Technologies and Nanostructures

1.3.1. Photocatalysis

1.3.1.1. Principle

According to International Union of Pure and Applied Chemistry (IUPAC), photocatalyst is a substance that is able to produce by absorption of light quanta, chemical transformation of reaction participants to intermediate reaction products, and regenerating its chemical composition after each cycle of such interaction.[20] Photocatalysts are solid state semiconductors which can absorb ultraviolet (UV) or visible light, chemically and biologically inert, photostable, inexpensive, and non-toxic.[21] The field of photocatalysis has been developed after the discovery of electrolysis of H_2O to H_2 and O_2 by the photosensitization effect of TiO_2 electrode by Honda and Fujishima.[22] Later, Shrauzer and Guth developed the mechanistic picture of TiO_2 photocatalysis involving the decomposition of H_2O on powdered TiO_2 with small amount of Pt or Rh metal.[23] The dye discoloration via photocatalysis process is according to the following mechanism. At ambient temperatures, the electron lies at the valance band for a photocatalyst. When UV light of energy greater than that of band-gap energy falls on the semiconductor, electrons present in the valence band (CB) are excited to the

conduction band (CB) and as a result electron-hole pairs are formed as shown in Fig 1.1. The electron and holes can be trapped as Ti^{3+} and O^- defects sites in the lattice, or they can dissipate energy by recombination,[24] or the charge carriers can migrate to the surface and causes redox reactions with the adsorbates.[25] The photo generated hole reacts with the adsorbed H_2O molecule and forms hydroxyl radicals ($^{\cdot}OH$) whereas the photo generated electron reacts with O_2 to produce superoxide radical anion of oxygen ($O_2^{\bullet -}$).[26]

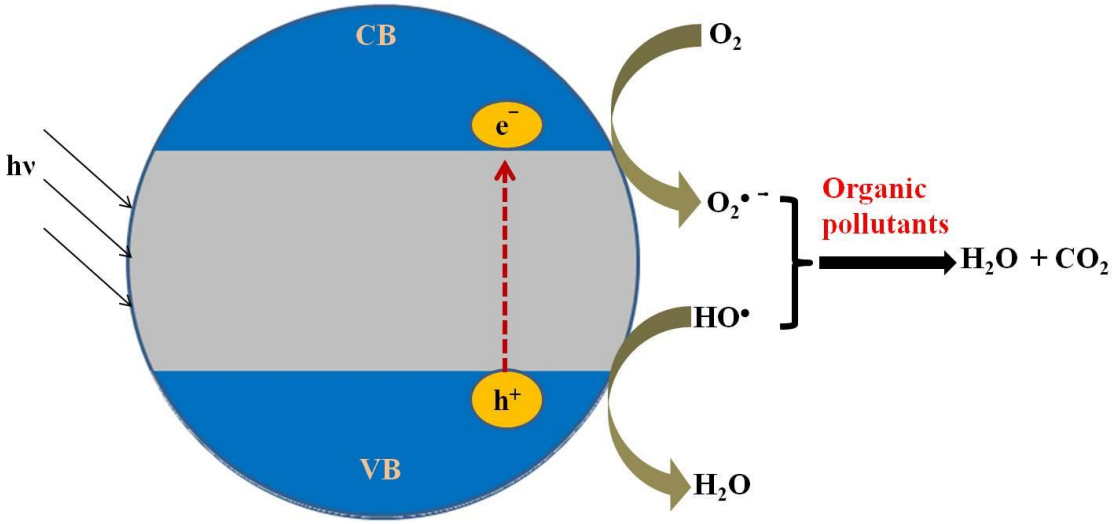

Fig. 1.1. Schematic of photocatalytic dye-degradation mechanism based on nanocrystalline TiO_2.

Finally, these radicals are responsible for the oxidation of organic compound producing end product as CO_2 and H_2O. The corresponding equations are given below,

$$TiO_2 + h\upsilon \rightarrow e^- + h^+ \quad (1.1)$$

$$h^+ + H_2O(ads) \rightarrow {}^{\bullet}OH(ads) + H^+(ads) \quad (1.2)$$

$$O_2 + e^- \rightarrow O_2^{\bullet -}(ads) \quad (1.3)$$

$$O_2^{\bullet -}(ads) + H^+ \leftrightarrow HO_2^{\bullet}(ads) \quad (1.4)$$

$$HO_2^{\bullet}(ads) \rightarrow H_2O_2(ads) + O_2 \quad (1.5)$$

$$H_2O_2(ads) \rightarrow 2HO^{\bullet}(ads) \quad (1.6)$$

$$HO^{\bullet} + dye \rightarrow \text{int}ermediates \rightarrow CO_2 + H_2O \quad (1.7)$$

The factors which influence the photocatalytic activity are pH, light intensity, concentration of reactants, and effect of ionic species.[27] Large surface area along with the presence of large surface density of adsorbents causes larger photocatalytic reaction rates. Other important factor which affects the photocatalytic reaction rate is the crystallinity. If the crystallinity is high, fewer will be the bulk defects which may lead to higher photocatalytic reaction rates. [28]

TiO_2 occurs in nature as three crystalline phases, anatase, rutile, and brookite out of which the least thermodynamically stable anatase phase is found to exhibit superior photocatalytic activity when compared to other two polymorphs.[29] Anatase crystal structure arises from corner sharing of the octahedra which forms (001) planes resulting in the tetragonal structure; whereas, the rutile the crystal structure arises from the edge sharing of (001) planes of octahedra which gives a tetragonal structure. In the case of brookite, both the edge and corner sharing give an orthorhombic structure.[30] The Ti-Ti distances in anatase are greater whereas the Ti-O distance is lower, and these structural differences cause differences in their electronic band structures.[31] The density of anatase is 9% less than that of rutile and these structural differences cause difference in their photocatalytic activity.

1.3.1.2. Nanomaterials developed

The photocatalytic dye degradation applications of nanomaterials with different morphologies are summarized in Table 1.4.

Table 1.4. Nanomaterials of different morphologies used for photocatalytic dye degradation applications.

Photocatalyst	Morphology	Target Pollutant	Remarks	Reference
TiO_2	Nanofibers	Basic Blue	Photocatalytic activity of TiO_2 nanofibers was comparable to that of TiO_2 nanoparticles	[32]
BiOCl	Nanosheets	Rhodamine B	High photoactivity of {001} facets	[33]
$Ba_5Ta_4O_{15}$	Nanosheets	Rhodamine B	Layered perovskite enhances the photocatalytic activity by promoting the charge separation and delocalization of photogenerated electrons and holes	[34]
PANI-CdS	Nanoparticles	Methylene Blue	Rapid transfer of hole and high separation efficiency of electron-hole pairs lead to the enhanced photoactivity	[35]
Ag-ZnO	Nanofibers	Rhodamine B	Heterojunction structure promoted the charge separation as well as the photon efficiency	[36]
ZnO	Nanotubes	Methylene Blue	ZnO nanotubes are potential materials for photocatalytic applications because of their stability and activity	[37]
3D wurtzite ZnSe	Nanoflowers	Methylene Blue	The high photoactivity of nanoflowers is due to the combined effects of large surface areas, the existence of mesopores, and high band-gap energy.	[38]
Rutile TiO_2	Nanorods	Rhodamine B	Low temperature synthesized superstructures showed significantly higher photocatalytic activities than commercial photocatalyst Degussa P25	[39]
ZnS	Nanoporous Nanoparticles	Eosin B	High specific surface area leads to more effective photocatalytic performance compared to that of Degussa P25 TiO_2 or ZnS nanocrystals	[40]
TiO_2	Nanotubes	Methylene Blue	Tubular geometry provides a short (straight) diffusion path for dye molecules from the solution to the active surface area	[41]

The main factors which control the photocatalytic activity of a semiconductor are its light absorption properties, oxidation-reduction rates at the surface by the electron-hole pair, and electron-hole recombination rate.[28] Even though various other semiconductors such

as ZnO, Fe_2O_3, WO_3, zinc sulfide (ZnS), cadmium sulfide (CdS), Cerium(IV) oxide (CeO_2), strontium titanate ($SrTiO_3$), gallium nitride (GaN), and bismuth(III) sulfide (Bi_2S_3) are used for photocatalysts, TiO_2 is the most widely used photocatalyst because it fulfills all the above requirements in addition to high conversion efficiencies.[42] Even if the conversion values are high for various TiO_2 photocatalysis, the calculated quantum yield is very low (below 10%).[43] Other advantages of TiO_2 for photocatalytic applications is its non-toxicity, water insolubility, hydrophilicity, cheap availability, stability against photocorrossion, and its suitable flat band potential (V_{fb}) that can induce the desired redox reaction without bias potential. Moreover, it can be easily supported on various substances such as glass, fibers, stainless steel, and inorganic materials.[44]

1.3.1.3. Nanocrystalline TiO_2

1.3.1.3.1. Sol-gel synthesis

Sol-gel processing is the widely used method for the processing of nanocrystalline TiO_2 photocatalyst because various parameters such as the nature of precursor, pH, temperature, and reaction time can be regulated which has a strong influence on the photocatalytic reaction rate. The important advantage of this synthetic method is that the species can be homogeneously mixed at the molecular level which leads to the formation of polycrystalline particle with special characteristics. Another advantage is that dopants can be easily introduced at any stage of processing to improve the photocatalytic properties.[45] During sol-gel process, a sol is first formed by the hydrolysis and polycondensation reactions of the precursor (usually metal alkoxides or metal salts) and further polymerization and condensation leads to loss of solvent resulting in the formation of gel phase. Another unique feature of this method is that there is an extraordinary control of the size and arrangement of pores within the framework.[46] The

steps involved in the synthesis of nanocrystalline TiO_2 via sol-gel method using titanium alkoxide $Ti(OR)_n$ as a precursor are,[47]

1. *Hydrolysis*

$$M(OR)_n + H_2O \rightarrow M(OR)_{n-1}(OH) + ROH \quad (1.8)$$

2. *Condensation*

Dehydration

$$2M(OR)_{n-1}(OH) \rightarrow M_2O(OR)_{2n-2} + H_2O \quad (1.9)$$

Dealcolation

$$M(OR)_n + M(OR)_{n-1}(OH) \rightarrow M_2O(OR)_{2n-2} + ROH \quad (1.10)$$

The overall reaction is

$$M(OR)_n + \frac{n}{2}H_2O \rightarrow MO_{n/2} + nROH \quad (1.11)$$

In order to obtain homogeneous network, the hydrolysis step is controlled by chelating agents like carboxylic acid, diketones, or diols are added in addition to titanium precursors.[48] The condensation involves gelation and calcination and during this step, the particles are pulled together to form a compact mass which leads to metal oxide crystal.[47] The formation of Ti-O-Ti chain is favored with low hydrolysis rate and low water content whereas the formation of $Ti(OH)_4$ is favored if hydrolysis rate and water content are high. Loosely packed particles of TiO_2 is obtained in the presence of large quantities of Ti-OH and insufficient polymer network where as closely packed particles are obtained from three dimensionally developed gel skeleton.[34] The sol-gel derived precipitates are amorphous in nature and calcination treatment gives rise to particle agglomeration and grain growth which may induce phase transformation.[49]

Recombination of photogenerated charge carriers result in the deactivation of excited species making them unavailable to react with the adsorbed species is the major

limitation of the semiconductor photocatalysis.[50] Recombination may be due to the presence of impurities, defects, or all factors which cause imperfection in the crystal.[51,52] Morphological modifications to improve the surface area and porosity or chemical modifications by the incorporation of additives into the nanocrystalline TiO_2 lattice are general strategies to improve the photocatalytic activity. Morphological modifications include the synthesis of other nano architectures like (nanosheets, nanofibers, and nanotubes) and functionalization of catalyst surface with anions and polymer groups. In chemical modifications, doping with metals such as Cr, Mo, Ni, Mn, V, Fe, Ag, Au, Cu, and Co (replaces 'Ti') or non-metals such as B, C, N, P, S, F, etc (replaces 'O').[53] Co-doping with either two metals or non-metals or its combination, oxygen-rich TiO_2 modification, metal-deposition, and coupling with other semiconductors are reported to improve the electron-hole pair separation; thereby, reducing the recombination rate and improving the photocatalytic activity.[21] The optical properties of any material is depends on its electronic structure which largely depends on the chemical composition, atomic arrangements and physical dimension of the material.[24] In modified nanocrystalline TiO_2, crystal lattice changes its chemical composition which improves the optical properties. Substitution of Ti^{4+} with other cations is easier than the substitution of O_2^- anions with other anions because of the differences in the ionic radii and charge state. Compared to the bulk materials, nanoparticles are more tolerant for modification in its chemical composition due to the inherent lattice strain. A red shift in the band-gap energy is observed by doping TiO_2, thereby improving the visible-light absorption attributed to the charge transfer between the d electron of dopant and valence or conduction band of TiO_2.[34]

1.3.1.3.2. Acid-catalyst effect

Modification of TiO_2 by inorganic acids like HCl, HNO_3, HF, H_3PO_4 and H_2SO_4 has attracted much attention.[54,55] It has been observed that the incorporation of acid-catalyst during or after the sol-gel process greatly affects the particle size, porosity, crystallinity, surface area and has a significant effect on the photocatalytic activity. It is also realized that the modification of TiO_2 with anions like F^-, PO_4^{3-}, SO_4^{2-}, and CF_3COO^- are effective to enhance the photocatalytic activity.[54] The main characteristic of these ions is their strong bonding ability to the surface of TiO_2, higher negative charge for easy formation of hydrogen bond, and inert nature against the photogenerated electrons and holes.[54] Acids such as hydrochloric acid (HCl) and nitric acid (HNO_3) are noted to increases the hydrolysis rate; and there, by inducing the anatase to rutile phase transformation. On the other hand, acids such as acetic acid (CH_3COOH), phosphoric acid (H_3PO_4), and sulfuric acid (H_2SO_4) are observed to prevent the phase transformation to rutile. Suresh et al. reported that acetic acid in the pH range up to 4 enhances the thermal stability of anatase phase by 100 ºC.[56] At low pH, condensation reaction is slow compared to hydrolysis because of charge-charge repulsion between protonated hydrated metal cations which allows branching to occur before particle growth to produce strongly cross-linked gel.[56] It is found that phosphoric acid modification results in the surface bound phosphate which helps to improve charge separation by inhibiting charge carrier recombination which essentially improves the photocatalytic activity. According to Chen et al., pH is an important parameter during the formation of TiO_2 nanocrystals.[57] The protons attack the alkoxide group decreasing its electronegativity with decrease in pH. As a result, Ti^{4+} gets attacked by OH^- ions which are beneficial for the formation of Ti-OH before polycondensation. Hence, at lower pH value (pH~1), higher amount of Ti-OH^{2+} groups is beneficial for the mass loss of H_2O molecules when polycondensation occurs resulting in

the formation of anatase TiO_6. On the other hand when pH increases, decrease the concentration of Ti-OH^{2+} which favors less loss of H_2O molecule, resulting the formation of brookite structure.[57] Various studies are carried to understand the effect of different acid-catalyst on the structure of sol-gel derived nanocrystalline TiO_2 and summarized in Table 1.5.

Table 1.5. Effect of acid-catalyst on the structure of sol-gel derived nanocrystalline TiO_2.

Precursor for TiO_2	**Acid**	**Conditions**	**Particle size (nm)**	**Key results**	**Reference**
TTIP	H_3PO_4	P:Ti ratios of 0.05, 0.10, and 0.20	9-12	Photodegradation is significantly accelerated by phosphate modification through hydroxyl radical attack pathway of substrates.	[54]
$TiCl_4$	HCl HNO_3, H_2SO_4 AcOH H_3PO_4	Acid-catalyzed sol–gel method at 80 ºC without calcination.	3.8-42.7	The presence of SO_4^{2-} and PO_4^{3-} groups was observed to inhibit the growth to rutile phase.	[55]
TTIP	AcOH	25 ml TTIP, 48 ml AcOH	--	Acetic acid in the pH range of 3-4 enhances the thermal stability of anatase phase	[56]
Tetrabutyl titanate	HNO_3	W=[H_2O]:[TBT]= 40-400	3-7	Formation of anatase structure is favored when pH is 1. When pH increases, the concentration of H^+ decreases, resulting in the formation of a brookite structure at pH 2–71.	[57]
TTIP	AcOH	AcOH/TTIP =1 to 10	14-22	Increasing AcOH/TTIP molar ratio, sol formation time, and synthesis temperature from 0 to 25ºC, increases crystallite size of synthesized nanoparticles.	[58]
TTIP	HNO_3, H_2SO_4, H_3PO_4	TTIP:H_2O = 0.05, Sol-gel product is treated with 1M acid	~30	Phosphate oxoanion, which is stable throughout the range of temperature studied (400-800 ºC)	[59]
TTIP	H_2SO_4	TTIP:H_2O = 0.05 The sol-gel product is treated with 1M acid	--	Anatase stabilization by sulfate ions up to 700 ºC	[60]

$Ti(OBu)_4$	HCl	$[Ti(OBu)_4]$=0.5M,	--	HCl found to promote the formation of rutile phase.	[61]
TTIP	H_3PO_4	The sol-gel product is treated with H_3PO_4 of 2.5, 12.6 and 25.2 mM	9.4-23.7	Surface-bound phosphate delays anatase-rutile phase transformation	[62]

(Note: TTIP-$Ti(OC_3H_7)_4$, AcOH-CH_3COOH, TBT- tetrabutyl titanate)

However, the practical application of TiO_2 is limited because of high electron-hole recombination rate at the surface and at the bulk of the semiconductor and low photoelectric conversion efficiency. In addition to this, its wide band-gap energy limits the absorption of light with wavelength less than 387 nm, which is about 3-5% of sunlight energy.[63]

1.3.1.4. Limitations and scope

For the industrial utilization of photocatalysis process, the major issues to be addressed are the reactor configuration and lower efficiency of illumination.[64] The two main factors which limit the scale-up of photocatalytic reactor are the light distribution inside the photoreactor through absorbing and scattering liquid onto nano-TiO_2 and providing nanocrystalline TiO_2 having higher specific surface-area.[41] Another important factor which limits the large scale use of nano-TiO_2 photocatalysis is its separation from the treated water and the requirement of an additional set up for controlling the loss of catalyst to the environment. Aeration is used in some reactor to keep the nano-TiO_2 in the suspended form.[41] Immobilization of photocatalyst on the inert support may eliminate the difficulty in separation and aeration step. However, it results in the reduction of a number of active sites and also causes reflection of light by the support along with enlarged mass transfer limitation.

To overcome some of the limitations of photocatalysis process, in the present thesis, high specific surface-area nanocrystalline TiO_2 predominantly containing single anatase phase would be synthesized by using the acid-catalysts modified sol-gel process. Further, its photocatalytic activity would be investigated and compared with that of commercially available nano-TiO_2. Moreover, the as-synthesized pure nanocrystalline anatase-TiO_2 synthesized via acid-catalysts modified sol-gel process would be subsequently utilized as precursors for the synthesis of 1-dimensional titania and titanate-based nanostructures and nanocomposites using the hydrothermal method. The 1-dimensional titania and titanate-based nanostructures and nanocomposites are known to be useful for the dye-removal from aqueous solutions via adsorption and AOPs without the use of any external irradiation.[65,66]

1.3.2. Adsorption

1.3.2.1. Principle

Adsorption is one of the widely used techniques for the removal of organic synthetic-dyes because of its low cost, easy operation, and availability of wide range of adsorbents.[67] Besides, it can be utilized for the removal of soluble and insoluble organic and inorganic pollutants. Adsorption is the cheapest method for the wastewater treatment. A comparison of cost effectiveness for different available methods for the water / wastewater treatment follows the following order adsorption > evaporation > aerobic > anaerobic > ion exchange > electrodialysis > micro- and ultra filtration > reverse osmosis > precipitation > distillation > oxidation > solvent extraction.[5] Adsorption of dyes is a mass transfer process which involves the transfer of dye molecules from the solution to the surface of adsorbent and its subsequent binding to the latter by physical or chemical interactions.[68] Adsorption is divided into chemical and physical sorption. In the chemical

absorption, there exists strong chemical association between the adsorbate and adsorbent generally due to exchange of ions which is irreversible; whereas, in the physical absorption, there is weak van der Waals intra-particle bond between the adsorbate and adsorbent which is reversible in most of the cases. The main physical forces involved in the adsorption process are hydrogen bonds, van der Waals forces, and dipole-dipole π-π interaction. Adsorption process is superior to other treatment process because of its simplicity of design, low initial cost, and ease of operation. Factors which affect the adsorption process include adsorbent surface-area, adsorbent particle size, type of interaction between adsorbent and adsorbate, adsorbent to adsorbate ratio, temperature, pH, and contact time.[69,70] pH is the one of the most influencing parameters for the adsorptive removal of dyes. Yagub et al. studied the variation of adsorption with pH for the removal of cationic dye methylene blue (MB) by adsorption on to raw pine leaf biomass and observed that adsorption increases with increase in the solution pH.[71]

The adsorption ability for the dyes and the type of catalyst surface are governed by the point-of-zero-charge (pH_{pzc}). The pH at which the surface charge is zero is called the point-of-zero-charge and this parameter is used to quantify the electrokinetic phenomenon at the surface. The adsorption of cationic dyes is favored when the pH >pHpzc where the surface becomes negatively charged, and adsorption of anionic dyes is favored when the pH< pH_{pzc} where the surface becomes positively charged.[72] The initial dye concentration has also have a strong influence on the adsorption. Yagub et al. studied the adsorption of MB on pine leaves and observed that when the initial dye concentration increases from 10 to 90 mg l^{-1}, the percentage of dye removed is decreased from 96.5 to 40.9%.[71] Temperature is another factor which strongly influences the adsorption. If the adsorption increases with temperature, the process is endothermic; and if the adsorption decreases with increase in temperature, then the adsorption is exothermic. However the

adsorption of dyes from aqueous solution is mostly found to be endothermic.[9] Another parameter which affects the adsorption is the amount of the adsorbent, in almost all cases the adsorption is reported to be increases with the quantity of adsorbent.

1.3.2.1.1. Kinetics

The mechanisms underlying the adsorption process such as the mass transfer coefficient, diffusion control, and chemical reaction are used to determine the kinetics model. The kinetics of adsorption process is prerequisite for choosing the optimum condition for scaling up the process of adsorption. Kinetics studies illustrate the rate of adsorption of solute onto the adsorbent surface and this rate is very important when developing an adsorptive system. The different kinetic models for the adsorption of dyes are discussed below.

Lagergren pseudo-first-order model

The linear form of Lagergren pseudo-first-order model is expressed as[73]

$$\log(q_e - q_t) = \log(q_e) - \left(\frac{k_1}{2.303}\right)t \qquad (1.12)$$

where, q_t and q_e are the adsorption capacities at time t and at equilibrium respectively (mg g^{-1}), k_1 the rate constant of pseudo-first-order adsorption (min^{-1}) and t the contact time (min). To plot $\log(q_e - q_t)$ versus t gives a linear relationship from which k_1 and predicted value of q_e can be determined from the slope and intercept of the plot respectively.

Pseudo-second-order model

The differential equation corresponds pseudo-second-order model is described as,[74]

$$\frac{dq_t}{dt} = K_2(q_e - q_t)^2 \qquad (1.13)$$

Where, k_2 (g mg^{-1} min^{-1}) is the second-order rate-constant of adsorption. Integrating the above equation at the boundary conditions, q_t =0 to q_t at t = 0 to t, we get the linear forms of Lagergren pseudo-second-order kinetics model, which can be expressed as,

$$\frac{t}{q_t} = \left(\frac{1}{q_e}\right)t + \frac{1}{q_e^2 k_2} \tag{1.14}$$

The plot of t/q_t versus t shows a linear relationship. The values of k_2 and equilibrium adsorption capacity q_e can be calculated from the intercept and slope of the plot of t/q_t versus t according to the above Eq. (1.14).

Intra-particle diffusion model

The adsorption process generally follows several steps involving the transport of adsorbate to the adsorbent surface, followed by the adsorption of molecule to the interior of solid pores. Weber and Morris investigated that the amount of adsorption varies almost proportional with $t_{1/2}$ rather than with the contact time and can be expressed as,[75]

$$q_t = (k_{id})t^{0.5} \tag{1.15}$$

Where, q_t is the adsorption capacity at time t, $t^{0.5}$ the half-life time in second, and k_{id} (mg g^{-1} min$^{-0.5}$) the rate constant of intraparticle diffusion. In order to find out the rate constants, plot of q_t versus $t^{0.5}$ gives a linear relationship, and k_{id} can be determined from the slope of the plot. The best fit model in which the adsorption follows can be calculated from the values of the linear regression correlation coefficient, $<r^2>$. Along with the values of $<r^2>$, the suitability of various kinetics models can be verified through the analysis of sum of squared errors (SSE, %) given by the Eq. (1.16).

$$SSE,\% = \sqrt{\frac{\sum (q_{e,\exp} - q_{e,cal})^2}{N}} \tag{1.16}$$

The higher the value of R^2 and lower the value of SSE, % will be the goodness of the fit for a particular kinetics model.

1.3.2.1.2. Isotherms

The adsorption isotherm study explains how the adsorbent interacts with the adsorbate and gives the idea of adsorption capacity. These isotherms are very important for understanding the mechanism of dye adsorption. Langmuir, Freundlich, and Dubinin-Kaganer-Radushkevich (DKR) models are the most widely used models for describing the adsorption.

Langmuir isotherm

Langmuir adsorption isotherm is depended upon the monolayer adsorption capacity of the adsorbent by assuming that adsorbate forms a uniform monolayer at the adsorption saturation. This adsorption isotherm model is based on three hypothesis, (i) the uptake of the adsorbate occurs on homogeneous surface by monolayer adsorption, (ii) there is no interaction between the ions of the adsorbate and (iii) there is no transmigration of the adsorbate in the plane of the surface of the adsorbent.[4,76] The Langmuir equation for adsorption can be expressed as,[76]

$$q_e = \frac{q_m K_L C_e}{1 + K_L C_e} \tag{1.17}$$

Where, q_e is the amount of dye adsorbed at equilibrium time (mg g^{-1}), C_e the equilibrium concentration of dye in solution (mg l^{-1}), q_m the maximum adsorption capacity (mg g^{-1}) and K_L the isotherm constants for Langmuir (l mg^{-1}). The linearised form of Langmuir isotherm can be written as,

$$\frac{C_e}{q_e} = \left(\frac{1}{q_m}\right) C_e + \frac{1}{q_m \times K_L} \tag{1.18}$$

From Langmuir plot, the separation factor, R_L can be determined as per the following relation,

$$R_L = \frac{1}{1+(K_L \times C_o)} \quad (1.19)$$

Where, C_0 is the initial dye concentration (mg l^{-1}) and R_L indicates the type of adsorption - irreversible (R_L =0), favorable (0 < R_L < 1), linear (R_L = 1), or unfavorable (R_L > 1). From the value K_L, the standard Gibb's free energy, ΔG^0 (J mol^{-1}), can be estimated using the relationship of the form,[77,78]

$$\Delta G^0 = -RT \ln K_L \quad (1.20)$$

Freundlich isotherm

Freundlich adsorption isotherm model is based on the assumption that the binding affinities on the adsorbent surface changes with interactions between adsorbed molecules. As a result the sites with higher affinities are occupied first. This model considers a heterogeneous adsorption surface that has unequal available site with different energies for adsorption. The equation corresponds to Freundlich adsorption model is given by,[79]

$$q_e = K_f C_e^{1/n} \quad (1.21)$$

The linearised form of Freundlich model can be expressed as,

$$\ln q_e = \left(\frac{1}{n}\right) \ln C_e + \ln K_F \quad (1.22)$$

Where, q_e is the amount adsorbed at equilibrium time (mg g^{-1}), C_e the equilibrium concentration of dye in solution (mg l^{-1}), K_F the Freundlich constant (mg g^{-1}) related to the Gibb's free-energy of adsorption and q_m, n the constant (g l^{-1}) which is related to the adsorption intensity. The plot of lnq_e versus lnC_e is employed to determine the values of K_F and n from the intercept and slope respectively.

DKR isotherm

The linear form of equation corresponding to DKR isotherm is given as,[77]

$$\ln q_e = \ln q_m - \beta\varepsilon^2 \tag{1.23}$$

Where, β (mol^2 J^{-2}) is a constant related to the adsorption energy and ε the Polanyi potential which is given by the equation of the form,[77,80]

$$\varepsilon = RT \ln(1 + \frac{1}{C_e}) \tag{1.24}$$

Where, R (J mol^{-1} K^{-1}) is a gas constant and T (K) the absolute temperature. The adsorption energy (E, k J mol^{-1}) can be calculated using the relationship of the form,[77,80]

$$E = \frac{1}{\sqrt{-2\beta}} \times 10^{-3} \tag{1.25}$$

1.3.2.2. Nanomaterials developed

Cost effectiveness and technical applicability are the main factors behind the selection of suitable adsorbents. Nanomaterials have high adsorption ability when compared to conventional adsorbents due to their small size, high specific surface-area, high porosity, and the presence of a large number of active surface sites. Nanoadsobents are capable of sequestration of large quantities of pollutants with varying molecular size, hydrophobicity, and speciation behavior without releasing any toxicity.[81] The main advantage of using nanomaterials for adsorption process are their rapid action, high adsorption capacities, and ease of regeneration of the adsorbent.[67] The above characteristics of nanomaterials make them to use as potential adsorbents for the removal of various pollutants like organic synthetic-dyes, heavy metal ions, and radioactive wastes.

Many textile industries use activated carbon (AC) as the adsorbent for the removal of dyes. Costly nature and difficulty in the separation from the treated solution are the main

drawbacks of activated carbon which leads to the search for other suitable dye adsorbent for the pollution control and prevention. To achieve high dye removal capacities, nanomaterials are becoming new alternative. Table 1.6 summarizes the different nanomaterials used for the adsorptive removal of MB dye from aqueous solution.

Table 1.6. Comparison of various nanomaterials used for the adsorptive removal of MB dye.

Nanomaterial	**Specific surface area** (m^2 g^{-1}**)**	pH	Adsorption capacity (mg g^{-1})	Reference
Alkali activated MWCNTs	534.6	7	399	[82]
Iron terephthalate (MOF-235)	-	10	187	[83]
Graphene/magnetite		11	35.42	[84]
Graphene oxide	-	6	714	[85]
Grapheme oxide/ Fe_3O_4	-	7	190.14	[86]
graphene	295.56	10	153.85	[87]
Grapheme/CNT	78.9	10	81.87 (Langmuir)	[88]
Carbon nanotube	160	7	46.2	[89]
Titanate nanotube	330	10	105	[78]
Titanate nanosheet	380	10	119	[90]
MWCNT/ Fe_3O_4	-	-	48.06 (Langmuir)	[91]
Fe_3O_4@ZIF-8	1068	7	20.2	[92]
Graphene Oxide sponge		10	374	[93]

(Note: MWCNT-multi-walled carbon nanotubes, GO-graphene oxide, MOF-metal organic framework, ZIF-Zeolitic imidazolate frameworks)

1.3.2.3. Titania and titanate-based nanomaterials

Layered titanate materials have attractive properties like large ion exchange capacity, fast ion diffusion, intercalation, and high surface charge density. This favorable property of titanate nanomaterials are due to their unique crystal structure were negatively charged titanium containing sheets are separated by large distance by exchangeable cations and molecules in the interlayer.[94] Another peculiar property of titanate-based nanomaterials is that they can be transformed to TiO_2; thus, allowing the use of titanate-based nanomaterials as a flexible precursor for TiO_2-nano engineering.[94] The wide world of titanate-based nanomaterials opened up after the synthesis of TiO_2 nanotubes by the alkaline hydrothermal treatment followed by the acid washing of TiO_2 nanoparticles by Kasuga et al..[95] TiO_2 nanotubes could be formed by simple process and low cost comparing the production of carbon nanotubes. Other titanate-based nanostructures including nanosheets, nanorods, nanowires, and nanobelts can be formed by adjusting the synthesis conditions. The crystal structure of layered titanates and TiO_2 has close resemblance, both composed of TiO_6 octahedra units connected by sharing corners and edges. The open crystal structure of layered titanate permits easy and uniform doping of atoms or molecular assembly which is hard to achieve with more compact TiO_2 polymorphs.[94] Because of the open crystal structure and large interlayer spacing in titanates, they can accommodate cations and neutral molecules in the interlayer spacing.[94] Large dipole moment exists in the titanate-based nanomaterials where the negative charge in the titanate layer is balanced by the positively charged interlayer cations.[94] Layered titanates have very good cation exchange capacity because the negative charge on titanate sheets can absorb positively charged molecular species effectively. This effect is applied in the wastewater treatment for the removal of radioactive ions and organic contaminants. Titanate-based nanomaterials find application in photocatalysis, Li-ion

batteries, photovoltaic, electrochromic devices, biomedical, self-cleaning and oil-water separation applications.[96,97]

1.3.2.3.1. Nanotubes

As mentioned earlier, Kasuga et al. developed a new hydrothermal route for the synthesis of TiO_2 nanotubes by the alkaline hydrothermal treatment of amorphous TiO_2 without the involvement of any templates.[95] This technique was later extended to different precursors of TiO_2 including anatase, rutile, and commercial P25.[98] In a typical process, TiO_2 powder is treated with concentrated solution of NaOH in a Teflon lined autoclave at temperature in the range of 110-150 ºC, followed by washing with HCl. In a highly alkaline surrounding, under the hydrothermal conditions, the precursor TiO_2 crystals are dissolved followed by the epitaxial growth and exfoliation of layered sheets of sodium titanate which then scroll or fold into nanotubes.[99] The mechanism of formation of nanotubes has been investigated widely and some studies indicate that the acid washing step after the hydrothermal treatment is necessary for the exchange of Na^+ ions with H^+ ions to form the nanotubes;[95,100] whereas, some other studies show that the nanotubes formation occurs during the hydrothermal step itself.[101] A general strategy for nanotube formation is 3D→2D→1D.[102] Under the highly alkaline condition during hydrothermal reaction, some of the chemical bonds (Ti-O-Ti) in the TiO_2 break into an intermediate containing Ti-O-Na and Ti-OH. The intermediate forms sheets by rearrangement of Na^+ and H^+ between sheets. The difference in surface charge arises due to the exchange of Na^+ with H^+ leads to the formation of nanotubes from sheets.[103] The walls of as synthesized nanotubes consists of multiple layers with the spacing between layers of about 0.78 nm. Moreover, the number of layers on either side of nanotubes are unequal which suggest that the nanotubular structure is evolved from the curling of

nanosheets.[104,105] According to the literature, the nanotubes formation via hydrothermal occurs through four steps,[72]

(1) In the primary stage, under the highly alkaline environment, TiO_2 precursor dissolves and then breaks Ti-O-Ti bonds.

(2) The formation followed by the growth of layered sheets of sodium titanate.

(3) Exfoliation of nanosheets.

(4) Growing of nanosheets with increasing tendency of curling leading to the formation of nanotubes.

Wang et al.[102] suggested that lamellar TiO_2 has a tendency to bend to saturate the dangling bond at the edge of layered structure, and thus, acts as a driving force for the formation of nanotubes. First principle ab initio calculations on single trititanates nanosheet indicate that the asymmetric distribution of H atoms on the two sides of surface of layered sheets provide the driving force for rolling it into nanotubes.[106] The acid washing conducted after the hydrothermal treatment has great influence on the crystallinity and specific surface-area of hydrothermal product.[107] Normally, acid washing has two effects– first, the elimination of Na^+ ions and structural H_2O; and secondly, the morphological evolution where nanosheets could transform into nanotubes by acid treatment.

The obtained hydrothermal product is multi-walled, scroll type, open ended nanotubes of having inner diameter ~6 nm with layer spacing of ~0.7 to 0.8 nm and the layered titanates having possible crystal forms like lepidocrocite-type titanate ($H_xTi_{2-x/4}V_{x/4}O_4$, where x∼0.7, V represents vacancy),[108] monoclinic trititanates ($H_2Ti_3O_7$) or tetratitanates, orthorhombic titanates ($H_2Ti_2O_4(OH)_2$, or $H_2Ti_4O_9{\cdot}H_2O$, $H_{4x}Ti_{2-x}\square_xO_4{\cdot}H_2O$), monoclinic TiO_2-(B), as well as tetragonal anatase.[97,109] The exact crystal structure of titanate nanotube is still incomplete due to the following several reasons. First, large number of

crystal modifications are possible for both pure TiO_2 and protonated forms of polytitanic acids $H_{2m}Ti_nO_{2n+m}$. Secondly, small crystal size leads to small value for coherence area resulting in the broadening of reflection in XRD pattern. Third, wrapping along certain crystallographic axes leads to widening of peaks for a given Miller indices making interpretation most difficult. Fourth, the instability of the structure of titanate undergoing easy phase transformation during heating, acid treatment, and chemical treatment.[97] The factors which affect the formation of nanotubes during the hydrothermal treatment are,

i) Phase and particle size of the starting material.

ii) Type and concentration of alkali solution.

iii) Hydrothermal temperature and duration.

iv) Washing procedure (acid concentration, time, sequence of washing with solvent and acid).

The as synthesized nanotubes are of sodium titanates rather than anatase TiO_2, this is supported by the following factors,[97]

(i) Characteristics of reflection at the small angle in the X-ray.

(ii) Low isoelectric point (~3) and negative value of zeta potential in aqueous solution due to the acid-base dissolution of titanates.

(iii) Adsorption of cations onto the surface of nanotubes.

(iv) Higher ion exchange capacity.

(v) Dependence of interlayer distance in nanotube wall on the amount of Na^+ ions inside the nanotubes.

The alkaline hydrothermal treatment of anatase TiO_2 followed by acid washing results in the formation of layered titanates. Even though the proposed crystalline phase of hydrothermal product first reported by Kasuga et al. was of anatase,[95] it was due to their wrong assumption. In order to synthesize anatase TiO_2 nanostructures, the hydrothermal

product must undergo thermal treatment.[110] Zakharova et al. synthesized anatase nanotubes with length around 150 nm, inner diameter around 4-6 nm, and outer diameter around 10-15 nm after the calcination at 500 ºC of hydrothermally synthesized nanotubes;[111] whereas, the calcination treatment at 400 ºC results in the formation of mixed anatase and TiO_2 (B).[112] Bavykin et al. reported that thermal treatment above 400 ºC which resulted in change in the morphology to nanorods.[113] However, the thermal treatment results in the reduction in aspect ratio of nanotubes as well as leads to its morphological transformation to another titania nanostructures.[96] This prevents the use of anatase nanotubes from many applications like solar cells.[114] Hence, the synthesis of anatase TiO_2 nanotubes without involvement of thermal treatment are highly beneficial for many functional applications. Hydrogen titanate nanotubes (HTN) are characterized by their high specific surface-area and large ion-exchange capacity. Hence, they are widely used as adsorbent for the removal of various kinds of organic and inorganic pollutants. Table 1.7 summarizes the application of titanate nanotubes for the adsorptive removal of MB dye.

Table 1.7. Adsorptive removal of MB dye using various titanate nanostructures.

Processing Method	**Morphology**	**Crystalline Characteristics**	**Specific Surface-Area ($m^2 g^{-1}$)**	**pH**	**Adsorption Capacity ($mg g^{-1}$)**	**Reference**
Hydrothermal, Calcination @400 ºC	Mixed nanobelts, nanotubes, and nanorods	$H_2Ti_3O_7$		7	92%	[65]
		$H_2Ti_3O_7$ (calcined 400 ºC)	180		97%	
Hydrothermal	Nanotubes	$H_2Ti_3O_7$	250	4-5		[115]
Hydrothermal	Nanotubes	Hydrogen titanate	210.4	7	55.8%	[116]

Hydrothermal	Hydroxyl group enriched TiO_2 nanotubes	Anatase TiO_2	196.5	8.3	57.14	[117]
Hydrothermal, calcination @550 ºC	Nanotubes	Titanate	157.9	7	133.33	[118]
Hydrothermal	Nanotubes	Titanate	91.7	7	197	[119]

1.3.2.3.2. Nanosheets

Conventionally, layered titanates are synthesized via two methods, either by alkali wet method or solid-state method. In alkali wet method, the titanium precursor is dissolved in concentrated alkali solution and the mixture is then undergoes refluxing or hydrothermal treatment. On the other hand, the solid-state method involves the calcination of mixture of TiO_2 and alkali carbonates such as Cs_2CO_3, Na_2CO_3, or K_2CO_3 at very high temperature (600-1000 ºC).[120] As a result of above two reactions, metal titanates are first produced which upon ion-exchange with protons during the treatment with acids (HCl and HNO_3) results in the formation of layered titanates. Table 1.8 summarizes the reported methods for the preparation of titanates nanosheets and its environmental application. Nanosheets up to the specific surface-area 420 m^2 g^{-1} are obtained and it is used for many applications including the removal of contaminants from the wastewater.

Table 1.8. Synthesis and environmental applications of titanate nanosheets.

Precursor	**Processing condition**	**Characteristics**	**Application**	**Reference**
$Ti(OBu)_4$	Urea is treated with TBOT at 90 ºC for seven days followed by washing with EtOH	Protonic titanate ($H_2Ti_2O_5 \cdot H_2O$) nanosheets S_{BET} = 379 m^2g^{-1}.	Adsorption for methylene blue and Pb^{2+}	[120]
TTIP	Hydrothermal treatment at 180 ºC for 24 h followed by calcination at 450 ºC for 30 min, followed by washing with EtOH and H_2O	Anatase TiO_2 nanosheets, S_{BET} = 44 m2g1	Adsorption of N719 Dye	[121]

$Ti(OBu)_4$	Hydrothermal with the assistance of HF solution at 180 ºC for 24 h followed by washing with EtOH and H_2O	Anatase TiO_2 nanosheets	Cyclic dye degradation by photocatalysis	[122]
Anatase-TiO_2 coated Flyash Particles	Hydrothermal at 120 ºC for 30 h followed by washing with HCl and H_2O	Hydrogen titanate nano-sheets, ($H_2Ti_nO_{2n+1}$) S_{BET} = 380 m^2g^{-1}.	Adsorption of MB Dye	[123]
Ti foil	Hydrothermal treatment in at 180 ºC for 30 h, washed with deionized water, immersed into 0.6 M HCl for 24 h, calcination	Titanate nanosheet	Photocatalytic catalytic activity under UV light	[124]
$Ti(OBu)_4$	Hydrothermal treatment at 180 °C for 24 h in mixture of KOH and NaOH followed by washing with distilled water and alcohol, again hydrothermally treated in HCl for temperatures 100-180 ºC	Lepidocrocite-like layered protonated titanate ($H_2Ti_2O_5 \cdot H_2O$), S_{BET} = 35-83 m^2g^{-1}.	Highly selective adsorption ability with excellent photocatalytic activity toward ciprofloxacin	[125]

(Note: TTIP-$Ti(OC_3H_7)_4$, EtOH-ethanol, TBOT- titanium n-butoxide)

Among these synthesis procedures, alkali wet method is more appropriate when compared to solid-state method because it involves high temperature treatment.[120] However, the alkali wet method after washing results in the formation of elongated morphologies of titanates such as the nanotubes or nanofibers, which consist of folded layers of nanosheets.[126-128] Unfolded titanate nanosheets can be prepared by adjusting the experimental conditions such as the reaction time, temperature, and concentration of alkali solution. Hareesh et al. investigated a novel method for the synthesis of hydrogen titanate nanosheet (HTNS) from the hydrothermal treatment of anatase TiO_2 coated flyash. In this case, flyash (FA) contains heavy metals/compounds such as SiO_2 which can prevent the rolling of layered titanate nanosheets into nanotubes, which may result in the stabilization of nanosheet morphology.[123] Since the titanate nanosheets have comparatively higher specific surface-area, it can be used for the adsorptive removal of various inorganic and organic contaminants from aqueous solution.[120,125,129] Even though many have synthesized and utilized titanate nanosheets for water decontamination

purpose, the magnetic nanocomposites of hydrogen titanate nanosheets, which may allow their easy separation from the treated solution, has not been processed yet. Interestingly, after the adsorption of contaminants, the magnetic nanosheets can be easily separated from the aqueous solution with the help of an external magnet and the adsorbent can be surface cleaned for its cyclic dye adsorption applications. Hence, the regeneration of magnetic nanosheets is also a challenging task for utilizing them for the treatment of wastewater.

1.3.1.4. Limitations and scope

Although several nanomaterials are observed to be very effective for the adsorptive removal of various contaminants from the aqueous solution, they suffer from various drawbacks. First, the adsorption process is noted to be ineffective typically when the initial concentration of contaminants is very high. Secondly, the formation, handling, storage, and reuse of large amount of sludge produced are the major concerns for this mechanism. Third, the separation, regeneration, and reuse of adsorbents after the removal of organic contaminants are the major obstacles in the effective use of this mechanism in the dye-removal application. Overall, all the aforementioned factors strongly limit the industrial application of adsorptive dye removal from the aqueous solutions and wastewater, which strongly demand the development of novel nanomaterials to resolve these issues.

In order to overcome some of the limitations associated with the adsorption process, in the present thesis, high specific surface-area nanotubes of pure and modified hydrogen titanate as well as those of anatase-TiO_2 would be synthesized using the combination of sol-gel and hydrothermal processes. Pure and magnetic nanocomposites based on the HTNS would also be synthesized by using the combination of modified hydrothermal

and ion-exchange processes. Further, the dye adsorption characteristics of these novel nanostructured adsorbents would be investigated. Moreover, the magnetic separation, regeneration, and reuse of novel adsorbents involving the innovative approaches (such as AOPs) would be demonstrated.

1.3.3. AOPs

1.3.3.1. Principle

AOPs are the set of processes which involve in-situ generation of $^{\bullet}OH$ having very high oxidative potential (standard potential=2.80V) and responsible for the degradation of organic contaminants present in the wastewater. AOPs are known to be the most efficient methods for the water decontamination because of their ability to mineralize the organic pollutants rapidly as compared to the traditional treatment technologies. AOPs are found to be effective for the degradation of halogenated hydrocarbon, aromatic com (1.26) volatile organic compounds, detergents, pesticides, and have non-hazardous eco-friendly end-product.[130,131] The degradation of organic compounds occurs through electron transfer, radical-radical interactions, hydrogen atom abstraction, or electrophilic additions depending on the structure of organic compounds.[132] AOPs based on the Fenton process is a strong oxidation system used for the degradation of recalcitrant organic compounds.[133,134] The reaction between H_2O_2 and Fe^{2+} produces $^{\bullet}OH$ according to the reactions,

$$Fe^{2+} + H_2O_2 \longrightarrow Fe^{3+} + OH^- + OH^{\bullet} \quad (1.26)$$

$$Fe^{3+} + H_2O_2 \longrightarrow Fe^{2+} + HO_2^{\bullet} + H^+ \quad (1.27)$$

In addition to the classical Fenton reaction, other oxidation systems developed for the AOPs are summarized in Table 1.9.

Table 1.9. Classification of AOPs.[135]

Non-photochemical	**Photochemical**
Homogeneous processes	
Ozonation	Photolysis
Ozonation with hydrogen peroxide (O_3/H_2O_2)	UV/H_2O_2
Fenton (Fe^{2+} or Fe^{3+}/H_2O_2)	UV/O_3
Wet air oxidation	$UV/O_3/H_2O_2$
Electrochemical oxidation	Photo-Fenton ($Fe^{3+}/H_2O_2/UV$)
Heterogeneous processes	
Catalytic wet air oxidation	Heterogeneous photocatalysis
Fenton catalytic ozonation	

The main advantages of AOPs are (i) it provides complete mineralization of pollutant into non-toxic products such as H_2O, CO_2, and inorganic salts, (ii) it is used for the treatment of organic pollutants which are resistant to other treatment methods, (iii) it has high bimolecular reaction rate-constant (10^8-10^{11} $M^{-1}s^{-1}$) and non-selectivity of $^{\bullet}OH$ results in high efficiency for removing recalcitrant organic compounds, (iv) it operates at ambient temperature and pressure and (v) it can be used in combination with other treatment methods. [135,136]

1.3.3.2. Nanomaterials developed

1.3.3.1.1. Heterogeneous activation of H_2O_2

Even though homogeneous Fenton process is an effective procedure for the decomposition of organic synthetic-dyes, it suffers from several disadvantages which include the formation of iron hydroxide sludge, narrow operational pH range, difficulty in the catalyst recovery, and high cost.[137] These drawbacks prevent the industrial application of homogeneous Fenton process for dye removal. Heterogeneous Fenton process is, hence, developed in which the active metal present on the surface of support

acts as catalyst for the production of reactive oxygen species (ROS), thereby degrading the dyes.[138] Heterogeneous Fenton process exhibits higher catalytic activity due to higher kinetics of the degradation of organic pollutants. The main advantages of heterogeneous AOPs are as follows. First, the oxidizing radicals are generated at ambient pressure and temperatures. Secondly, it is a simple process, and hence, easy to implement and couple with other processes such as the coagulation, adsorption, filtration, and biological oxidation. Third, the reaction time for dye-removal is relatively lower. Fourth, it results in a complete mineralization of the pollutant into harmless products such as CO_2 and H_2O.[136] Various solid catalysts such as iron minerals and iron oxide loaded materials are found to have greater ability to degrade organic pollutants; on the other hand, materials such as FA, activated carbon, clay materials, zeolites, and alumina are found to be effective catalyst supports.[139] Substitution of iron oxide with transition metal via co-precipitation method is found to be effective for the degradation of dyes.[140] Various advanced nanostructures and their composites which are effective in the degradation of organic pollutants by the activation of H_2O_2 are given in the Table 1.10.

Table 1.10. Nanomaterials for heterogeneous activation of H_2O_2.

Catalyst	**Concentration of H_2O_2**	**Dye**	**Remarks**	**Reference**
Au/TiO_2 nanotubes	0.15 M	Methyl orange	83 % TOC removal is achieved when T=80 ºC	[141]
CuO nanowires supported on Graphite film	30 wt%	Congo red	97.5% dye degradation is achieved in 36 min	[142]
CuO nanowires and nanorods	30 wt%	Rhodamine B	1D nanomaterials shows improved catalytic activity compared to nanoparticles	[143]
Titanate nanotubes	0.1 M	Methylene blue	Titanate nanotubes have higher catalytic activity than anatase TiO_2 or P25	[144]

Fe_3O_4/MWCNTs	30 wt%	Methylene orange	99.86% of dye discoloration obtained	[145]
Cylindrical mesopores of MWCNTs	1 M	C.I. Reactive Red 241	Oxidized sample shows reduction in catalytic activity	[146]
GO–Fe_3O_4	22 mM	Acid Orange 7	98% of dye degradation after 3 h	[147]

(Note: MWCNT-multi-walled carbon nanotubes, GO-graphene oxide, TOC-total organic carbon)

Babitha et al. reported that MB dye could be decomposed on the surface of HTN by the AOP using H_2O_2.[66] The mechanism for the formation of active species are given as,

$$H_2O_2 \xrightarrow{HTN} O_2^{\bullet -} + 2H^+ + \bar{e} \quad (1.28)$$

$$H_2O_2 + O_2^{\bullet -} \xrightarrow{HTN} HO^{\bullet} + OH^- + O_2 \quad (1.29)$$

Both $^{\bullet}OH$ and $O_2^{\bullet -}$ will react with the dye molecules attached to the surface of nanotubes resulting in its mineralization and demonstrated the degradation of dyes for eight consecutive cycles. Bonino et al. suggested that Ti(IV) can interact with H_2O_2 to produce the ROS.[148] Lorencon et al. studied the catalytic wet oxidation of MB dye in the presence of titanate nanotubes by using electron paramagnetic resonance (EPR) spectra analysis and reported the formation of $O_2^{\bullet -}$ by the interaction of H_2O_2 with the terminal sites $TiO:^-$ of titanate nanotubes.[144] They also observed that the thermal treatment results in the reduction of catalytic activity. Chen et al. studied the oxidation of three different dyes (rhodamine 6G, methyl blue, and methyl orange) using the hydrothermally prepared Fe-titanate catalyst and studied the effect of pH, concentration of H_2O_2, dosage of catalyst, and reaction time and successfully demonstrated the dye degradation for three cycles.[149] It is found that this catalyst can be used near neutral pH which is beneficial for the dye degradation compared to the classic Fenton catalyst which is operated at pH~3. The proposed mechanism for the formation of active species is given by,

$$\equiv Fe^{2+} + H_2O_2 \rightarrow Fe^{3+} + HO^{\bullet} + HO^{-} \quad (1.30)$$

1.3.3.1.2. Heterogeneous activation of persulfate

The major drawback of H_2O_2 based AOP is that H_2O_2 is hazardous in nature, generates storage problems and high capital cost for the industrial application. Hence, the development of cost-effective, efficient, and non-hazardous oxidants as an alternative to H_2O_2 is essential. Oxidants such as persulfate and peroxymonosulfate, which are chemically stable crystalline solid, cheaper, more convenient to transport, store and use, are effective in replacing H_2O_2 in AOPs.[150,151] Table 1.11 **s**ummarizes the redox potential (E^0) of various oxidants in aqueous solution.

Table 1.11. The redox potential (E^0) of various oxidants in aqueous solution.[152]

Oxidant	**Redox-potential (E^0)**
Fluorine	3.03
Hydroxyl radical	2.70
Sulfate radical	2.60
Atomic oxygen	2.42
Ozone	2.07
Persulfate anion	2.01
Hydrogen peroxide	1.78
permanganate	1.68

The peroxo (O-O) bond distance and its energy is 1.497 Å and 140 kJ mol^{-1}, respectively.[153] Various studies are conducted to activate persulfate to form ROS like $^{\bullet}OH$ and $SO_4^{\bullet-}$ or non radical pathway to induce oxidation, which includes the use of iron-

based materials like Fe^0, Fe^{2+}, goethite (α-FeO(OH)), magnetite (nano-Fe_3O_4), heat, UV light, electrochemical, and ultrasonication methods.[154] The activation of persulphate results in the formation of sulfate radicals ($SO_4^{\bullet-}$) and $^{\bullet}OH$ which are responsible for the mineralization of organic compounds into CO_2 and H_2O. Persulphate anion ($S_2O_8^{2-}$) is stable at room temperature and the cleavage of peroxide bond is initiated by heat, UV light, or transition metal ions according to the following reactions,[154]

$$S_2O_8^{2-} \xrightarrow{\Delta / h\upsilon} 2SO_4^{\bullet-} \quad (1.31)$$

$$S_2O_8^{2-} + M^{n+} \longrightarrow SO_4^{\bullet-} + SO_4^{2-} + M^{(n+1)+} \quad (1.32)$$

$$SO_4^{\bullet-} + H_2O \longrightarrow HO^{\bullet} + H^{+} \quad (1.33)$$

$$SO_4^{\bullet-} + HO^{-} \longrightarrow SO_4^{2-} + HO^{\bullet} \quad (1.34)$$

$SO_4^{\bullet-}$ initiate a chain reaction leading to the degradation of dyes.[155]

$$S_2O_8^{2-} + R \longrightarrow 2SO_4^{\bullet-} + R^{\bullet} \quad (1.35)$$

$$2SO_4^{\bullet-} + H_2O \longrightarrow HO^{\bullet} + HSO_4^{-} \quad (1.36)$$

$$SO_4^{\bullet-} + R \longrightarrow R^{\bullet} + SO_4^{2-} \quad (1.37)$$

$$R^{\bullet} + S_2O_8^{2-} \longrightarrow SO_4^{\bullet-} + products \quad (1.38)$$

$$HO^{\bullet} + R \longrightarrow R^{\bullet} + OH^{-} \quad (1.39)$$

The persulfate activated dye degradation kinetics is increases with its concentration, but some studies reported that the degradation is inhibited by the use of higher concentration of persulphate, pH, and presence of interfering ions.[154] Table 1.12 summarizes the different studies showing the persulfate activated dye degradation processes.

Table 1.12. Persulfate activated dye degradation by using various nanomaterials.

Catalyst	**Concentration of persulphate** (mmol l^{-1})	**Dye**	**Remarks**	**Reference**
Granular activated carbon	5.7	Acid Orange 7	Decomposition follows first-order kinetics behavior, near-neutral was the optimal initial pH, active species involved are $SO_4^{-\bullet}$ or $^{\bullet}OH$	[156]
Ultrasonication plus Fe^0	1.3	Acid Orange 7	Maximum 96.4% removal, The optimal initial pH for decolorization was found as 5.8, and ultrasonic power of 60 W	[157]
$Fe^{2+}/S_2O_8^{2-}$ and $Fe^0=S_2O_8^{2-}$	pH= 5.52, $[Fe^0]$=4.27 mM, and $[S_2O_8^{2-}]$=138.43 mM,	C.I. Reactive Red 45	54.38% mineralization	[158]
Co_3O_4 nanoparticles	[KPS]=0.5 to 2.0 mM	Orange G	Smaller particle size of catalyst, higher dosage of persulfate and catalyst, higher temperature promoted the degradation rate, Both $SO_4^{\cdot-}$ and $^{\cdot}OH$ were proved to be the primary oxidative species.	[159]
Iron-loaded activated carbon	100 mg L^{-1}	Rhodamine B	Rhodamine B removal efficiencies at pH 3, 6, and 9 were 99%, 96%, and 98% respectively.	[160]

1.3.3.3. Flyash-based nanocomposites

Flyash is a by-product of coal combustion in thermal power plants and it is estimated that the current annual production of FA is about 500 million tons.[161] FA consists of fine, powdery, spherical particles which are either solid or hollow and are amorphous in nature. The specific gravity of FA varies from 2.1-3.0 while its surface area ranges from 170-1000 m^2 Kg^{-1} and its color varies from white to dark depending on the amount of carbonaceous material present.[162] The principal component of FA are silica, iron oxide, alumina, and calcium with varying amount of carbon. The dominant mineral phases present in the FA are quartz, illite, siderite, and kaolinite. The harmful effect of FA can

be largely reduced by its reuse. It finds major application in the cement industry and also used in the preparation of zeolite. FA is used as an adsorbent for sulfur, nitrogen compounds, Hg, gaseous organics such as aromatic hydrocarbons.

Another important utilization of FA is in the wastewater treatment process. In addition to this, the alkaline nature of flyash makes it as a good neutralizing agent.[162] FA find its wide application for water decontamination processes such as the adsorption of heavy metals, anions like phosphate, organic compounds like phenols, pesticides, and dyes. However, the major limitation of FA for its application in water decontamination is the leaching of the various compounds present in the flyash to the solution and this becomes a secondary environmental pollution.[163] Various studies have been conducted to improve the properties of FA for environmental applications and are summarized in Table 1.13.

Table 1.13. Flyash based nanocomposites for environmental applications.

Modification of flyash	**Application**	**Remarks**	**Reference**
Silicalite-1/FA cenosphere-zeolite composite	Adsorption of methyl tert-butyl ether	Enhanced adsorption rate and capacity	[164]
ZnO-FA nanocomposite	Photocatalytic degradation of methyl orange	Transformation of FA structure into a mesoporous adsorber with photocatalytic properties after the in situ ZnO growth	[165]
TiO_2-FA nanocomposites	Photocatalytic degradation of methyl orange	Pronounced performance is attributed to the transformation of FA to a mesoporous structure	[166]
FA incorporated TiO_2 nanofibers	Photocatalytic removal of methylene blue and microorganism from water	Incorporation of FA into TiO_2 nanofiber strongly enhanced photocatalytic and antibacterial properties.	[167]
ZnS enwrapped FA (ZnS/A-FA) nanocomposite	Photocatalytic degradation of methylene blue	ZnS/A-FA material shows higher photocatalytic activity and antimicrobial activity compare to that of bare ZnS nanoparticles	[168]
Fe^{3+}-doped TiO_2 on FA cenospheres	Photodegradation of methyl blue under visible light	The Fe–TiO_2/FAC particles can float in water due to the low density in favor of phase separation to recover	[169]

(Fe-TiO_2/FAC)	these photocatalyst after the reaction

(Note: FA-flyash)

1.3.3.4. Limitations and scope

As mentioned earlier, AOPs provide many benefits in the removal of organic synthetic-dyes from the aqueous solutions. Nevertheless, similar to the previous dye removal processes, they are also associated with some major limitations which provide hurdles for their effective utilization for the treatment of industrial effluents on commercial scales. First, as compared to the other methods, AOPs require relatively higher capital and operating costs due to the involvement of costlier chemicals (oxidants). Secondly, in some cases, the control of solution pH and oxidant concentration becomes the most critical parameters for the successful implementation of the process. Third, the strong oxidants used in the process can produce secondary pollution. Hence, their levels must be controlled below the optimum values which can affect the overall kinetics of the dye removal process. The development of novel nanomaterials which can be used as environmental friendly solid activators for the activation of H_2O_2 and persulfate anions appears to be essential to overcome the above mentioned issues associated with the commercialization of dye-removal technology based on AOPs.

In order to overcome some of the limitations associated with the AOPs, in the present thesis, high specific surface-area nanotubes of pure and surface-modified hydrogen titanate as well as the magnetic nanocomposite based on the nanosheets of hydrogen titanate would be synthesized using the combination of sol-gel, hydrothermal, and ion-exchange processes. The regeneration of aforementioned 1-dimentsional nanostructures and nanocomposites, in the dye-removal application involving the adsorption mechanism, would be demonstrated by the involvement of AOPs. The use of magnetic flyash-based nanocomposite, as reported recently elsewhere by us,[170] would be utilized

for the removal industrial azo reactive dyes from aqueous solutions via AOPs involving cost-effective oxidizers.

1.4. Motivation and Objectives

The literature review presented here suggests that the photocatalysis, adsorption and AOPs are the three major mechanisms reported in the literature for the removal organic synthetic-dyes from the aqueous solutions and industry wastewaters. These mechanisms are, however, associated with the several limitations which pose serious hurdles in the commercialization of these technologies in the dye-removal application. It also appears that the development of novel nanomaterials processed via innovative approaches could possibly provide innovative solutions to resolve some of these major issues in the near future. This is the prime motivation for undertaking the present thesis work.

In this perspective, the overall broad objectives of the present thesis are as follows-

(1) To investigate different mechanisms such as the photocatalysis, adsorption, and AOPs for the removal of organic synthetic-dyes from the aqueous solutions.

(2) To develop the titania, titanate, and flyash-based nanostructures (such as the nanoparticles, nanotubes, and nanosheets) and nanocomposites via novel methods.

(3) To develop innovative approaches such as the sol-gel, hydrothermal, ion-exchange, inverse co-precipitation, electroless deposition, and their combination for the processing of above mentioned nanostructures and nanocomposites.

(4) To utilize the titania, titanate, and flyash-based nanostructures and nanocomposites for the removal of organic synthetic-dyes from the aqueous solutions.

(5) To understand the dye-removal characteristics of titania, titanate, and flyash-based nanostructures and nanocomposites involving three different dye-removal mechanisms.

(6) To identify a suitable dye-removal technology, involving the newly developed nanostructures and nanocomposites, for the possible commercialization in the near future based on the obtained results.

References

(1) Dowling, A. P. *Mater. Today* **2004**, *7*, 30.

(2) Whitesides, G. M. *Small* **2005**, *1*, 172.

(3) Grieneisen, M. L.; Zhang, M. *Small* **2011**, *7*, 2836.

(4) Sharma, S. K. *Green Chemistry for dyes removal from waste water: research trends and applications*; John Wiley & Sons, 2015.

(5) Ali, I. *Chem. Rev* **2012**, *112*, 5073.

(6) Qu, X.; Alvarez, P. J.; Li, Q. *Water Res.* **2013**, *47*, 3931.

(7) Bhatnagar, A.; Jain, A. *J. Colloid Interface Sci.* **2005**, *281*, 49.

(8) Hunger, K. *Industrial dyes: chemistry, properties, applications*; John Wiley & Sons, 2007.

(9) Yagub, M. T.; Sen, T. K.; Afroze, S.; Ang, H. M. *Adv. Colloid Interface Sci.* **2014**, *209*, 172.

(10) Mirshra, G.; Tripathy, M.; *Colourage*: 1993.

(11) Gupta, G.; Prasad, G.; Singh, V. *Water Res.***1990**, *24*, 45.

(12) Fu, Y.; Viraraghavan, T. *Bioresour. Technol.* **2001**, *79*, 251.

(13) Kadirvelu, K.; Kavipriya, M.; Karthika, C.; Radhika, M.; Vennilamani, N.; Pattabhi, S. *Bioresour. Technol.* **2003**, *87*, 129.

(14) Robinson, T.; McMullan, G.; Marchant, R.; Nigam, P. *Bioresour. Technol.* **2001**, *77*, 247.

(15) Asgher, M.; Bhatti, H. N. *Ecol. Eng.* **2012**, *38*, 79.

(16) Midha, V.; Dey, A. *Int. J. Chem. Sci* **2008**, *6*, 472.

(17) Buthiyappan, A.; Aziz, A.; Raman, A.; Daud, W.; Ashri, W. M. *Rev. Chem. Eng.* **2016**, *32*, 1.

(18) Mohmood, I.; Lopes, C. B.; Lopes, I.; Ahmad, I.; Duarte, A. C.; Pereira, E. *Environ. Sci. Pollut. Res.* **2013**, *20*, 1239.

(19) Ahmad, A.; Mohd-Setapar, S. H.; Chuong, C. S.; Khatoon, A.; Wani, W. A.; Kumar, R.; Rafatullah, M. *RSC Adv.* **2015**, *5*, 30801.

(20) Braslavsky, S. E. *Pure Appl. Chem.* **2007**, *79*, 293.

(21) Kubacka, A.; Fernandez-Garcia, M.; Colon, G. *Chem. Rev* **2011**, *112*, 1555.

(22) Fujishima, A. *nature* **1972**, *238*, 37.

(23) Schrauzer, G.; Guth, T. *J. Am. Chem. Soc.* **1977**, *99*, 7189.

(24) Tachikawa, T.; Fujitsuka, M.; Majima, T. *J. Phys. Chem. C* **2007**, *111*, 5259.

(25) Cozzoli, P.; Comparelli, R.; Fanizza, E.; Curri, M.; Agostiano, A. *Mater. Sci. Eng., C* **2003**, *23*, 707.

(26) Mahmoodi, N. M.; Arami, M.; Limaee, N. Y.; Tabrizi, N. S. *J. Colloid Interface Sci.* **2006**, *295*, 159.

(27) Ahmad, R.; Ahmad, Z.; Khan, A. U.; Mastoi, N. R.; Aslam, M.; Kim, J. *J. Environ. Chem. Eng.* **2016**, *4*, 4143.

(28) Chen, X.; Mao, S. S. *Chem. Rev* **2007**, *107*, 2891.

(29) Hanaor, D. A. H.; Sorrell, C. C. *J. Mater. Sci.* **2011**, *46*, 855.

(30) Pelaez, M.; Nolan, N. T.; Pillai, S. C.; Seery, M. K.; Falaras, P.; Kontos, A. G.; Dunlop, P. S.; Hamilton, J. W.; Byrne, J. A.; O'shea, K. *Appl. Catal., B* **2012**, *125*, 331.

(31) Burdett, J. K.; Hughbanks, T.; Miller, G. J.; Richardson Jr, J. W.; Smith, J. V. *J. Am. Chem. Soc.* **1987**, *109*, 3639.

(32) Doh, S. J.; Kim, C.; Lee, S. G.; Lee, S. J.; Kim, H. *J. Hazard. Mater.* **2008**, *154*, 118.

(33) Ye, L.; Zan, L.; Tian, L.; Peng, T.; Zhang, J. *Chem. Commun.* **2011**, *47*, 6951.

(34) Xu, T. G.; Zhang, C.; Shao, X.; Wu, K.; Zhu, Y. F. *Adv. Funct. Mater.* **2006**, *16*, 1599.

(35) Zhang, H.; Zhu, Y. *J. Phys. Chem. C* **2010**, *114*, 5822.

(36) Lin, D.; Wu, H.; Zhang, R.; Pan, W. *Chem. Mater.* **2009**, *21*, 3479.

(37) Chu, D.; Masuda, Y.; Ohji, T.; Kato, K. *Langmuir* **2010**, *26*, 2811.

(38) Cao, F.; Shi, W.; Zhao, L.; Song, S.; Yang, J.; Lei, Y.; Zhang, H. *J. Phys. Chem. C* **2008**, *112*, 17095.

(39) Wang, Y.; Zhang, L.; Deng, K.; Chen, X.; Zou, Z. *J. Phys. Chem. C* **2007**, *111*, 2709.

(40) Hu, J.-S.; Ren, L.-L.; Guo, Y.-G.; Liang, H.-P.; Cao, A.-M.; Wan, L.-J.; Bai, C.-L. *Angew. Chem.* **2005**, *117*, 1295.

(41) Macak, J. M.; Zlamal, M.; Krysa, J.; Schmuki, P. *Small* **2007**, *3*, 300.

(42) Fox, M. A.; Dulay, M. T. *Chem. Rev* **1993**, *93*, 341.

(43) Pérez, M. H.; Peñuela, G.; Maldonado, M. I.; Malato, O.; Fernández-Ibáñez, P.; Oller, I.; Gernjak, W.; Malato, S. *Appl. Catal., B* **2006**, *64*, 272.

(44) Kumar, S. G.; Devi, L. G. *J. Phys. Chem. A* **2011**, *115*, 13211.

(45) Zaleska, A. *Recent Patents on Engineering* **2008**, *2*, 157.

(46) Dunn, B.; Zink, J. I. *Acc. Chem. Res.* **2007**, *40*, 729.

(47) Su, C.; Hong, B.-Y.; Tseng, C.-M. *Catal. Today* **2004**, *96*, 119.

(48) Wu, M.; Lin, G.; Chen, D.; Wang, G.; He, D.; Feng, S.; Xu, R. *Chem. Mater.* **2002**, *14*, 1974.

(49) Wang, C.-C.; Ying, J. Y. *Chem. Mater.* **1999**, *11*, 3113.

(50) Sclafani, A.; Herrmann, J. *J. Phys. Chem.* **1996**, *100*, 13655.

(51) Choi, W.; Termin, A.; Hoffmann, M. R. *J. Phys. Chem.* **1994**, *98*, 13669.

(52) Serpone, N. *J. Photochem. Photobiol., A* **1997**, *104*, 1.

(53) Soria, J.; Conesa, J.; Augugliaro, V.; Palmisano, L.; Schiavello, M.; Sclafani, A. *J. Phys. Chem.* **1991**, *95*, 274.

(54) Zhao, D.; Chen, C.; Wang, Y.; Ji, H.; Ma, W.; Zang, L.; Zhao, J. *J. Phys. Chem. C* **2008**, *112*, 5993.

(55) Kanna, M.; Wongnawa, S. *Mater. Chem. Phys.* **2008**, *110*, 166.

(56) Suresh, C.; Biju, V.; Mukundan, P.; Warrier, K. *Polyhedron* **1998**, *17*, 3131.

(57) Chen, Z.; Zhao, G.; Li, H.; Han, G.; Song, B. *J. Am. Ceram. Soc.* **2009**, *92*, 1024.

(58) Behnajady, M. A.; Eskandarloo, H.; Modirshahla, N.; Shokri, M. *Photochem. Photobiol.* **2011**, *87*, 1002.

(59) Colón, G.; Sanchez-Espana, J.; Hidalgo, M.; Navío, J. *J. Photochem. Photobiol., A* **2006**, *179*, 20.

(60) Colon, G.; Hidalgo, M.; Munuera, G.; Ferino, I.; Cutrufello, M.; Navio, J. *Appl. Catal., B* **2006**, *63*, 45.

(61) Juengsuwattananon, K.; Jaroenworaluck, A.; Panyathanmaporn, T.; Jinawath, S.; Supothina, S. *Phys. Status Solidi A* **2007**, *204*, 1751.

(62) Körösi, L.; Papp, S.; Bertóti, I.; Dékány, I. *Chem. Mater.* **2007**, *19*, 4811.

(63) Xing, M.; Zhang, J.; Chen, F. *Appl. Catal., B* **2009**, *89*, 563.

(64) Zangeneh, H.; Zinatizadeh, A.; Habibi, M.; Akia, M.; Isa, M. H. *J. Ind. Eng. Chem.* **2015**, *26*, 1.

(65) Baiju, K. V.; Shukla, S.; Biju, S.; Reddy, M. L. P.; Warrier, K. G. K. *Mater. Lett.* **2009**, *63*, 923.

(66) Babitha, K. B.; Warrier, K. G.; Shukla, S. *Adv. Sci. Eng. Med.* **2014**, *6*, 173.

(67) Santhosh, C.; Velmurugan, V.; Jacob, G.; Jeong, S. K.; Grace, A. N.; Bhatnagar, A. *Chem. Eng. J.* **2016**, *306*, 1116.

(68) Pollard, S.; Thompson, F.; McConnachie, G. *Water Res.* **1995**, *29*, 337.

(69) Crini, G. *Bioresour. Technol.* **2006**, *97*, 1061.

(70) Allen, S.; Koumanova, B. *Journal of the University of Chemical Technology and Metallurgy* **2005**, *40*, 175.

(71) Yagub, M. T.; Sen, T. K.; Ang, H. *Water Air Soil Pollut.* **2012**, *223*, 5267.

(72) Liu, W.; Yao, C.; Wang, M.; Ji, J.; Ying, L.; Fu, C. *Environ. Prog. Sustainable Energy* **2013**, *32*, 655.

(73) Nandi, B.; Goswami, A.; Purkait, M. *Appl. Clay Sci.* **2009**, *42*, 583.

(74) Ho, Y.-S.; McKay, G. *Process Biochem.* **1999**, *34*, 451.

(75) Weber, W. J.; Morris, J. C. *Journal of the Sanitary Engineering Division* **1963**, *89*, 31.

(76) Langmuir, I. *J. Am. Chem. Soc.* **1918**, *40*, 1361.

(77) Narayani, H.; Kunniveetil, S. P.; Shukla, S. *Adv. Sci. Eng. Med.* **2013**, *5*, 63.

(78) Wang, S.; Boyjoo, Y.; Choueib, A.; Zhu, Z. *Water Res.* **2005**, *39*, 129.

(79) Freundlich H. M. F., *Z. Phys. Chem.*, **1906**, *57*, 385.

(80) Lee, C.-K.; Lin, K.-S.; Wu, C.-F.; Lyu, M.-D.; Lo, C.-C. *J. Hazard. Mater.* **2008**, *150*, 494.

(81) Pacheco, S.; Medina, M.; Valencia, F.; Tapia, J. *J. Environ. Eng.* **2006**, *132*, 342.

(82) Ma, J.; Yu, F.; Zhou, L.; Jin, L.; Yang, M.; Luan, J.; Tang, Y.; Fan, H.; Yuan, Z.; Chen, J. *ACS Appl. Mater. Interfaces* **2012**, *4*, 5749.

(83) Haque, E.; Jun, J. W.; Jhung, S. H. *J. Hazard. Mater.* **2011**, *185*, 507.

(84) Ai, L.; Zhang, C.; Chen, Z. *J. Hazard. Mater.* **2011**, *192*, 1515.

(85) Yang, S.-T.; Chen, S.; Chang, Y.; Cao, A.; Liu, Y.; Wang, H. *J. Colloid Interface Sci.* **2011**, *359*, 24.

(86) He, F.; Fan, J.; Ma, D.; Zhang, L.; Leung, C.; Chan, H. L. *Carbon* **2010**, *48*, 3139.

(87) Liu, F.; Chung, S.; Oh, G.; Seo, T. S. *ACS Appl. Mater. Interfaces* **2012**, *4*, 922.

(88) Ai, L.; Jiang, J. *Chem. Eng. J.* **2012**, *192*, 156.

(89) Yao, Y.; Xu, F.; Chen, M.; Xu, Z.; Zhu, Z. *Bioresour. Technol.* **2010**, *101*, 3040.

(90) Padinhattayil, H.; Augustine, R.; Shukla, S. *J. Nanosci. Nanotechnol.***2013**, *13*, 3035.

(91) Ai, L.; Zhang, C.; Liao, F.; Wang, Y.; Li, M.; Meng, L.; Jiang, J. *J. Hazard. Mater.* **2011**, *198*, 282.

(92) Zheng, J.; Cheng, C.; Fang, W.-J.; Chen, C.; Yan, R.-W.; Huai, H.-X.; Wang, C.-C. *CrystEngComm* **2014**, *16*, 3960.

(93) Liu, T.; Li, Y.; Du, Q.; Sun, J.; Jiao, Y.; Yang, G.; Wang, Z.; Xia, Y.; Zhang, W.; Wang, K.; Zhu, H.; Wu, D. *Colloids Surf., B* **2012**, *90*, 197.

(94) Zhang, Y.; Jiang, Z.; Huang, J.; Lim, L. Y.; Li, W.; Deng, J.; Gong, D.; Tang, Y.; Lai, Y.; Chen, Z. *RSC Adv.* **2015**, *5*, 79479.

(95) Kasuga, T.; Hiramatsu, M.; Hoson, A.; Sekino, T.; Niihara, K. *Langmuir* **1998**, *14*, 3160.

(96) Ou, H.-H.; Lo, S.-L. *Sep. Purif. Technol.* **2007**, *58*, 179.

(97) Bavykin, D. V.; Walsh, F. C. *Eur. J. Inorg. Chem.* **2009**, *2009*, 977.

(98) Lee, K.; Mazare, A.; Schmuki, P. *Chem. Rev* **2014**, *114*, 9385.

(99) Liu, N.; Chen, X.; Zhang, J.; Schwank, J. W. *Catal. Today* **2014**, *225*, 34.

(100) Kasuga, T.; Hiramatsu, M.; Hoson, A.; Sekino, T.; Niihara, K. *Adv. Mater.* **1999**, *11*, 1307.

(101) Morgado, E.; de Abreu, M. A.; Pravia, O. R.; Marinkovic, B. A.; Jardim, P. M.; Rizzo, F. C.; Araújo, A. S. *Solid State Sci.* **2006**, *8*, 888.

(102) Wang, Y.; Hu, G.; Duan, X.; Sun, H.; Xue, Q. *Chem. Phys. Lett.* **2002**, *365*, 427.

(103) Tsai, C.-C.; Teng, H. *Chem. Mater.* **2006**, *18*, 367.

(104) Chen, Q.; Du, G.; Zhang, S.; Peng, L.-M. *Acta Crystallogr., Sect. B: Struct. Sci* **2002**, *58*, 587.

(105) Yao, B.; Chan, Y.; Zhang, X.; Zhang, W.; Yang, Z.; Wang, N. *Appl. Phys. Lett.* **2003**, *82*, 281.

(106) Zhang, S.; Chen, Q.; Peng, L.-M. *Phys. Rev. B* **2005**, *71*, 014104.

(107) Lee, C.-K.; Liu, S.-S.; Juang, L.-C.; Wang, C.-C.; Lyu, M.-D.; Hung, S.-H. *J. Hazard. Mater.* **2007**, *148*, 756.

(108) Ma, R.; Fukuda, K.; Sasaki, T.; Osada, M.; Bando, Y. *J. Phys. Chem. B* **2005**, *109*, 6210.

(109) Pang, Y. L.; Lim, S.; Ong, H. C.; Chong, W. T. *Appl. Catal., A* **2014**, *481*, 127.

(110) Harsha, N.; Ranya, K.; Babitha, K.; Shukla, S.; Biju, S.; Reddy, M.; Warrier, K. *J. Nanosci. Nanotechnol.* **2011**, *11*, 1175.

(111) Zakharova, G.; Jahne, C.; Popa, A.; Täschner, C.; Gemming, T.; Leonhardt, A.; Buchner, B.; Klingeler, R. *J. Phys. Chem. C* **2012**, *116*, 8714.

(112) Feist, T. P.; Davies, P. K. *J. Solid State Chem.* **1992**, *101*, 275.

(113) Bavykin, D. V.; Friedrich, J. M.; Walsh, F. C. *Adv. Mater.* **2006**, *18*, 2807.

(114) Allam, N. K.; Grimes, C. A. *Langmuir* **2009**, *25*, 7234.

(115) Bavykin, D. V.; Redmond, K. E.; Nias, B. P.; Kulak, A. N.; Walsh, F. C. *Aust. J. Chem.* **2010**, *63*, 270.

(116) Nam, C. T.; Falconer, J. L.; Duc, L. M.; Yang, W.-D. *Mater. Res. Bull.* **2014**, *51*, 49.

(117) Natarajan, T. S.; Bajaj, H. C.; Tayade, R. J. *J. Colloid Interface Sci.* **2014**, *433*, 104.

(118) Xiong, L.; Yang, Y.; Mai, J.; Sun, W.; Zhang, C.; Wei, D.; Chen, Q.; Ni, J. *Chem. Eng. J.* **2010**, *156*, 313.

(119) Kazuya, N.; Baoshun, L.; Yosuke, I.; Munetoshi, S.; Hidenori, S.; Tsuyoshi, O.; Hideki, S.; Taketoshi, M.; Masahiko, A.; Katsuhiko, T.; Akira, F. *Chem. Lett.* **2011**, *40*, 1107.

(120) Lin, C.-H.; Wong, D. S.-H.; Lu, S.-Y. *ACS Appl. Mater. Interfaces* **2014**, *6*, 16669.

(121) Fan, J.; Cai, W.; Yu, J. *Chem. Asian J.* **2011**, *6*, 2481.

(122) Han, X.; Kuang, Q.; Jin, M.; Xie, Z.; Zheng, L. *J. Am. Chem. Soc.* **2009**, *131*, 3152.

(123) Hareesh, P.; Babitha, K. B.; Shukla, S. *J. Hazard. Mater.* **2012**, *229–230*, 177.

(124) Wang, C.; Zhang, X.; Zhang, Y.; Jia, Y.; Yang, J.; Sun, P.; Liu, Y. *J. Phys. Chem. C* **2011**, *115*, 22276.

(125) Wu, Q.; Yang, X.; Liu, J.; Nie, X.; Huang, Y.; Wen, Y.; Khan, J.; Khan, W. U.; Wu, M.; An, T. *ACS Appl. Mater. Interfaces* **2014**, *6*, 17730.

(126) Du, W. L.; Xu, Z. R.; Han, X. Y.; Xu, Y. L.; Miao, Z. G. *J. Hazard. Mater.* **2008**, *153*, 152.

(127) Yang, J.; Jin, Z.; Wang, X.; Li, W.; Zhang, J.; Zhang, S.; Guo, X.; Zhang, Z. *Dalton Trans.* **2003**, 3898.

(128) Nakahira, A.; Kubo, T.; Numako, C. *Inorg. Chem.* **2010**, *49*, 5845.

(129) Hareesh, P.; Babitha, K. B.; Shukla, S. *J. Hazard. Mater.* **2012**, *229–230*, 177.

(130) Muruganandham, M.; Suri, R.; Jafari, S.; Sillanpää, M.; Lee, G.-J.; Wu, J.; Swaminathan, M. *Int. J. Photoenergy* **2014**, *2014*.

(131) Munter, R. *Proc. Estonian Acad. Sci. Chem* **2001**, *50*, 59.

(132) Nogueira, R. F. P.; Trovó, A. G.; da Silva, M. R. A.; Villa, R. D.; de Oliveira, M. C. *Quim. Nova* **2007**, *30*, 400.

(133) Rocha, E. M.; Vilar, V. J.; Fonseca, A.; Saraiva, I.; Boaventura, R. A. *Sol. Energy* **2011**, *85*, 46.

(134) Ortiz de la Plata, G. B.; Alfano, O. M.; Cassano, A. E. *Appl. Catal., B* **2010**, *95*, 1.

(135) Atalay, S.; Ersöz, G. *Novel Catalysts in Advanced Oxidation of Organic Pollutants*; Springer, 2016.

(136) Bokare, A. D.; Choi, W. *J. Hazard. Mater.* **2014**, *275*, 121.

(137) Tian, S.; Tu, Y.; Chen, D.; Chen, X.; Xiong, Y. *Chem. Eng. J.* **2011**, *169*, 31.

(138) Garrido-Ramírez, E.; Theng, B.; Mora, M. *Appl. Clay Sci.* **2010**, *47*, 182.

(139) Nidheesh, P. *RSC Adv.* **2015**, *5*, 40552.

(140) Pouran, S. R.; Raman, A. A. A.; Daud, W. M. A. W. *J. Cleaner Prod.* **2014**, *64*, 24.

(141) Drašinac, N.; Erjavec, B.; Dražić, G.; Pintar, A. *Catal. Today* **2017**, *280*, 155.

(142) Liao, J.; Li, L.; Li, H. *J. Chem. Eng. Jpn.* **2016**, *49*, 771.

(143) Li, H.; Liao, J.; Zeng, T. *Catal. Commun.* **2014**, *46*, 169.

(144) Lorençon, E.; Brandão, F. D.; Krambrock, K.; Alves, D. C.; Silva, J. C.; Ferlauto, A. S.; Lago, R. M. *J. Mol. Catal. A: Chem.* **2014**, *394*, 316.

(145) Xu, H.-Y.; Shi, T.-N.; Zhao, H.; Jin, L.-G.; Wang, F.-C.; Wang, C.-Y.; Qi, S.-Y. *Front. Mater. Sci. China* **2016**, *10*, 45.

(146) Soria-Sánchez, M.; Castillejos-López, E.; Maroto-Valiente, A.; Pereira, M.; Órfão, J.; Guerrero-Ruiz, A. *Appl. Catal., B* **2012**, *121*, 182.

(147) Zubir, N. A.; Yacou, C.; Zhang, X.; da Costa, J. C. D. *J. Environ. Chem. Eng.* **2014**, *2*, 1881.

(148) Bonino, F.; Damin, A.; Ricchiardi, G.; Ricci, M.; Spanò, G.; D'Aloisio, R.; Zecchina, A.; Lamberti, C.; Prestipino, C.; Bordiga, S. *J. Phys. Chem. B* **2004**, *108*, 3573.

(149) Chen, Y.; Li, N.; Zhang, Y.; Zhang, L. *J. Colloid Interface Sci.* **2014**, *422*, 9.

(150) Zhang, T.; Chen, Y.; Wang, Y.; Le Roux, J.; Yang, Y.; Croué, J.-P. *Environ. Sci. Technol.* **2014**, *48*, 5868.

(151) Oh, W.-D.; Dong, Z.; Lim, T.-T. *Appl. Catal., B* **2016**, *194*, 169.

(152) Liang, C. J.; Bruell, C. J.; Marley, M. C.; Sperry, K. L. *Soil Sediment Contam.* **2003**, *12*, 207.

(153) Duan, X.; Sun, H.; Kang, J.; Wang, Y.; Indrawirawan, S.; Wang, S. *ACS Catal.* **2015**, *5*, 4629.

(154) Matzek, L. W.; Carter, K. E. *Chemosphere* **2016**, *151*, 178.

(155) Berlin, A. A. *Kinet. Catal.(Engl. Transl.);(United States)* **1986**, *27*.

(156) Yang, S.; Yang, X.; Shao, X.; Niu, R.; Wang, L. *J. Hazard. Mater.* **2011**, *186*, 659.

(157) Wang, X.; Wang, L.; Li, J.; Qiu, J.; Cai, C.; Zhang, H. *Sep. Purif. Technol.* **2014**, *122*, 41.

(158) Kusic, H.; Peternel, I.; Koprivanac, N.; Loncaric Bozic, A. *J. Environ. Eng.* **2010**, *137*, 454.

(159) Zhang, J.; Chen, M.; Zhu, L. *RSC Adv.* **2016**, *6*, 758.

(160) Nidheesh, P.; Rajan, R. *RSC Adv.* **2016**, *6*, 5330.

(161) Joshi, R. C.; Lohita, R. *Fly ash in concrete: production, properties and uses*; CRC Press, 1997; Vol. 2.

(162) Ahmaruzzaman, M. *Prog. Energy Combust. Sci.* **2010**, *36*, 327.

(163) Iyer, R. *J. Hazard. Mater.* **2002**, *93*, 321.

(164) Lu, J.; Xu, F.; Wang, D.; Huang, J.; Cai, W. *J. Hazard. Mater.* **2009**, *165*, 120.

(165) Ökte, A.; Karamanis, D. *Appl. Catal., B* **2013**, *142*, 538.

(166) Ökte, A.; Karamanis, D.; Tuncel, D. *Catal. Today* **2014**, *230*, 205.

(167) Saud, P. S.; Pant, B.; Park, M.; Chae, S.-H.; Park, S.-J.; Ei-Newehy, M.; Al-Deyab, S. S.; Kim, H.-Y. *Ceram. Int.* **2015**, *41*, 1771.

(168) Kalpana, K.; Selvaraj, V. *RSC Adv.* **2015**, *5*, 47766.

(169) Wang, B.; Li, Q.; Wang, W.; Li, Y.; Zhai, J. *Appl. Surf. Sci.* **2011**, *257*, 3473.

(170) Narayani, H.; Augustine, R.; Sumi, S.; Jose, M.; Nair, K. D.; Samsuddin, M.; Prakash, H.; Shukla, S. *Sep. Purif. Technol.* **2017**, *172*, 338.

Chapter 2

Photocatalytic Activity of Acid-Catalyst-Modified Sol-Gel Processed Nanocrystalline Titania : On Dual-Role of Active Surface-Sites

Graphical Abstract

Highlights

- TiO_2 photocatalyst synthesized via conventional and the acid-catalyst (HNO_3, CH_3COOH, H_3PO_4) modified sol-gel method.
- Studied the effect of acid-catalyst on the morphological, chemical, and structural evolution of the modified catalyst.
- Compared the photocatalytic activity of the acid modified catalyst.
- Studied the dual role of PO_4^{3-} ion on the surface of TiO_2 and photocatalytic reaction rate.

Abstract

Stabilizing anatase-phase in pure and doped nanocrystalline TiO_2 with enhanced photocatalytic activity has been a challenging task. In this report, we synthesize nanocrystalline anatase-TiO_2 via the conventional and acid-catalyst-modified sol-gel processes. Three different types of acid-catalysts, HNO_3, acetic acid CH_3COOH, and H_3PO_4 have been utilized for this purpose. The effect of acid-catalyst on the morphological, chemical and structural evolution of samples has been analyzed using different analytical techniques. The photocatalytic activity has been measured under the UV-radiation exposure by varying the acid-catalyst used, initial dye-concentration, and initial concentration of H_3PO_4. The maximum photocatalytic activity has been exhibited by the sample processed using the H_3PO_4 as an acid-catalyst which has been attributed to the ability of PO_4^{3-} anions to bind strongly with the surface of anatase-TiO_2 and their dual-role in the dark and under the UV-radiation exposure leading to the largest amount of dye-adsorption on the surface and highest dye-degradation kinetics. Nanocrystalline anatase-TiO_2 with PO_4^{3-} anions having the lowest crystallinity shows the largest photocatalytic activity which confirms the role of PO_4^{3-} anions in enhancing the photocatalytic activity.

2.1. Introduction

Photocatalysis using the nanocrystalline particles and nanotubes of TiO_2 has been widely investigated process to decompose the organic synthetic-dyes from an aqueous solution.[1-5] For this application, the anatase polymorph has been known to be relatively more photoactive than the other polymorphs (rutile and brookite) of TiO_2. The sol-gel method has been very attractive technique for the synthesis of nanocrystalline anatase-TiO_2 since it can process both pure and doped photocatalyst particles in the powder form in large quantities with the controlled particle size, mesoporosity, specific surface-area, phase-structure, surface-chemistry, and high reproducibility. Both the processing of nanocrystalline mesoporous anatase-TiO_2, typically via sol-gel method and its photocatalytic activity have been demonstrated recently.[6]

The sol-gel process, modified using an acid-catalyst, has been investigated by others to study its effect on the above mentioned material parameters which in turn strongly affect the photocatalytic activity of nanocrystalline anatase-TiO_2.[7-12] It has been observed that when the mesoporous-TiO_2 xerogels are washed using the hydrochloric acid (HCl)-ethanol solution, under the reflux condition, it results in the crystallization into anatase-TiO_2 with higher photocatalytic activity.[7] The incorporation of HCl-catalyst during the early stages of sol-gel processing has been observed to form hard-aggregates stabilizing the anatase-TiO_2.[12] Although these reports support the formation of anatase-TiO_2 using HCl-modified sol-gel process, there are few other reports which show an opposite trend. According to the latter report, the incorporation of HCl, HNO_3, and H_2SO_4 as acid-catalysts during the early stages of sol-gel processing promotes the anatase-to-rutile phase transformation, which in turn reduces the photocatalytic activity of sol-gel TiO_2. However, the latter investigation also involves the use of a surfactant, such as

cetyltrimethyl ammonium bromide (CTAB) as a structure-directing agent, which has its own effect in controlling the above mentioned material parameters, and hence, the photocatalytic activity. As a result, it appears that in order to understand the precise role of acid-catalyst in controlling the phase-structure and photocatalytic activity of nanocrystalline TiO_2 further detailed investigation without the use of surfactant is required. Moreover, the role of anionic-part of acid-catalyst in controlling the morphological and structural evolution during the sol-gel processing of nanocrystalline TiO_2 has been hardly elucidated.[11] The effect of different acid-catalysts in the generation of $^{\bullet}OH$ has not been demonstrated yet using the $^{\bullet}OH$-trapping experiments.

It has been well established that various material parameters such as the powder morphology,[13] specific surface-area,[14-16] average pore size, pore volume and its distribution,[14-16] average nanocrystallite size,[6] amount of rutile-phase,[17] amount and nature of surface-deposited metal / metal oxide nanoparticles,[18] and amount and nature of dopants[19] significantly affect the photocatalytic activity of nanocrystalline anatase-TiO_2. In addition to these parameters, the crystallinity of nanocrystalline anatase-TiO_2 is also considered to be one of the most important factors in controlling its photocatalytic activity.[14-15,20-21] In general, the higher the crystallinity of nanocrystalline anatase-TiO_2, the higher the photocatalytic activity, and vice a versa. As far as our knowledge goes, there is no report in the literature which has shown higher photocatalytic activity for the nanocrystalline anatase-TiO_2 having lower crystallinity. The techniques to enhance the photocatalytic activity of nanocrystalline anatase-TiO_2 having lower crystallinity, which may even surpass that of highly crystalline anatase-TiO_2, are presently unknown.

From these points of view, in this investigation, we process the nanocrystalline-TiO_2 via sol-gel method without the use of any surfactant and also modify the process by using

different acid-catalysts to study their effect in stabilizing the anatase-phase through the controlled morphological, chemical, and structural evolutions. The best acid-catalyst providing the maximum photocatalytic activity through the stabilization of anatase-TiO_2 has been identified, and the role of anionic-part of acid-catalyst has been explained which was lacking in the current literature. Simultaneously, we process the nanocrystalline anatase-TiO_2 having both higher and lower crystallinity via the conventional and modified sol-gel methods, and demonstrate for the first time that under the given processing conditions, the photocatalytic activity of nanocrystalline anatase-TiO_2 having lower crystallinity can be higher than that of its highly crystalline form. The results are further corroborated for the first time using the $^{\bullet}OH$ trapping experiments which strongly indicate the dual-role of surface-active sites for the dye-adsorption in the dark and dye-decomposition under the UV-radiation exposure. The dual-role of PO_4^{3-} anions has been proved via demonstrating the linear relationship between the apparent first-order-reaction rate-constant (k_{app}) and the amount of surface-adsorbed MB dye under the different processing and test-conditions.

In addition to this, the doping of nanocrystalline anatase-TiO_2 with metal-cations, without causing the anatase-to-rutile phase transformation, has been recently shown to be effective via the acid-catalyst-modified sol-gel.[22] Hence, it appears that the optimum parameters obtained in this investigation for the synthesis nanocrystalline anatase-TiO_2 would possibly help in future to achieve the doping of different metal-cations in anatase-TiO_2 via the sol-gel method to enhance its photocatalytic activity without causing any phase transformation.

2.2 Experimental

2.2.1. Chemicals

Titanium(IV) iso-propoxide ($Ti(OC_3H_7)_4$, 97%), phosphoric acid (H_3PO_4, 85 wt% in water, 99.99%), and terephthalic acid (TA, 98%) were purchased from Sigma-Aldrich Chemicals, Bengaluru, India; 2-propanol (99.5%, ACS reagent), nitric acid (HNO_3, ACS reagent 69-72%), sodium hydroxide (NaOH, Assay 97%), MB (96%) from S.D. Fine-Chem Ltd., Mumbai, India; glacial acetic acid (CH_3COOH, 99.8%) from Merk, India; and Degussa-P25 from Evonik Industries, Mumbai, India. All chemicals were used as-received without any further purification and/or modification.

2.2.2. Sol-gel processing of nanocrystalline TiO_2 via conventional and acid-catalyst-modified sol-gel

Nanocrystalline TiO_2 powders were synthesized via sol-gel method involving the hydrolysis and condensation of $Ti(OC_3H_7)_4$ in 2-propnaol.[6] First, the measured quantities of water and acid-catalyst were dissolved in 125 ml of 2-propanol. A second solution was then prepared in which 0.12 M (final concentration) of $Ti(OC_3H_7)_4$ was dissolved completely in 125 ml of 2-propanol. Both the solutions were sealed immediately and stirred rapidly using the magnetic stirrer (C MAG HS 7, IKA, Germany) to obtain the homogeneous solutions. The ratio of molar concentration of water to that of alkoxide-precursor (*R*) was 90.[23] Three different acid-catalysts, HNO_3, CH_3COOH, and H_3PO_4, were selected for the synthesis of nanocrystalline TiO_2. The ratio of molar concentration of acid-catalyst to that of alkoxide-precursor was 10:1 for HNO_3 and CH_3COOH, and within the range of 0.11 to 0.46 for the amount of H_3PO_4 varying in the range of 1.7-6.8 g l^{-1} (Note: For the H_3PO_4 catalyst, 10:1 and 5:1 ratios resulted in the formation of gel and powder which after the calcination treatment at higher temperature transformed to

titanium phosphate (Ti_3PO_4) instead of anatase- or rutile-TiO_2). The water-part of solution was then added drop-wise to alkoxide-part under the continuous magnetic stirring. The initial solution-pH was measured to be 7.8, 0.7, 4.1, and 5.9 for the conventional sol-gel process and that modified with HNO_3, CH_3COOH, and H_3PO_4 as acid-catalysts respectively. As a result of hydrolysis and condensation reactions of $Ti(OC_3H_7)_4$ due to its reaction with water, the color of solution changed from colorless to white. After the complete addition of water-part of solution to that of alkoxide-part, the resulting suspension was stirred for 7 h before drying in an oven at 80 ^oC for the complete removal of solvent and residual water. The dried powders were then calcined at 600 ^oC for 2 h at the heating rate of 3 $^oC\ min^{-1}$ for the crystallization of amorphous-TiO_2 powders. Hereafter, the nanocrystalline sol-gel TiO_2 processed without and with the acid-catalysts (HNO_3, CH_3COOH, and H_3PO_4) are represented as NoAc, NiAc, AcAc, and HpAc-samples respectively. In the following text, unless otherwise stated, the HpAc-sample can be assumed to be processed with the ratio of molar concentration of acid-catalyst to that of alkoxide-precursor having the value of 0.11.

In order to compare crystallinity and photoactivity, another set of photocatalyst samples was processed via conventional sol-gel process discussed above in which the dried powders were calcined at 300, 350, 400 ^oC for 1 h and 600 ^oC for 2 h, with the heating rate of 3 $^oC\ min^{-1}$, for the crystallization of amorphous-TiO_2 powders.

2.2.3. Characterization

The morphology and average nanocrystallite size of different samples were determined using the transmission electron microscope (TEM, Tecnai G^2, FEI, The Netherlands) operated at 300 kV. The chemical constituents and crystalline nature of samples were confirmed via energy dispersive X-ray (EDX) and selected-area electron diffraction

(SAED) techniques. The crystalline phases present were determined using the X-ray diffraction (XRD, PW1710 Phillips, The Netherlands). The broad-scan analysis was typically conducted within the 2-θ range of 10-80^o using the Cu $K\alpha$ (λ_{Cu}=1.542 Å) X-radiation. The obtained XRD patterns were then utilized to determine the weight-fraction of anatase-TiO_2 (X_A) using the Eq. (2.1),[11]

$$X_A = \left[1+1.26\left(\frac{I_R}{I_A}\right)\right] \tag{2.1}$$

where, I_A and I_R represent the linear-intensities of main-peaks of anatase-TiO_2 $(101)_A$ and rutile-TiO_2 $(110)_R$. The thermal analyses of dried samples were performed using the PerkinElmer (STA 6000, U.S.A.) thermogravimetry differential thermal analyzer (TG/DTA) at the heating rate of 10 °C min^{-1} under the oxygen atmosphere. The surface-chemistry of different samples was analyzed using the Fourier Transform Infrared (FTIR, IRPrestige-21 Shimadzu, Japan) spectroscope within the frequency range of 4000-400 cm^{-1} using the powders dispersed in the potassium bromide (KBr) pellets. The zeta potential values were measured (Zetasizer Nanoseries, M3-PALS, Malvern-ZEN 3600, United Kingdom) to determine the surface-charge on the different samples by taking the average of three measurements having the deviation in between ±0.5-1.0 mV. The specific surface-area was measured using the Brunauer-Emmett-Teller (BET) surface-area measurement technique (Micrometrics Gemini 2375 Surface Area Analyzer, U.S.A.) via nitrogen (N_2) adsorption using the multi-point method after degassing the nanocrystalline TiO_2 powders in flowing N_2 at 200 °C for 2 h.

2.2.4. Photocatalytic activity measurements

The photocatalytic activity was studied by monitoring the degradation of MB dye in an aqueous suspension containing the photocatalyst particles under continuous UV-radiation exposure. 125 ml of aqueous suspension was prepared by completely dissolving 7.5 μM

of MB dye and then dispersing 0.4 g l^{-1} of photocatalyst particles under continuous magnetic stirring. The resulting suspension was equilibrated via stirring in the dark for 1 h to stabilize the adsorption of MB dye on the surface of photocatalyst particles.[24] The stable aqueous suspension was then irradiated with the UV-light under the continuous magnetic stirring using a Photoreactor (Luzchem Inc., Canada) containing 16 UVA tubes as the UV-source having the illuminance of 255 lm m^{-2} (lux) and emitting the radiation having the peak-wavelength at ~350 nm. Following the UV-radiation exposure, 8 ml aliquot was taken out of UV-chamber after the specific time interval for total 1 h for obtaining the absorption spectra. The photocatalyst particles were separated from the sample suspension using a centrifuge (Hettich EBA 20, Sigma-Aldrich, India) and the filtrate was then examined using a UV-visible absorption spectrophotometer (UV-2401 PC, Shimadzu, Japan) to study the degradation kinetics of MB dye. The absorption spectra of MB dye solution were obtained within the range of 200-800 nm as a function of UV-radiation exposure time. The intensity of main absorbance peak (A_t) of MB dye solution located at ~656 nm was taken as a measure of residual MB dye concentration (C_t). The UV-visible absorption spectrum of MB dye solution obtained after stirring the suspension for 1 h in the dark was regarded as a reference spectrum corresponding to the initial MB dye concentration (C_o). The normalized residual concentration of MB dye was calculated using the relationship of form,

$$\left(\frac{C_t}{C_0}\right)_{MB} = \left(\frac{A_t}{A_0}\right)_{656nm} \tag{2.2}$$

The amount of MB dye adsorbed on the surface of photocatalyst particles after stirring in the dark for 1 h was calculated using the relationship of the form,

$$\left(\frac{C_{-60} - C_0}{C_{-60}}\right)_{MB} = \left(\frac{A_{-60} - A_0}{A_{-60}}\right)_{656nm} \tag{2.3}$$

where, C_{-60} and A_{-60} are the MB dye concentration and corresponding absorbance just

before the addition of photocatalyst particles. A photocatalysis experiment was also performed in the absence of photocatalyst particles to confirm the stability of MB dye in an aqueous solution under the continuous UV-radiation exposure. Under this condition, the MB dye concentration (C_{-60}) remained unchanged even after irradiating the sample for total 3 h.

2.2.5. $^{\bullet}$OH trapping

These experiments were typically performed to trap the $^{\bullet}$OH using the TA which were produced under the continuous UV-radiation exposure of photocatalyst particles in an aqueous solution. These experiments were similar to the one described above for the photocatalytic activity measurements except that the MB dye was replaced with 10^{-4} M of TA and 2×10^{-3} M of NaOH. The solubility of TA in the neutral and acidic water is relatively lower which is enhanced by the addition of NaOH. Moreover, TA is a non-fluorescent molecule; however, the trapping of free $^{\bullet}$OH by TA results in the formation of 2-hydroxyterephthalic acid which exhibits a characteristic photoluminescence (PL) peak located at ~425 nm.[25-26] The PL spectra of 2-hydroxyterephthalic acid were recorded as a function of UV-radiation exposure time using the spectrofluorometer (Cary Eclipse, Varian, The Netherlands) at an excitation wavelength of ~315 nm. The intensity of PL peak is regarded as the measure of amount of $^{\bullet}$OH produced by the photocatalyst particles at a given time under the UV-radiation exposure. The nanocrystalline sol-gel TiO_2 particles processed via conventional and acid-catalyst-modified sol-gel methods were tested using $^{\bullet}$OH trapping experiments.

In order to study the effect of amount of MB dye surface-adsorbed in the dark on the amount of $^{\bullet}$OH produced under the UV-radiation exposure, separate $^{\bullet}$OH trapping experiments were conducted typically using NoAc- and HpAc-samples. The

photocatalyst particles with the surface-adsorbed MB dye were first prepared by stirring NoAc- and HpAc-samples in dark for 1 h in 125 ml aqueous solution having the initial MB dye concentration varying within the range of 7.5-90 μM. The photocatalyst particles with the surface-adsorbed MB dye were separated from the dye solution using the centrifuge, dried in an oven at 80 ^{o}C overnight, and then used for the $^{\bullet}$OH trapping experiment as described above. The HpAc-samples processed under the varying initial concentrations of H_3PO_4 catalyst were also tested using the free $^{\bullet}$OH trapping experiments.

2.3. Results and Discussions

2.3.1. Morphological, structural, and chemical analyses of photocatalysts

The TEM images of nanocrystalline sol-gel TiO_2 processed via conventional and acid-catalyst-modified sol-gel methods are presented in Fig. 2.1. The corresponding SAED patterns are presented as insets which show the concentric ring patterns indicating the crystalline nature of these samples. The specific surface-area and zeta potential values of different samples have been tabulated in Table 2.1.

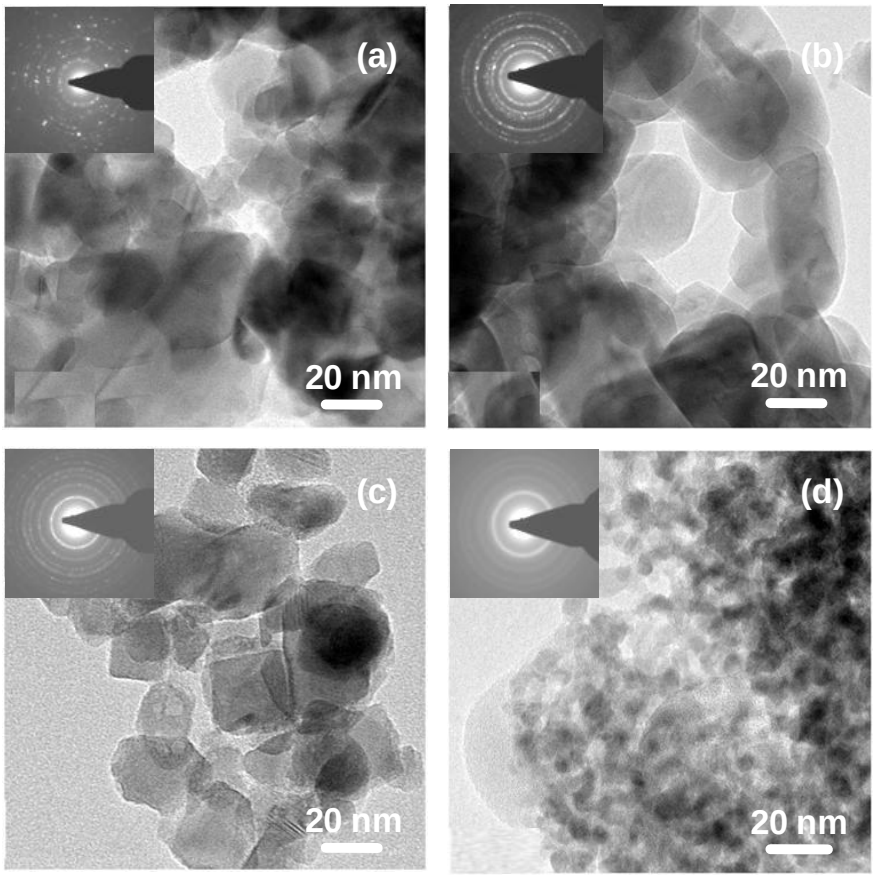

Fig. 2.1. TEM images of NoAc (a), NiAc (b), AcAc (c), and HpAc (d) samples. The insets show corresponding SAED patterns.

In Figs. 2.1a-d, all samples show aggregated nanocrystallites with different size-distribution. The nanocrystallite size is noted to be within the range of 15-30 nm, 25-80 nm, 15-40 nm, 3-7 nm for the NoAc, NiAc, AcAc, and HpAc-samples respectively.

The TEM images of nanocrystalline anatase-TiO_2 processed via conventional (calcined at 300 ^{o}C for 1 h and 600 ^{o}C for 2 h) and modified sol-gel methods are presented in Fig. 2.2. The corresponding SAED patterns are presented as insets, which show the concentric ring patterns indicating the nanocrystalline nature of all samples, which consist of aggregated nanocrystallites having the different size-distribution. Typically, the average nanocrystallite size is noted to be ~10 nm and ~20 nm for the nanocrystalline anatase-

TiO_2 processed via conventional sol-gel method, Fig. 2.2a,b; while, it is ~7 nm for that processed via modified sol- gel method, Fig. 2.2c.

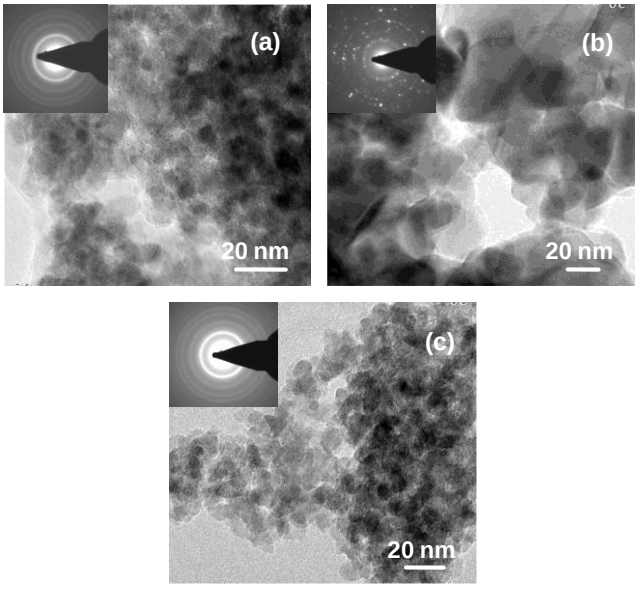

Fig. 2.2. TEM images of nanocrystalline-TiO_2 processed via conventional (a,b) and modified (c) sol-gel methods. In (a), the sample is calcined at 300 ^oC for 1 h, and in (b) and (c), the sample is calcined at 600 ^oC for 2 h. The insets show the corresponding SAED patterns.

The nanocrystallite size distribution of NoAc- and AcAc-samples appears to be comparable; however, the specific surface-area of latter is larger than that of former, Table 2.1, which is supported by less aggregation tendency of nanocrystallites as observed for latter, Fig. 2.1c, than that observed for former, Fig. 2.1a. Comparison further reveals an excessive growth in the case of NiAc-sample, Fig. 2.1b, and the size-reduction for HpAc-sample, Fig. 2.1d, relative to that of NoAc-sample, Fig. 2.1a. The faceted morphology is typically observed for AcAc-sample; while, the near-spherical morphology is noted for NoAc- and HpAc-samples.

Table 2.1. Values of typical physical parameters as obtained for the sol-gel derived nanocrystalline TiO_2 synthesized via conventional and acid-catalyst-modified sol-gel methods.

Sample	**Specific Surface-Area (m^2 g^{-1})**		**Zeta Potential (mV)**
	Dried	**Calcined**	
NoAc	259	8	-38.7
NiAc	194	4.5	-7.8
AcAc	236	28	-0.36
HpAc	478	144	-23.2

The EDX spectra obtained for different samples are presented in Fig. 2.3 which show the presence of Ti and O as the major constituents of all samples. For NiAc- and AcAc-samples, the presence of N and C could not be observed, Fig. 2.3b and c, suggesting the complete decomposition and/or oxidation of NO_3^- and CH_3COO^- anions from the region below the surface.

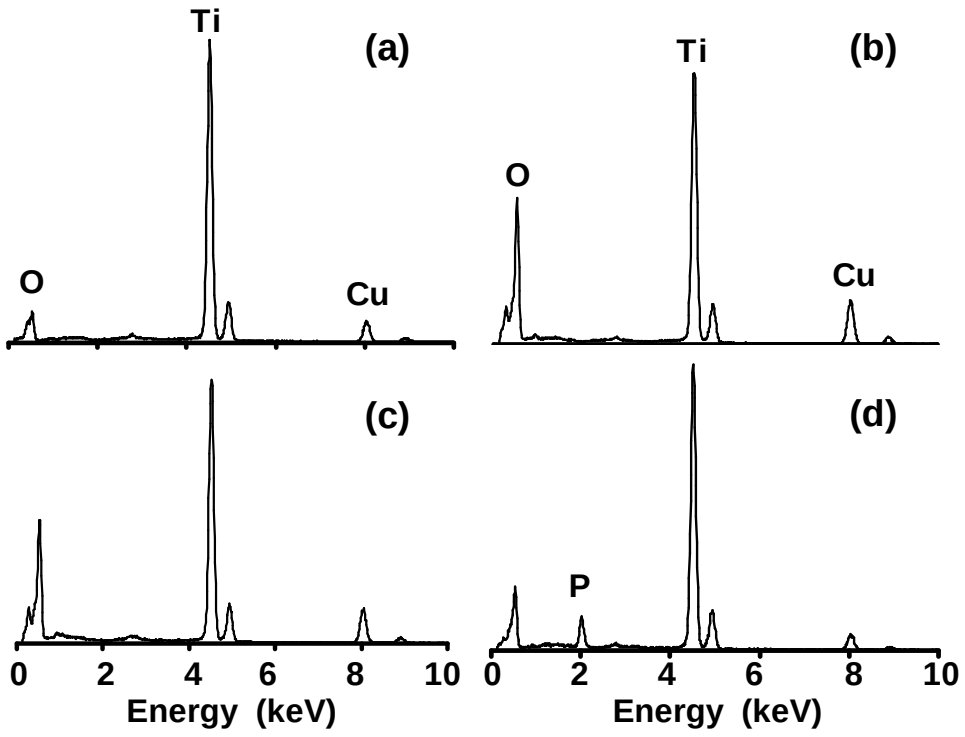

Fig. 2.3. EDX spectra obtained using the NoAc (a), NiAc (b), AcAc (c), and HpAc (d) samples.

For HpAc-sample, an additional peak of P is however detected, Fig. 2.3d, which suggests the presence of PO_4^{3-} anions on the surface. Very fine, near-spherical, porous, and high specific surface-area morphology, Fig. 2.1d, as typically observed for HpAc-sample is hence related to the presence of PO_4^{3-} anions on the surface. The variation in the specific surface-area of NiAc, AcAc, and HpAc-samples, Table 2.1, is noted to follow an increasing trend in both the dried and calcined conditions. Typically in the dried-state, relative to the specific surface-area of NoAc-sample, those of NiAc- and AcAc-samples are lower; while, that of HpAc-sample is higher. On the other hand, in the calcined-condition, relative to the specific surface-area of NoAc-sample, that of NiAc-sample is lower; while, those of AcAc- and HpAc-samples are higher. The maximum specific surface-area, under both the dried and calcined states, is exhibited by the HpAc-sample which is consistent with the TEM analysis, Fig. 2.1d.

The XRD patterns obtained for nanocrystalline sol-gel TiO_2 processed via conventional and acid-catalyst-modified sol-gel methods are presented in Fig. 2.4. The NoAc-sample, Fig. 2.4a, shows the predominant presence of anatase-TiO_2 with the small amount (15 wt%) of rutile-TiO_2. The NiAc-sample, Fig. 2.3b, shows the presence of mixed-phases with 52 wt% of anatase-TiO_2 indicating considerable anatase-to-rutile phase transformation. AcAc- and HpAc-samples, however, show the stabilization of 100% anatase-TiO_2, Fig. 2.4c and d. The main anatase-TiO_2 peak appears to be relatively shorter and broader for HpAc-sample, Fig. 2.4d, which is consistent with its very small average nanocrystallite size, Fig. 2.1d, and larger specific surface-area, Table 2.1. Among all samples, the crystallinity of HpAc-sample is observed to be the lowest. The XRD patterns obtained using HpAc-samples processed using higher concentrations H_3PO_4 acid-catalyst are presented in Fig. 2.5. Considering Fig. 2.5 together with Fig. 2.4d, it appears that HpAc-samples tend to remain amorphous with the increasing concentration H_3PO_4 acid-catalyst. This suggests greater resistance to the crystallization of anatase-TiO_2 from amorphous-TiO_2 with increasing concentration H_3PO_4 acid-catalyst.

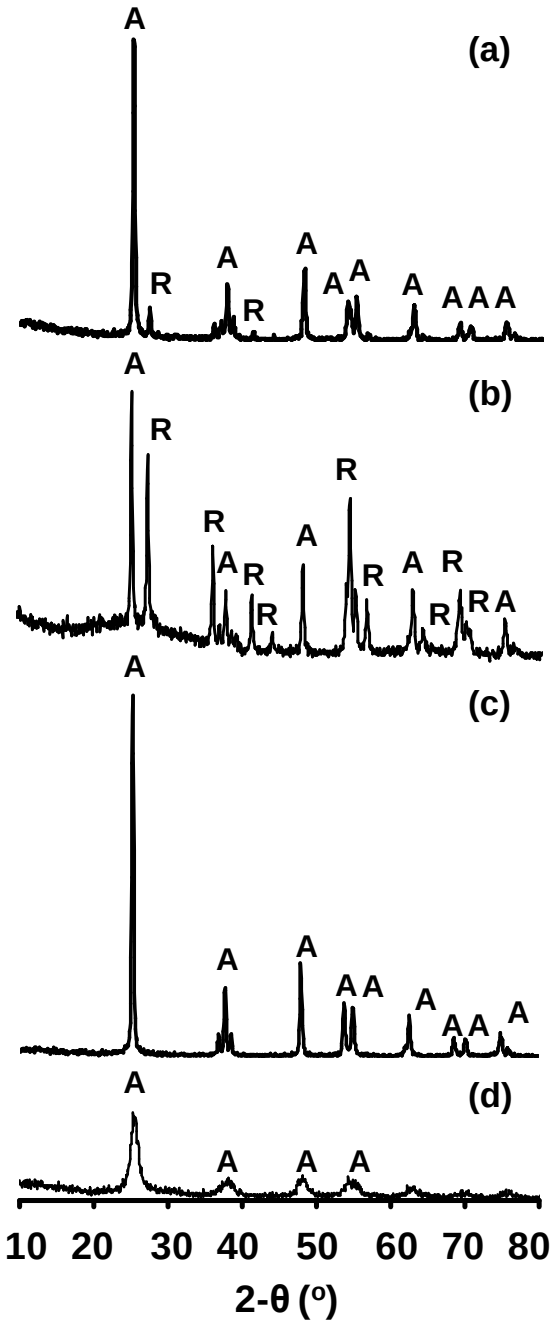

Fig. 2.4. XRD patterns obtained using NoAc (a), NiAc (b), AcAc (c), and HpAc (d) samples.

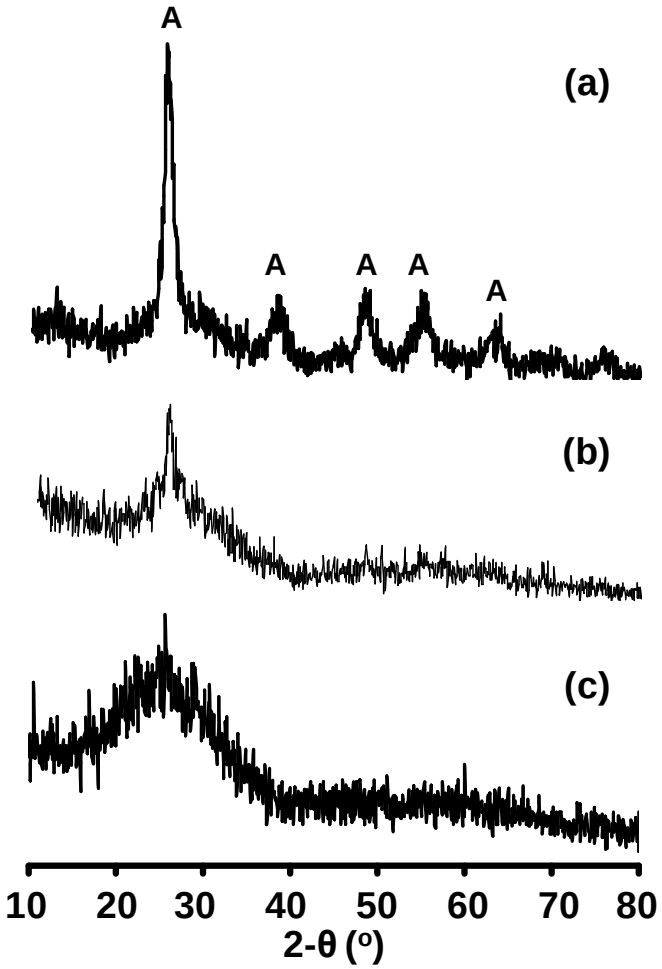

Fig. 2.5. XRD patterns obtained using the HpAc samples processed using higher concentrations H_3PO_4 acid-catalyst. The ratio of molar concentration of acid-catalyst to that of alkoxide-precursor varies as 0.23 (a), 0.4 (b), and 0.46 (c).

The XRD patterns of pure sol-gel TiO_2 processed with different calcination temperature and modified sol-gel TiO_2 samples are presented in Fig. 2.6. All samples are noted to crystallize predominantly into the anatase-TiO_2 after the calcination treatment. For the nanocrystalline-TiO_2 processed via conventional sol-gel method, Fig. 2.6a-d, the intensity of main anatase-peak is observed to increase with the calcination temperature. Moreover, the crystallinity of sample calcined at 600 ^oC for 2 h is observed to be the maximum with the presence of small amount (11 wt.%) of rutile-TiO_2, Fig. 2.6a.

Comparision further shows that the intensity of main anatase-peak is the lowest for nanocrystalline anatase-TiO_2 processed via modified sol-gel method, Fig. 2.6e, and it is comparable with that processed via conventional sol-gel method which is calcined at 300 ^oC for 1 h, Fig. 2.6d.

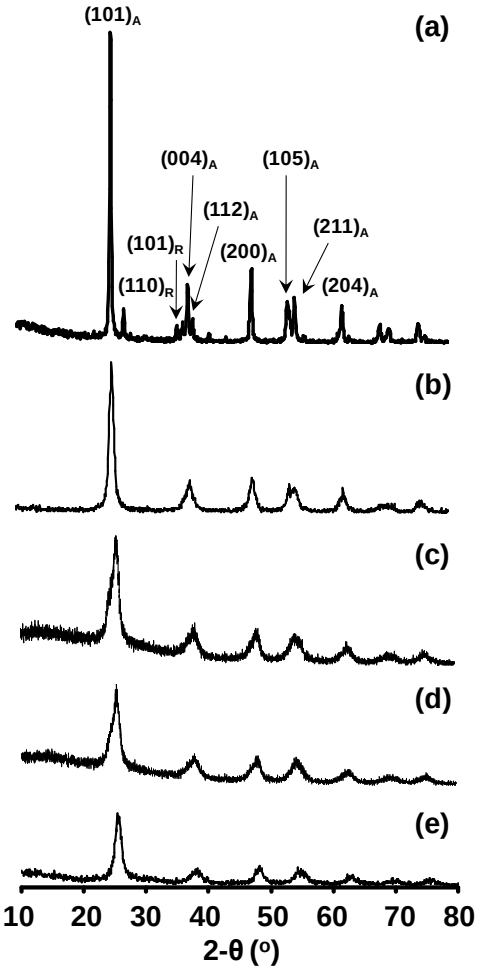

Fig. 2.6. XRD patterns obtained using the nanocrystalline-TiO_2 processed via conventional (a-d) and modified (e) sol-gel methods. The samples are calcined at 600 ^oC for 2 h (a,e), 400 ^oC for 1 h (b), 350 ^oC for 1 h (c), and 300 ^oC for 1 h (d). A and R represent anatase-TiO_2 and rutile-TiO_2.

The FTIR spectra obtained for nanocrystalline TiO_2 processed via conventional and acid-catalyst-modified sol-gel processes are presented in Fig. 2.7. For all samples, the absorbance peak within the frequency range of 3134-3400 cm^{-1} has been attributed to the

stretching vibrations of surface-adsorbed hydroxyl (–OH) groups; while, that within the frequency range of 1632-1651 cm^{-1} has been attributed to the bending vibrations of surface-adsorbed H_2O.[8,11]

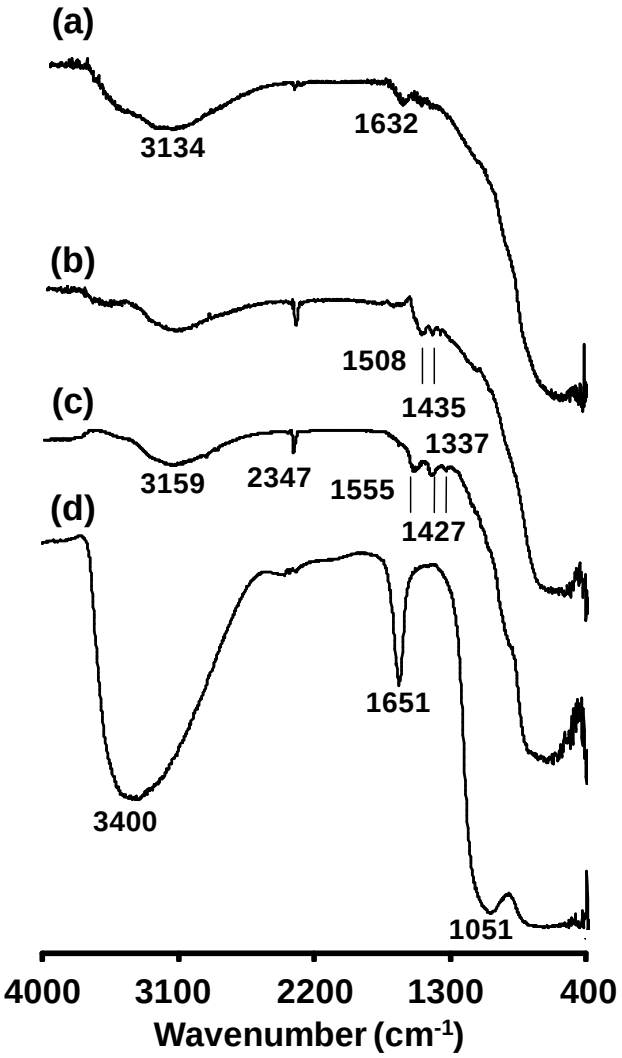

Fig. 2.7. FTIR spectra, obtained using NoAc (a), NiAc (b), AcAc (c), and HpAc (d) samples.

The absorbance peak in lower frequency region, 400-800 cm^{-1}, is related to Ti-O-Ti bonds. For AcAc-sample, in addition to the above peaks, the absorbance peaks at 1427 and 1555 cm^{-1} are observed which are related to the residual CH_3COO^- anions[27] and that at 1337 cm^{-1} is related to $–CH_2$ / $-CH_3$ functional groups,[23] which suggest the deposition

of carbon-residue as the surface-contamination produced due to the partial decomposition and/or oxidation of CH_3COO^- anions during the high temperature calcination treatment. The doublet at 1427 and 1555 cm^{-1} have been assigned to the asymmetric and symmetric stretching vibrations of carboxylic group coordinated to Ti as a bidentate ligand.[8] Moreover, these signals are separated by $\Delta\nu$=128 cm^{-1} which is less than 150 cm^{-1}; hence, the difference suggests that the CH_3COO^- anions act preferentially as a bidentate rather than as a bridging ligand between two Ti^{4+} ions. For HpAc-sample, an additional absorbance peak located at 1051 cm^{-1} is noted which corresponds to the stretching vibrations of PO_4^{3-} anions on the surface.[11] Compared with the other samples, HpAc-sample exhibits the presence of large amount of OH-groups and moisture adsorbed possibly via hydrogen bonding with PO_4^{3-} anions present on the surface.[11] Although not shown here, no drastic variation in the intensity of absorbance peak of PO_4^{3-} anions is noted with the increasing initial concentration of H_3PO_4 catalyst as utilized during the synthesis of HpAc-samples.

The FTIR spectra of pure sol-gel TiO_2 processed with different calcination temperature and modified sol-gel TiO_2 samples are presented in Fig. 2.8.

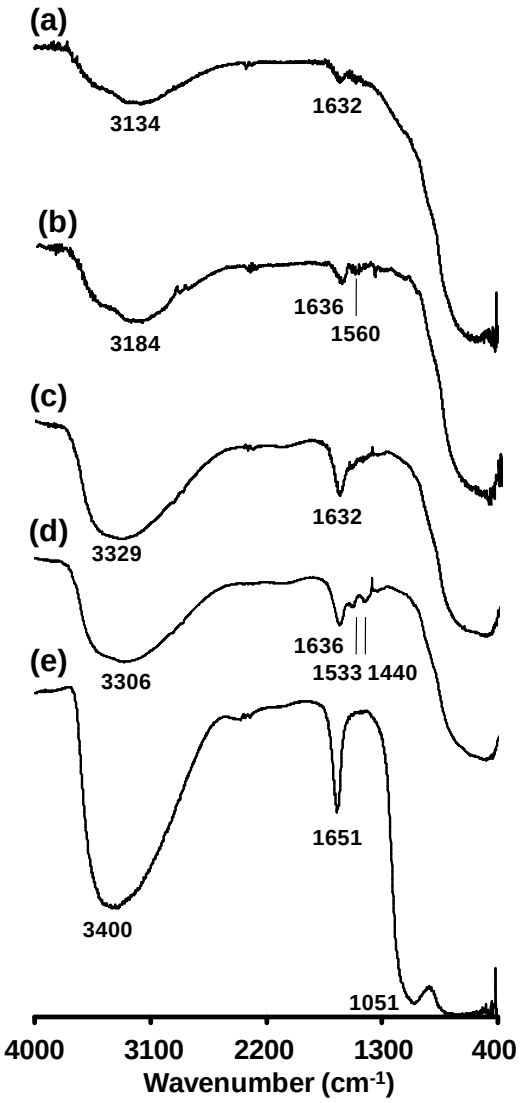

Fig. 2.8. FTIR spectra obtained using the nanocrystalline anatase-TiO_2 processed via the conventional (a-d) and modified (e) sol-gel methods. The samples are calcined at 600 ^oC for 2 h (a,e), 400 ^oC for 1 h (b), 350 ^oC for 1 h (c), and 300 ^oC for 1 h (d).

For all samples, the absorbance peaks within the frequency range of 3134-3400 cm^{-1} have been attributed to the stretching vibrations of surface-adsorbed –OH groups; while, those within the frequency range of 1632-1651 cm^{-1} have been attributed to the bending vibrations of surface-adsorbed H_2O.[8,11] The absorbance peak in lower frequency region, 400-800 cm^{-1}, is related to Ti-O-Ti bonds. For the nanocrystalline anatase-TiO_2 processed via conventional sol-gel method, obtained after the calcination treatment in

lower temperature range (300-400 ^{o}C), the small absorbance peaks located at 1440, 1533, and 1560 cm^{-1} are observed, Fig. 2.8b-d, which are related to the residual organics such as –CH_2/-CH_3 functional groups suggesting the deposition of carbon-residue as a surface-contamination due to the incomplete decomposition and/or oxidation of unhydrolyzed alkoxide (C_3H_7O)-groups.[28] No organic-residue has been detected on the surface of nanocrystalline anatase-TiO_2 which is obtained typically after the calcination treatment at 600 ^{o}C (Fig. 2.8a, e). For the nanocrystalline anatase-TiO_2 processed via modified sol-gel method, Fig. 2.8e, an additional absorbance peak located at 1051 cm^{-1} is noted which corresponds to the stretching vibrations of PO_4^{3-} anions on the surface.[11] Compared with the other samples, this sample exhibits the presence of relatively large amount of OH-groups and moisture adsorbed on the surface possibly via hydrogen bonding with PO_4^{3-} anions.

The FTIR spectra obtained for HpAc-sample before and after the photocatalytic activity measurement are presented and compared in Fig. 2.9. It is observed that the intensity of absorbance peak of PO_4^{3-} anions decreases following the photocatalytic activity measurement which suggests the involvement of PO_4^{3-} anions in decomposing the MB dye resulting in loss of some of PO_4^{3-} anions from the surface. Moreover, the amount of OH-groups and moisture adsorbed on the surface are also seen to decrease after the photocatalytic activity measurement in accordance with the reduced concentration of PO_4^{3-} anions observed after the photocatalytic activity measurement. The amount of P content of HpAc-sample, however, remains the same (~8 atomic %) before and after the photocatalytic activity measurement as determined via the EDX analysis. This implies that although PO_4^{3-} anions are decomposed during the photocatalysis process, as revealed via FTIR analysis, P remains adsorbed on the surface of HpAc-sample after the photocatalysis process and is not leached out into the solution.

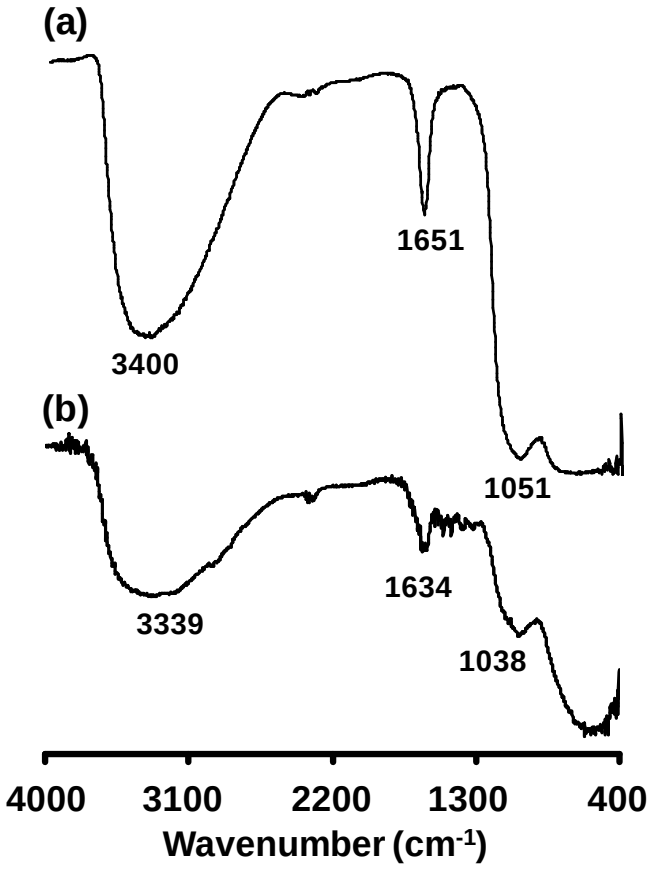

Fig. 2.9. FTIR spectra obtained using HpAc-sample before (a) and after (b) the photocatalytic activity measurements. In (b), the photocatalytic activity measurements are conducted using the initial MB dye concentration of 60 μM.

2.3.2. MB adsorption in dark, photocatalytic activity, and amount of $^{\bullet}$OH generated

The variation in the normalized residual MB dye concentration as a function of UV-radiation exposure time, as obtained for different nanocrystalline TiO_2 samples, is presented in Fig. 2.10a. The corresponding plots for obtaining k_{app} are presented in Fig. 2.10b. The calculated values of k_{app} and related amount of MB dye adsorbed after 1 h stirring in the dark are tabulated in Table 2.2. It is noted that the largest values of MB dye adsorption and k_{app} are exhibited by HpAc-sample; while, the lowest values are associated with AcAc-sample. NoAc- and NiAc-samples show the moderate amount of

MB dye adsorption and k_{app}. Relative to NoAc-sample, NiAc-sample possesses higher amount of MB dye adsorption but lower k_{app}. On the other hand, HpAc-sample exhibits the amount of MB dye adsorption and k_{app} twice as much as those of NoAc-sample.

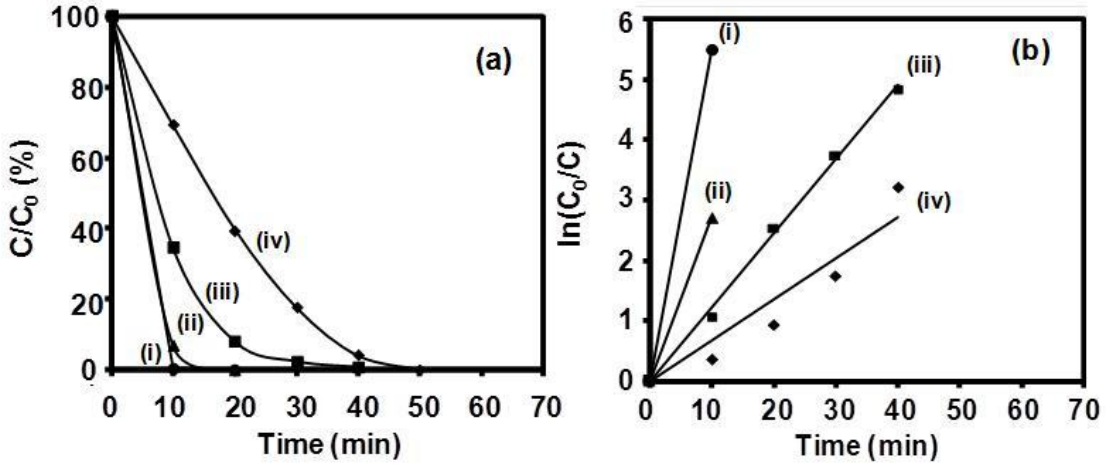

Fig. 2.10. (a) Variation in the normalized residual MB dye concentration as a function of UV-radiation exposure time obtained using HpAc (i), NoAc (ii), NiAc (iii), and AcAc (d) samples. (b) Corresponding plots for determining k_{app}. The initial MB concentration is 7.5 μM.

Table 2.2. Comparison of values of parameters of photocatalytic activity measurements obtained using the nanocrystalline TiO_2 synthesized via conventional and acid-catalyst-modified sol-gel methods.

Acid Catalyst	**MB Adsorbed After 1 h Stirring in Dark (%)**	k_{app} **(min^{-1})**
NoAc	15	0.27
NiAc	22	0.12
AcAc	4	0.07
HpAc	30	0.55

The variation in the PL intensity of 2-hydroxyterephthalic acid obtained for NoAc-sample as a function of UV-radiation exposure time is presented in Fig. 2.11a and that obtained for the samples processed using different acid-catalysts, just after 10 min of UV-radiation exposure, is presented in Fig. 2.11b. It appears that NoAc-sample shows the increasing concentration of $^{\bullet}OH$ with the UV-radiation exposure time, Fig. 2.11a, the trend which is also exhibited by all other samples. The concentration of $^{\bullet}OH$ is however the largest and lowest for NoAc- and HpAc-samples, Fig. 2.11b. AcAc and NiAc-samples produce $^{\bullet}OH$ concentration within these two extreme ranges at a given UV-radiation exposure time. The trend, observed in Fig. 2.11b, is noted to remain the same with increasing UV-radiation exposure time. Hence, the maximum value of k_{app} as exhibited by HpAc-sample appears to be contributed by larger amount of MB dye-adsorbed on the surface rather than the formation of $^{\bullet}OH$ under the UV-radiation exposure.

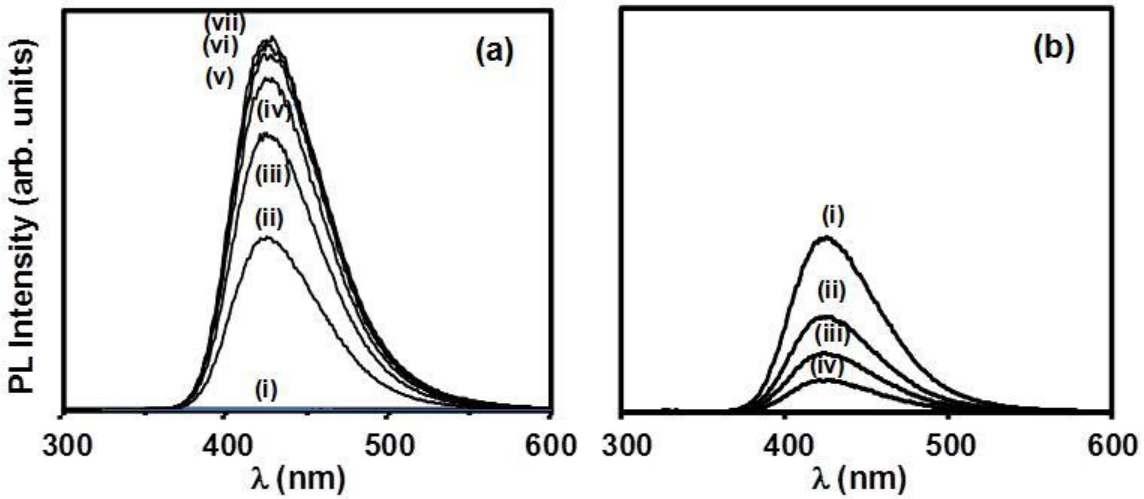

Fig. 2.11. (a) Variation in the PL intensity of 2-hydroxyterephthalic acid obtained using NoAc-sample. The UV-radiation exposure time varies as 10 (i), 20 (ii), 30 (iii), 40 (iv), 50 (v), and 60 min (vi). (b) Comparison of PL intensity of 2-hydroxyterephthalic acid, after the constant UV-radiation exposure time of 10 min, obtained using NoAc (i), AcAc (ii), NiAc (iii), and HpAc (iv) samples.

The variation in the normalized residual MB dye concentration as a function of UV-radiation exposure time as obtained for NoAc- and HpAc-samples for varying amount of initial MB dye concentration is presented in Figs. 2.12a and 2.13a. The corresponding plots for obtaining k_{app} are presented in Figs. 2.12b and 2.13b. The obtained variations in k_{app} and amount of MB dye adsorbed on the surface in the dark as a function of initial MB dye concentration, for the above two samples, are presented and compared in Fig. 2.14a and b. Within the investigated range, it is noted that the k_{app} value is always higher for HpAc-sample and it decreases with increasing initial MB dye concentration for both the samples. It is further observed that the amount of MB dye adsorbed on the surface in the dark is always higher for HpAc-sample. Moreover, it increases substantially for HpAc-sample and decreases for NoAc-sample with increasing initial MB dye concentration. The variation in the PL intensity of 2-hydroxyterephthalic acid after 60 min of UV-radiation exposure, as obtained for NoAc- and HpAc-samples which are prior stirred in the aqueous solutions having varying initial MB dye concentrations (hence, different amounts of MB dye pre-adsorbed on its surface), is presented in Fig. 2.15a and b. It appears that, in general, the concentration of $^{\bullet}OH$ generated is decreased due to the surface-adsorbed MB dye, although its variation as a function of initial MB dye concentration is not systematic for NoAc-sample. However, it decreases systematically for HpAc-sample with increasing initial MB dye concentration.

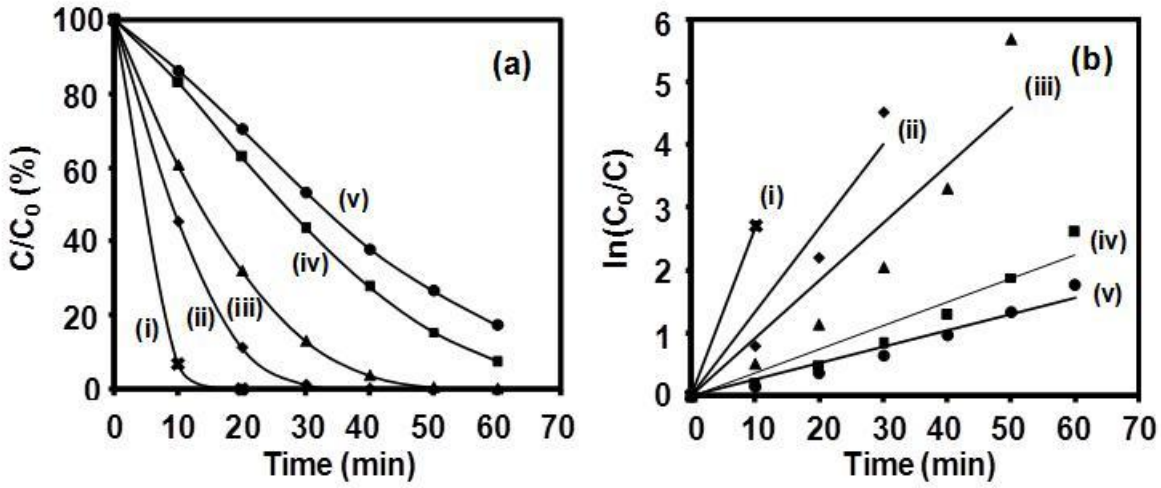

Fig. 2.12. (a) Variation in the normalized residual MB dye concentration as a function of UV-radiation exposure time, obtained using NoAc-sample. The initial MB dye concentration is varied as 7.5 (i), 15 (ii), 30 (iii), 60 (iv), and 90 μM (v). (b) Corresponding plots for determining k_{app}.

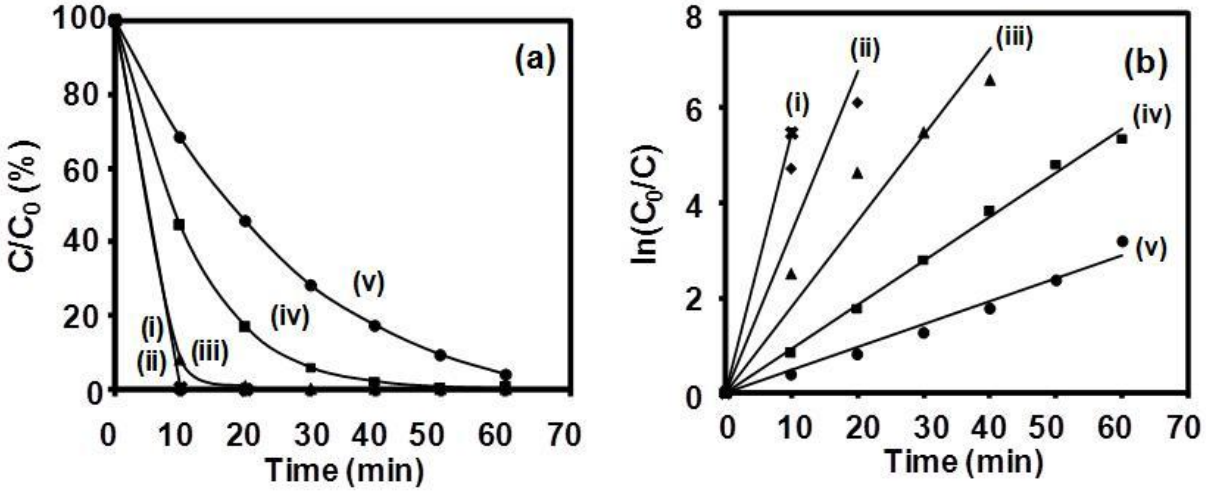

Fig. 2.13. (a) Variation in the normalized residual MB dye concentration as a function of UV-radiation exposure time, obtained using HpAc-sample. The initial MB dye concentration is varied as 7.5 (i), 15 (ii), 30 (iii), 60 (iv), and 90 (v) μM. (b) Corresponding plots for determining k_{app}.

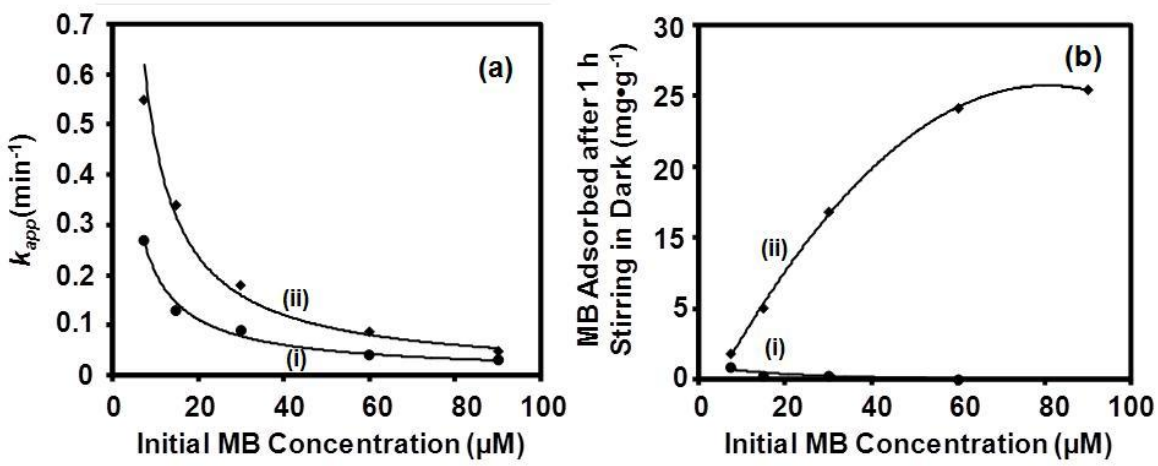

Fig. 2.14. Variation in the k_{app} (a) and amount of MB dye adsorbed after 1 h stirring in dark per gram of the photocatalyst (b) as a function of initial MB dye concentration obtained using the NoAc (i) and HpAc (ii) samples.

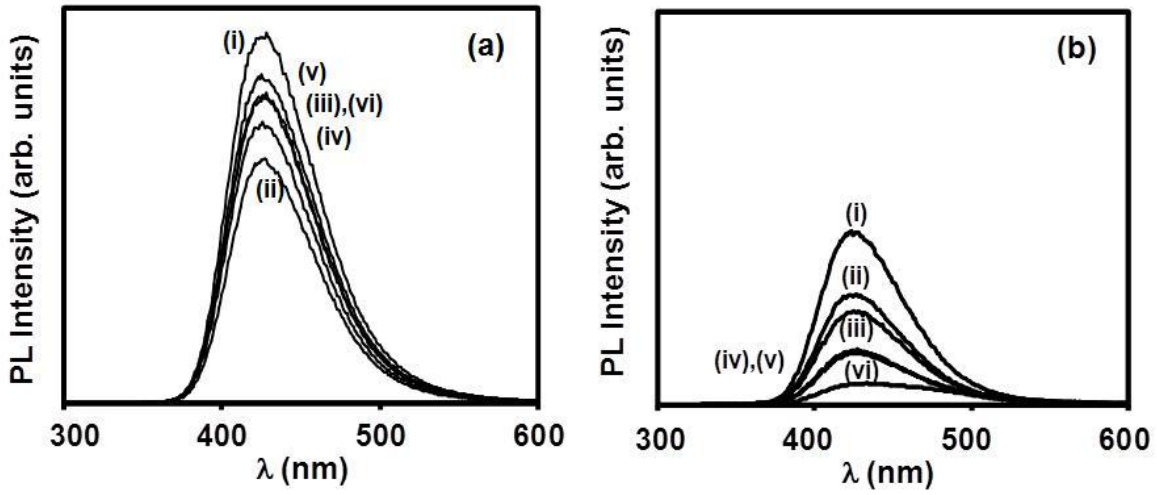

Fig. 2.15. Variation in the PL intensity of 2-hydroxyterephthalic acid, at the UV-radiation exposure time of 60 min, obtained using the NoAc- (a) and HpAc- (b) samples having different amount of surface-adsorbed MB dye. Before the PL measurements, both the samples are stirred in dark for 1 h in aqueous solutions having varying initial MB dye concentrations: 0 (i), 7.5 (ii), 15 (iii), 30 (iv), 60 (v), and 90 μM (vi).

The variation in the normalized residual MB dye concentration as a function of UV-radiation exposure time, as obtained for HpAc-samples processed with different initial concentration of H_3PO_4 catalyst, is presented in Fig. 2.16a and the corresponding plots for obtaining k_{app} are presented in Fig. 2.16b.

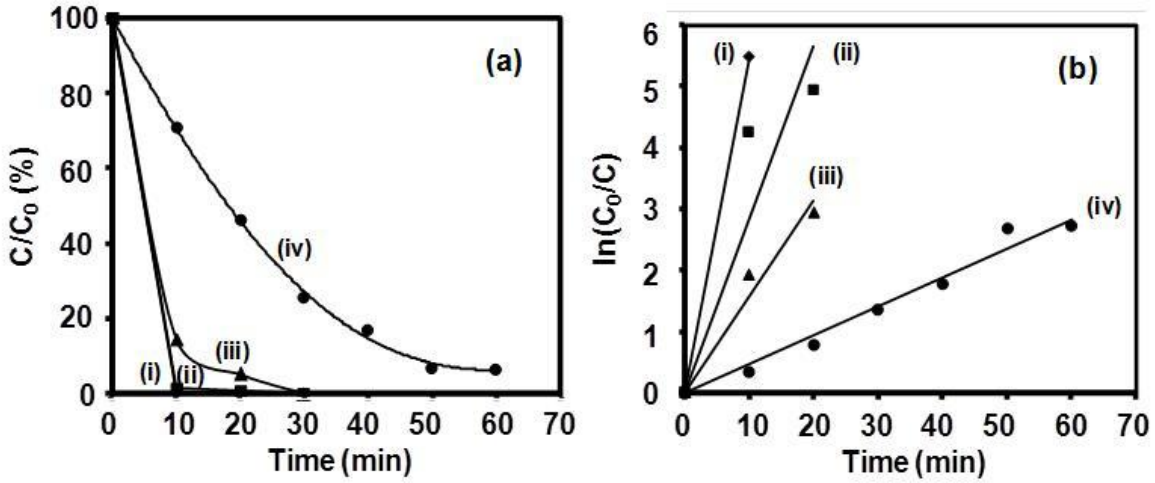

Fig. 2.16. (a) Variation in the normalized residual MB dye concentration as a function of UV-radiation exposure time, obtained using HpAc-samples processed with varying initial concentration of H_3PO_4 catalyst: 1.7 (i), 3.4 (ii), 5.73 (iii), and 6.8 g l^{-1} (iv). The initial MB dye concentration is 7.5 µM. (b) Corresponding plots for determining k_{app}.

The obtained variations in k_{app} and amount of MB dye adsorbed on the surface in the dark as a function of initial H_3PO_4 concentration are presented in Fig. 2.17a and b.

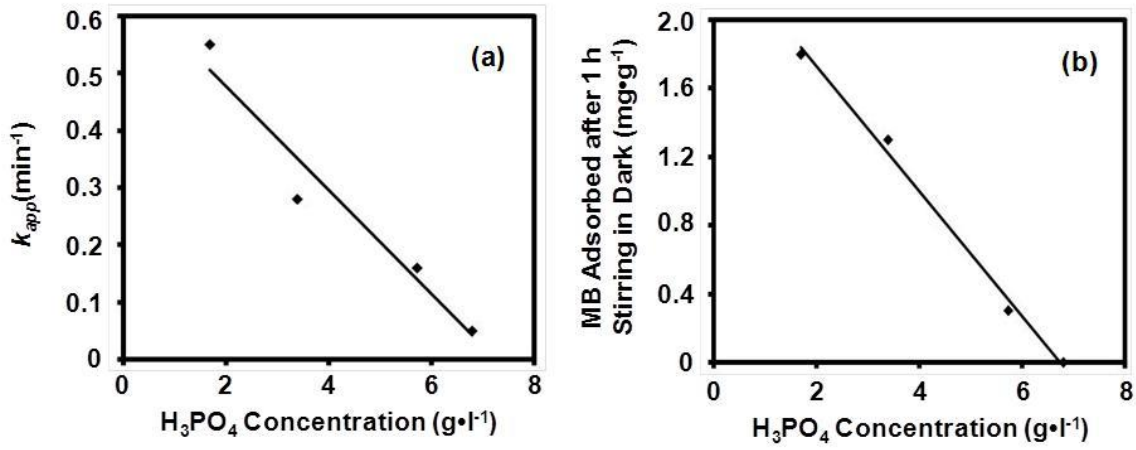

Fig. 2.17. Variation in k_{app} (a) and amount of MB dye adsorbed after 1 h stirring in dark per gram of photocatalyst (b) as a function of initial concentration of H_3PO_4 catalyst as obtained for HpAc-samples processed under different conditions.

It is noted that both k_{app} and amount of MB dye adsorbed on the surface in the dark decrease continuously with increasing initial concentration of H_3PO_4 catalyst. The variation in the PL intensity of 2-hydroxyterephthalic acid, as obtained for HpAc-samples processed with the different initial concentrations of H_3PO_4 catalyst, is presented in Fig. 2.18. It is noted that the concentration of $^{\bullet}OH$ generated decreases systematically with increasing initial concentration of H_3PO_4 catalyst.

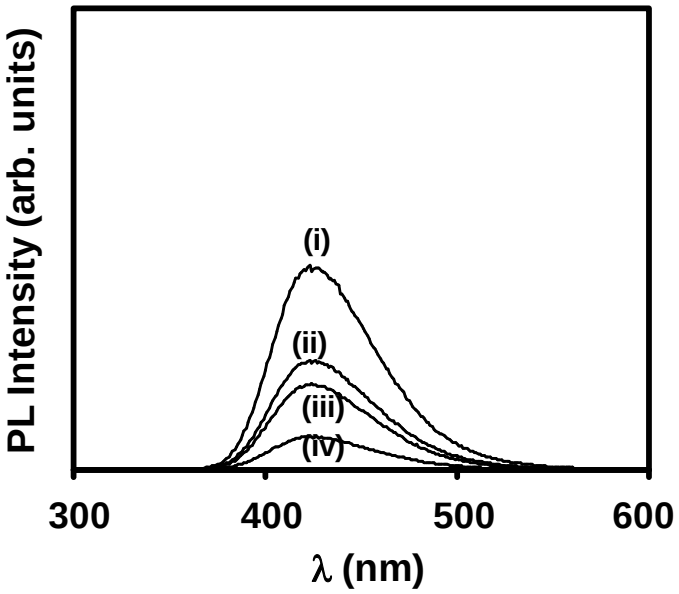

Fig. 2.18. Variation in the PL intensity of 2-hydroxyterephthalic acid, at the UV-radiation exposure time of 60 min, obtained using the HpAc-samples processed with increasing initial concentration of H_3PO_4 catalyst: 1.7 (i), 3.4 (ii), 5.73 (iii), and 6.8 g l^{-1} (iv).

2.3.3. Effect of acid-catalyst on morphological and phase evolution of nanocrystalline TiO_2

In the present investigation, the nanocrystalline TiO_2 has been synthesized via conventional and acid-catalyst-modified sol-gel using an alkoxide precursor. The overall chemical reactions responsible for the formation of nanocrystalline TiO_2 via the conventional sol-gel method can be described as[6]

$$Ti(OC_3H_7)_4 + 4H_2O \rightarrow Ti(OH)_4 + 4C_3H_7OH \quad (2.4)$$

$$Ti(OH)_4 \rightarrow TiO_2 + 2H_2O \quad (2.5)$$

$$Ti(OC_3H_7)_4 + 2H_2O \rightarrow TiO_2 + 4C_3H_7OH \quad (2.6)$$

For NoAc-sample, the calcination of amorphous-TiO_2 at higher temperature produces predominantly anatase-TiO_2 with the nanocrystallite size-distribution in the range of 10-30 nm. The sol-gel process has been modified here using three different acid-catalysts,

HNO_3, CH_3COOH, and H_3PO_4, having the pKa values of -1.64, 4.76, and 2.1 respectively which suggest that HNO_3 is a strong-acid and the latter two are the weak-acids. When the acid-catalyst is used during the processing of nanocrystalline TiO_2 via sol-gel method, it tends to protonate the electronegative alkoxy-group within the alkoxide precursor through the attack of H_3O^+.[12,29] The stronger the acid, the greater the degree of protonation. This results in both an increased positive-charge on the alkoxide-precursor and an increased repulsive force between the central Ti^{4+} ions and protonated alkoxy-groups. This in turn makes the central Ti^{4+} ion more susceptible to the attack of H_2O. In the case of HNO_3, being a strong-acid, all four alkoxy-groups are likely to be protonated which enhances significantly the rate of hydrolysis reaction relative to that obtained in the absence of an acid-catalyst.

$$Ti(OC_3H_7)_4 + H_3O^+ \rightarrow (OC_3H_7)_3Ti\text{-}OC_3H_7 \cdots H_3O^+ \quad (2.7)$$

$$(OC_3H_7)_3Ti\text{-}OC_3H_7 \cdots H_3O^+ + 4H_2O \rightarrow (OH)_3Ti\text{-}OH \cdots H_3O^+ + 4C_3H_7OH \quad (2.8)$$

In the case of CH_3COOH and H_3PO_4, being the weak-acids, all four alkoxy-groups are not protonated and as a consequence although the rate of hydrolysis is faster than that obtained without the use of acid-catalyst, it is relatively slower than that obtained using HNO_3 as an acid-catalyst.[12,26] Following hydrolysis reaction, the OH-groups within the titanium hydroxide ($Ti(OH)_4$) remain protonated which produce the repulsive forces between the adjacent hydroxide molecules within the sol preventing the condensation reaction to occur. The greater the degree of protonation, the lower the condensation rate, and hence, the smaller the size of hydroxide species. Thus, both the rate of condensation reaction and the size of hydroxide species are the lowest when the HNO_3 is used as an acid-catalyst and the largest when no acid is utilized as a catalyst. During the drying process, the solvent and H_2O are evaporated, resulting in the formation of amorphous-

TiO_2 particles from the hydroxide precursor. Hence, the average nanoparticle size of amorphous-TiO_2 in the dried-state should vary as per the sequence of NiAc < HpAc < AcAc < NoAc. Thus, the strength of acid-catalyst plays a significant role in determining the average nanoparticle size of amorphous-TiO_2 in the dried-state by controlling the rate of hydrolysis and condensation reactions within the sol. Since smaller nanoparticles have greater tendency to aggregate and form bigger size nanoparticles, the specific surface-area of amorphous-TiO_2 obtained in the dried-state should also vary with pKa-values of acid-catalyst in the same sequence as NiAc < HpAc < AcAc < NoAc. However, the values tabulated in Table 2.1 show that the specific surface-area of amorphous-TiO_2 obtained in the dried-state varies as per the sequence of NiAc < AcAc < NoAc < HpAc which is more or less similar to the trend obtained after the calcination treatment. Careful comparison shows that it is only the HpAc-sample which exhibits a different trend than that of the expected one. It hence appears that, relative to NoAc-sample, the presence of NO_3^- and CH_3COO^- anions on the surface of amorphous-TiO_2 nanoparticles does not affect the above sequence. However, due to the strong repulsive forces between the adjacent nanoparticles created by their greater anionic-charge and ability to bind strongly to the TiO_2 surface, only the presence of PO_4^{3-} anions results in a change as observed in the above sequence.

The anions are known to remain adsorbed on the surface of amorphous-TiO_2 particles in the dried-state.[8] These anions further play a major role in controlling the morphological, chemical, and structural variations during the calcination treatment. The NO_3^- anions have weaker affinity towards Ti^{4+} and are decomposed and/or oxidized completely at about 200-400 ^oC.[9,11] These anions are also not detected here for NiAc-sample via EDX and FTIR analyses. During the calcination treatment, their decomposition and/or oxidation suddenly exposes the clean-surfaces resulting in the rapid growth of TiO_2

nanoparticles since their size is possibly the smallest in the dried-state which provides the maximum driving force for the nanoparticle growth via the classical coarsening and oriented aggregation/coarsening models.[10] The resulting large average nanocrystallite size, Fig. 2.1b, with the considerable anatase-to-rutile phase transformation, Fig. 2.4b, strongly supports this hypothesis.[9] The CH_3COO^- anions are also known to be easily decomposed and/or oxidized at about 300-400 ^oC.[8] However, being organic in nature, their removal results in the deposition of carbon-residue as a contamination on the surface of TiO_2 particles. Similar observation has been reported earlier when an organic polymer is utilized for the synthesis of nanocrystalline TiO_2 via sol-gel method.[23] The presence of residual CH_3COO^- anions and/or the carbon-residue as contamination on the surface may effectively suppress an excessive nanoparticle growth relative to that observed in the case of NiAc-sample. When NO_3^- anions are decomposed at higher temperature, they leave no residue on the surface. In contrast to this, when CH_3COO^- anions are decomposed and/or oxidized, they leave behind the carbon-residue and/or residual CH_3COO^- anions. This has been demonstrated here via the FTIR, Fig. 2.7, analyses. The surface-chemistry of NiAc- and AcAc-samples after the calcination at higher temperature is hence different which is then reflected in the different values of various parameters such as the average nanoparticle size, zeta potential, amount of MB dye-adsorbed in the dark, concentration of $^{\bullet}OH$ produced under the UV-radiation exposure, and k_{app} as well as the degree of stabilization of anatase-TiO_2. As far as the adventitious carbon is concerned, which normally exists as a mono-atomic layer, its amount on the surface of both samples can be assumed to be the same. Hence, for the comparison purpose, its effect on the measured values of different parameters can also be assumed to be the same, and hence, can be neglected. In the case of AcAc-sample, the thickness of adventitious carbon-film is however increased after the calcination treatment

and possibly produces the steric-hindrance effect on the nanoparticle growth similar to that of surface-adsorbed organic polymer.[23] The stabilization of anatase-TiO_2 due to an enhanced resistance of amorphous-carbon to the anatase-to-rutile phase transformation by inhibiting the growth in the average nanocrystallite size has been reported in the literature.[30] In addition to this, the negative-charge on the residual acetate-ions may also contribute to some extent in controlling the growth of nanoparticles. As a result, after the calcination treatment, the nanocrystallite size distribution of AcAc-sample is restricted to the range comparable with that of NoAc-sample; however, its specific surface-area remains larger than that of NoAc- and NiAc-samples. The deposition of carbon-residue as the surface-contamination has been reflected in the lowest value of negative surface-potential (-0.4 mV) as observed for AcAc-sample. Further, PO_4^{3-} anions are known to have the strongest ability to bind with the surface of TiO_2 nanoparticles relative to that of other anions such as NO_3^-, CH_3COO^-, and Cl^-.[11,31] The detection of P via EDX and that of PO_4^{3-} groups via FTIR analyses strongly support the presence of latter on the surface of HpAc-sample. It appears that their presence provide a negative surface-potential (-23 mV) which strongly limits the close approach of neighboring TiO_2 nanocrystallites resulting in the formation of a sponge-like mesoporous morphology having very high specific surface-area consistent with the other report.[11] As evidenced via TEM, XRD, and BET analyses, the maximum restriction to the particle growth and anatase-to-rutile phase transformation has been achieved during the calcination treatment of HpAc-sample due to resistance to the growth of nanocrystallites created by the presence of PO_4^{3-} anions on the surface.

The maximum stabilization of anatase-TiO_2 as observed for NoAc-, AcAc-, and HpAc-samples, and considerable anatase-to-rutile phase transformation as noted for NiAc-sample appear to be governed by their final nanocrystallite size distribution and strong

aggregation tendency. There exists a critical size of ~14 nm for the stabilization of anatase-phase in a single strain-free TiO_2 nanocrystallite as a size-induced effect, above which the rutile-phase is thermodynamically stable.[6,32] The critical size for the above phase stabilization is known to shift to higher values due to the strong aggregation tendency of TiO_2 nanocrystallites which generates excessive internal stresses opposing the volume changes associated with the phase transformation.[6,33] In the present investigation, the stabilization of anatase-TiO_2 is observed for the nanocrystallite size as large as ~40 nm which has been attributed to the possible modification in the interfacial energy, presence of strain energy, and change in the interface structure due to the strong aggregation of TiO_2 nanocrystallites. This also explains the formation of large amount of rutile-TiO_2 in the case of NiAc-sample which exhibits large nanocrystallite size distribution (~25-80 nm) due to rapid growth in the nanoparticle size during the calcination treatment.[9]

From the literature data presented in Fig. 2.19 (obtained at the initial solution-pH~1) superimposed with the data obtained in this investigation as indicated by arrows (although not obtained at a constant initial solution-pH), it appears that the amount of anatase-TiO_2 formed is a function of pKa-value of acid-catalyst used during the synthesis. The strong and mild acids (pKa<2) result in the anatase-to-rutile phase transformation; while, the weak-acids (pKa>2) results in the stabilization of anatase-TiO_2. As demonstrated in Fig. 2.19, the data obtained in this investigation tends to follow the reported trend.[11] Hence, we believe that the analysis presented here is also applicable to the data reported by Ao et al.[11] which is obtained for the catalyst-powders processed under the constant initial solution-pH (~1).

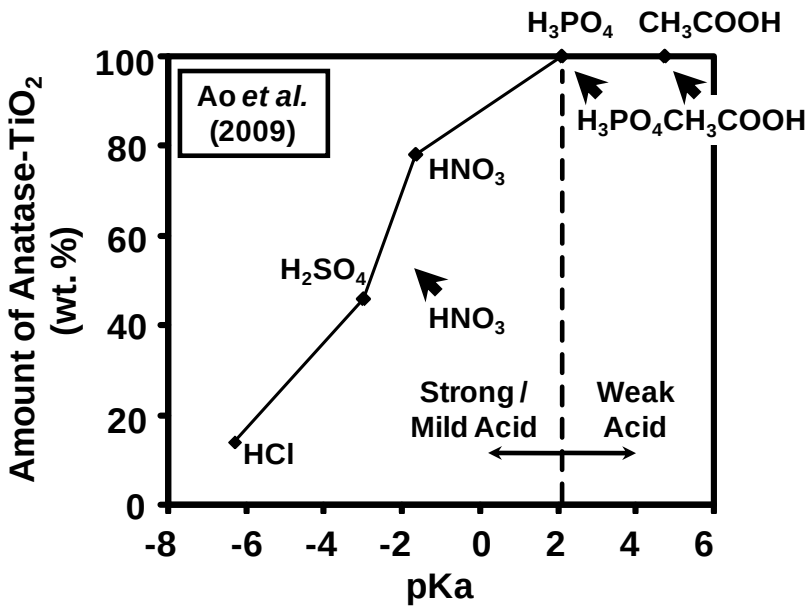

Fig. 2.19. Variation in the amount of anatase-TiO_2 formed as a function of pKa-value of acid-catalyst reported in the literature for the nanocrystalline TiO_2 processed via acid-catalyst-modified sol-gel. The data points in the graph are obtained from Ao et al.[11] at the initial solution-pH~1; while, the arrows indicate the data points obtained in this investigation.

2.3.4. Effect of acid-catalyst on negative surface-potential and $^{\bullet}OH$ formation

For NoAc-sample, the negative surface-potential is the largest (-39 mV), as confirmed via zeta potential measurements, which is primarily governed by the presence of large amount of surface-adsorbed hydroxyl (OH^-) and super-oxide (O_2^-) ions on the clean-surface provided by the NoAc-sample.[18,34] Under the UV-radiation exposure, the $^{\bullet}OH$ are produced via the following modified chemical reactions.[24]

$$TiO_2 + h\nu \rightarrow e^- + h^+ \quad (2.9)$$

$$OH^- + h^+ \rightarrow {}^{\bullet}OH \quad (2.10)$$

$$O_2 + e^- \rightarrow O_2^- \quad (2.11)$$

$$2O_2^- + 2H^+ \rightarrow H_2O_2 + O_2 \quad (2.12)$$

$$H_2O_2 + e^- \rightarrow^{\bullet} OH + OH^- \quad (2.13)$$

The concentration of $^{\bullet}$OH produced is noted to increase with the UV-radiation exposure time as confirmed via $^{\bullet}$OH trapping experiments. In addition to its clean-surface, the largest concentration of $^{\bullet}$OH produced by NoAc-sample is aided by the combination of smaller average nanocrystallite size, predominantly anatase-structure, and synergy-effect between the anatase-rutile phases.[17] The nanocrystalline sol-gel TiO_2 processed using the different acid-catalysts however shows reduced concentration of $^{\bullet}$OH produced at a given UV-radiation exposure time. For AcAc- and NiAc-samples, this reduction is ascribed to the presence of carbon-residue as a surface-contamination and considerably large amount of rutile-phase respectively (note: apart from the adventitious carbon, the carbon-residue in the NiAc-sample may be originated from the incomplete combustion of residual alkoxy-groups present in the dried-sample). A drastic reduction in the negative surface-potential (-0.4 mV) of AcAc-sample is also due to the presence of carbon-residue (contamination) on the surface. The latter reduces the effective amount of potential surface-sites available for the adsorption of OH^- and O_2^- ions which are subsequently converted to $^{\bullet}$OH via the chemical reactions presented in Eqs. (2.9)-(2.13). Moreover, the photo-induced electron-hole pair life-time is known to be minimum for the rutile-TiO_2 relative to that for the anatase-TiO_2,[35-38] which is due to larger average size of former relative to the critical size required for the band-gap energy enhancement.[39] The band-gap energies of connected nanocrystallites of rutile-TiO_2 having different sizes hence remain the same which make it easier for the generated electron-hole pairs to recombine.[17] Lower photo-induced electron-hole pair life-time in the rutile-TiO_2 is thus responsible for lower concentration of $^{\bullet}$OH produced by NiAc-sample. The comparison of HpAc-sample with NoAc-sample shows that the negative surface-potential (-23 mV) of former is primarily governed by the presence of PO_4^{3-} anions on the surface instead of OH^- ions

since the negative surface potential created by the presence of PO_4^{3-} anions may repel OH^- ions in the solution, thus reducing their concentration on the surface. In addition to this, the photo-induced holes, which are required for the formation of $^{\bullet}OH$, are decayed relatively rapidly by the PO_4^{3-} anions present on the surface.[5,40] As a consequence of above factors, the concentration of $^{\bullet}OH$ produced under the UV-radiation exposure is observed to be the lowest for HpAc-sample.

2.3.5. Effect of acid-catalyst on dye-adsorption in dark and photocatalytic activity

In **t**he photocatalytic degradation of MB dye, both the dye-adsorption on the surface and the attack of $^{\bullet}OH$ are considered to be the important steps involved. By using the different types of dyes, it has been recently demonstrated that the mechanism of dye-degradation is dependent on whether the dye is weakly or strongly adsorbing on the surface of photocatalyst particles.[31] When the dye is weakly-adsorbing (< 10% adsorption) on the surface, the dye-degradation via the attack of free $^{\bullet}OH$ is considered to be the predominant mechanism; while, for strongly-adsorbing (> 25% adsorption) dye, the dye-degradation via direct hole-oxidation is considered to be the predominant mechanism. In the present investigation, although only one type of dye is used, the amount of MB dye-adsorbed on the surface of nanocrystalline anatase-TiO_2 is varied from weakly-adsorbing to strongly-adsorbing by changing the processing conditions of photocatalyst particles. As a result, the MB dye degradation may be affected in the present investigation by the nature of acid-catalyst used during the synthesis of the photocatalyst.

Typically for the samples containing predominantly anatase-TiO_2, MB dye adsorption on the surface of photocatalyst particles is controlled by the combination of negative surface-potential and specific surface-area. As a result, as per the aforementioned

mechanisms,[31] NoAc-sample exhibits mild-adsorbing conditions (15%) where the attack of free $^{\bullet}OH$ possibly has significant contribution to MB dye degradation. However, in the present investigation it also appears that, the surface-adsorbed OH^- ions which provide the negative surface-potential are the potential surface-sites for the adsorption of MB dye. Moreover, these sites simultaneously take part in the generation of $^{\bullet}OH$ via hole-oxidation process under the UV-radiation exposure (that is, dual-role of surface-active sites). Thus, the conditions are such that the dye-adsorption and dye-degradation occur at a given surface-site. For AcAc-sample, due to the presence of surface-contamination in the form of carbon-residue, the amount of MB dye adsorbed in the dark is observed to decrease (4 %) substantially. As per the aforementioned mechanisms,[31] the MB dye is weakly-adsorbing on this sample which favours the attack of free $^{\bullet}OH$ for the dye-degradation under the UV-radiation exposure. The photocatalytic activity is decreased for this sample as this mechanism of dye-degradation is mainly dependent on the rate of charge transfer to dissolved O_2 and OH^- (which subsequently produces free $^{\bullet}OH$) which is affected by the surface-contamination. On the other hand, it also appears that for this sample, the concentration of surface-adsorbed OH^- ions is decreased as a result of surface contamination which in turn reduces both the amount of surface-adsorbed MB dye and the concentration of $^{\bullet}OH$ produced via hole-oxidation process under the UV-radiation exposure (that is, dual-role of surface-active sites). As pointed out earlier, in the case of HpAc-sample, the negative surface-potential is governed by PO_4^{3-} anions rather than OH^- ions. The former also provides the potential surface-sties for MB dye adsorption which is drastically enhanced by their uniform distribution on the surface caused by higher specific surface-area of HpAc-sample and greater ionic-charge of PO_4^{3-} anions relative to that of OH^- ions. The amount of MB dye adsorbed in the dark on the surface of HpAc-sample is hence observed to be doubled relative to that observed on the surface of NoAc-

sample. The large amount of moisture and OH-groups present on the surface of HpAc-sample, Fig. 2.7d, appears to be replaceable with MB dye in an aqueous solution resulting in the largest amount of MB dye adsorbed (30%) on the surface of this sample. As per the aforementioned mechanisms,[31] this indicates that HpAc-sample exhibits strongly-adsorbing condition favouring the dye-degradation via direct hole-oxidation. This is partially supported by the highest photocatalytic activity of this sample among all samples investigated here even when the concentration of $^{\bullet}OH$ produced is the lowest as confirmed via $^{\bullet}OH$ trapping experiments. However, the decrease in the concentration of PO_4^{3-} anions present on the surface of HpAc-sample, Fig. 2.9b, as observed after the photocatalysis experiment cannot be explained using this mechanism. In our view, since PO_4^{3-} anions are known to react with and decay the photo-induced holes relatively rapidly,[5,40] they can actively take part in the hole-oxidation process. PO_4^{3-} anions thus not only provide the negative surface-potential for the surface-adsorption of cationic MB dye molecules but may undergo hole-oxidation process causing the dye-degradation under the UV-radiation exposure (that is, dual-role of surface-active sites). The PO_4^{3-} anions can either mediate the transfer of photo-induced holes from the photocatalyst particles to MB dye or the interaction of PO_4^{3-} anions with the photo-induced holes may degrade the former to P and O_2^- ions with the latter subsequently attacking and decomposing the MB dye.[41] Since the concentration of PO_4^{3-} anions present on the surface of HpAc-sample is observed to be reduced after the photocatalysis process, the latter mechanism appears to be a dominant process in decomposing MB dye under the UV-radiation exposure. In addition to this, significantly larger amount of MB adsorption on the surface of HpAc-sample, Table 2.2, is also justified by the presence of PO_4^{3-} anions which provide potential surface-sites for MB dye adsorption. The maximum photocatalytic activity (k_{app}=0.55 min^{-1}) exhibited by HpAc-sample is hence attributed here to its ability to

absorb large amount of MB dye on the surface in the dark simultaneously aided by the active part of PO_4^{3-} anions in the degradation of MB dye under the UV-radiation exposure. Under these situations relatively lower crystallinity of photocatalyst particles, Fig. 2.4d, does not appear to affect its photocatalytic activity which is contrary to the observation often reported in the literature for the nanocrystalline TiO_2 processed under the different conditions.[6,42]

2.3.6. Dual-role of active surface-sites (OH^- and PO_4^{3-} ions)

It appears that for the samples containing predominantly anatase-TiO_2, OH^- and PO_4^{3-} anions present on the surface act as potential surface-sites for dye-adsorption in the dark and dye-decomposition under the UV-radiation exposure. As shown in Fig. 2.20, k_{app} values of these samples are observed to vary linearly (regression correlation coefficient, $<r^2>=1.0$) with the amount of MB dye adsorbed on their surfaces in the dark. The graph reveals that when the active surface-sites (OH^- and PO_4^{3-} ions) which are responsible for both surface-adsorption of MB dye and dye-degradation under the UV-radiation exposure, then k_{app} varies linearly with the amount of MB dye adsorbed on the surface. This has been attributed to the fact that under these conditions the amount of MB dye adsorbed on the surface and k_{app} are proportional to the number of active surface-sites available for adsorption and those available for the generation of $^{\bullet}OH/O_2^{\bullet-}$ respectively. This in turn makes k_{app} to vary linearly as a function of amount of MB dye adsorbed on the surface. To confirm this hypothesis, the dependence of k_{app} on the amount of MB dye adsorbed in the dark is further examined using NoAc- and HpAc-samples by changing the initial MB dye and H_3PO_4 concentrations.

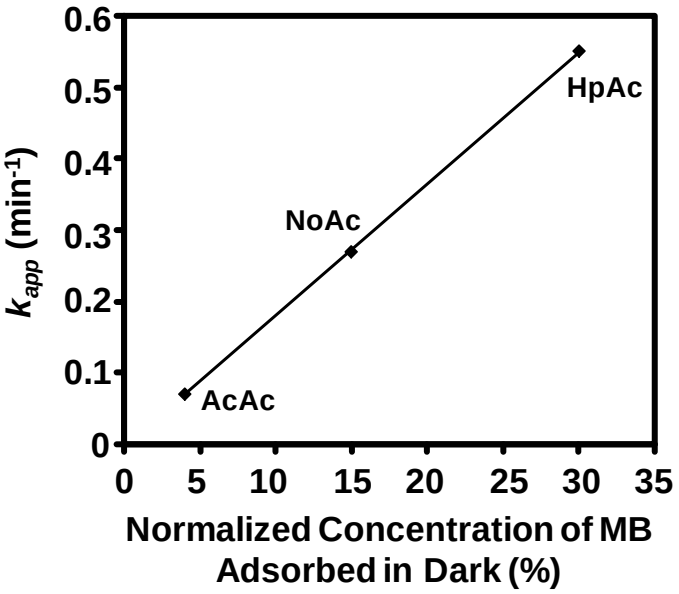

Fig. 2.20. Variation in k_{app} as a function of amount of MB dye adsorbed on the surface after 1 h stirring in dark obtained using the samples containing predominantly nanocrystalline anatase-TiO_2 processed via conventional and acid-catalyst-modified sol-gel.

Within the initial MB dye concentration range of 7.5-90 µM, for NoAc- and HpAc-samples, the amount of MB dye adsorbed in the dark is respectively noted to decrease and increase substantially with increasing initial MB dye concentration. It has been demonstrated that when the photocatalyst particles are suspended in the MB dye solution, the amount of OH^- ions adsorbed on the surface of photocatalyst particles strongly depends on the interaction between the cationic MB dye molecules and OH^- ions within the solution.[43,44] The higher the initial MB dye concentration, the stronger the interaction which can reduce the negative surface-potential by reducing the amount of surface-adsorbed OH^- ions. Hence, the surface-potential of NoAc-sample possibly becomes progressively less negative which is reflected here in the decreasing amount of MB dye adsorbed on the surface with increasing initial MB dye concentration, Fig. 2.14b. For HpAc-sample, the potential surface-sites for MB dye adsorption are provided by PO_4^{3-}

anions rather than OH^- ions present on the surface. As a result, the number of potential surface-sites available for MB dye adsorption is not drastically affected by the interaction of cationic MB dye molecules and OH^- ions within the solution. The amount of MB dye adsorbed in the dark on the surface of HpAc-sample hence increases substantially with the initial MB dye concentration. Due to the gradual consumption of potential surface-sites available for dye-adsorption, the amount of MB dye adsorbed on the surface of HpAc-sample tends to saturate at higher initial MB dye concentrations, Fig. 2.14b.

The k_{app} values for both the samples are however noted to decrease with increasing initial MB dye concentration. As confirmed via $^{\bullet}OH$ trapping experiments, Fig. 2.15, with increasing initial MB dye concentration, the concentration of $^{\bullet}OH$ produced under the UV-radiation exposure is reduced for NoAc-sample due to lower concentration of OH^- ions adsorbed on the surface. Such decrease has also been confirmed for HpAc-sample which is relatively more systematic than that observed for NoAc-sample. It is to be noted that higher amount of MB dye adsorbed on the surface can reduce the amount of UV-radiation reaching the volume of photocatalyst particles which may in turn reduce the number of electron-hole pairs generated, thus affecting the kinetics of dye-degradation. For HpAc-sample, k_{app} value is hence observed to decrease with increasing initial MB dye concentration. Interestingly, for both the samples, the variation in k_{app} as a function of amount of MB dye adsorbed in the dark, derived using Fig. 2.14, can be fitted using a linear relationship ($<r^2>$=0.92 and 0.91), Fig. 2.21a and b. Hence, comparison with Fig. 2.20 strongly suggests that even with increasing initial MB dye concentration, the active surface-sites (OH^- and PO_4^{3-} ions) which are responsible for MB dye adsorption in the dark also play a key role in the degradation of MB dye under the UV-radiation exposure.

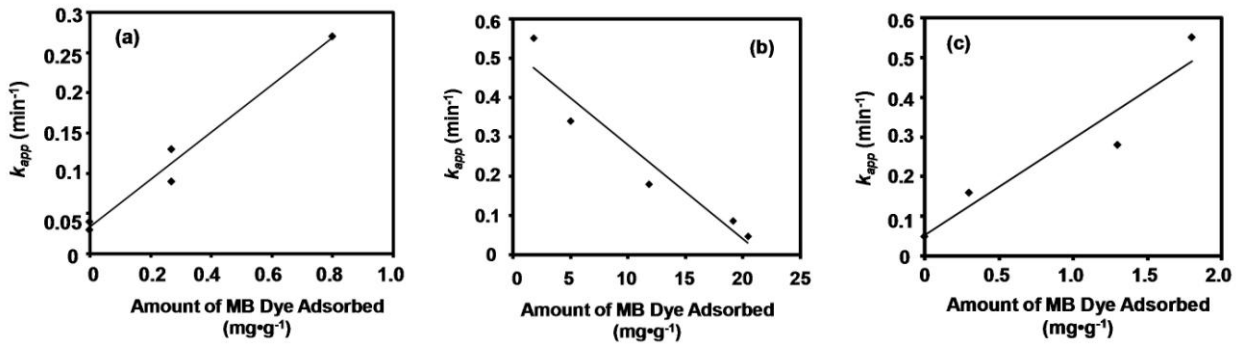

Fig. 2.21. Variation in k_{app} as a function of amount of MB dye adsorbed on the surface per gram of photocatalyst after 1 h stirring in dark as obtained using NoAc (a) and HpAc (b, c) samples. The graphs in (a) and (b) are derived from Fig. 2.14 and that in (c) is derived from Fig. 2.17.

To further confirm the dual-role of PO_4^{3-} anions, the dye-adsorption and photocatalytic activity measurements in the dark and under the UV-radiation exposure were conducted with increasing initial concentration of H_3PO_4 acid-catalyst. Under these conditions, the increasing concentration of PO_4^{3-} anions on the surface is noted to enhance the thermal stability of amorphous-to-anatase phase transformation, Fig. 2.5, which is consistent with the earlier reports.[31] As a result, the band-structure of anatase-TiO_2 is not completely developed for higher concentrations of PO_4^{3-} anions on the surface. The amount of MB dye adsorbed is noted to decrease with increasing concentration of PO_4^{3-} anions which is attributed to decreasing crystallinity of samples with increasing initial concentration of H_3PO_4 acid-catalyst, Fig. 2.5. This further suggests decrease in the number of potential surface-sites for MB adsorption with decreasing crystallinity of HpAc-samples. The concentration of $^{\bullet}OH$ is also decreased with increasing concentration of PO_4^{3-} anions on the surface as confirmed via $^{\bullet}OH$ trapping experiments, Fig. 2.18. This is ascribed to the undeveloped band-structure of TiO_2 and large concentration of lattice- and surface-defects which reduce both the number of photo-induced electron-hole pairs and their life-

time.~~,~~ The k_{app} is, hence, noted to decrease continuously with the increasing initial concentration of H_3PO_4 acid-catalyst. The variation in k_{app} as a function of amount of MB dye adsorbed in the dark as derived using Fig. 2.17 can be fitted using a linear relationship ($<r^2>$=0.91), Fig. 2.21c, which further supports the dual-role of PO_4^{3-} anions as the active surface-sites for the dye-adsorption in the dark and dye-decomposition under the UV-radiation exposure. Thus, the direct dependence of k_{app} on the amount of MB dye adsorbed on the surface in the dark indicates the dual-role of active surface-sites (OH^- and PO_4^{3-} anions) which has been confirmed here by changing the nature of acid-catalyst, initial MB dye concentration, and initial concentration of H_3PO_4 catalyst, Figs. 2.20 and 2.21. It is to be noted that, the maximum photocatalytic activity is exhibited by HpAc-sample having relatively lower crystallinity, Fig. 2.4, which appears to be compensated by the dual-role of PO_4^{3-} anions present on the surface.

Further, variation in the normalized residual MB dye concentration as a function of UV-radiation exposure time, and the corresponding plots for determining the apparent first-order-reaction rate-constants (k_{app}), as obtained for different samples are presented in Fig. 2.22a and b.

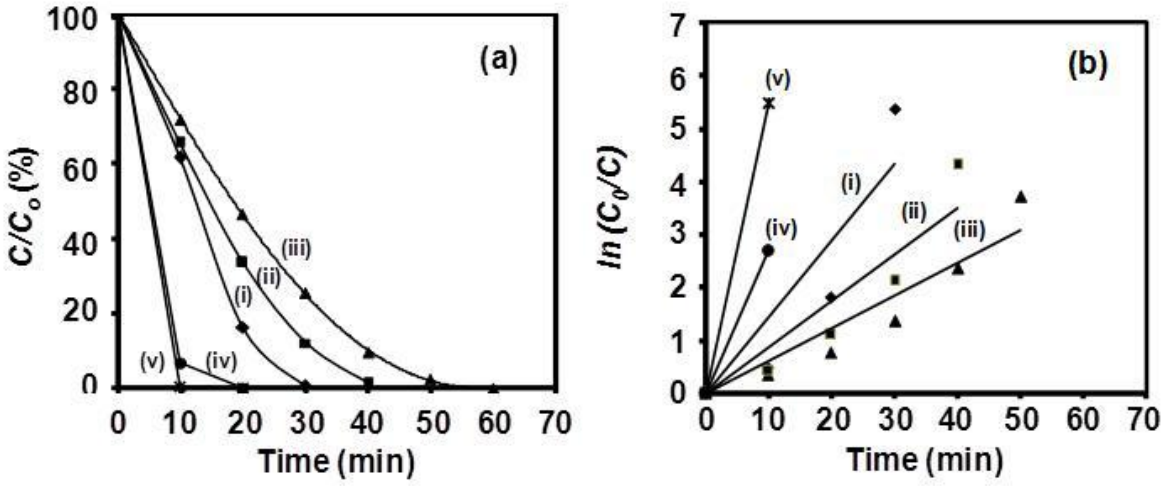

Fig. 2.22. (a) Variation in the normalised concentration of residual MB dye as a function of UV-radiation exposure time, as obtained using the nanocrystalline anatase-TiO_2 processed via conventional (i-iv) and modified (v) sol-gel methods. (b) The corresponding plots for determining k_{app} values. The samples are calcined at 300 ^oC for 1 h (i), 350 ^oC for 1 h (ii), 400 ^oC for 1 h (iii), and 600 ^oC for 2 h (iv,v).

The obtained values of k_{app} and amount of MB dye adsorbed on the surface after 1 h stirring in the dark are presented in Fig. 2.23a and b.

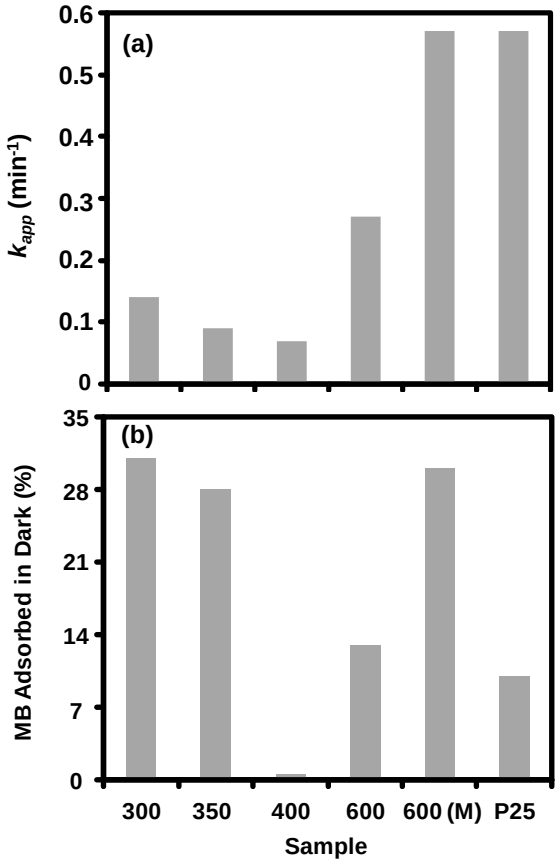

Fig. 2.23. Bar-charts comparing the obtained values of k_{app} (a) and amount of MB dye adsorbed on the surface after 1 h stirring in the dark (b) for nanocrystalline anatase-TiO_2 processed via conventional and modified (M) sol-gel methods. For comparison, the corresponding values obtained for Degussa-P25 are also included. The numbers along the abscissa represent the calcination temperature (^{o}C) of the respective samples.

The corresponding variation in the concentration of $^{\bullet}$OH produced as a function of UV-radiation exposure time, as obtained for the above samples, is presented in Fig. 2.24.

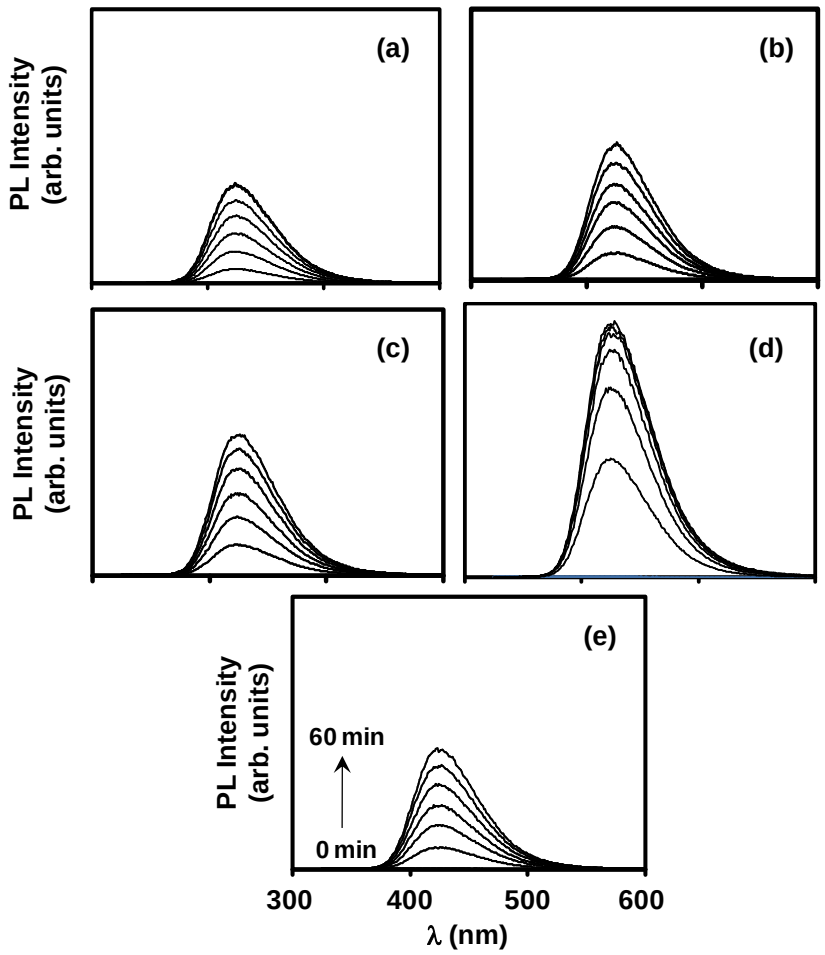

Fig. 2.24. The variation in the PL intensity associated with the formation of 2-hydroxyterephthalic acid as a function of UV-radiation exposure time as obtained using the nanocrystalline anatase-TiO_2 processed via conventional (a-d) and modified (e) sol-gel methods. The samples are calcined at 300 ^oC for 1 h (a), 350 ^oC for 1 h (b), 400 ^oC for 1 h (c), and 600 ^oC for 2 h (d,e). (Note: the maximum scale on the ordinate is identical in (a-e)).

For the nanocrystalline anatase-TiO_2 processed via conventional sol-gel method, both k_{app} and amount of MB dye adsorbed on the surface in dark are noted to decrease with increasing calcination temperature within the range of 300-400 ^oC and then to increase at 600 ^oC, Fig. 2.23. For these samples, the crystallinity (Fig. 2.6a-d) and the concentration of $^{\bullet}OH$ produced (Fig. 2.24a-d) are observed to increase with the calcination temperature.

These trends are, however, conducive in enhancing the photocatalytic activity of nanocrystalline anatase-TiO_2 with the calcination temperature. On the other hand, the concentration of surface-OH groups is noted to decrease with increasing calcination temperature (Fig. 2.8a-d), which is likely to decrease the photocatalytic activity with increasing calcination temperature by decreasing the amount of MB dye adsorbed on the surface in the dark.[45] Moreover, it appears that the amount of MB dye adsorbed on the surface in dark is also affected by the residual organics such as the $–CH_2$/-CH_3 functional groups remaining on the surface of photocatalyst particles after the calcination treatment conducted in a relatively lower temperature range, Fig. 2.8b-d. These groups have been reported to contaminate the surface of nanocrystalline anatase-TiO_2 resulting in a decrease in both the amount of MB dye adsorbed on the surface and k_{app}.[23] Hence, within the calcination temperature range of 300-400 ^oC, the photocatalytic activity is predominantly governed by the variation in the concentration of surface-adsorbed MB dye than that in the concentration of $^{\bullet}OH$ produced. Among the different nanocrystalline anatase-TiO_2 processed via conventional sol-gel method, the maximum k_{app} value is exhibited by the sample calcined at 600 ^oC for 2 h which is contributed by the combination of its clean-surface (Fig. 2.8a), highest crystallinity, presence of small amount of rutile-TiO_2 providing the synergy effect (Fig. 2.6a),[17,46] moderate amount of MB dye adsorbed on the surface in dark (Fig. 2.23b), and largest concentration of free $^{\bullet}OH$ produced under the UV-radiation exposure (Fig. 2.24d).

However, comparison with the nanocrystalline anatase-TiO_2 processed via modified sol-gel method, Fig. 2.22, shows that the latter sample exhibits the highest k_{app} value among all the samples processed here, which is also comparable with that of Degussa-P25. Surprisingly, the crystallinity of this sample is the lowest, Fig. 2.6e. Moreover, this sample exhibits higher amount of MB dye adsorbed on the surface when compared with

that related to the best sample processed via conventional sol-gel method, Fig. 2.23b. However, the concentration of $^{\bullet}OH$ produced by this sample is relatively lower to exhibit very high MB dye degradation kinetics (compare Fig. 2.24d and e). These factors strongly suggest the contribution of some other mechanism responsible for higher MB dye degradation kinetics which is possibly not present in the case of nanocrystalline anatase-TiO_2 processed via conventional sol-gel method. This is further supported by the comparison of nanocrystalline anatase-TiO_2 processed via conventional sol-gel method (calcined at 300 ^{o}C for 1 h) with the sample processed via modified sol-gel method (calcined at 600 ^{o}C for 2 h). Both of these samples have comparable values of average nanocrystallite size (Fig. 2.2a and c), crystallinity (Fig. 2.6d and e), amount of MB dye adsorbed on the surface in dark (Fig. 2.23b), and concentration of $^{\bullet}OH$ produced under the UV-radiation exposure (Fig. 2.24a and e). In spite of these similarities, these two samples exhibit large difference in k_{app} value. This further supports the fact that some other mechanism, other than the formation and attack of $^{\bullet}OH$, is also responsible for higher MB dye degradation kinetics which is possibly not present in the case of nanocrystalline anatase-TiO_2 processed via conventional sol-gel method. It is to be noted that the nanocrystalline anatase-TiO_2 processed via modified sol-gel method possesses large concentration of PO_4^{3-} anions on the surface (Fig. 2.8e) which provide the negative surface-potential conducive for the adsorption of large amount of cationic MB dye. This negative surface-potential is also responsible for repelling the OH^- ions away from the surface in an aqueous solution; thus, reducing the concentration of free $^{\bullet}OH$ produced under the UV-radiation exposure, Fig. 2.24e. It is known that PO_4^{3-} anions interact readily with the photo-induced holes than with the photo-induced electrons.[5,40] Such interaction may possibly lead to the decomposition of PO_4^{3-} anions to the superoxide-ions (O_2^-). As demonstrated in Fig. 2.25 (compare this figure with Fig. 2.8e), the

nanocrystalline anatase-TiO_2 processed via modified sol-gel method shows decrease in the concentration of PO_4^{3-} anions present on the surface after the photocatalytic process, which strongly supports the role of PO_4^{3-} anions in the degradation of surface-adsorbed MB dye under the UV-radiation exposure. Nevertheless, the formation of O_2^- ions should also enhance the concentration of $^{\bullet}OH$ formed under the UV-radiation exposure,[6] which is not reflected here in the free $^{\bullet}OH$ trapping experiments (compare Fig. 2.24d and e). This suggests that the O_2^- ions produced as a result of the decomposition of PO_4^{3-} anions cannot enhance the concentration of $^{\bullet}OH$; however, can degrade the MB dye through the direct attack under the UV-radiation exposure.[40] Consequently, due to the attack of both O_2^- ions and $^{\bullet}OH$ produced under the UV-radiation exposure, the maximum photocatalytic activity is obtained for the nanocrystalline anatase-TiO_2 processed via modified sol-gel method which has the lowest crystallinity.

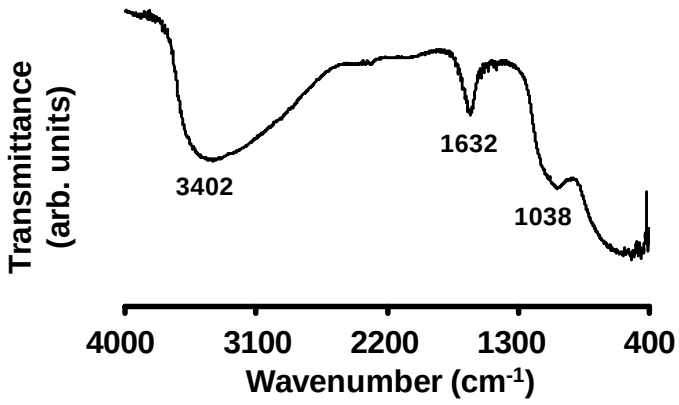

Fig. 2.25. FTIR spectrum obtained using the nanocrystalline anatase-TiO_2 processed via the modified sol-gel method. The sample is calcined at 600 ^{o}C for 2 h. The FTIR spectrum is acquired after using the sample for the photocatalytic activity measurements under the UV-radiation exposure using 7.5 μM of MB dye solution.

Overall, the most striking observation made in this investigation is the largest photocatalytic activity of nanocrystalline anatase-TiO_2 processed via modified sol-gel

method, which has the relatively lower crystallinity of all the samples processed here. The effect of lower crystallinity on the photocatalytic activity appears to be compensated by the presence of PO_4^{3-} anions on the surface, which help adsorb relatively larger amount of MB dye in the dark and subsequently take part in the generation of O_2^- ions under the UV-radiation exposure by the trapping of photo-induced holes, which along with $^{\bullet}OH$ produced, attack and degrade the surface-adsorbed MB dye. The obtained results strongly suggest that the mechanism of MB dye degradation as proposed above can lead to the highest photocatalytic activity under the UV-radiation exposure even when the crystallinity of anatase-TiO_2 is lower.

2.4. Conclusions

Nanocrystalline TiO_2 with the pure-anatase and mixed anatase-rutile structures has been successfully synthesized via conventional and acid-catalyst-modified sol-gel processes. Among the three different acid-catalysts investigated, CH_3COOH and H_3PO_4 stabilize the anatase-TiO_2; while, HNO_3 results in a considerable anatase-to-rutile phase transformation. This has been attributed to the combined effect of controlled rates of hydrolysis and condensation reactions which are governed by the pKa-values of acid-catalysts used, and the final average nanocrystallite size and the degree of their aggregation which are governed by their anionic-part (organic/inorganic) especially during the calcination stage of acid-catalyst-modified sol-gel process. The surface-adsorbed OH^- and PO_4^{3-} anions play a dual-role in the photocatalysis process as the active surface-sites for dye-adsorption in the dark and dye-decomposition under the UV-radiation exposure which has been reflected in a linear relationship between the k_{app} and amount of MB dye adsorbed on the surface under the different processing and test-conditions. The maximum photocatalytic activity (k_{app}=0.55 min^{-1}) under the UV-

radiation exposure is exhibited by the nanocrystalline anatase-TiO_2, processed using the H_3PO_4 as an acid-catalyst which has the lowest crystallinity. This has been attributed to its ability to absorb the largest amount of MB dye on the surface which is supported by the dual-role of PO_4^{3-} anions in the dark and under the UV-radiation exposure. The lowest crystallinity of this sample appears to be highly compensated by the dual-role of PO_4^{3-} anions.

References

(1) Fujishima, A.; Honda, K. *Nature* **1972**, *238*, 37.

(2) Fujishima, A.; Rao, T. N.; Tryk, D. A. *J. Photochem. Photobiol. C* **2000**, *1*, 1.

(3) Nakata, K.; Fujishima, A. *J. Photochem. Photobio.* C **2012**, *13*, 169.

(4) Nakata, K.; Ochiai, T.; Murakami, T.; Fujishima, A. *Electrochem. Acta* **2012**, *84*, 103.

(5) Nakata, K.; Liu, B.; Ishikawa, Y.; Sakai, M.; Saito, H.; Ochiai, T.; Sakai, H.; Murakami, T.; Abe, M.; Takagi.; Fujishima, A. K. *Chem. Lett.* **2011**, *40*, 1107.

(6) Baiju, K. V; Shukla, S.; Sandhya, K.; James, J.; Warrier, K. G. K. *J. Phys. Chem. C* **2007**, *111*, 7612.

(7) Serrano, D. P.; Calleja, G.; Sanz, R.; Pizarro, P. *J. Mater. Chem.* **2007**, *17*, 1178.

(8) Parra, R.; Góes, M. S.; Castro, M. S.; Longo, E.; Bueno, P. R.; Varela, J. A. *Chem. Mater*. **2008**, *20*, 143.

(9) Wang, Z.; Xia, D.; Chen, G.; Yang, T.; Chen, Y. *Mater. Chem. Phys.***2008**, *111*, 313.

(10) Isley, S. L.; Penn, R. L. *J. Phys. Chem. C* **2008**, *112*, 4469.

(11) Ao, Y.; Xu, J.; Fu, D. *Appl. Surf. Sci.* **2009**, *256*, 239.

(12) Termnak, S.; Triampo, W.; Triampo, D. *J. Ceram. Process. Res.* **2009**, *10*, 491.

(13) Baiju, K. V; Shukla, S.; Biju, S.; Reddy, M.; Warrier, K. *Catal. Lett.* **2009**, *131*, 663.

(14) Tian, G.; Fu, H.; Jing, L.; Tian, C. *J. Hazard. Mater.* **2009**, *161*, 1122.

(15) Loryuenyong, V.; Angamnuaysiri, K.; Sukcharoenpong, J.; Suwannasri, A. *Ceram. Int.* **2012**, *38*, 2233.

(16) Li, S.; Ye, G.; Chen, G. *J. Phys. Chem. C* **2009**, *113*, 4031.

(17) Zachariah, A.; Baiju, K. V.; Shukla, S.; Deepa, K. S.; James, J.; Warrier, K. G. K. *J. Phys. Chem. C* **2008**, *112*, 11345.

(18) Priya, R.; Baiju, K.; Shukla, S.; Biju, S.; Reddy, M.; Patil, K.; Warrier, K. *J. Phys. Chem. C* **2009**, *113*, 6243.

(19) Wang, C.; Ao, Y.; Wang, P.; Hou, J.; Qian, *J. Powder Technol.* **2011**, *210*, 203.

(20) Inagaki, M.; Nonaka, R.; Tryba, B.; Morawski, A. W. *Chemosphere* **2006**, *64*, 437.

(21) Maeda, M.; Watanabe, T. *Surf. Coat. Tech.* **2007**, *201*, 9309.

(22) Seery, M. K.; George, R.; Floris, P.; Pillai, S. C. *J. Photochem. Photobio. A* **2007**, *189*, 258.

(23) Baiju, K. V.; Shukla, S.; Sandhya, K. S.; James, J.; Warrier, K. G. K. *J. Sol-Gel Sci. Technol.* **2008**, *45*, 165.

(24) Houas, A.; Lachheb, H.; Ksibi, M.; Elaloui, E.; Guillard, C.; Herrmann, J.-M. *Appl. Catal. B* **2001**, *31*, 145.

(25) Ishibashi, K.-i.; Fujishima, A.; Watanabe, T.; Hashimoto, K. *J. Photochem. Photobiol. A* **2000**, *134*, 139.

(26) Hirakawa, T.; Nosaka, Y. *Langmuir* **2002**, *18*, 3247.

(27) Lee, G. H.; Zuo, J.-M. *J. Am. Ceram. Soc.* **2004**, *87*, 473.

(28) Maira, A.; Coronado, J.; Augugliaro, V.; Yeung, K.; Conesa, J.; Soria, *J. Catal.*

2001, *202*, 413.

(29) Gopal, M.; Moberly Chan, W. J.; De Jonghe, L. C. *J. Mater. Sci.* **1997**, *32*, 6001.

(30) Zhang, D.; Yang, D.; Zhang, H.; Lu, C.; Qi, L. Chem. Mater. **2006**, 18, 3477.

(31) Zhao, D.; Chen, C.; Wang, Y.; Ji, H.; Ma, W.; Zang, L.; Zhao, J. *J. Phys. Chem. C* **2008**, *112*, 5993.

(32) Zhang, H.; F. Banfield, J. *J. Mater. Chem.* **1998**, *8*, 2073.

(33) Shukla, S.; Seal, S. *Int. Mater. Rev*. **2005**, *50*, 45.

(34) Miyauchi, M.; Ikezawa, A.; Tobimatsu, H.; Irie, H.; Hashimoto, K. *Phys. Chem. Chem. Phys.* **2004**, *6*, 865.

(35) Kolen'ko, Y. V.; Churagulov, B. R.; Kunst, M.; Mazerolles, L.; Colbeau-Justin, C. *Appl. Catal. B* **2004**, *54*, 51.

(36) Yamada, Y.; Kanemitsu, Y. *Appl. Phys. Lett.* **2012**, *101*, 133907.

(37) Sumita, T.; Yamaki, T.; Yamamoto, S.; Miyashita, A. *Appl. Surf. Sci.* **2002**, *200*, 21.

(38) Xu, M.; Gao, Y.; Moreno, E. M.; Kunst, M.; Muhler, M.; Wang, Y.; Idriss, H.; Wöll, C. *Phys. Rev. Lett.* **2011**, *106*, 138302.

(39) Lin, H.; Huang, C. P.; Li, W.; Ni, C.; Shah, S. I.; Tseng, Y.-H. *Appl. Catal. B* **2006**, *68*, 1.

(40) Jing, L.; Zhou, J.; Durrant, J. R.; Tang, J.; Liu, D.; Fu, H. *Energy Environ. Sci.* **2012**, *5*, 6552.

(41) Lachheb, H.; Puzenat, E.; Houas, A.; Ksibi, M.; Elaloui, E.; Guillard, C.; Herrmann, J.-M. *Appl. Catal. B* **2002**, *39*, 75.

(42) Yang, J.; Zhang, J.; Zhu, L.; Chen, S.; Zhang, Y.; Tang, Y.; Zhu, Y.; Li, Y. *J. Hazard. Mater.* **2006**, *137*, 952.

(43) Babu, B. K.; Purayil, J. V.; Padinhattayil, H.; Shukla, S.; Warrier, K. G. *Int. J. Appl. Ceram. Technol.* **2013**, *10*, 186.

(44) Akyol, A.; Bayramoğlu, M. *J. Hazard. Mater.* **2005**, *124*, 241.

(45) Li, S.; Ye, G.; Chen, G. *J. Phys. Chem. C* **2009**, *113*, 4031.

(46) Wu, C.; Yue, Y.; Deng, X.; Hua, W.; Gao, Z. *Catal. Today* **2004**, *93*, 863.

Chapter 3

Modified-Hydrothermal Synthesis of Highly Crystalline Pure and Silver-Doped Anatase-Titania Nanotubes / Nanoplates via Double Ion-Exchange Mechanism and Their Dye-Adsorption Characteristics

Graphical Abstract

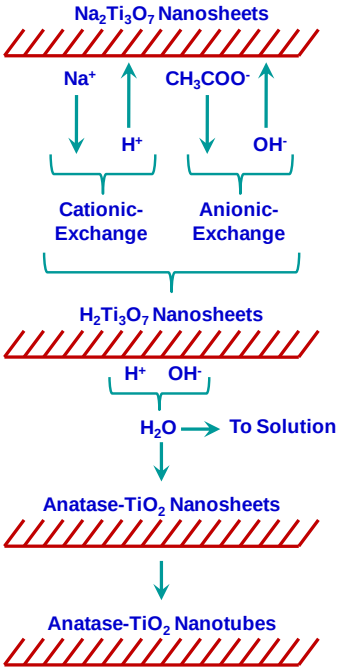

Highlights

- Pure and Ag-doped nanotubes / nanoplates of anatase-TiO_2 are successfully synthesized via modified-hydrothermal technique without the involvement of thermal treatment.
- Involvement of double ion exchange mechanism for the formation of nanotubes / nanoplates of anatase-TiO_2.
- Pure and Ag-doped nanotubes / nanoplates of anatase-TiO_2 find application as adsorbent for the removal of organic synthetic-dye from an aqueous solution.

Abstract

Highly crystalline nanotubes / nanoplates of anatase-TiO_2 with high aspect-ratio have been synthesized, without the involvement of thermal treatment, using the hydrothermal method with the acetic-acid-modified sol-gel processed nanocrystalline anatase-TiO_2 as a precursor. The samples have been characterized via TEM, SAED, XRD, and FTIR for examining their morphology, structure, and surface-chemistry. It has been proposed that the formation of nanotubes / nanoplates of anatase-TiO_2 instead of those of hydrogen titanate, under the given processing conditions, is due to the operation of double ion-exchange mechanism which is in contrast to that of conventional single-ion-exchange mechanism responsible for the formation of latter phase. The as processed nanotubes / nanoplates of pure and silver (Ag)-doped anatase-TiO_2 have been utilized for the dye-removal application involving the surface-adsorption mechanism. The dye-adsorption measurements have been carried out in the aqueous solutions by varying the initial dye-concentration (7.5-250 μM), initial solution-pH (2.5-11), and the amount of Ag-doping (Ag/Ti ratio of 0, 1, and 5 %). The dye-adsorption capacity of pure anatase-TiO_2 nanotubes (ATN) has been determined to be 32 mg g^{-1} at the initial solution-pH of ~10. At the neutral solution-pH of 7.5, the Ag-doped nanotubes of anatase-TiO_2 having the Ag/Ti ratio of 1 % exhibit the maximum dye-adsorption on the surface (39 mg g^{-1}). Hence, controlling the initial solution-pH and the amount of Ag-doping appear to be two different effective approaches for enhancing the amount of dye-adsorbed on the surface of nanotubes of anatase-TiO_2. Further analysis reveals that the Langmuir isotherm model shows the best-fit to the equilibrium adsorption data and the kinetics of dye-adsorption follows the pseudo-second-order model.

3.1. Introduction

TiO_2 is one of the promising semiconductor oxides extensively studied in the past decades due to its versatility in physiochemical properties and technological applications, chemical stability, non-toxicity, low cost, corrosion resistance, and high activity. Recently, different nano-architectures such as the nanotubes, nanorods, nanosheets, and nanobelts have been synthesized which show significant enhancement in the physiochemical properties which are utilized for wide variety of applications. Among these, the nanotubes have been utilized for many functional applications including hydrogen sensors,[1] photocatalysis,[2-5] dye sensitized solar batteries,[6] as supports for CdS quantum dots,[7] electrochromism,[8] ion-exchange material,[9-10] and bone regeneration.[11] Several attempts have been made to tune the physiochemical properties of TiO_2 nanotubes with respect to their application.[8,12-13]

mong the various techniques, hydrothermal synthesis is one of the easiest methods for the synthesis of TiO_2 nanotubes. Highly alkaline condition during the hydrothermal treatment results in the rupturing of Ti—O—Ti bond[14-15] and the formation of lamellar titanate nanosheets which by the exchange of Na^+ and H^+ leads to the formation of a disordered intermediate containing Ti, O, and Na. These intermediates are likely to have trititanate ($Na_xH_{2-x}Ti_3O_7$), tetratitanate ($H_2Ti_4O.H_2O$), or lepidocrocite titanate ($H_xTi_{2-x/4\gamma x/4}O_4$ where x~0.7 and γ=vacancy) structures.[16] The completion of ion-exchange process results in the formation nanosheets of hydrogen titanate which instantly roll-up to form the HTN. It is well known that the HTN obtained via the above reaction mechanism can be transformed into those of anatase-TiO_2 at the temperatures above 400 °C. However, the thermal treatment induces the morphological transformation as well breaking down the nanotubes into either smaller nanotubes or nanoparticles.[17] This limits

the use of nanotubes for the temperature sensitive applications like polymers for flexible solar cell application.[18]

Although the processing of anatase-TiO_2 nanowires and nanofibers via the post hydrothermal treatment of titanate nanotubes have been reported,[19-20] which does not involve any thermal treatment, the processing of anatase-TiO_2 nanotubes via such technique has remained as a challenge. Even the ultrasound- and microwave-assisted hydrothermal techniques require a thermal treatment for obtaining the nanotubes of anatase-TiO_2.[21-22] Studies have shown that highly crystalline anatase-TiO_2 nanoparticles can be obtained via the modification of sol-gel precursor with an acid.[23-30] However, there is no report in the literature which demonstrate the processing of highly crystalline anatase-TiO_2 nanotubes via hydrothermal method using the acid-catalyst modified sol-gel precursor which can eliminate the thermal treatment. In view of this, the first major objective of the present investigation is to introduce a systematic procedure for demonstrating the effect of prior precursor-modification using an acid-catalyst on the development of highly crystalline pure and Ag-doped nanotubes/nanoplates of anatase-TiO_2 (instead of those of hydrogen titanate) via hydrothermal method without the involvement of thermal treatment; while, the second major objective of the present investigation is to propose a possible mechanism for obtaining this new phase under the given processing conditions (that is, with the use of an acid-catalyst-modified sol–gel precursor and without the involvement of thermal treatment). Thirdly, the nanotubes of undoped and Ag-doped anatase-TiO_2 synthesized via the modified hydrothermal method have been utilized to determine their dye adsorption characteristics using a cationic dye such as MB by varying the initial solution pH, initial dye concentration, and amount of Ag doping. The dye adsorption on the surface of undoped and Ag-doped nanotubes of anatase-TiO_2 has been further analyzed by using the different kinetics and equilibrium

adsorption isotherm models. The comparison between the dye adsorption characteristics of hydrothermally synthesized nanotubes (and also the nanosheets) of $H_2Ti_3O_7$ and anatase-TiO_2 has been made.

3.2. Experimental

3.2.1. Chemicals

$Ti(OC_3H_7)_4$, (97 %) is purchased from Sigma-Aldrich Chemicals, Bengaluru, India; 2-propanol (99.5 %, ACS reagent), NaOH (97%), silver nitrate ($AgNO_3$, 99.9 %), and MB (96 %) from S.D. Fine-Chem Ltd., Mumbai, India; CH_3COOH (99.8 %) from Merk, India; and ammonium hydroxide (NH_4OH, 25 % NH_3) from Qualigens Fine Chemicals, Mumbai, India. All chemicals were used as-received without any further purification and/or modification.

3.2.2. Processing of pure and Ag-doped nanocrystalline TiO_2 via conventional and CH_3COOH-modified sol-gel method

Nanocrystalline TiO_2 powders were synthesized via conventional and CH_3COOH-modified sol-gel methods involving the hydrolysis and condensation of $Ti(OC_3H_7)_4$ in 2-propanol. First, the measured quantities of water and CH_3COOH (used only in the case of modified sol-gel process) were dissolved in 125 ml of 2-propanol. A second solution was then prepared in which 0.12 M (final concentration) of $Ti(OC_3H_7)_4$ was dissolved completely in 125 ml of 2-propanol. Both the solutions were sealed immediately and stirred rapidly using the magnetic stirrer to obtain the homogeneous solutions. The ratio of molar concentration of water to that of alkoxide-precursor (*R*) was 90.[31] The ratio of molar concentration of acid-catalyst to that of alkoxide-precursor was 10. The water-part of solution was then added drop-wise to the alkoxide-part under the continuous magnetic

stirring. The initial solution-pH was measured to be 7.8 and 4.1 for the conventional and CH_3COOH-modified sol-gel processes. As a result of the hydrolysis and condensation reactions of $Ti(OC_3H_7)_4$ due to its reaction with water, the color of solution changed from colorless to white. After the complete addition of water-part of solution to that of alkoxide-part, the resulting suspension was stirred for 7 h before drying in an oven (Labline Instruments, Thiruvananthapuram, India) at 80 ^oC for the complete removal of solvent and residual water. The dried powders were then crushed for 10 min using the mortar and pestle (Avio Enterprises, Thiruvananthapuram, India). The dried and crushed powders were then calcined in a muffle furnace (Thermo systems, Thiruvananthapuram, India) at 600 ^oC for 2 h at the heating rate of 3 $^oC\ min^{-1}$ for the crystallization of amorphous-TiO_2 powders. Ag-doped nanocrystalline TiO_2 samples, having Ag/Ti ratio of 1 and 5%, were also processed via conventional and CH_3COOH-modified sol-gel methods. For this, appropriate amount of $AgNO_3$ was dissolved in the water-part of solution before adding to the alkoxide-part of solution. All other steps were identical to those described above.

3.2.3. Processing of nanotubes / nanoplates of pure and Ag-doped anatase-TiO_2 via modified-hydrothermal method without involving thermal treatment

To process the nanotubes and nanoplates of pure and Ag-doped anatase-TiO_2, 3 g of nanocrystalline pure and Ag-doped anatase-TiO_2 powders was suspended in a highly alkaline aqueous solution containing 10 M NaOH filled up to 84 vol% of Teflon-beaker placed in a stainless-steel (SS 316) vessel of 200 ml capacity. The process was carried out with the continuous overhead stirring in an autoclave (Amar Equipment Pvt. Ltd., Mumbai, India) at 120 ^oC for 30 h under an autogenous pressure. The autoclave was allowed to cool naturally to room temperature and hydrothermal product was separated by decanting the top solution. The initial hydrothermal product was separated from the

remaining solution using a centrifuge (R23, Remi Instruments India Ltd.) and washed using 100 ml of 1 M HCl solution for 1 h followed by centrifuging and washing using 100 ml of distilled-water for 1 h. The product obtained after first washing-cycle was then subjected to second washing-cycle. In the latter, the product was washed once using 100 ml of 1 M HCl for 1 h and then multiple times (# 6) using 100 ml of distilled-water for 1 h till the pH of filtrate became almost constant or neutral. The product was separated from the solution using a centrifuge and dried in an oven at 80 ^{o}C overnight to obtain the final hydrothermal product.

3.2.4. Characterization

The morphology and average size of different samples were determined using the TEM operated at 300 kV. The crystalline phases present were determined using the XRD. The broad-scan analysis was typically conducted within the 2θ range of 10-80^{o} using the Cu$K\alpha$ (λ_{Cu}=1.542 Å) X-radiation. The obtained patterns were utilized to determine the weight-fraction of rutile-TiO_2 using the equation,

$$Rutile(wt.\%) = \frac{I_{(110)R} \times 100}{I_{(110)R} + (0.8)I_{(101)A}} \tag{3.1}$$

where, I_A and I_R represent the linear-intensities of main-peaks of anatase-TiO_2 $(101)_A$ and rutile-TiO_2 $(110)_R$. The specific surface-area was measured using the BET surface-area measurement technique via N_2 adsorption using the multi-point method after degassing the nanocrystalline TiO_2 powders in flowing N_2 at 200 °C for 2 h. The surface-chemistry of different samples was analyzed using the FTIR spectroscope within the frequency range of 4000-400 cm^{-1} using the powders dispersed in the KBr pellets.

3.2.5. Dye-adsorption characteristics of nanotubes / nanoplates of pure and Ag-doped anatase-TiO_2

The dye-adsorption experiments in the dark were conducted using the MB as a model catalytic dye-agent. 7.5-250 μM of MB dye was dissolved in an aqueous solution, having an initial solution-pH within the range of 2.5-11 adjusted using HCl and NH_4OH solutions, to prepare total 125 ml dye solution. 0.4 g l^{-1} of powder consisting of nanotubes / nanoplates of pure and Ag-doped anatase-TiO_2 was then dispersed in this solution and the resulting suspension was stirred continuously in the dark for 60 min using a magnetic stirrer. 8 ml aliquot was separated after each 10 min time interval for obtaining the absorption spectra, using the UV-visible absorption spectrophotometer, of filtrate obtained after separating the adsorbent using a centrifuge. The normalized concentration of surface-adsorbed MB dye was calculated using the equation of form,

$$\%MB_{adsorbed} = \left(\frac{\boldsymbol{C_0} - C_t}{\boldsymbol{C_0}} \right)_{MB} \times 100 \qquad (3.2)$$

which is equivalent of form,

$$\%MB_{adsorbed} = \left(\frac{\boldsymbol{A_0} - A_t}{\boldsymbol{A_0}} \right)_{MB} \times 100 \qquad (3.3)$$

where, C_0 (mg l^{-1}) and C_t (mg l^{-1}) correspond to the MB dye concentration at the start and after stirring time t (min) with the corresponding absorbance of A_0 and A_t.

3.3. Results and Discussion

3.3.1. Nanocrystalline particles and nanotubes / nanoplates of pure and Ag-doped anatase-TiO_2 processed via conventional sol-gel and modified-hydrothermal methods

The TEM images of nanocrystalline-TiO_2 particles processed without and with Ag-doping (Ag/Ti ratio of 0.05) via conventional sol-gel method are presented in Fig. 3.1a, b. The corresponding SAED patterns, consisting of concentric ring patterns, are shown as insets which confirm the nanocrystalline nature of both samples. Although for the two samples, the average nanocrystallite size of anatase-TiO_2 is determined to be ~25 nm, the nanocrystallites of average size ~100 nm are also observed in Fig. 3.1b which correspond to rutile-TiO_2. Very fine Ag nanoparticles having the average size of ~10 nm are observed to be uniformly dispersed on the surface of nanocrystalline-TiO_2 particles, Fig. 3.1b. It appears that Ag-doping with Ag/Ti ratio of 0.05 results in the precipitation of Ag^+ ions due to the oversaturation of nanocrystallites of TiO_2 and the subsequent formation of Ag nanoparticles on the surface during the thermal treatment. Such precipitation of Ag^+ ions and formation of Ag nanoparticles, however, are not observed for Ag doping with Ag/Ti ratio of 0.01. The pure nanocrystalline-TiO_2 processed via conventional sol-gel method exhibits BET specific surface-area of 8 m^2 g^{-1}.

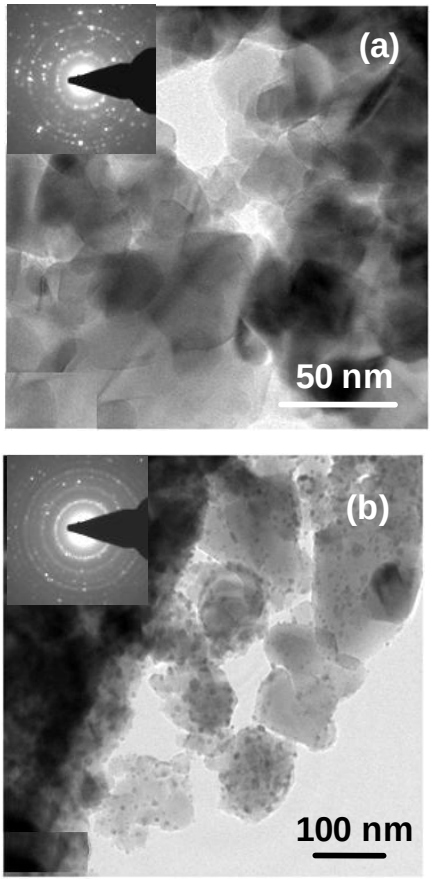

Fig. 3.1. Typical TEM images of pure (a) and Ag-doped (Ag/Ti ratio of 0.05) (b) nanocrystalline TiO_2 processed via conventional sol-gel method. The insets show the corresponding SAED patterns.

The broad-scan XRD patterns obtained using the nanocrystalline-TiO_2 processed without and with Ag-doping (Ag/Ti ratio of 0.01 and 0.05) via conventional sol-gel method are presented in Fig. 3.2. It is observed that the nanocrystalline-TiO_2 processed without and with the Ag-doping (Ag/Ti ratio of 0.01) predominantly contains anatase-TiO_2 along with small amount (15 and 5 wt.%) of rutile-TiO_2. Thus, the conventional sol-gel method inherently results in the formation of small amount of rutile-TiO_2. However, considerable anatase-to-rutile phase transformation (48% rutile-TiO_2) is observed for the Ag-doped nanocrystalline-TiO_2 having the Ag/Ti ratio of 0.05. The average anatase-TiO_2

nanocrystallite size of 26, 27, and 23 nm is calculated for the three samples using the well-known Scherrer equation.

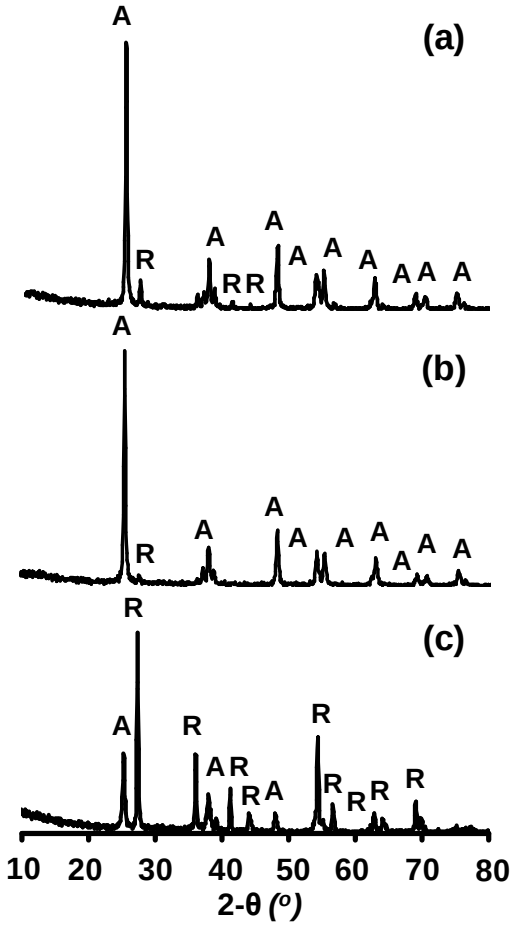

Fig. 3.2. Typical XRD patterns of pure (a) and Ag-doped (Ag/Ti ratio of 0.01 and 0.05) (b,c) nanocrystalline TiO_2 processed via conventional sol-gel method. A and R represent the anatase- and rutile-TiO_2.

Thus, both the average anatase-TiO_2 nanocrystallite size and its weight-fraction are noted to decrease with increasing Ag/Ti ratio which can be explained based on the similar results reported earlier by Chao et al..[32] According to the reported results, the variation in the average anatase-TiO_2 nanocrystallite size as a function of Ag concentration ratio exhibits a depression at Ag concentration in the range of ~2-4% and the former increases with the latter beyond this range. Since the atomic radii of Ag^+ (1.26 Å) is almost twice

that of Ti^{4+} (0.68 Å), the doping of Ag^+ ions into the TiO_2 lattice generates internal stresses which are relieved due to the diffusion of Ag^+ ions to the particle surface during the calcination treatment. As a result, for the given amount of doping, Ag^+ ion concentration is possibly higher near the particle surface than that in the particle interior. The excessive Ag-doping may also result in the precipitation of Ag^+ ions and the formation of Ag nanoparticles on the surface of TiO_2 nanoparticles as observed here in Fig. 3.1b. These Ag^+ ions and Ag nanoparticles present on the surface of TiO_2 nanoparticles produce a pinning effect on the grain boundary migration; thus, restricting the particle growth and anatase-to-rutile phase transformation during the calcination treatment. At higher Ag/Ti ratio, the average size of Ag nanoparticles formed on the surface of TiO_2 nanoparticles increases which reduce the pinning effect on the grain boundary migration. In addition to this, as the oxygen-ion vacancies are created for the charge-balance, their concentration is also likely to be higher near the particle-surface than that in the particle interior (although no direct measurements are conducted here to confirm this hypothesis). However, the presence of large concentration of oxygen-ion vacancies are known to trigger the anatase-to-rutile phase transformation through the reduction in the activation energy for the grain boundary migration resulting in a rapid grain boundary movement.[33-34] Moreover, the anatase-to-rutile phase transformation is an exothermic process which is accompanied by other exothermic reactions during the calcination treatment, such as the decomposition of residual organics and nitrates groups if present in the sample. All these exothermic reactions increase the local temperatures around the anatase-grains within the nanocrystalline TiO_2 powder during the calcination treatment; thus, facilitating the anatase-to-rutile phase transformation. The combined effect of above three major factors, an increase in the average size of Ag nanoparticles, presence of large concentration of oxygen-ion vacancies, and occurrence of exothermic

reactions, is to increase the driving force for an increase in the size of TiO_2 nanoparticles and subsequent the anatase-to-rutile phase transformation. It appears that for lower Ag/Ti ratio, the grain boundary pinning by Ag^+ ions and Ag nanoparticles dominates over the combined effect of other three major factors; while, above a critical Ag/Ti ratio, the effect of latter dominates over that of former. Accordingly, in the present investigation, large amount of rutile-TiO_2 is formed for Ag/Ti ratio of 0.05, Fig. 3.2c, with relatively larger average nanocrystallite size, Fig. 3.1b.

Thus, the XRD diffraction analysis shows that the structures of pure and Ag-doped nanocrystalline TiO_2 are different. In order to avoid the effect of different precursor-structures on the morphological and structural evolution of final hydrothermal products, it is essential to eliminate the anatase-to-rutile phase transformation so as to obtain the precursor-powders having only the nanocrystalline anatase-TiO_2. Hence, the nanocrystalline-TiO_2 was processed using the CH_3COOH-modified sol-gel process.[35] The broad-scan XRD patterns obtained using the nanocrystalline-TiO_2 precursor-powders processed without and with Ag-doping (Ag/Ti ratio of 0.01 and 0.05) via CH_3COOH-modified sol-gel method are presented in Fig. 3.3. It is clearly observed that all three samples exhibit only the anatase-structure indicating that the anatase-to-rutile phase transformation is completely avoided by processing the nanocrystalline-TiO_2 via CH_3COOH-modified sol-gel method.

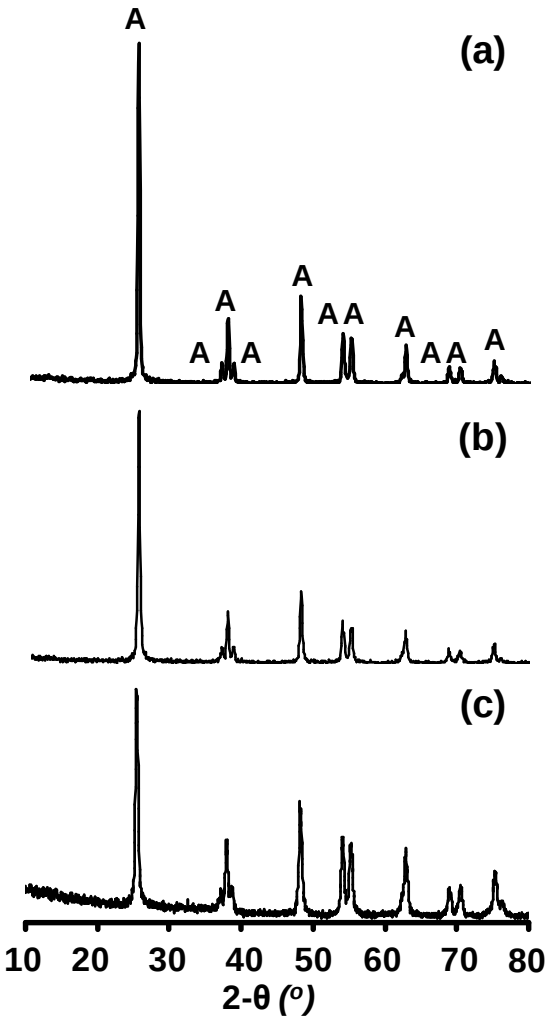

Fig. 3.3. XRD patterns obtained for the nanocrystalline TiO_2 processed via CH_3COOH-modified sol-gel methods with Ag/Ti ratio of 0 (a), 0.01 (b), and 0.05 (c)

The average anatase-TiO_2 nanocrystallite size of 28, 22, and 17 nm is calculated using the well-known Scherrer equation which is in accordance with that reported by Chao et al..[32] (Note: pure nanocrystalline anatase-TiO_2 processed via CH_3COOH-modifed sol-gel method possesses BET specific surface-area of 28 m^2 g^{-1} which is larger than that of similar sample processed via conventional sol-gel method and is primarily attributed to the effect of acid-catalyst used.) The stabilization of anatase-TiO_2 concurrent with Ag-doping as obtained via CH_3COOH-modified sol-gel method is attributed here to the decreased average nanocrystallite size of anatase-TiO_2 as the effect of an acid-catalyst

and has been reported earlier by Seery et al..[35] Hence, it appears that the modification of conventional sol-gel process using CH_3COOH has a significant effect on the anatase-to-rutile phase transformation.

The FTIR spectra obtained for the nanocrystalline anatase-TiO_2 processed via conventional and CH_3COOH-modified sol-gel processes are presented in Fig. 3.4a, b. For both the samples, the absorbance-peak within the frequency range of 2992-3400 cm^{-1} is attributed to the stretching vibrations of surface-adsorbed -OH groups; while, that within the frequency range of 1632-1651 cm^{-1} is attributed to the bending vibrations of surface-adsorbed H_2O.[23,36] The absorbance-peak in lower frequency region, 400-800 cm^{-1}, is related to Ti-O-Ti bonds. Typically, for the nanocrystalline anatase-TiO_2 processed using CH_3COOH-modified sol-gel method, in addition to the above peaks, the absorbance-peaks observed at 1337, 1427, and 1555 cm^{-1} are related to $–CH_2$ / $-CH_3$ functional groups,[31,37] which suggest the deposition of carbon-residue as the surface-contamination produced due to the decomposition and/or oxidation of CH_3COO^- anions during the high temperature calcination treatment. (Note: the absorbance-peaks at 2347 and 2359 cm^{-1} are attributed to CO_2 adsorbed on the surface of samples from the surrounding atmosphere .[31])

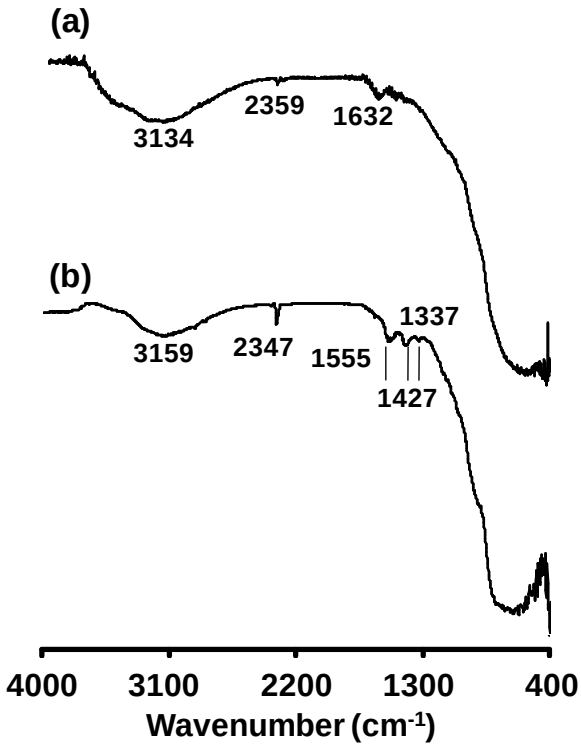

Fig. 3.4. FTIR spectra obtained for the pure nanocrystalline TiO_2 processed via the conventional (a) and CH_3COOH-modified (b) sol-gel methods.

Thus, the FTIR spectra strongly suggest the presence of residual carbon only on the surface of nanocrystalline anatase-TiO_2 processed via CH_3COOH-modified sol-gel method. It is pointed out earlier that the anatase-to-rutile phase transformation is favored by the grain boundary movement which may be retarded by grain boundary pinning effect of Ag^+ ions and finely dispersed Ag nanoparticles. It appears that the grain boundary pinning effect is further enhanced by the presence of residual carbon; thus, stabilizing anatase-TiO_2 phase in all three samples, Fig. 3.3. The stabilization of anatase-TiO_2 due to an enhanced resistance of amorphous-carbon to anatase-to-rutile phase transformation by inhibiting the growth in the average nanocrystallite size has been reported in the literature.[38]

3.3.2. Nanotubes / nanoplates of pure and Ag-doped anatase-TiO_2 processed via modified-hydrothermal method without involving thermal treatment

Pure and Ag-doped nanocrystalline anatase-TiO_2 obtained via CH_3COOH-modified sol-gel method are then utilized for the processing of nanotubes / nanoplates of anatase-TiO_2 via hydrothermal technique. The TEM images of final hydrothermal products are presented in Fig. 3.5. In the case of pure and Ag-doped sample having Ag/Ti ratio of 0.01, the final hydrothermal products exhibit the nanotube morphology, Fig. 3.5a, b; on the other hand, that in the case of Ag-doped sample having Ag/Ti ratio of 0.05 is noted to be nanoplate which is decorated with the finely distributed Ag-nanoparticles on the surface, Fig. 3.5c. The nanotubes in Fig. 3.5b are noted to be more curved than those in Fig. 3.5a. The average internal and outer diameters, wall-thickness, and length of pure and Ag-doped (Ag/Ti ratio of 0.01) nanotubes are determined to be ~4.3, 8, 3.7, and 150 nm respectively; while, in the case of Ag-doped (Ag/Ti ratio of 0.05) nanoplates, the average width and length are determined to be ~25 nm and ~3 μM. Very fine Ag nanoparticles with the average size of ~10 nm are also observed to be uniformly dispersed on the surface of nanoplates, Fig. 3.5c. The BET specific surface-area of pure and Ag-doped (Ag/Ti ratio of 0.01 and 0.05) samples is estimated to be ~130, 127, and 183 $m^2 g^{-1}$ respectively.

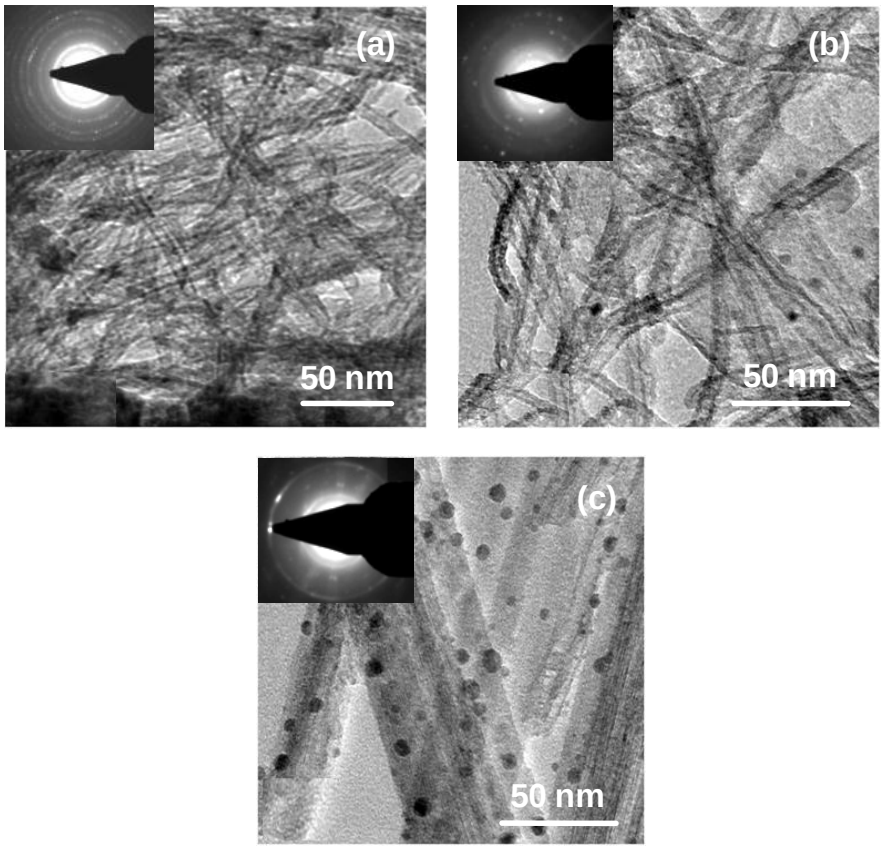

Fig. 3.5. Typical TEM images of final hydrothermal products obtained using the nanocrystalline anatase-TiO_2 as a precursor processed using the CH_3COOH-modified sol-gel method. The samples are processed with the Ag/Ti ratio of 0 (a), 0.01 (b), and 0.05 (c). The insets show the corresponding SAED patterns

The formation of nanotube morphology, as observed in the case of former two samples, is in accordance with the well-known roll-up mechanism.[39-40] In the case of latter, it appears that the roll-up mechanism is hindered by the presence of Ag^+ ions and Ag-nanoparticles on the surface which does not allow the nano-sheets to roll-up resulting in the formation of nanoplates.[41] As shown in Fig. 3.1b, the nanocrystalline TiO_2 particles are not only doped with Ag^+ ions but also decorated with Ag nanoparticles. As a result, the nanosheets formed during the subsequent washing-steps conducted after the hydrothermal treatment also remain doped with Ag^+ ions and decorated with the Ag

nanoparticles.[42] However, the presence of these species on the surface results in the formation of nanoplates rather than that of nanotubes.

The broad-scan XRD patterns obtained using the three final hydrothermal products are presented in Fig. 3.6. It is noted that pure and Ag-doped (Ag/Ti ratio of 0.01) nanotubes are essentially made up of anatase-TiO_2, Fig. 3.6a, b. In the case of Ag-doped sample with the Ag/Ti ratio of 0.05, Fig. 3.6c, along with the anatase-TiO_2, the major-peaks of pure-Ag are also identified by comparing the obtained pattern with the Joint Committee on Powder Diffraction Standards (JCPDS) card number 04–0783. It is, thus, unambiguously confirmed that when the nanocrystalline anatase-TiO_2 processed via CH_3COOH-modified sol-gel method is used as a precursor during hydrothermal processing, the final hydrothermal products (nanotubes / nanoplates) also have highly crystalline anatase-structure irrespective of the amount of Ag-doping. Since several investigations have already reported the formation of nanotubes of hydrogen titanate when the anatase-TiO_2 is used as a precursor,[43-47] the formation of nanotubes / nanoplates of anatase-TiO_2 is striking and attributed here to the effect of precursor-modification due to its processing via CH_3COOH-modified sol-gel method.

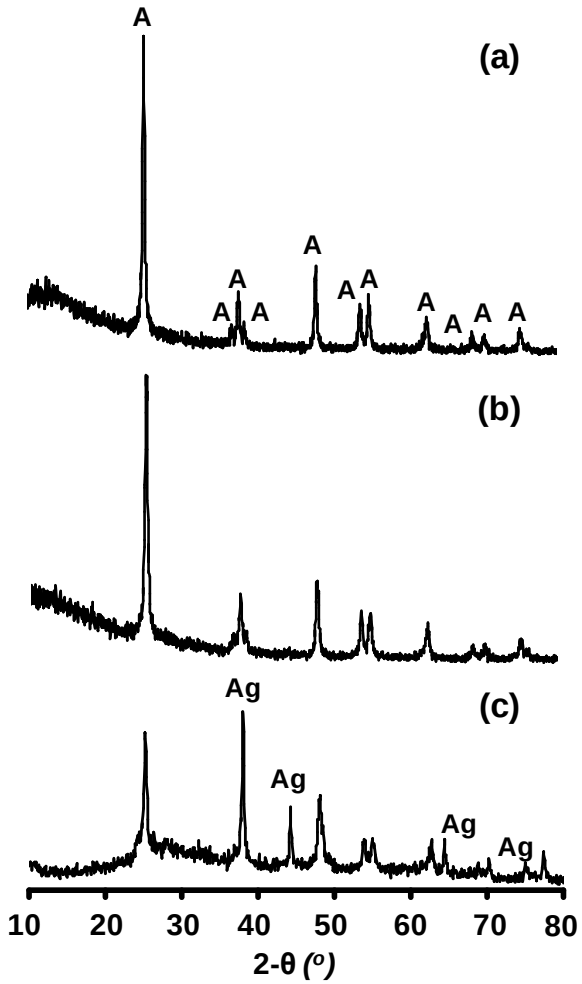

Fig. 3.6. XRD patterns of final hydrothermal products obtained using the nanocrystalline anatase-TiO_2 as a precursor processed using the CH_3COOH-modified sol-gel method with the Ag/Ti ratio of 0 (a), 0.01 (b), and 0.05 (c). A represents anatase-TiO_2.

The FTIR spectrum obtained for pure nanotubes of anatase-TiO_2, processed via hydrothermal treatment involving CH_3COOH-modified sol-gel processed nanocrystalline anatase-TiO_2 as a precursor, is presented in Fig. 3.7. Comparison with Fig. 3.4b suggests the absence of any residual carbon and/or CH_3COO^- anions on the surface of hydrothermally processed pure nanotubes of anatase-TiO_2.

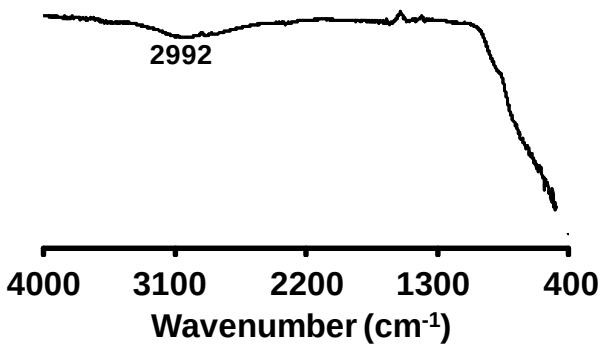

Fig. 3.7. FTIR spectrum obtained for pure nanotubes of anatase-TiO_2 processed via hydrothermal treatment involving CH_3COOH-modified sol-gel processed nanocrystalline anatase-TiO_2 as a precursor.

3.3.3. Mechanism of formation of nanotubes / nanoplates of pure and Ag-doped anatase-TiO_2 via modified-hydrothermal without involving thermal treatment

Interestingly, after the thermal treatment at 600 ^oC for 2 h, CH_3COO^- anions are possibly decomposed completely leaving behind only the carbon-residue on the surface of TiO_2 particles.[23,37,48] As a result, the absorbance-peaks located at 1337, 1427, and 1555 cm^{-1} are rather weak in intensity, Fig. 3.4b. It is to be, however, noted that such decomposition of CH_3COO^- anions is possible only on the surface of TiO_2 particles. In the present investigation, the TiO_2 nanocrystallites are observed to be highly aggregated forming larger size nanoparticles. Moreover, the adsorption of CH_3COO^- anions on the surface of TiO_2 nanocrystallites / nanoparticles takes place during the sol formation stage. As a result, large concentration of CH_3COO^- anions is likely to be trapped inside the aggregated TiO_2 nanoparticles formed within the sol. During the calcination treatment of dried powders at higher temperature (600 ^oC), the entrapped-CH_3COO^- anions are possibly not decomposed and escaped through the aggregated TiO_2 nanocrystallites, and also not detected via FTIR analysis. However, as described below during the hydrothermal processing, since the mechanism of formation of nanotubes / nanoplates

involves an exfoliation of $Na_2Ti_3O_7$ nanosheets, the entrapped-CH_3COO^- anions are likely to be exposed on the surface of these nanosheets which then play a major role during the first washing-cycle resulting in the operation of as-proposed double ion-exchange mechanism.

The mechanism of formation of hydrogen titanate nanotubes / nanoplates via hydrothermal technique using an unmodified anatase-TiO_2 precursor has been described in detail elsewhere by us[41,43] and others[39-40] which is also shown here in the Scheme 3.1a. In short, the hydrothermal treatment of anatase-TiO_2 under the autoclave conditions, in a highly alkaline solution, results in the formation of blocks of $Na_2Ti_3O_7$ phase which has a layered-structure. During the washing treatment, this phase undergoes an exfoliation into the nanosheets of $Na_2Ti_3O_7$ and concurrent single ion-exchange mechanism between Na^+ and H^+ ions resulting in the formation of $H_2Ti_3O_7$ nanosheets which immediately roll-up to form the nanotubes of $H_2Ti_3O_7$ due to the presence of dangling bonds and reduced repulsive forces on the surface. The nanotubes of anatase-TiO_2 are then derived via thermal treatment of $H_2Ti_3O_7$ nanotubes typically in the range of 300-400 ^oC by expelling the moisture from the structure.[43]

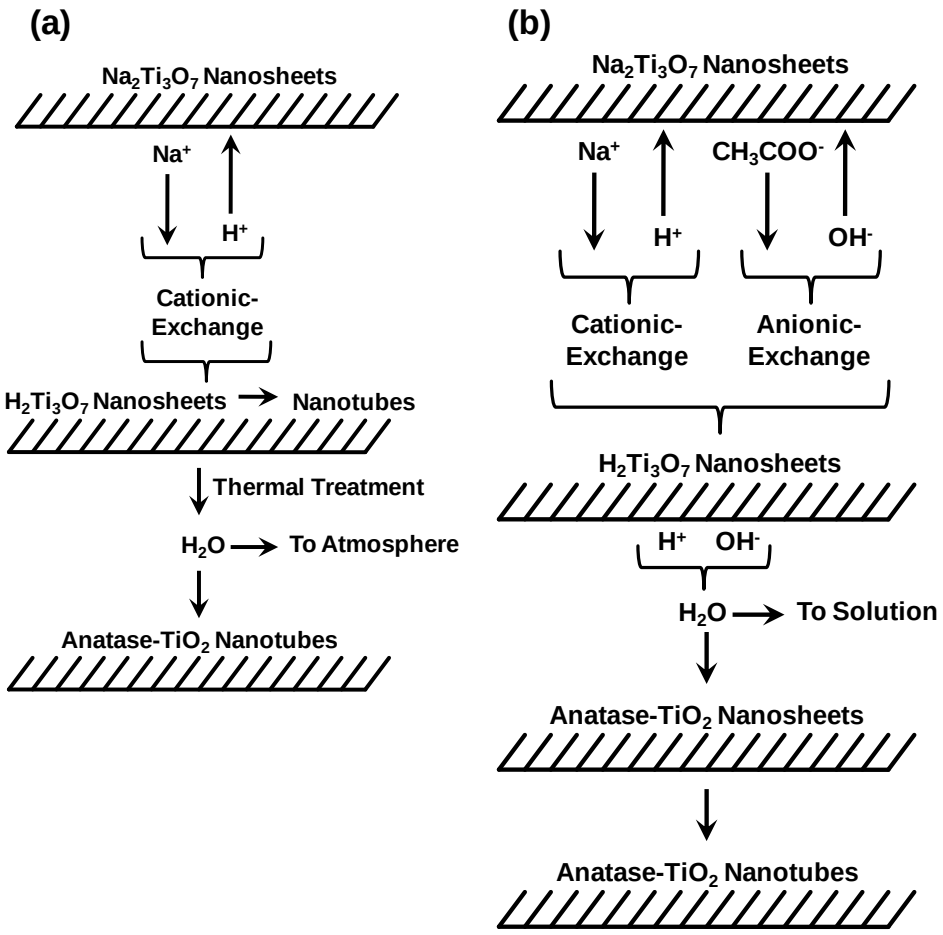

Scheme 3.1. Single ion-exchange (a) and as-proposed double ion-exchange (b) mechanisms which lead to the formation of nanotubes / nanoplates of hydrogen titanate and anatase-TiO_2 obtained via hydrothermal treatment of pure and CH_3COOH-modified anatase-TiO_2 precursors and the subsequent washing of hydrothermal products.

$$H_2Ti_3O_7 \xrightarrow{\Delta} 3TiO_2 + H_2O \tag{3.4}$$

In the present investigation, although the pure and doped nanotubes are formed directly after the washing and drying steps, they exhibit anatase structure instead of hydrogen titanate. Hence, it appears that the mechanism of formation of these nanotubes is different than the one described in the Scheme 3.1a as the latter does not account for the formation of nanotubes of anatase-TiO_2 without the involvement of thermal treatment. In order to explain the mechanism of formation of pure and doped nanotubes / nanoplates of

anatase-TiO_2, the variation in solution-pH during the washing-cycles is measured which is tabulated and compared in Table 3.1 for nanocrystalline anatase-TiO_2 precursors processed via conventional and CH_3COOH-modified sol-gel methods.

Table 3.1. Comparison of variation in solution-pH values obtained during the two washing-cycles conducted immediately after the hydrothermal treatment of pure nanocrystalline anatase-TiO_2 precursor processed using two different methods.

Washing Cycle #	**Washing Step**	**Initial Solution-pH**	**Final Solution-pH**	
			Sol-Gel	**CH_3COOH-Modified Sol-Gel**
1	1 M HCl	0.05	13.0	1.04
	Distilled H_2O	7.25	12.4	2.23
2	1 M HCl	0.05	1.0	0.43
	Distilled H_2O # 1	7.25	1.8	1.12
	# 2	7.25	2.5	2.49
	# 3	7.25	3.0	3.38
	# 4	7.25	4.7	6.98
	# 5	7.25	5.9	7.69
	# 6	7.25	6.5	7.8

It is noted that the variation in solution-pH is significantly different for the two precursors during the first washing-cycle. For the precursor processed via the conventional sol-gel method, after washing the initial hydrothermal product with 1 M

HCl solution and distilled H_2O (cycle-1), the initial solution-pH is noted to increase from highly acidic- / neutral-region to highly basic-region which is the result of a single ion-exchange mechanism, Scheme 3.1a. On the other hand, for the nanocrystalline anatase-TiO_2 precursor processed via CH_3COOH-modified sol-gel method, the final solution-pH is noted to be reduced back to highly acidic-region under the similar washing conditions. As explained below, it strongly appears that the latter reduction in the solution-pH is caused by the concurrent reaction occurring on the surface of $Na_2Ti_3O_7$ nanosheets. Hence, the mechanism of formation of pure and doped nanotubes / nanoplates of anatase-TiO_2 is possibly related to this concurrent reaction. As described in the Scheme 3.1b, the CH_3COO^- anions possibly play a key role in the formation of nanotubes / nanoplates of pure and Ag-doped anatase-TiO_2 via the hydrothermal method without the involvement of thermal treatment. These CH_3COO^- anions may undergo an anionic-exchange with OH^- in the solution simultaneously with the cationic-exchange between Na^+ and H^+ ions. This double ion-exchange mechanism, involving both the cationic and anionic exchanges, can lead to the accumulation of large concentration of H^+ and OH^- ions within the structure and on the surface of simultaneously formed $H_2Ti_3O_7$ nanosheets. These H^+ and OH^- ions then possibly undergo a condensation reaction forming H_2O which is immediately released into the surrounding solution. Thus, H^+ ions present within the structure of $H_2Ti_3O_7$ nanosheets is instantly pulled out by the surface-adsorbed OH^- ions. The release of H_2O appears to be very similar to the release of moisture during the thermal treatment of $H_2Ti_3O_7$ nanotubes, Eq. 3.4, which results in the formation of nanotubes of anatase-TiO_2. Hence, as described in the Scheme 3.1b, due to the release of H_2O as a consequence of double ion-exchange mechanism, $H_2Ti_3O_7$ nanosheets spontaneously transform to anatase-TiO_2 nanosheets which then roll-up to form the nanotubes of anatase-TiO_2. The double ion-exchange mechanism ceases to operate in the

second washing-cycle, due to the complete loss of CH_3COO^- anions from the surface in the first-cycle, for which the variation in the solution-pH is comparable for both the precursors. The complete loss of CH_3COO^- anions is supported by FTIR analysis, Fig. 3.7, where the presence of residual carbon and/or CH_3COO^- anions is not detected on the surface of nanotubes of anatase-TiO_2, Fig. 3.7.

3.3.4. MB dye adsorption using undoped nanotubes of anatase-TiO_2

The hydrothermally synthesized undoped nanotubes of anatase-TiO_2 are utilized for MB dye-adsorption from the aqueous solutions. The variations in the normalized concentration of MB dye adsorbed on the surface of undoped nanotubes of anatase-TiO_2 as a function of contact time, as obtained for different initial MB dye concentrations and initial solution pH, are presented in Fig. 3.8. It is observed that the normalized concentration of MB dye adsorbed on the surface of undoped nanotubes of anatase-TiO_2 increases rapidly within the first 10 min of contact time and then it tends to attain equilibrium with further increase in the contact time. For the initial solution pH within the range of ~2.5-10, the normalized concentration of MB dye adsorbed on the surface at equilibrium is the highest at the lowest initial MB dye concentration and former decreases with increase in the latter, Fig. 3.8a-c. Comparison, however, shows that the trend is reversed in a highly basic solution (pH~11), Fig. 3.8d. Under this condition, the normalized concentration of MB dye adsorbed at equilibrium is relatively lower at the lowest initial MB dye concentration and the former increases with the latter within the range of 7.5-30 µM. Above this range (60-200 µM), the normalized concentration of MB dye adsorbed at equilibrium is noted to decrease with the increasing initial MB dye concentration. This reverse trend observed in a highly basic solution is attributed to the interaction of excess OH^- ions within the solution with the cationic MB dye molecules

which restrict and delay the adsorption of latter on the surface of nanotubes of anatase-TiO_2 under these test-conditions.[46]

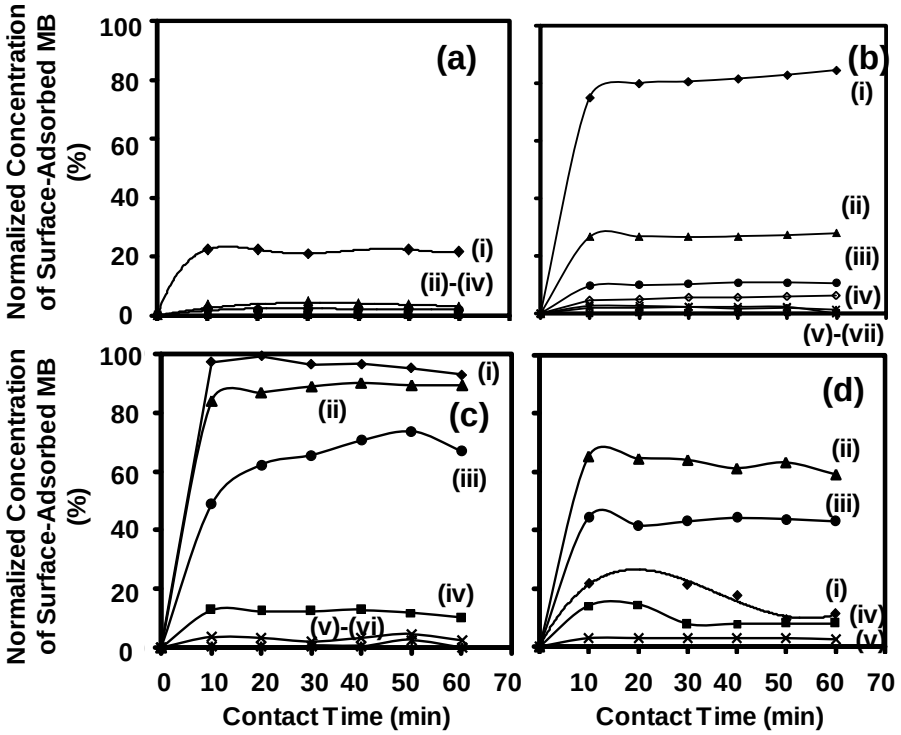

Fig. 3.8. Typical variations in the normalized concentration of surface-adsorbed MB as a function of contact time obtained using the undoped nanotubes of anatase-TiO_2 for the different initial solution pH values: 2.5 (a), 7.5 (b), 10 (c), and 11 (d). In (a), the initial MB dye concentration is varied as 7.5 (i), 30 (ii), 60 (iii), and 150 µM (iv). In (b), it is varied as 7.5 (i), 30 (ii), 60 (iii), 90 (iv), 150 (v), 200 (vi), and 250 µM (vii). In (c), it is varied as 7.5 (i), 30 (ii), 60 (iii), 150 (iv), 200 (v), and 250 µM (vi). In (d), it is varied as 7.5 (i), 30 (ii), 60 (iii), 150 (iv), and 200 µM (v).

The adsorption data presented in Fig. 3.8 is utilized to calculate the amount of MB dye adsorbed on the surface at equilibrium per unit mass of adsorbent, q_e (mg g^{-1}), for a given initial MB dye concentration using the equation of form,[46,49]

$$q_e = \frac{(C_0 - C_e)V}{m_{ads}} \tag{3.5}$$

where, C_o (mg l^{-1}) and C_e (mg l^{-1}) are the MB dye concentrations within the solution at the beginning and equilibrium (that is, after the contact time of 60 min), V (l) the initial volume of MB dye solution, and m_{ads} (g) the amount of adsorbent used. The obtained variation in q_e as a function of initial MB dye concentration is presented in Fig. 3.9 for the different values of initial solution pH.

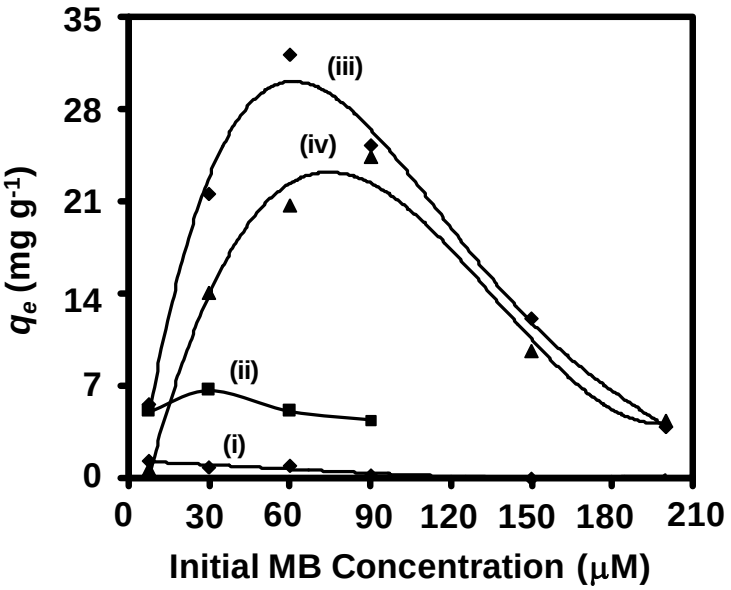

Fig. 3.9. Variation in q_e as a function of initial MB concentration as obtained for the undoped nanotubes of anatase-TiO_2 for the different initial solution pH values: 2.5 (i), 7.5 (ii), 10 (iii), and 11 (iv).

It is noted that at a given initial solution pH, q_e increases with the initial MB dye concentration, reaches a maximum value (q_m (mg g^{-1})) and then decreases with further increase in the initial MB dye concentration. This decrease in q_e at higher initial MB concentration is also related to the interaction of excess cationic MB dye molecules with OH^- ions within the solution which reduces the amount of negative-charge developed on the surface of nanotubes of anatase-TiO_2, and hence, the amount of surface-adsorbed

MB.[46] It is also noted that q_m increases within the initial solution pH range of ~2.5-10, reaches the largest value (termed here as the dye-adsorption capacity of nanotubes of anatase-TiO_2) at the initial solution pH of ~10, and then decreases in a highly basic solution, Fig. 3.10. It appears that the initial solution pH has a significant effect on q_m, and as a result, the dye-adsorption capacity of undoped nanotubes of anatase-TiO_2 is noted to be 32 mg g^{-1} at the initial solution pH of ~10. The MB dye-adsorption capacity of nanotubes of anatase-TiO_2 is observed to be lower than that (105 mg g^{-1}) reported earlier for the hydrothermally synthesized nanotubes of $H_2Ti_3O_7$ which is ascribed to lower specific surface-area (130 m^2 g^{-1}) of former compared with that (330 m^2 g^{-1}) of latter.[46,50]

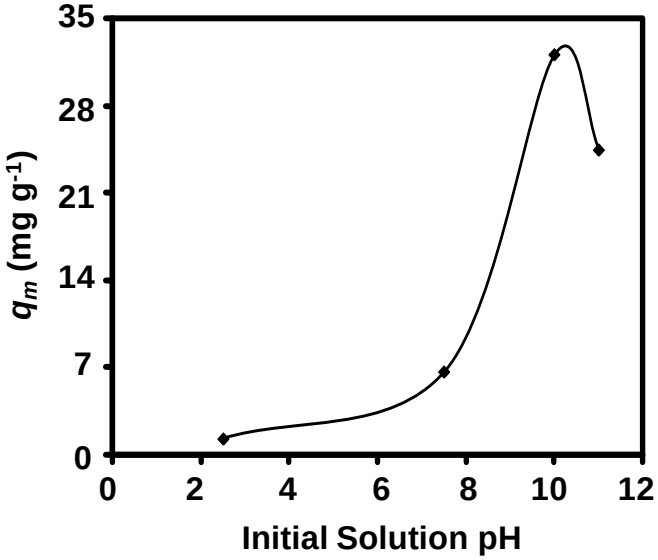

Fig. 3.10. Variation in q_m as a function of initial solution pH as obtained for undoped nanotubes of anatase-TiO_2.

The rate at which the MB dye is adsorbed from an aqueous solution on the surface of undoped nanotubes of anatase-TiO_2 is analyzed using three different kinetics models: Lagergren pseudo-first-order, pseudo-second-order, and intra-particle diffusion.[46,51] The adsorption data presented in Fig. 3.8 is utilized to fit the above kinetics models at the

different initial solution pH, Fig. 3.11, and the values of different parameters derived from the slopes and intercepts of the best-fitted straight-lines are tabulated in Table 3.2 typically for initial solution pH of ~10. It is noted that the regression correlation coefficient, $<r^2>$, values are the highest and closest to 1 for the pseudo-second-order kinetics model. Moreover, the values of q_e estimated using this model are comparable with the experimentally determined values of q_e. Hence, it appears that the adsorption of MB dye on the surface of undoped nanotubes of anatase-TiO_2 follows the pseudo-second-order kinetics.

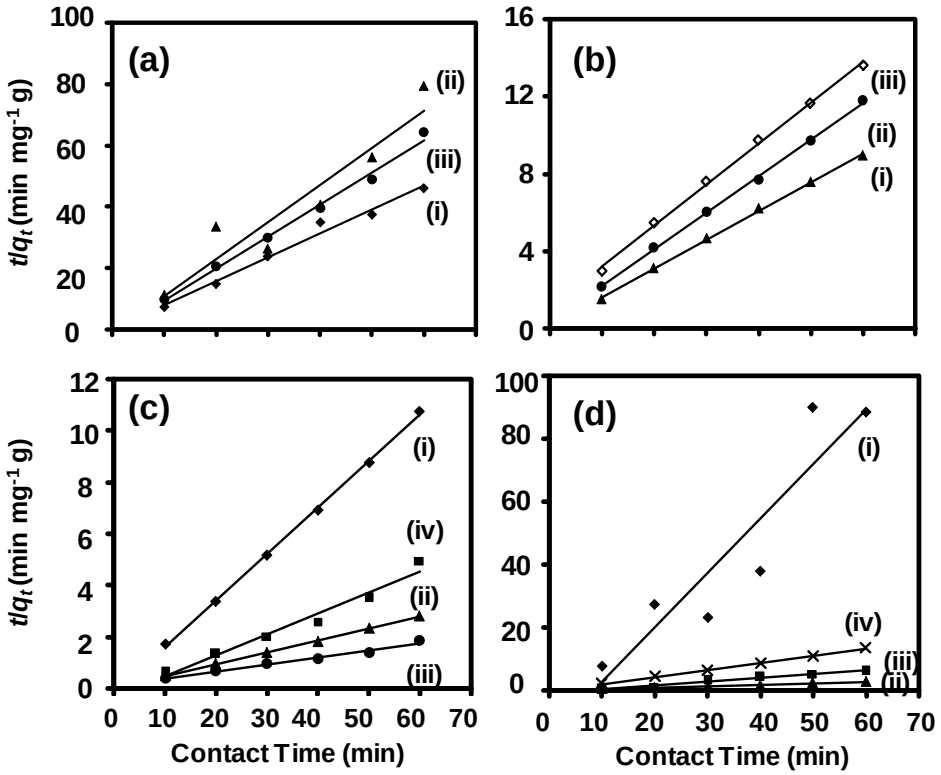

Fig. 3.11. Typical pseudo-second-order kinetics plots for the adsorption of MB dye on the surface of undoped nanotubes of anatase-TiO_2 at the different initial solution pH values: 2.5 (a), 7.5 (b), 10 (c), and 11 (d). In (a), the initial MB dye concentration is varied as 7.5 (i), 30 (ii), and 60 µM (iii). In (b), it is varied as 30 (i), 60 (ii), and 90 µM (iii). In (c), it is varied as 7.5 (i), 30 (ii), 60 (iii), and 150 µM (iv). In (d), it is varied as 7.5 (i), 60 (ii), 150 (iii), and 200 µM (iv). (Note: for clarity, the graphs are shown only for the selected initial MB dye concentrations).

Table 3.2. Kinetics constants for MB adsorption on the surface of undoped nanotubes of anatase-TiO_2 at the initial solution pH of ~10.

[MB]	q_e **(EXP)**	**Pseudo-First-Order Kinetics Model**			**Pseudo-Second-Order Kinetics Model**			**Intra-Particle Diffusion Model**		
		q_e	k_1	r^2	q_e	k_2	r^2	k_{id}	C	r^2
7.5	5.6	--	--	--	5.55	-0.161	0.999	0.645	1.787	0.617
30	21.5	8.6	0.12	0.908	22.2	0.06	0.999	0.293	19.46	0.789
60	32.1	31.5	0.127	0.999	37	0.006	0.985	2.113	18.94	0.741
90	25.2	9.7	0.023	0.328	25	0.0105	0.96	0.412	19.57	0.154
150	12.1	--	--	--	12.3	-0.019	0.97	-0.513	17.39	0.498
200	3.9	--	--	--	4.67	-0.134	0.736	-0.039	5.529	0.002
250	0.3	--	--	--	0.38	-0.163	0.435	0.305	-0.021	0.79

The equilibrium dye-adsorption data, presented in Fig. 3.8, is fitted using the Langmuir, Freundlich, and DKR isotherms.[46,49,51-52] The values of different parameters of three isotherm models obtained from the slopes and intercepts of the best-fitted straight-lines, Fig. 3.12., as well as those of ε, E, ΔG^0, and R_L are tabulated in the Table 3.3 for different initial solution pH values. It is noted that none of the isotherm models are followed at the lowest initial solution pH (~2.5 and 7.5). On the other hand, at higher initial solution pH (~10 and 11), the Langmuir, DKR and Langmuir, Freundlich models are followed. Overall, the equilibrium adsorption of MB dye on the surface of undoped nanotubes of anatase-TiO_2 predominantly follows the Langmuir isotherm.

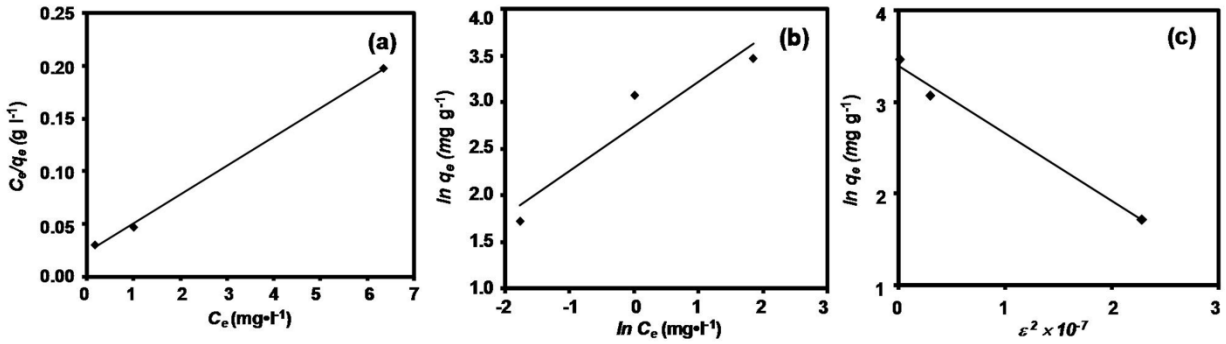

Fig. 3.12. Langmuir (a), Freundlich (b), and DKR (c) isotherm plots for the adsorption of MB dye on the surface of undoped nanotubes of anatase-TiO_2 at the initial solution pH of ~10.

Table 3.3. Values of equilibrium isotherms related parameters for the MB adsorption on the surface of undoped nanotubes of anatase-TiO_2.

pH	q_m ***(EXP)***	**Langmuir**					**Freundlich**			**DKR**			
		q_m	K_L	r^2	R_L	ΔG^0	n	K_F	r^2	q_m	β	r^2	E
2.5	0.93	0.23	-0.2	0.77	--	--	-2.1	2	0.564	0.45	5×10^{-7}	0.172	1
7.5	6.7	4.5	-2.1	0.992	--	--	-21	5.6	0.341	5.2	5×10^{-9}	0.021	10
10	32.1	37	1.23	0.998	0.04-0.25	-34.7	2.1	15.5	0.904	29.6	7×10^{-8}	0.988	2.7
11	24.4	30.3	0.21	0.998	0.14-0.33	-30.4	2.8	8.8	0.996	36.8	8×10^{-5}	0.972	0.08

Thus, the undoped nanotubes of anatase-TiO_2 exhibit q_m of 6.7 mg g^{-1} in the neutral solution which is enhanced to 32 mg g^{-1} (dye-adsorption capacity) at the initial solution pH of ~10. It appears that since the point-of-zero-charge of anatase-TiO_2 is 5.9,[53] when the anatase-TiO_2 nanotubes are suspended in the solution having the initial solution pH of ~10, their surface is highly negatively charged due to the adsorption of large amount of OH^- ions from the solution. The highly negatively charged surface of anatase-TiO_2 nanotubes is then responsible for the surface-adsorption of cationic MB dye molecules via electrostatic attraction mechanism. Hence, controlling the initial solution pH is one

way to enhance the q_m for hydrothermally synthesized undoped nanotubes of anatase-TiO_2.

3.3.5. MB dye adsorption using Ag-doped nanotubes of anatase-TiO_2

In order to enhance q_m, typically at the initial solution pH of ~10, the nanotubes of anatase-TiO_2 are doped with Ag with Ag/Ti ratio of 0.01 and 0.05. The variations in the normalized concentration of MB dye adsorbed on the surface of Ag-doped nanotubes of anatase-TiO_2 as a function of contact time, as obtained for different initial MB dye concentrations and Ag/Ti ratio, at initial solution pH of ~10, are presented in Fig. 3.13. Although the trend in the obtained variations is similar to those observed for the undoped nanotubes of anatase-TiO_2, the comparison of Fig. 3.13 with Fig. 3.8c shows that the curves are shifted upwards for the Ag-doped samples. The adsorption data presented in Fig. 3.13 is utilized to calculate q_e using the Eq. (3.5) which shows that the maximum q_m (~39 mg g^{-1}) is exhibited by Ag-doped nanotubes of anatase-TiO_2 having Ag/Ti ratio of 0.01 which is larger than that (32 and 34 mg g^{-1}) exhibited by the undoped and Ag-doped (Ag/Ti ratio of 0.05) samples. Since an enhancement in the dye-adsorption capacity is observed at the initial solution pH of ~10 relative to that of undoped nanotubes of anatase-TiO_2, Ag-doping is another effective approach for increasing the amount of MB adsorption on the surface of nanotubes of anatase-TiO_2. It appears that the effect of Ag-doping on the amount of MB dye adsorbed may be attributed to the variation in the concentration of superoxide-ions (such as O_2^- ions) pre-adsorbed on the surface in air rather than that in the concentration of surface-adsorbed OH^- ions in an aqueous solution since the dye-adsorption measurements for Ag-doped samples are conducted at the constant initial solution pH of ~10. It is well-known that the presence of surface oxygen-ion vacancies is required for the adsorption of O_2^- ions on the surface of anatase-TiO_2,[54]

$$O_{2(gas)} + V_o^{**} + e^- \rightarrow O_{2(ads)}^- \quad (3.6)$$

where, V_o is an oxygen-ion vacancy. As per the earlier reports,[12,19] the doping of nanocrystalline anatase-TiO_2 with Ag^+ ions results in the generation of oxygen-ion vacancies in large concentrations at the particle surface. These oxygen-ion vacancies are then responsible for the adsorption of O_2^- ions on the surface of nanotubes of anatase-TiO_2 which contribute to their negative surface-charge. This in turn leads to higher MB dye adsorption for Ag-doped sample as observed here for Ag/Ti ratio of 0.01. For Ag-doped sample with Ag/Ti ratio of 0.05, Ag nanoparticles are detected on the surface of nanoplates, Fig. 3.1b.[55] It further appears that the deposited Ag nanoparticles possibly react with the surface-adsorbed O_2^- ions forming a thin layer of Ag_2O on the surface of Ag nanoparticles.[53] This may reduce the negative surface-charge and consequently the dye-adsorption capacity. Overall, controlling the amount of Ag-doping is another effective approach, along with controlling the initial solution pH, to adsorb the MB dye on the surface of nanotubes of anatase-TiO_2 in large amount.

It is to be noted that Ag-doped nanotubes of anatase-TiO_2 having Ag/Ti ratio of 0.05 exhibit the largest specific surface-area among all the three samples[55] which is conducive in enhancing the amount of MB dye adsorbed on the surface. Nevertheless, the dye-adsorption measurements reveal that the effect of reduction in the surface concentration of superoxide-ions (that is, the value of Ag/Ti ratio) dominates that of higher specific surface-area resulting in lower dye-adsorption capacity at Ag/Ti ratio of 0.05. When the dye-adsorption capacity of undoped samples (that is, the nanotubes of anatase-TiO_2 and $H_2Ti_3O_7$[46]) is compared, it appears that the dye-adsorption capacity is primarily governed by the specific surface-area of samples. The MB dye-adsorption capacity of 43 mg g^{-1} has been reported at the initial solution pH of ~10 for the thermally derived nanotubes of

anatase-TiO_2 which possess the specific surface-area of 184 m^2 g^{-1}.[43] In comparison, the nanotubes of anatase-TiO_2 synthesized via modified hydrothermal method, which possess the specific surface-area of 130 m^2 g^{-1}, exhibit the MB dye-adsorption capacity of 32 mg g^{-1}. The observed difference in the dye-adsorption capacity is attributed to the difference in the specific surface-area of these two undoped samples. However, for Ag-doped nanotubes of anatase-TiO_2, the amount of Ag-doping appears to be a dominating factor compared with the specific surface-area.

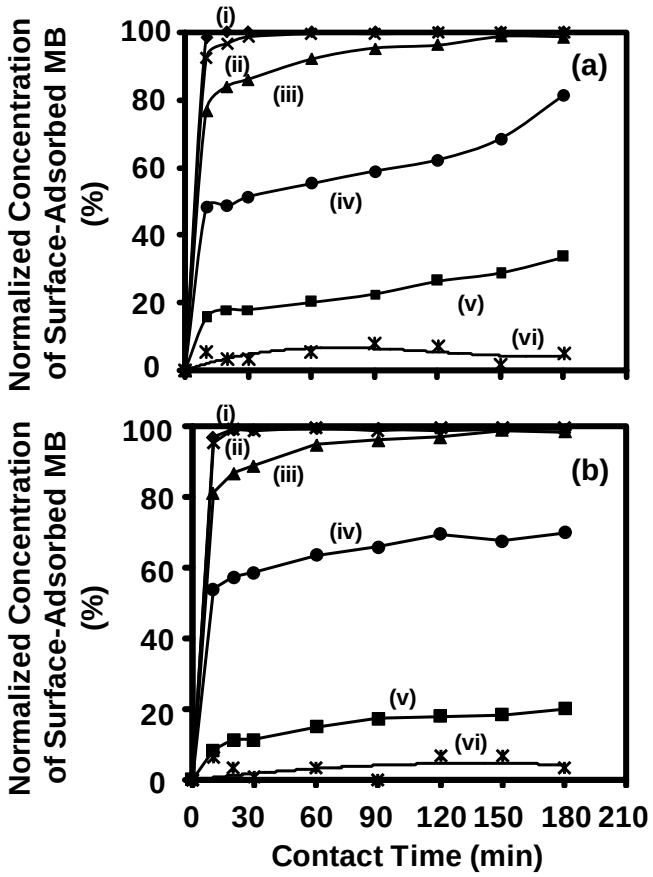

Fig. 3.13. Typical variations in the normalized concentration of surface-adsorbed MB as a function of contact time obtained using Ag-doped nanotubes of anatase-TiO_2 with the Ag/Ti ratio of 0.01 (a) and 0.05 (b) at the initial solution pH of ~10. In (a) and (b), the initial MB dye concentration is varied as 7.5 (i), 15 (ii), 30 (iii), 60 (iv), 100 (v), and 250 µM (vi).

The rate at which the MB dye is adsorbed from an aqueous solution on the surface of Ag-doped nanotubes of anatase-TiO_2 is analyzed using three different kinetics models, and the equilibrium adsorption data is fitted using three different isotherm models. The values of different parameters of three different kinetics models derived from the slopes and intercepts of the best-fitted straight-lines, Fig. 3.14, are tabulated in Table 3.4 for the nanotubes of anatase-TiO_2 having Ag/Ti ratio of 0.01. The values of different parameters of three different equilibrium isotherm models as well as those of ε, E, ΔG^0, and R_L are tabulated in Table 3.5 for varying Ag/Ti ratio at the initial solution pH of ~10. It is noted that the equilibrium adsorption of MB dye on the surface of Ag-doped nanotubes of anatase-TiO_2 follows the pseudo-second-order kinetics and the adsorption isotherm follows the Langmuir, Freundlich and Langmuir, DKR models for Ag/Ti ratio of 0.01 and 0.05. In general, within the investigated range of Ag/Ti ratio, Langmuir model appears to be followed by MB adsorption on the surface of Ag-doped nanotubes of anatase-TiO_2 at the initial solution pH of ~10.

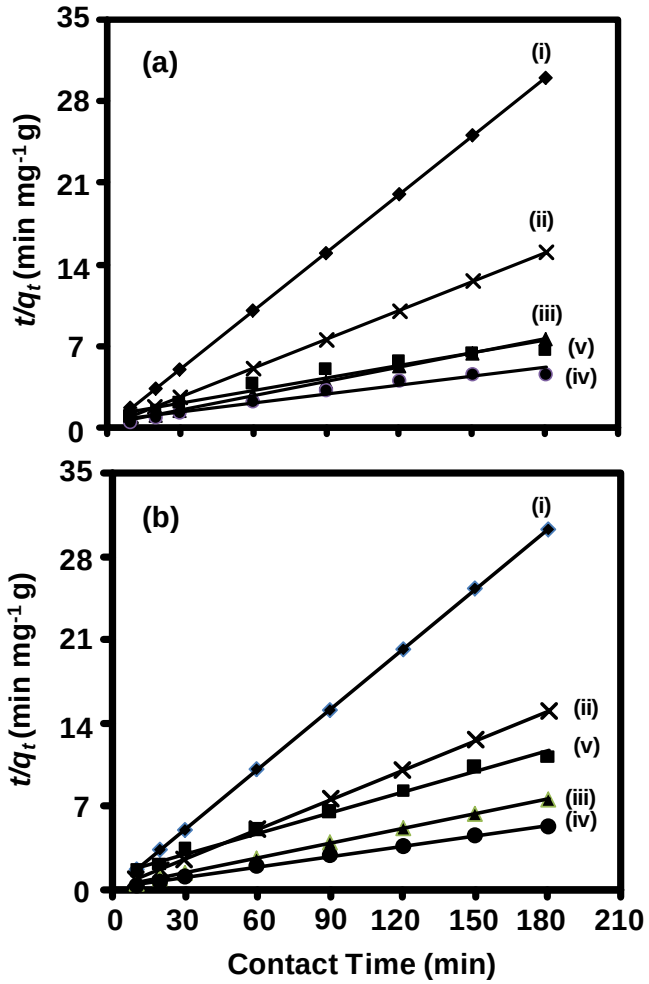

Fig. 3.14. Typical pseudo-second-order kinetics plots for the adsorption of MB dye on the surface of Ag-doped nanotubes of anatase-TiO_2, having the Ag/Ti ratio of 0.01 (b) and 0.05 (b), at the initial solution pH of ~10. In (a) and (b), the initial MB dye concentration is varied as 7.5 (i), 15 (ii), 30 (iii), 60 (iv), and 100 µM (v).

Overall, the equilibrium adsorption of MB dye on the surface of both undoped and Ag-doped nanotubes of anatase-TiO_2 predominantly follows the Langmuir model.

Table 3.4. Kinetics constants for the MB adsorption on the surface of Ag-doped nanotubes of anatase-TiO_2 (Ag/Ti ratio of 0.01) at the initial solution pH of ~10.

[MB] (μM)	**q_e (Exp)**	**Pseudo-First-Order Kinetics Model**			**Pseudo-Second-Order Kinetics Model**			**Intra-Particle Diffusion Model**		
		q_e	k_1	r^2	q_e	k_2	r^2	k_{id}	C	r^2
7.5	6	--	--	--	6	3.1	1	0.004	5.941	0.311
15	12	1.98	0.044	0.845	12	0.116	1	0.066	11.23	0.654
30	23.6	8.93	0.025	0.842	24.4	0.009	0.999	0.486	17.73	0.928
60	39.1	22.4	0.007	0.763	40	0.001	0.958	1.346	17.17	0.869
100	26	19	0.009	0.901	28.6	0.001	0.946	1.277	7.631	0.933
150	10.6	--	--	--	6.94	-0.014	0.525	0.163	8.681	0.021

Table 3.5. Values of equilibrium isotherms related parameters for MB adsorption on the surface of Ag-doped nanotubes of anatase-TiO_2 at the initial solution pH of ~10.

Ag/Ti	**q_m (EXP)**	**Langmuir**					**Freundlich**			**DKR**			
		q_m	K_L	r^2	R_L	ΔG^0	n	K_F	r^2	q_m	β	r^2	E
0.01	39.1	40	3.1	0.997	0.016-0.12	-37	5.2	22	0.999	30.4	-3×10^{-3}	0.792	13
0.05	34	34.5	29	0.999	0.002-0.014	-34	3.85	25.5	0.73	33.2	-1×10^{-2}	0.996	2.67

3.3.6. Comparison of MB dye-adsorption characteristics of HTN and HTNS with those of undoped and Ag-doped ATN

In the Table 3.6a, the best-fit equilibrium adsorption isotherm models followed by undoped nanotubes of anatase-TiO_2, within the initial solution pH range of ~2.5-11, are compared with those of nanotubes and nanosheets of $H_2Ti_3O_7$.[46,56] It is noted that HTN exhibit the specific surface-area and dye-adsorption capacity of 330 m^2 g^{-1} and 105 mg g^{-1}. Under these conditions, HTN follows Langmuir and DKR models at the lowest (~2.5) and highest (~11) initial solution pH values; while, transition from Langmuir to DKR model is observed over the intermediate initial solution pH values.[46] In contrast to this, for HTNS which exhibit the specific surface-area and dye-adsorption capacity of 380 m^2 g^{-1} and 119 mg g^{-1}, Langmuir model is seen to be extended over relatively larger range of initial solution pH which has been attributed to the effect of increased specific surface-area and dye-adsorption capacity of HTNS relative to those of HTN.[56] The comparison with undoped nanotubes of anatase-TiO_2 which exhibit the specific surface-area and dye-adsorption capacity of 130 m^2 g^{-1} and 32 mg g^{-1} indicates that the Langmuir model is obeyed only above higher values (≥10) of initial solution pH which has been attributed here to relatively lower values of specific surface-area and dye-adsorption capacity of undoped nanotubes of anatase-TiO_2. Hence, the specific surface-area and dye-adsorption capacity are the two major factors for hydrothermally synthesized adsorbents which control the range of initial solution pH over which the Langmuir model is typically obeyed. The significance of these parameters is also reflected in the Table 3.6b which shows the emergence of Langmuir model as a dominant equilibrium adsorption isotherm followed with the increasing value of Ag/Ti ratio.

Table 3.6. (a) The best-fit adsorption isotherm models observed for undoped nanotubes of anatase-TiO_2 at the different initial solution pH and their comparison with those reported earlier for other samples synthesized via hydrothermal method. (b) The best-fit adsorption isotherm models observed for Ag-doped nanotubes of anatase-TiO_2 having varying Ag/Ti ratio.

(a)

Initial Solution pH	**HTN[46]**	**HTNS[56]**	**ATN**
2.5	Langmuir	Langmuir	--
7.5	Langmuir, DKR	Langmuir	--
10	Langmuir, Freundlich, DKR	Langmuir	Langmuir, DKR
11	DKR	Langmuir, Freundlich, DKR	Langmuir, Freundlich

(b)

Initial Solution pH	**Ag/Ti**		
	0	**0.01**	**0.05**
10	---	Langmuir, Freundlich	Langmuir, DKR

Considering that the specific surface-area of undoped and doped samples varies as ~130, 127, and 183 $m^2\ g^{-1}$ with the increasing Ag/Ti ratio,[55] the surface-coverage of MB for three samples is calculated (as per the method described elsewhere[46]) to be 40, 50, and 30% which also strongly support the dominance of Langmuir model. It is also noted that the dye-adsorption capacity in terms of mol per specific surface-area is calculated to be 3.8×10^{-8}, 4.8×10^{-8}, and 2.9×10^{-8} mol g m^{-2} with the Ag/Ti ratio varying as 0, 0.01, and

0.05 respectively where the maximum adsorption is again noted for the sample with Ag/Ti ratio of 0.01.

3.4. Conclusions

Pure and Ag-doped nanotubes / nanoplates of anatase-TiO_2 are successfully synthesized via modified-hydrothermal technique without the involvement of thermal treatment. The formation of nanotubes / nanoplates of anatase-TiO_2 is due to the double ion-exchange mechanism which is the result of prior precursor-modification via processing through the CH_3COOH-modified sol-gel method. The pure and Ag-doped nanotubes / nanoplates of anatase-TiO_2 find application as adsorbent for the removal of organic synthetic-dye from an aqueous solution. The dye-adsorption capacity of pure nanotubes of anatase-TiO_2 is determined to be 32 mg g^{-1} at the initial solution-pH of ~10. At the neutral solution-pH of ~7.5, the Ag-doped nanotubes of anatase-TiO_2 having Ag/Ti ratio of 1% exhibit the maximum dye-adsorption on the surface (39 mg g^{-1}). Controlling the initial solution-pH and the amount of Ag-doping appear to be two different effective approaches for enhancing the amount of dye-adsorbed on the surface of nanotubes of anatase-TiO_2. The MB adsorption on the surface of pure and Ag-doped nanotubes / nanoplates of anatase-TiO_2 follows pseudo-second-order kinetics and adsorption isotherm follows Langmuir models.

References

(1) Varghese, O. K.; Gong, D.; Paulose, M.; Ong, K. G.; Dickey, E. C.; Grimes, C. A. *Adv. Mater.* **2003**, *15*, 624.

(2) Adachi, M.; Murata, Y.; Harada, M.; Yoshikawa, S. *Chem. Lett* **2000**, 942.

(3) Akita, T.; Okumura, M.; Tanaka, K.; Ohkuma, K.; Kohyama, M.; Koyanagi, T.; Date, M.; Tsubota, S.; Haruta, M. *Surf. Interface Ana.* **2005**, *37*, 265.

(4) Nakahira, A.; Kubo, T.; Yamasaki, Y.; Suzuki, T.; Ikuhara, Y. Jpn. *J. Appl. Phys.* **2005**, *44*, L690.

(5) Kubo, T.; Nagata, H.; Takeuchi, M.; Matsuoka, M.; Anpo, M.; Nakahira, A. *Res. Chem. Intermed.* **2008**, *34*, 339.

(6) Uchida, S.; Chiba, R.; Tomiha, M.; Masaki, N.; Shirai, M. *Electrochemistry* **2002**, *70*, 418.

(7) Cao, J.; Sun, J.-Z.; Li, H.-Y.; Hong, J.; Wang, M. *J. Mater. Chem.* **2004**, *14*, 1203.

(8) Tokudome, H.; Miyauchi, M. *Angew. Chem. Int. Ed.* **2005**, *44*, 1974.

(9) Sun, X.; Li, Y. *Chem. Eur. J.* **2003**, *9*, 2229.

(10) Yang, J.; Jin, Z.; Wang, X.; Li, W.; Zhang, J.; Zhang, S.; Guo, X.; Zhang, Z. *Dalton Trans.* **2003**, 3898.

(11) Kubota, S.; Johkura, K.; Asanuma, K.; Okouchi, Y.; Ogiwara, N.; Sasaki, K.; Kasuga, T. *J. Mater. Sci. - Mater. Med.* **2004**, *15*, 1031.

(12) Nakahira, A.; Kubo, T.; Numako, C. *Inorg. Chem.* **2010**, *49*, 5845.

(13) Tian, Z. R.; Voigt, J. A.; Liu, J.; Mckenzie, B.; Xu, H. *J. Am. Chem. Soc.* **2003**, *125*, 12384.

(14) Kasuga, T.; Hiramatsu, M.; Hoson, A.; Sekino, T.; Niihara, K. *Langmuir* **1998**, *14*, 3160.

(15) Kasuga, T.; Hiramatsu, M.; Hoson, A.; Sekino, T.; Niihara, K. *Adv. Mater.* **1999**, *11*, 1307.

(16) Ou, H.-H.; Lo, S.-L. *Sep. Purif. Technol.* **2007**, *58*, 179.

(17) Zhu, H. Y.; Lan, Y.; Gao, X.; Ringer, S. P.; Zheng, Z.; Song, D. Y.; Zhao, J.-C. *J. Am. Chem. Soc.* **2005**, *127*, 6730.

(18) Allam, N. K.; Grimes, C. A. *Langmuir* **2009**, *25*, 7234.

(19) Yu, J.; Yu, H.; Cheng, B.; Zhao, X.; Zhang, Q. *J. Photochem. Photobiol., A* **2006**, *182*, 121.

(20) Nian, J.-N.; Teng, H. *J. Phys. Chem. B* **2006**, *110*, 4193.

(21) Wei, X.; Wang, H.; Zhu, G.; Chen, J.; Zhu, L. *Ceram. Int.* **2013**, *39*, 4009.

(22) Cui, L.; Hui, K.; Hui, K.; Lee, S.; Zhou, W.; Wan, Z.; Thuc, C.-N. H. *Mater. Lett.* **2012**, *75*, 175.

(23) Parra, R.; Góes, M.; Castro, M.; Longo, E.; Bueno, P. R.; Varela, J. A. *Chem. Mater.* **2007**, *20*, 143.

(24) Daoud, W. A.; Xin, J. H. *Chem. Commun.* **2005**, 2110.

(25) Serrano, D. P.; Calleja, G.; Sanz, R.; Pizarro, P. *J. Mater. Chem.* **2007**, *17*, 1178.

(26) Wang, C.; Deng, Z.-X.; Li, Y. *Inorg. Chem.* **2001**, *40*, 5210.

(27) Zhang, X.; Ge, X.; Wang, C. *Crys. Growth. Des.* **2009**, *9*, 4301.

(28) Han, S.; Choi, S. H.; Kim, S. S.; Cho, M.; Jang, B.; Kim, D. Y.; Yoon, J.; Hyeon, T. *Small* **2005**, *1*, 812.

(29) Nolan, N. T.; Seery, M. K.; Pillai, S. C. *J. Phys. Chem. C* **2009**, *113*, 16151.

(30) Beyers, E.; Cool, P.; Vansant, E. F. *J. Phys. Chem. B* **2005**, *109*, 10081.

(31) Baiju, K. V.; Shukla, S.; Sandhya, K. S.; James, J.; Warrier, K. G. K. *J. Sol-Gel. Sci. Technol.* **2008**, *45*, 165.

(32) Chao, H.; Yun, Y.; Xingfang, H.; Larbot, A. *J. Eur. Ceram. Soc.* **2003**, *23*, 1457.

(33) McKenzie, K. J. D. *Trans. J. Br. Ceram. Soc.* **1975**, 74, 77.

(34) Hishita, S.; Mutoh, I.; Koumoto, K.; Yanagida, H. *Ceram. Int.* **1983**, *9*, 61.

(35) Seery, M. K.; George, R.; Floris, P.; Pillai, S. C. *J. Photochem. Photobiol., A* **2007**, *189*, 258.

(36) Ao, Y.; Xu, J.; Fu, D. *Appl. Surf. Sci.* **2009**, *256*, 239.

(37) Lee, G. H.; Zuo, J.-M. *J. Am. Ceram. Soc.* **2004**, *87*, 473.

(38) Zhang, D.; Yang, D.; Zhang, H.; Lu, C.; Qi, L. *Chem. Mater.* **2006**, *18*, 3477.

(39) Chen, Q.; Zhou, W.; Du, G.; Peng, L.-M. *Adv. Mater.* **2002**, *14*, 1208.

(40) Wang, W.; Varghese, O. K.; Paulose, M.; Grimes, C. A.; Wang, Q.; Dickey, E. C. *J Mater. Res.* **2004**, *19*, 417.

(41) Hareesh, P.; Babitha, K. B.; Shukla, S. *J. Hazard. Mater.* **2012**, *229–230*, 177.

(42) Neville, E. M.; MacElroy, J. D.; Thampi, K. R.; Sullivan, J. A. *J. Photochem. Photobiol., A* **2013**, *267*, 17.

(43) Harsha, N.; Ranya, K.; Babitha, K.; Shukla, S.; Biju, S.; Reddy, M.; Warrier, K. *J. Nanosci. Nanotechnol.* **2011**, *11*, 1175.

(44) Harsha, N.; Ranya, R.; Shukla, S.; Biju, S.; Reddy, M.; Warrier, K. *J. Nanosci. Nanotechnol.* **2011**, *11*, 2440.

(45) Baiju, K. V.; Shukla, S.; Biju, S.; Reddy, M. L. P.; Warrier, K. G. K. *Mater. Lett.* **2009**, *63*, 923.

(46) Narayani, H.; Kunniveetil, S. P.; Shukla, S. *Adv. Sci. Eng. Med.* **2013**, *5*, 63.

(47) Yu, J.; Yu, H.; Cheng, B.; Trapalis, C. *J. Mol. Catal. A* **2006**, *249*, 135.

(48) Jose, M.; Narayani, H.; Kumar, J.; Shukla, S. *Sci. Adv. Mater.* **2015**, 7, 729.

(49) Matheswaran, M.; Karunanithi, T. *J. Hazard. Mater.* **2007**, *145*, 154.

(50) Aphairaj, D.; Wirunmongkol, T.; Niyomwas, S.; Pavasupree, S.; Limsuwan, P. *Ceram. Int.* **2014**, *40*, 9241.

(51) Kumar, K. V.; Ramamurthi, V.; Sivanesan, S. *J. Colloid. Interface. Sci.* **2005**, *284*, 14.

(52) Lee, C.-K.; Lin, K.-S.; Wu, C.-F.; Lyu, M.-D.; Lo, C.-C. *J. Hazard. Mater.* **2008**, *150*, 494.

(53) Shih, Y.-H.; Zhuang, C.-M.; Tso, C.-P.; Lin, C.-H. *J. Nanopart. Res.* **2012**, 14, 1.

(54) Priya, R.; Baiju, K.; Shukla, S.; Biju, S.; Reddy, M.; Patil, K.; Warrier, K. *J. Phys. Chem. C* **2009**, *113*, 6243.

(55) Jose, M.; Kumari, M.; Karunakaran, R.; Shukla, S. *J. Sol-Gel. Sci. Technol.* **2015**, *73*, 38.

(56) Padinhattayil, H.; Augustine, R.; Shukla, S. *J. Nanosci. Nanotechnol.* **2013**, *13*, 3035.

Chapter 4

Novel Method and Its Validation for Predicting Dye-Adsorption Capacity of Hydrogen Titanate Nanotubes via One-Step Dye-Removal Method of Novel Chemically-Activated Catalytic Process Conducted in Dark

Graphical Abstract

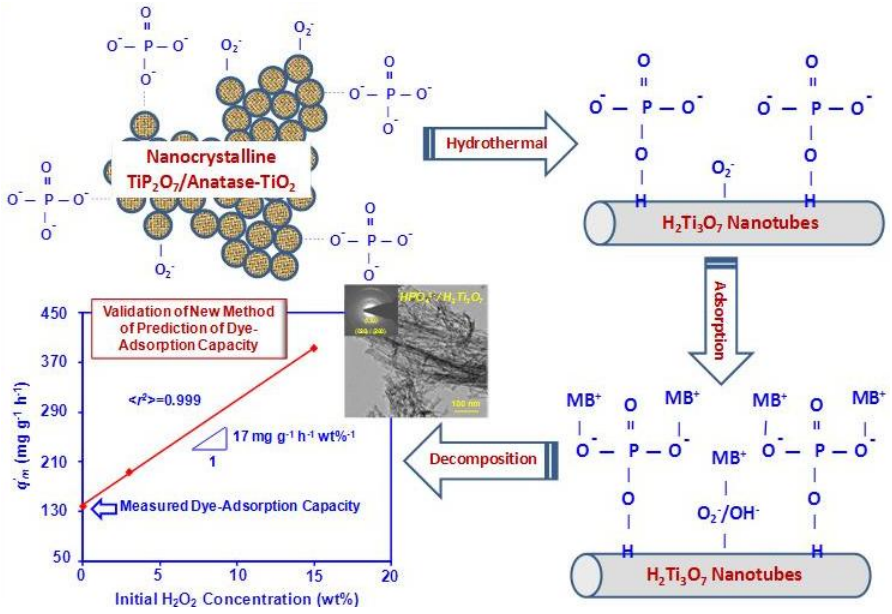

Highlights

- Synthesized HTN and phosphate ion modified HTN (HP-HTN) by the alkaline hydrothermal treatment of corresponding sol-gel derived anatase TiO_2.
- Measured the dye-adsorption capacity and the dye degradation rate-capacity.
- For the *first-time*, the dye adsorption capacity of HTN was predicted using the one step method of chemically activated catalytic process conducted in the dark and validated using HP-HTN.

Abstract

Pure and hydrogen phosphate (HP, HPO_4^{2-}) modified HTN have been synthesized via hydrothermal treatment of sol-gel derived nanocrystalline anatase-TiO_2 and titanyl phosphate (TiP_2O_7) / phosphate (PO_4^{3-}) ions modified nanocrystalline anatase-TiO_2 respectively. The samples have been characterized using TEM, SAED, EDX, XRD, FTIR, UV-visible, and zeta-potential measurement system. The MB adsorption capacity of HP-HTN has been determined to be 139 mg g^{-1} which is higher than that (105-121 mg g^{-1}) of pure HTN. By varying the initial MB (7.5-1000 μM) and initial H_2O_2 (3-50 wt%) concentrations, it has been demonstrated that both HTN and HP-HTN can decompose MB dye in an aqueous solution via H_2O_2 activation. A new method for predicting the adsorption capacity via one-step dye-removal method of chemically-activated catalytic process conducted in the dark has been demonstrated. It is also observed that HP-HTN exhibit higher dye-decomposition rate-capacity compared with that of pure-HTN. The validity of new method for predicting the adsorption capacity is confirmed by applying the proposed method to the dye-adsorption and dye-decomposition data obtained using the HP-HTN.

4.1. Introduction

TiO_2 is one of the most studied semiconductor oxides due to its diversity in physiochemical properties and technological applications, chemical stability, non-toxicity, low cost, corrosion resistance, and high catalytic activity. One of the most promising application of TiO_2 is utilizing its ability to act as a heterogeneous photocatalyst for removing the harmful organic synthetic-dyes from the aqueous solutions and industrial effluents under an exposure to the external radiation.[1-2] Even though the reusability of photocatalyst is one of the main advantages of TiO_2 photocatalyst, this process suffers major disadvantages such as the need for an external radiation source and consequent requirement of tuning of its band-gap energy, difficulties in the separation of photocatalyst from the treated solution, and inability to remove the dyes quickly, typically from the highly concentrated dye solutions. Due to these factors, the scope of photocatalytic degradation of organic pollutants is limited for the large scale commercial applications.

Adsorption is one of the simplest, fastest, and cost effective techniques which can be used as an alternative to the photocatalysis process for the removal of toxic organic synthetic-dyes from the aqueous solutions and industry wastewater. Although different types of low cost adsorbents effective in the dye-removal application have been reported in the literature,[3-5] HTN synthesized via hydrothermal treatment of anatase-TiO_2 nanoparticles have received special attention in the recent years after their discovery by Kasuga et al..[6-9] Apart from the nanotubes, hydrogen titanate can also be synthesized in various other forms including the nanorods, nanofibers, and nanosheets using different techniques such as the template-based, anodization, electrospinning, and hydrothermal.[10-12] However, the latter technique offers some unique advantages of processing of large

quantity of free standing (substrate-free) nanotubes having very high specific surface-area, high aspect ratio, and the ability to exchange ions in an aqueous solution.[13-14] Hydrothermal derived pure and modified HTN have been utilized for the different applications including ion-intercalated devices (electrochromic and Li-ion batteries), dye-sensitized solar cells, supercapacitors, hydrogen (H_2) technology, and environmental cleaning.[10,12-13,15-18] Nevertheless, the formation, handling, and reuse of large amount of sludge have been the major issues associated with the adsorption mechanism.

To overcome the limitations of photocatalysis and adsorption, a new dye-removal technology based on the chemically-activated catalytic process conducted in the dark (that is, without any radiation-exposure) has been recently developed which involves the two-step and one-step dye-removal methods.[19] In the two-step dye-removal method, organic synthetic-dye is adsorbed on the surface of hydrothermally processed semiconductor-oxides nanotubes (such as HTN and ATN) in the dark and decomposed in another aqueous solution, also in the dark, containing a strong oxidizer such as H_2O_2. In contrast to this, in the one-step dye-removal method, Scheme 4.1, the organic synthetic-dye is simultaneously adsorbed and decomposed, in the dark, on the surface of hydrothermally processed semiconductor-oxides nanotubes in the presence of a strong oxidizer such as H_2O_2. In both the methods of chemically-activated catalytic process, the dye-decomposition in an aqueous solution takes place in the dark which is in contrast to the photocatalytic dye-degradation which involves the radiation-exposure for dye-degradation.

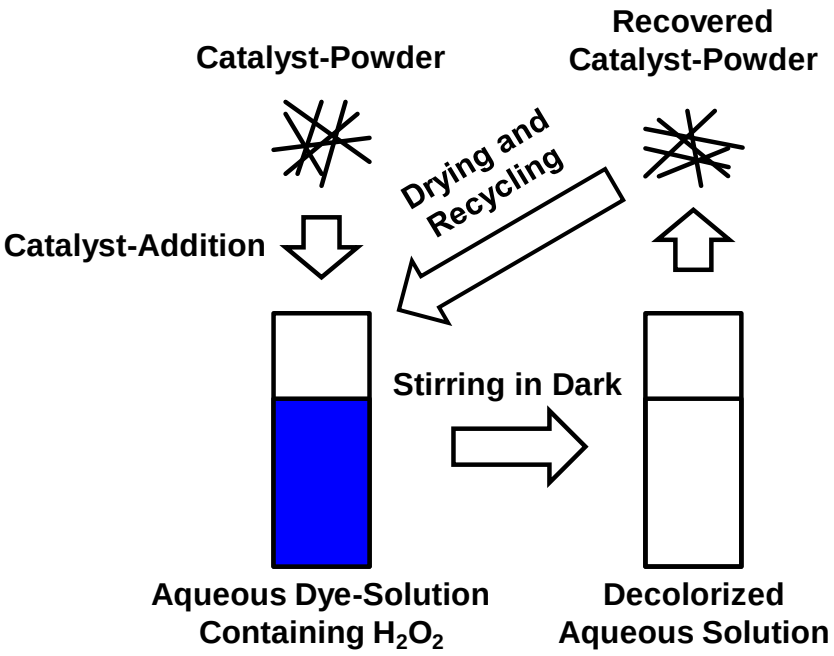

Scheme 4.1. One-step dye-removal method of chemically-activated catalytic process conducted in the dark.

Relative to different dye-adsorbents as reported in the literature, although the HTN-based adsorbents exhibit comparable adsorption capacity, they offer several advantages which are not simultaneously possessed by other adsorbents. First, they exhibit adsorption via both electrostatic and ion-exchange mechanisms which are conducive in increasing the amount of dye adsorbed on their surfaces. Secondly, their surface chemistry can be easily tailored depending on the nature of dye to increase the adsorption capacity. Third, they can be easily attached to the magnetic nanoparticles via the ion-exchange mechanism to ease the solid-liquid separation after the dye-adsorption process using an external magnetic field. Fourth, they can be regenerated via simple H_2O_2 activation process and reused multiple times in the dye-adsorption application which eliminates the sludge formation, its handling and recycling issues, and hence, the secondary pollution. Fifth, they can remove an organic synthetic-dye from an aqueous solution without the use of

any external radiation (such as the UV, solar, visible, and infrared) and power-source (such as the potential difference, sonicator, and microwave).

At present, for the one-step dye-removal method of novel chemically-activated catalytic process conducted in the dark, the effect of initial H_2O_2 concentration on the amount of dye-decomposed in the dark has not been investigated in the literature. Moreover, the dye-adsorption capacity of semiconductor-oxides nanotubes has never been predicted using the one-step dye-removal method of novel chemically-activated catalysis process conducted in the dark. In view of this, the major goals of this investigation are as follows – (1) to synthesize HTN and HP-HTN via hydrothermal processing of pure and titanyl phosphate (TiP_2O_7) / phosphate (PO_4^{3-}) ions modified nanocrystalline anatase-TiO_2, (2) to study the adsorption of MB dye on the surface of HTN and HP-HTN, (3) to study the effect of initial H_2O_2 concentration on the amount of dye-decomposed in the dark as obtained using the HTN and HP-HTN, (4) to demonstrate the prediction of dye-adsorption capacity of HTN via one-step dye-removal method of novel chemically-activated catalytic process conducted in dark by comparing the obtained data with the dye-adsorption capacity determined using the conventional equilibrium adsorption / desorption method, and (5) to validate the above method of prediction of dye adsorption capacity using HP-HTN.

4.2. Experimental

4.2.1. Chemicals

$Ti(OC_3H_7)_4$ (97%), H_3PO_4 (85 wt%, 99.99 %), H_2O_2 (3 wt%), and TA (98%) were purchased from Sigma-Aldrich Chemicals, Bengaluru, India; HCl (35 wt%) from Ranbaxy Fine Chemicals Ltd., India; MB (96%), 2-propanol (99.5%, ACS reagent), NaOH (Assay 97%), and H_2O_2 (30 wt%) from S.D. Fine-Chem Ltd., Mumbai, India;

NH_4OH (25% NH_3) from Qualigens Fine Chemicals, Mumbai, India; and luminol (5-Amino-2,3-dihydro-pthalazine-1,4-dione) from Merck Specialties Pvt. Ltd., India. All chemicals were used as received without any further purification.

4.2.2. Synthesis of pure and titanyl phosphate (TiP_2O_7) / phosphate (PO_4^{3-}) ions modified nanocrystalline anatase-TiO_2

The nanocrystalline anatase-TiO_2 powder was synthesized via sol-gel process using the hydrolysis and condensation of $Ti(OC_3H_7)_4$ in an alcohol medium.[20-22] The '*R*' value of 90 was selected for the present experiment.[21-22] First, the measured quantities of water and acid-catalyst were dissolved in 125 ml of 2-propanol. A second solution was then prepared in which 0.12 M (final concentration) of $Ti(OC_3H_7)_4$ was dissolved completely in 125 ml of 2-propanol. Both the solutions were sealed immediately and stirred rapidly using the magnetic stirrer to obtain the homogeneous solutions. The ratio of molar concentration of water to that of alkoxide-precursor (*R*) was 90. The water-part of solution was then added drop-wise to alkoxide-part under the continuous magnetic stirring. As a result of the hydrolysis and condensation reactions of $Ti(OC_3H_7)_4$ due to its reaction with water, the color of solution changed from colorless to white. After the complete addition of water-part of solution to that of alkoxide-part, the resulting suspension was stirred for 7 h before drying in an oven at 80 ^oC for the complete removal of solvent and residual water. The dried powders were then calcined at 600^oC for 2 h at the heating rate of 3 $^oC\ min^{-1}$ for the crystallization of amorphous-TiO_2 powders.

The TiP_2O_7/PO_4^{3-}-ions modified nanocrystalline anatase-TiO_2 was synthesized by modifying the above sol-gel process with H_3PO_4 in which the concentration of H_3PO_4 used in the sol-gel synthesis was 1.7 g l^{-1} (that is, P:Ti mole ratio of 0.11). The dried-

powder obtained was calcined at 800 ^{o}C for 2 h with the heating rate of 3 ^{o}C min^{-1} for the crystallization of amorphous-TiO_2 into anatase-TiO_2.

4.2.3. Hydrothermal processing of HTN and HP-HTN

The nanocrystalline anatase-TiO_2 obtained via the conventional and TiP_2O_7/PO_4^{3-}-ions modified sol-gel process is used as a precursor for the hydrothermal processing of HTN and HP-HTN respectively. The hydrothermal processing of HTN and HP-HTN are as described in third chapter (section 3.2.3.).

4.2.4. Determination of dye-adsorption characteristics

The MB dye-adsorption experiments in the dark were carried out via the procedure already described in the third chapter (section 3.2.5).

4.2.5. Determination of dye-adsorption capacity via one-step method of novel chemically-activated catalytic process conducted in dark

In the one-step dye-removal method, 125 ml of H_2O_2 solution (with the initial concentration varying in the range of 3-50 wt%) containing MB dye (with the initial concentration varying in the range of 7.5-1000 μM) was first prepared. (Note: 15 wt% H_2O_2 solution was prepared via dilution method. Moreover, 3, 15, 30, and 50 wt% H_2O_2 approximately correspond to 1, 5, 10, and 16.7 M of H_2O_2 respectively and the ratio of molar concentrations of MB and H_2O_2 is within the range of 1.8×10^{-6} to 10^{-3}). 0.4 g l^{-1} of catalyst was suspended in this solution and stirred in the dark for total 1 h. (Note: although the solution-pH is slightly decreased within the first 10-20 min of contact time, it remains constant thereafter within the range of 3.7-0.96 for the initial H_2O_2 concentration within the range of 3-50 wt% as typically observed for the initial MB concentration of 150 μM). The aliquots were taken out after 10 min time interval and

centrifuged to separate the nanotubes. The filtrates were used for obtaining the absorption spectra using the UV-visible absorption spectrophotometer to determine the concentration of MB dye remaining in the solution. The data was further used to calculate the amount of MB dye simultaneously adsorbed and decomposed on the surface of nanotubes using the Eqs. (3.2) and (3.3). The obtained data was then analyzed to determine the dye-degradation rate-capacity (mg g^{-1} h^{-1}) for a given initial H_2O_2 concentration defined as the amount of dye simultaneously adsorbed and decomposed in the dark per unit gram of catalyst per unit hour of contact time. The data was further analyzed to predict the dye-adsorption capacity. The blank experiments (that is, the dye-decomposition experiments conducted in the dark in the presence of H_2O_2 but without the addition of catalyst) were conducted typically for the initial MB concentration of 150 μM. All other experimental conditions were similar to those described above. Under these conditions, Eqs. (3.2) and (3.3) provide the amount of MB decomposed as a result of H_2O_2 only (that is, the bleaching effect of H_2O_2).

4.2.6. Characterization

The morphology and average size of samples were confirmed using the TEM operated at 300 kV. The elemental constituents, nanocrystalline nature, and crystalline structures of samples were determined via EDX and SAED techniques. The crystalline phases present were also analyzed using the XRD method. The broad-scan analysis was typically conducted within the 2θ range of 10-80^o using the Cu$K\alpha$ (λ_{Cu}=1.542 Å) X-radiation. The obtained patterns were utilized to determine the weight-fraction of rutile-TiO_2 using the Eq. (3.1). The surface chemistry of different samples was analyzed using the FTIR spectroscope within the frequency range of 4000–400 cm^{-1} using the powders dispersed in the KBr pellets. The specific surface-area was measured using the BET surface-area

measurement technique via N_2 adsorption using the multi-point method after degassing the samples in flowing N_2 at 200 ^oC for 2 h. The band-gap energy measurements were conducted by obtaining the absorption spectra using the UV-visible spectrophotometer, operated in the diffuse reflectance (DR) mode, for the wavelengths within the range of 200-800 nm. The zeta potential measurements were performed using the electrophoretic light scattering in the initial solution-pH range from 2 to 9.

4.2.7. Trapping of $O_2^{\bullet-}$ using luminol

125 ml of aqueous suspension containing 3 and 15 wt% H_2O_2 was prepared by completely dissolving 2.4×10^{-3} M (0.278 g l^{-1}) of luminol and 10^{-2} M (0.4 g l^{-1}) of NaOH. Then, 0.4 g l^{-1} of catalyst was dispersed under the continuous magnetic stirring. 8 ml aliquot was taken out after 5 min of contact time for obtaining the PL spectra. The catalyst was separated from the sample suspension using a centrifuge and the filtrate was then examined using a spectrofluorometer. The luminol molecules react with the generated $O_2^{\bullet-}$ species and produce 3-aminophthalate (AP) which exhibits a characteristic broad PL peak located at ~420 nm at an excitation wavelength of ~350 nm (or ~387 nm).[23-24] In the present investigation, this emission peak is observed to be located within the wavelength range of 426-473 nm after the background subtraction. (Note: the initial H_2O_2 solution, in the absence of a catalyst, contains small amount of $O_2^{\bullet-}$ species. The intensity of PL peak obtained from this blank solution is considered as a reference (background) which is subtracted from the PL intensity observed in the presence of a catalyst). The intensity of PL peak obtained after the background subtraction is regarded as the measure of the concentration of free $O_2^{\bullet-}$ species produced by the interaction of a catalyst with H_2O_2. For comparison, the PL measurements were also conducted for the pure HTN which was synthesized in our previous investigation.[19]

4.3. Results and discussion

4.3.1. Morphological and structural analyses

The TEM images of sol-gel derived precursor (pure TiO_2) and the final hydrothermal product (HTN) are shown in Fig. 4.1a and b. Although the sol-gel derived precursor consists of nanoparticles of average size of ~25 nm, the morphology of final hydrothermal product is confirmed to be the nanotube. The corresponding SAED patterns, shown as insets in Fig. 4.1a and b, exhibit concentric ring patterns which are identified to be those of anatase-TiO_2 and $H_2Ti_3O_7$.[22,25]

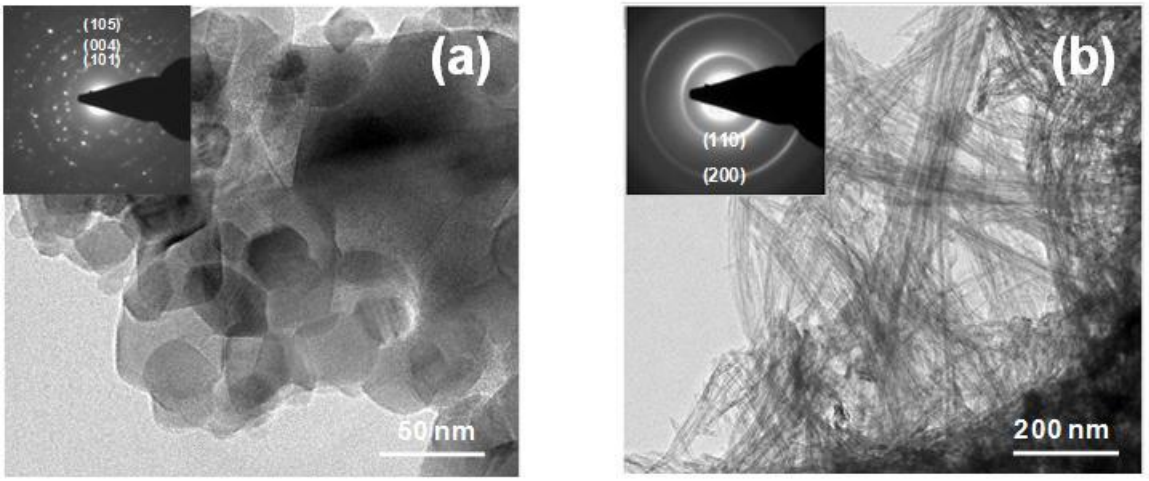

Fig. 4.1. Typical TEM images of nanocrystalline anatase-TiO_2 (a) and HTN (b). The insets show the corresponding SAED patterns.

The TEM images of titanyl phosphate (TiP_2O_7) / phosphate (PO_4^{3-}) ions modified nanocrystalline anatase-TiO_2 and its hydrothermal derived products (HP-HTN) are shown in Figs. 4.2 and 4.3 respectively. In Fig. 4.2, fine (~15-25 nm), highly porous, and aggregated morphology of nanocrystalline particles is seen as obtained via H_3PO_4 modified sol-gel method. The SAED pattern presented as an inset in Fig. 4.2a shows the continuous concentric diffused rings which are indexed as per the reported pattern of nanocrystalline anatase-TiO_2.[26]

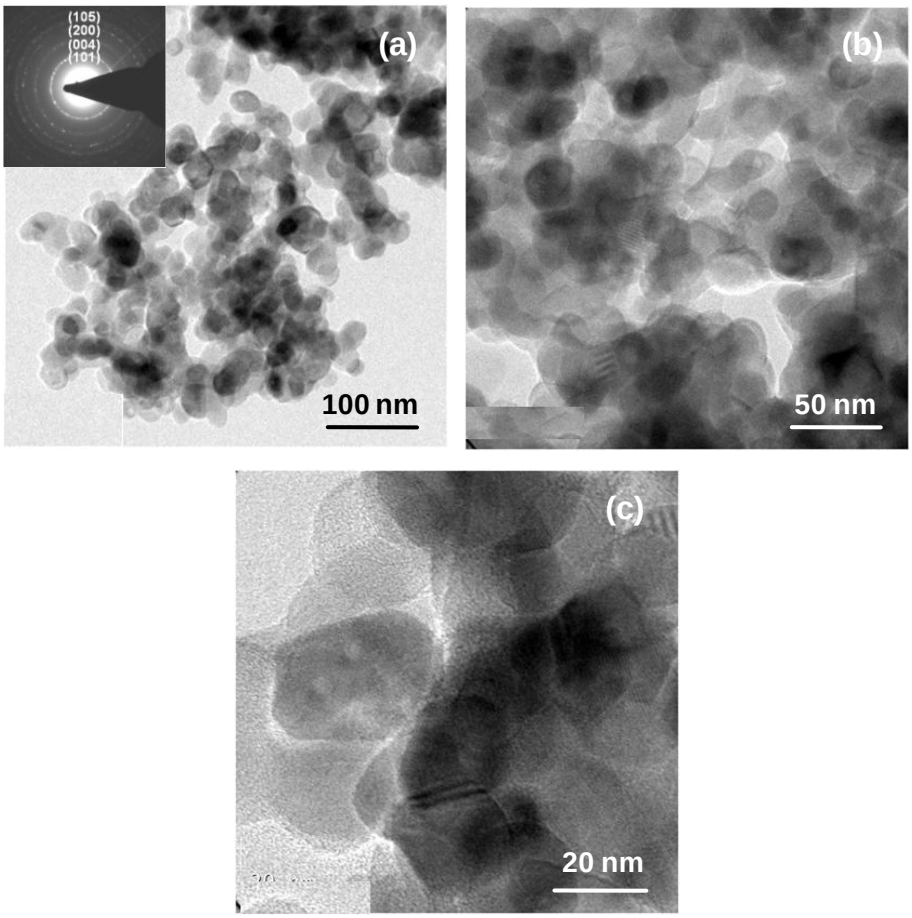

Fig. 4.2. (a-c) TEM images of the final sol-gel derived product at different magnifications. The inset in (a) shows the corresponding SAED pattern.

The TEM images presented in Fig. 4.3 suggest that the morphology of final hydrothermal product is nanotube having the average length of ~250 nm with the average internal and external diameters of ~7 nm and ~11 nm. The continuous concentric two diffused rings as observed in the SAED pattern, shown as an inset in Fig. 4.3a, confirm the nanocrystalline nature of final hydrothermal product and are identified to be those of either monoclinic $H_2Ti_3O_7$[27] or orthorhombic protonic lepidocrocite titanate ($H_xTi_{2-x/4}\square_{x/4}O_4$, where x~0.7 and □ is a vacancy).[25] In the inset of Fig. 4.3a, the second electron diffraction ring can be indexed as either (020) if the structure is assumed to be

monoclinic $H_2Ti_3O_7$[27] or (200) if the structure is assumed to be orthorhombic lepidocrocite-type.[25]

The HRTEM images obtained using the final sol-gel and hydrothermal derived products (acid modified) are presented in Fig. 4.4a and b respectively. In Fig. 4.4a, the lattice fringes exhibit a constant interplanar spacing of 0.35 nm which corresponds to that of (101) plane of anatase-TiO_2 as per the JCPDS card number 21-1272.[25] In Fig. 4.4b, the interlayer spacing is noted to vary in between 0.83-1.4 nm. The lower limit is closer to the interplanar spacing of 0.786 nm and 0.926 nm corresponding to either (200) plane of $H_2Ti_3O_7$ or (020) plane of lepidocrocite-type titanate.[25,27-29] Considerable variation in the interlayer spacing is noted along the length of the nanotube, Fig. 4.4b, which is attributed to the possible non-uniform distribution of PO_4^{3-} ions intercalated within the lattice planes.

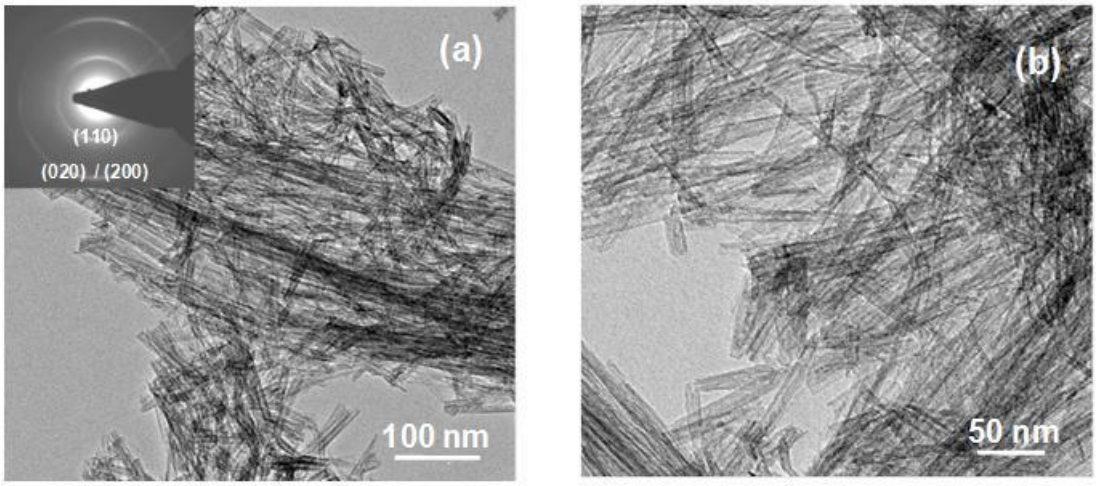

Fig. 4.3. (a,b) TEM images of the final hydrothermal derived product at different magnifications. The inset in (a) shows the corresponding SAED pattern.

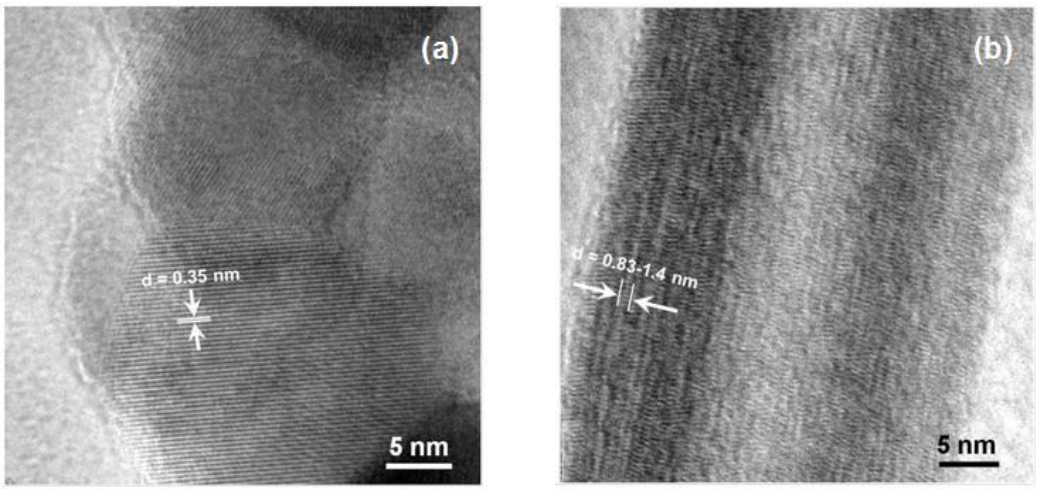

Fig. 4.4. HRTEM images of the final sol-gel (a) and hydrothermal (b) derived products.

The XRD patterns of pure sol-gel and HTN are presented in Fig. 4.5a and b. The XRD pattern of sol-gel derived precursor, Fig. 4.5a, consists of peaks of anatase-TiO_2 and small amount (15 wt%) of rutile-TiO_2 which are identified after comparing the obtained patterns with the JCPDS card numbers 21-1272 and 21-1276. The XRD pattern of final hydrothermal product, Fig. 4.5b, consists of peaks of $H_2Ti_3O_7$[30] and small amount of untransformed rutile-TiO_2. The amount of rutile-TiO_2 in the final hydrothermal product is calculated to be 11 wt%. (Note: since the rutile-TiO_2 does not take part in the dye-adsorption and dye-decomposition processes conducted in the dark, for the purpose of calculations, its actual mass is subtracted from the total mass of catalyst used to obtain the mass of HTN. Hence, unless otherwise stated, hereafter the final hydrothermal product is assumed to be consisting of HTN only.)

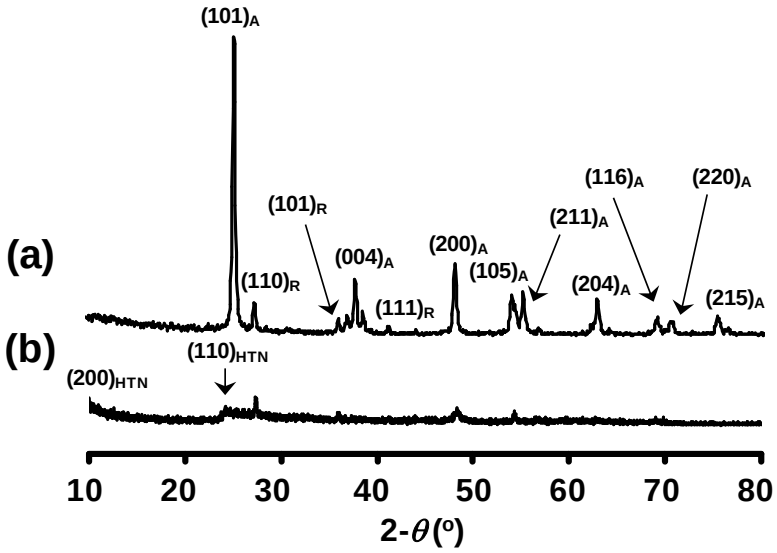

Fig. 4.5. XRD patterns of nanocrystalline anatase-TiO_2 (a) and HTN (b). A and R represent anatase-TiO_2 and rutile-TiO_2.

The EDX spectra and XRD patterns of titanyl phosphate (TiP_2O_7) / phosphate (PO_4^{3-}) ions modified nanocrystalline anatase-TiO_2 and its hydrothermal derived products (HP-HTN) are presented and compared in Figs. 4.6 and 4.7 respectively. The EDX spectra are nearly identical for both the products which show the presence of Ti and O as the major elements with the additional presence of P either on the surface or intercalated into the lattice planes or doped into the bulk of different samples. For the final sol-gel and hydrothermal derived products, the fractions of Ti, O, and P are calculated to be 76.1, 21.3, 2.6 wt% and 62.5, 37, 0.5 wt% respectively.

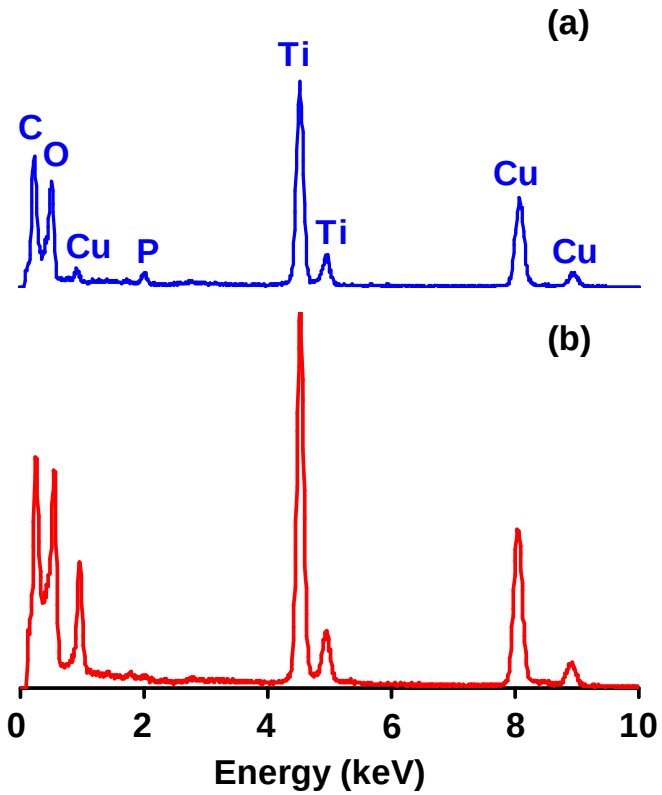

Fig. 4.6. EDX spectra obtained using the final sol-gel (a) and hydrothermal (b) derived products.

In Fig. 4.7a, the XRD peaks observed at the 2θ values of 25.3, 36.9, 37.8, 38.5, 48.1, 53.9, 55.1, 62.8, 68.8, 70.3, and 75.1^{o} also suggest that the nanocrystalline particles belong to anatase-TiO_2 phase, as identified and indexed after comparing the obtained pattern with the JCPDS card number 21-1272.[26] The XRD pattern of final hydrothermal product consisting small intensity peaks at the 2θ values of 24.5^{o} and 48.5^{o}, Fig. 4.7b, belongs to either monoclinic $H_2Ti_3O_7$[27,31-33] or orthorhombic lepidocrocite-type[25,34-36] or $H_2Ti_2O_4(OH)_2$-type[37-39] hydrogen titanate structures.

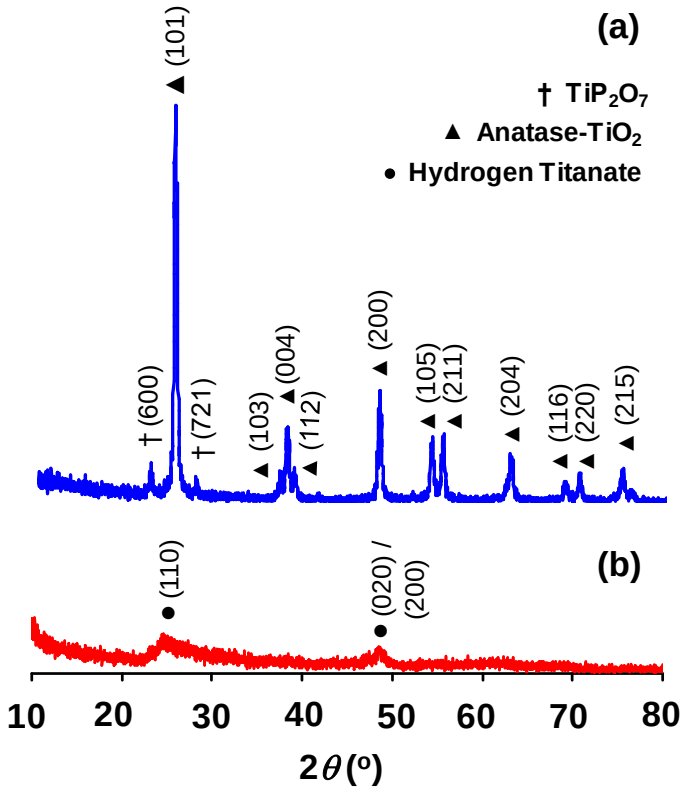

Fig. 4.7. XRD patterns obtained using the final sol-gel (a) and hydrothermal (b) derived products.

In Fig. 4.7b, the XRD peak located at 2θ value of 48.5° can be indexed as either (020) if the structure is assumed to be monoclinic $H_2Ti_3O_7$[27] or orthorhombic $H_2Ti_2O_4(OH)_2$-type[37-38] or (200) if the structure is assumed to be orthorhombic lepidocrocite-type.[25] However, considering the 2θ values relative to those reported by Chen et al.,[27] it strongly appears that in the present investigation, the structure of HTN resembles that of $H_2Ti_3O_7$ than the other types of structures. The formation of nanotubes via hydrothermal treatment of nanocrystalline anatase-TiO_2 involving the roll-up mechanism has been already described in detail elsewhere .[40-42] In Fig. 4.7a, the two additional low intensity peaks located at the 2θ values of 22.5° and 27.7° are observed which do not belong to anatase-TiO_2. It appears that a new phase is formed on the surface of nanocrystalline anatase-TiO_2 after the calcination treatment at 800 °C. In our previous investigation, no new

phase formation was detected via XRD after the calcination treatment at 600 ^{o}C.[43] Hence, the formation of new phase is due to increase in the calcination temperature from 600 ^{o}C to 800 ^{o}C. These new XRD peaks are indexed as $(600)_{TP}$ and $(721)_{TP}$ planes of cubic structured titanyl phosphate phase (TiP_2O_7 (TP), also known as titanium pyrophosphate[44]) as per the JCPDS card no. 38-1468, in which TiO_6 octahedra and PO_4 tetrahedra share the corners in a three-dimensional network.[45-46] The formation of TiP_2O_7 phase on the surface of nanocrystalline anatase-TiO_2 has been reported earlier by Korosi et al.[45] and Yu et al.[47] which is possibly due to the reaction of surface-adsorbed PO_4^{3-} ions with the core anatase-TiO_2.

$$2TiO_2 + 4PO_4^{3-} + 9O_2 \rightarrow 2TiP_2O_7 + 12O_2^{\bullet-} \quad (4.1)$$

(Note: the generated $O_2^{\bullet-}$ species may remain adsorbed on the surface of nanocrystalline anatase-TiO_2 particles). There is also a possibility of the formation of other phases of titanium phosphate such as $(TiO)_2P_2O_7$ and $Ti_5O_4(PO_4)_4$.[48] However, these phases are normally formed at higher calcination temperatures (>1000 ^{o}C) and P/Ti ratio (>0.2).[47-48] Since in the present investigation, the values of P/Ti ratio (0.11) and calcination temperature (800 ^{o}C) employed are relatively lower, we rule out the possibility of formation of $(TiO)_2P_2O_7$ and $Ti_5O_4(PO_4)_4$ phases. On the contrary, the latter synthesis conditions strongly favor the formation of TiP_2O_7 phase in agreement with Yu et al..[47] Moreover, the powder containing $Ti_5O_4(PO_4)_4$ phase is reported to be yellow in color.[48] However, all powders synthesized in this investigation are white in color which supports the formation of TiP_2O_7 phase. It is interesting to note that since TiP_2O_7 phase is not detected in Fig. 4.7b, it appears that this phase is also converted to the nanotubes of $H_2Ti_3O_7$ after the hydrothermal treatment.

The N_2 adsorption / desorption curves obtained using HTN are shown in Fig. 4.8 which suggest its mesoporous nature further supporting its nanotube morphology. The specific surface-area of final hydrothermal product is estimated to be 288 m^2 g^{-1}. Thus, the final hydrothermal product primarily consists of a high surface-area mesoporous HTN mixed with the small amount of nanocrystalline particles of rutile-TiO_2.

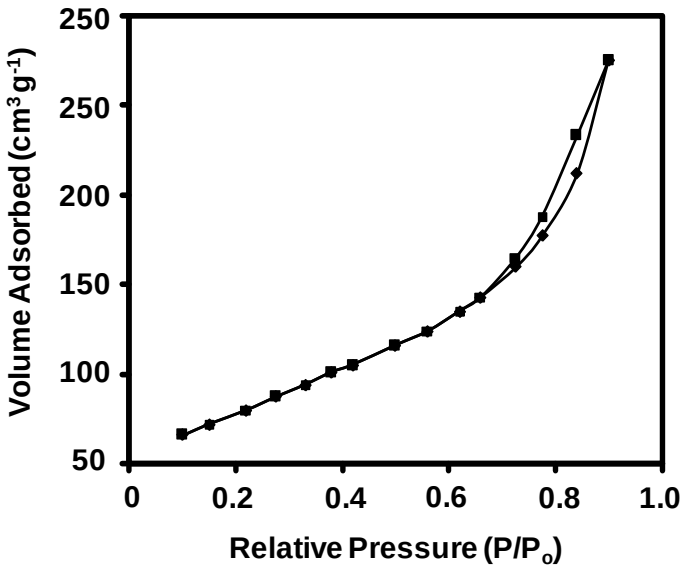

Fig. 4.8. Nitrogen adsorption / desorption isotherms obtained using the HTN.

The FTIR spectra obtained for the final sol-gel and hydrothermal derived products are shown in Fig. 4.9a and b respectively. The broad absorbance band from 400-750 cm^{-1} with the peak located at 457 cm^{-1} is assigned to Ti–O and Ti–O–Ti skeletal frequency region in the nanocrystalline anatase-TiO_2.[39] In our previous study,[49] the sample calcined at 600 ^oC exhibited a single band appearing at 1051 cm^{-1} which can be assigned to P-O vibration mode in Ti-O-P matrix. However, Li et al..[48] and Korosi et al.[45] observed an absorbance peak located at 1060 cm^{-1} corresponding to a broad band from 980-1200 cm^{-1} which was assigned to the characteristic stretching vibrations of PO_4 groups. In our view, in the absence of characteristic frequency of P=O bond (1260-1450 cm^{-1}), it is appropriate to assign the single peak band appearing at 1051 cm^{-1} to Ti-O-P matrix than

to PO_4 units. In Fig. 4.9a, after the calcination at 800^oC, this single absorbance peak appears to split into four distinct absorbance peaks located at 750, 956, 1054, and 1205 cm^{-1}, which according to the present XRD results, may be related to the formation of new TiP_2O_7 phase. Similar spectral variations have also been reported earlier by Li et al.,[48] who ascribed these modifications to the changes in the coordination of P from Ti-O-P vibrations to ordinary PO_4 forms which indicate the formation of new phosphate species on the surface of TiO_2. This is also in accordance with Kalita et al.[50] who observed six different vibrational modes located at 620, 744, 924, 987, 1050 and 1242 cm^{-1} for the new TiP_2O_7 phase which were assigned to the asymmetric and symmetric stretching and bending vibrations of PO_4 tetrahedral units. In particular, Li et al.[48] assigned different absorbance peaks located at 752, 926, 1064, 1213 cm^{-1} to the symmetric and asymmetric stretching vibrations of P-O-P, asymmetric P-O stretching in PO_4 unit (shifted to higher frequency due to Ti effect), and asymmetric stretching vibrations in PO_2 respectively. Kuo et al. suggested that the peaks at 1000–1050 cm^{-1} and 1100 cm^{-1} could result from Ti–O–P framework vibrations.[51] Thus, based on the available literature, the four absorbance peaks as observed here within the frequency range of 750-1205 cm^{-1} are primarily attributed to the presence of PO_4 units in the TiP_2O_7 phase. It is interesting to note that Li et al.[48] also attributed the absorbance peaks located at 960 and 1043 / 1100 cm^{-1} to the symmetric and asymmetric P-O stretching in the PO_4 groups which are close to the observed peaks located at 956 and 1054 cm^{-1}, Fig. 4.9a. In addition to this, according to Li et al.[48] and Kuo et al.,[51] the P=O bonds, the characteristic feature of the PO_4 groups, are normally observed in the frequency region of 1260-1450 cm^{-1} and 1300-1400 cm^{-1}. Hence, the small absorbance peak located at 1363 cm^{-1}, Fig.9a, is ascribed here to the presence of P=O vibrations. This strongly suggests that the residual PO_4^{3-} ions (see Eq. (4.1)) are also present along with the TiP_2O_7 phase on the surface of

nanocrystalline anatase-TiO_2 after the calcination treatment at 800 ^oC. The very broad absorbance band in between 1400-4000 cm^{-1} range is attributed to the presence of complex -OH and H_2O groups present on the surface of final sol-gel derived product consisting of TiP_2O_7 / PO_4^{3-}-ions modified nanocrystalline anatase-TiO_2.

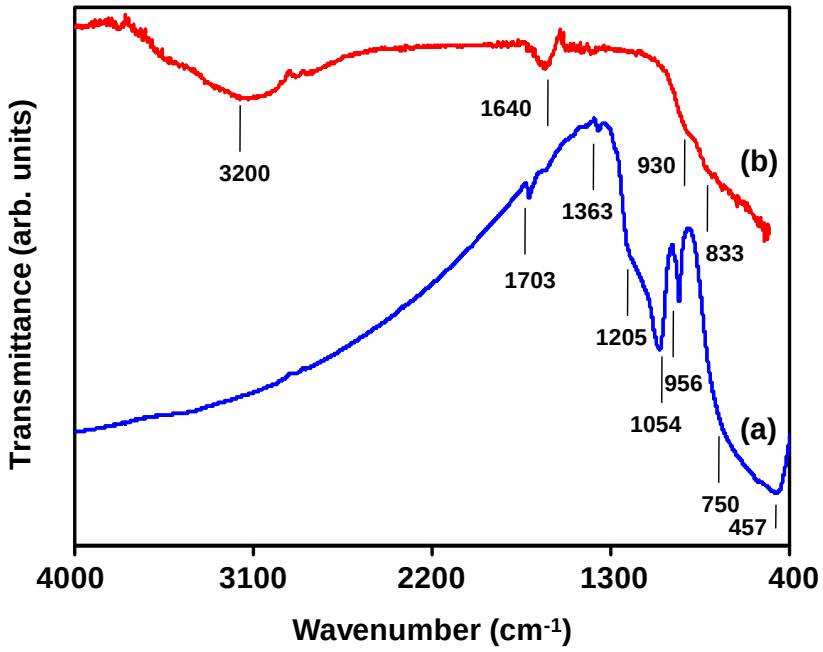

Fig. 4.9. FTIR spectra obtained using the final sol-gel (a) and hydrothermal (b) derived products.

The FTIR spectrum of final hydrothermal product (HP-HTN), Fig. 4.9b, shows two absorbance peaks located at the frequency of 3400 cm^{-1} and 1651 cm^{-1} which are attributed to the stretching vibrations of surface-adsorbed –OH groups and the bending vibrations of surface-adsorbed H_2O.[39,49] The four characteristic peaks of TiP_2O_7 located in the frequency range of 750-1205 cm^{-1} and that of P=O groups located at 1363 cm^{-1}, as observed in Fig. 4.9a, are totally disappeared after the hydrothermal treatment, Fig. 4.9b, which is in agreement with the XRD results presented in Fig. 4.7. It appears that the hydrothermal treatment of TiP_2O_7 / PO_4^{3-}-ions modified nanocrystalline anatase-TiO_2

results in a complete decomposition of TiP_2O_7 phase in a highly alkaline condition according to the following reaction.

$$TiP_2O_7 + 6OH^- \xrightarrow{120^oC,30\,psi,30h} TiO_2 + 2PO_4^{3-} + 3H_2O \quad (4.2)$$

The above decomposition reaction can enhance the concentration of PO_4^{3-} ions adsorbed on the surface of nanocrystalline anatase-TiO_2 during the hydrothermal treatment. Although PO_4^{3-} ions may remain intact under the hydrothermal conditions (including the subsequent washing steps), the anatase-TiO_2 may finally be transformed to the nanotubes of $H_2Ti_3O_7$ with the retention of PO_4^{3-} ions on their surfaces. (Note: The $O_2^{\bullet-}$ species, Eq. (4.1), may also remain adsorbed on the surface of final hydrothermal product (HP-HTN) which may enhance the concentration of former on the surface of latter relative to that on the surface of pure HTN). These PO_4^{3-} ions may form chemical bonds with H^+ ions intercalated in between the walls of $H_2Ti_3O_7$ nanotubes forming new hydrogen phosphate species, such as the HPO_4^{2-} or $H_2PO_4^-$, which would be chemisorbed on the surface of HTN. Liang et al.[52] demonstrated that the characteristic modes of HPO_4^{2-} anionic species in the FTIR spectrum appear at 975 and 870 cm^{-1}; while, those of $H_2PO_4^-$ species appear at 1116 and 948 cm^{-1}. In Fig. 4.9b, the two small shoulder peaks are seen to be located at 930 and 833 cm^{-1} which are close to the characteristic modes of HPO_4^{2-} anionic species. It, hence, appears that the PO_4^{3-} ions are chemisorbed on the surface of HTN forming the chemical bonds with the intercalated H^+ ions belonging to the structure of HTN. The presence of any residual unreacted PO_4^{3-} ions is not detected on the surface of HTN. Thus, the final hydrothermal product primarily consists of HPO_4^{2-} anions modified HTN.

The N_2 adsorption / desorption isotherms as obtained for the final sol-gel and hydrothermal derived products are presented in Fig. 4.10a and b respectively; while, the corresponding Barrett-Joyner-Halenda (BJH) pore size distribution graphs are shown as

an inset. According to the IUPAC classification,[53] all the isotherms are of type IV which are the characteristic features of capillary condensation taking place in the mesopores; while, the hysteresis behavior is in between the types H1 and H2.[54-59]

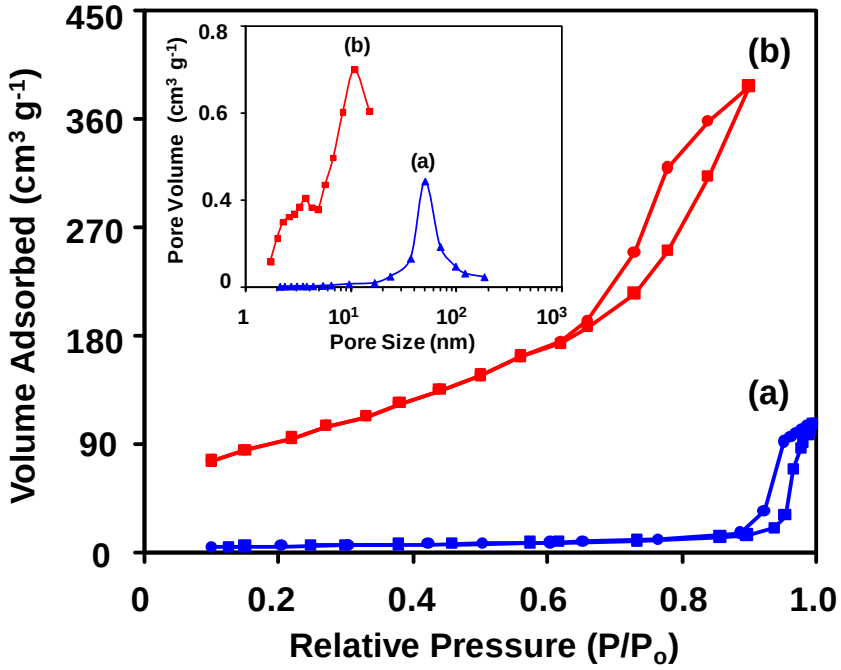

Fig. 4.10. Nitrogen adsorption / desorption isotherms obtained using the final sol-gel (a) and hydrothermal (b) derived products. The inset shows the corresponding BJH pore size distribution curves.

The type H1 hysteresis is often associated with the porous materials consisting of agglomerates of approximately uniform size in fairly regular array having narrow pore size distribution. On the other hand, the type H2 hysteresis is a typical of mesoporous materials having ink-bottle-like pores with narrow necks and wider bodies. In Fig. 4.10a, the uptake is observed to be limited over a higher range of P/P_0 (=0.9-1.0) with the presence of a small hysteresis loop which is closer to the type H1 than to the type H2. In accordance with this, as seen in Fig. 4.10a (inset) and the data tabulated in Table 4.1, the final sol-gel derived product exhibits unimodal and narrow pore size distribution with relatively larger average pore size, smaller pore volume, and lower specific surface-area.

In Fig. 4.10b, the broad hysteresis behavior (P/P_0=0.6-0.9) is closer to type H2 indicating highly mesoporous nature of final hydrothermal product (compared with that in Fig. 4.10a) with the presence of long unfilled pores having smaller average pore size and relatively wider pore size distribution. This is supported by the bimodal pore size distribution, as noted in Fig. 4.10b (inset), which is related to the internal diameter of the nanotubes (corresponding to smaller peak located at ~3.7 nm as seen in Fig. 4.10(b) (inset)) as well as the inter / intra-aggregate porosity (corresponding to larger peak located at ~11 nm as seen in Fig. 4.10b (inset)) formed by the bundles of nanotubes. (Note: The long and small size internal pores within the nanotubes connected to the larger size inter / intra aggregate pores, Fig. 4.3b, may resemble the ink-bottle-like pore structure). The latter is possibly contributed by the presence of HPO_4^{2-} anions on the surface of HTN which tend to reduce the aggregation tendency of nanotubes. The associated higher specific surface-area and pore volume of HP-HTN relative to those of sol-gel derived product and pure HTN, Table 4.1, corroborate these inferences.

Table 4.1. BET specific surface-area and pore volume as measured for the different samples.

Sample	BET Specific Surface-Area ($m^2\ g^{-1}$)	Pore Volume ($cm^3\ g^{-1}$)
TP/PO_4^{3-}-TiO_2	20	0.16
HP-HTN	345	0.61
Pure HTN[43]	288	0.43

The UV-visible absorption graphs obtained for the final sol-gel and hydrothermal derived products are presented in Fig. 4.11a and b respectively. Both the samples show light

absorption in the UV-region below 400 nm wavelength. The band-gap energy values of these samples are estimated from the plots of modified Kubelka–Munk function $((\alpha h\nu)^{1/2}$, where α is the absorption coefficient (cm^{-1}), h the Plank's constant, and ν the frequency of absorbed photons) versus the energy ($h\nu$) of absorbed photons as shown an inset in Fig. 4.11.[60] The band-gap energy value of ~3.2 eV is estimated for both of these samples. Lin et al.[61] also reported the band-gap energy value of ~3.2 eV for the nanocrystalline anatase-TiO_2 having the average nanocrystallite size of ~18 nm. It appears that the average nanocrystallite size of ~20 nm observed in the TEM images, Fig. 4.2, is relatively larger to have any quantum-size effect on the band-gap energy enhancement which is normally reported for the average size below 10 nm.[62] Yu et al.[62] observed that P doping results in the blueshift in the absorption spectrum of anatase-TiO_2 since former can restrict the growth in the average TiO_2 nanocrystallite size below 10 nm during the calcination treatment.

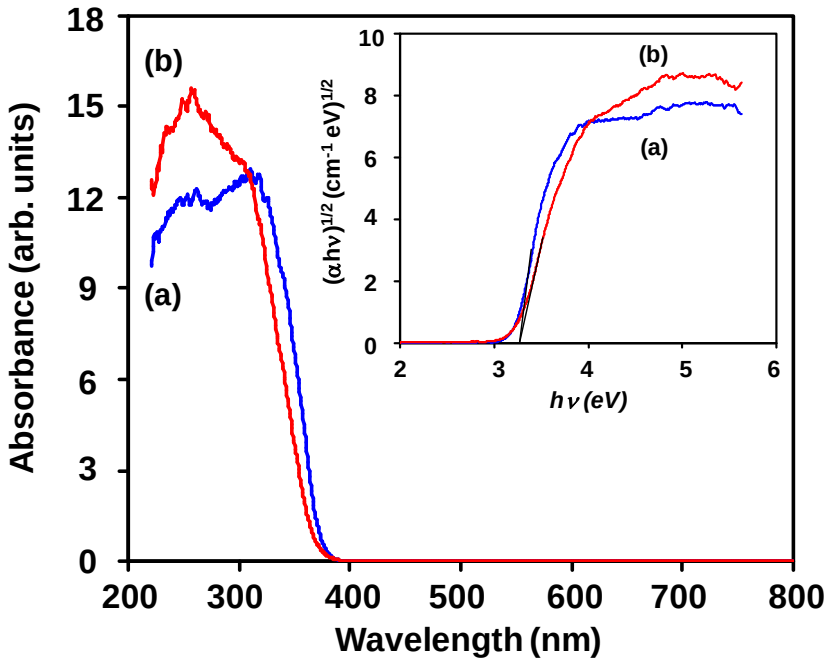

Fig. 4.11. UV-visible diffuse reflectance spectra obtained using the final sol-gel (a) and hydrothermal (b) derived products. The inset shows the corresponding plots of transformed Kubelka−Munk function versus the energy of absorbed light.

Gopal et al.,[63] however, reported an opposite trend involving the redshift in the absorption spectrum due to the effect of substitution of pentavalent phosphorous (P^{5+}) in Ti^{4+} sites. However, considering the average size of nanocrystallites of anatase-TiO_2, the quantum-size effect is neglected in this work. Moreover, according Li et al.,[48] the titanyl phosphate phases, such as $(TiO)_2P_2O_7$ and $Ti_5O_4(PO_4)_4$, generally have higher band-gap energy values compared with that of anatase-TiO_2. Since, in the present investigation, the nanocrystalline anatase-TiO_2 exhibits the band-gap energy comparable with that of the bulk sample, it appears that the possible blueshift and redshift in the absorption spectrum caused by the presence of TiP_2O_7 and P-doping respectively are either well balanced or not at all present in the system. Considering the small amount of P in the present sample (P:Ti ratio of 0.11), Fig. 4.6a, and the formation of distinct TiP_2O_7 phase and PO_4^{3-} ions

on the surface nanocrystallites of anatase-TiO_2, Figs. 4.7a and 4.9a, we rule out the possibility of P doping in significant amount in the final sol-gel derived product. As a result, the effect of presence of TiP_2O_7 phase on the band-gap energy of final sol-gel derived product is possibly negligible. Since the nanocrystalline anatase-TiO_2 is not doped with P, the hydrothermally synthesized HTN are also not doped with P as per the method described by Neville et al. who demonstrated the formation of C-doped HTN via the hydrothermal treatment of C-doped anatase-TiO_2.[64] The band-gap energy of 3.2 eV estimated for the final hydrothermal product is, hence, comparable with that (3.22 eV) reported for pure HTN by Asapu et al..[60] The latter also showed that P-doping in HTN results in significant decrease in the band-gap energy value of HTN to 2.95 eV. As a result, we deduce that similar to the sol-gel derived product, HTN are also not doped with the P consistent with the above analysis. It appears that the surface adsorption of HPO_4^{2-} anions has no effect on the band-gap energy value of HTN. The overall results, thus, reveal that the final sol-gel derived product consists of TiP_2O_7/PO_4^{3-} ions modified nanocrystalline anatase-TiO_2 which is hydrothermally transformed to HPO_4^{2-} anion modified pure HTN.

4.3.2. Prediction and confirmation of dye-adsorption capacity of pure HTN

The proposed mechanism of dye-decomposition in the dark using $H_2Ti_3O_7$ nanotubes as catalyst and H_2O_2 as a strong oxidizer involves the generation of O_2^- and $^{\bullet}OH$ in the dark which attack and decompose the dye adsorbed on the surface of nanotubes.[19]

$$H_2O_2 \xrightarrow{H_2Ti_3O_7} O_2^- + 2H^+ + e^- \quad (4.3)$$

$$H_2O_2 + O_2^- \xrightarrow{H_2Ti_3O_7} OH^{\bullet} + OH^- + O_2 \quad (4.4)$$

(Note: Due to the generation of O_2^- and $^{\bullet}OH$ in the presence of H_2O_2 and a catalyst without the radiation-exposure, the novel chemically-activated catalytic process

conducted in the dark can be classified as either AOP (Fenton-like system) or CWPO process).[65-66] As a result, the surface of nanotubes remains clean after the dye-decomposition process conducted in the dark and can be recycled for the successive cycles of dye-decomposition. The catalytic nature of HTN has been demonstrated earlier via conducting the several successive cycles of dye-decomposition in the dark.[19] Since the solution-pH remains constant in an acidic region during the dye-decomposition via one-step method of novel chemically-activated catalytic process conducted in the dark, within the investigated range of initial H_2O_2 concentration, it presently appears that the dye-decomposition predominantly takes place via the generation and attack of O_2^- ions rather than that of $^{\bullet}OH$.

The variation in the normalized MB concentration, simultaneously adsorbed and decomposed in the dark, as a function of contact time is presented in Fig. 4.12a-d for the initial MB and H_2O_2 concentrations varying in the range of 30-1000 μM and 3-50 wt%. In general, for a given initial H_2O_2 concentration, higher degradation kinetics is observed at lower initial MB concentrations and the former is noted to decrease with increase in the latter. With the increasing initial H_2O_2 concentration, the MB degradation kinetics is noted to increase; that is, the curves simultaneously tend to shift upwards and to left-side for a given initial MB concentration with the increasing initial H_2O_2 concentration. The blank experiments (that is, the dye-decomposition experiments typically conducted, under the dark in the presence of H_2O_2 but without the addition of catalyst, for the initial MB concentration of 150 μM with the initial H_2O_2 concentration varying in the range of 3-50 wt%) suggest that, within its investigated range of initial concentration, H_2O_2 has no bleaching effect on the MB dye. Moreover, no other chemical reagents, such as catalase, sodium hypochlorite, sodium thiosulfate and sodium sulfite, have been added externally which can quench the H_2O_2.[67]

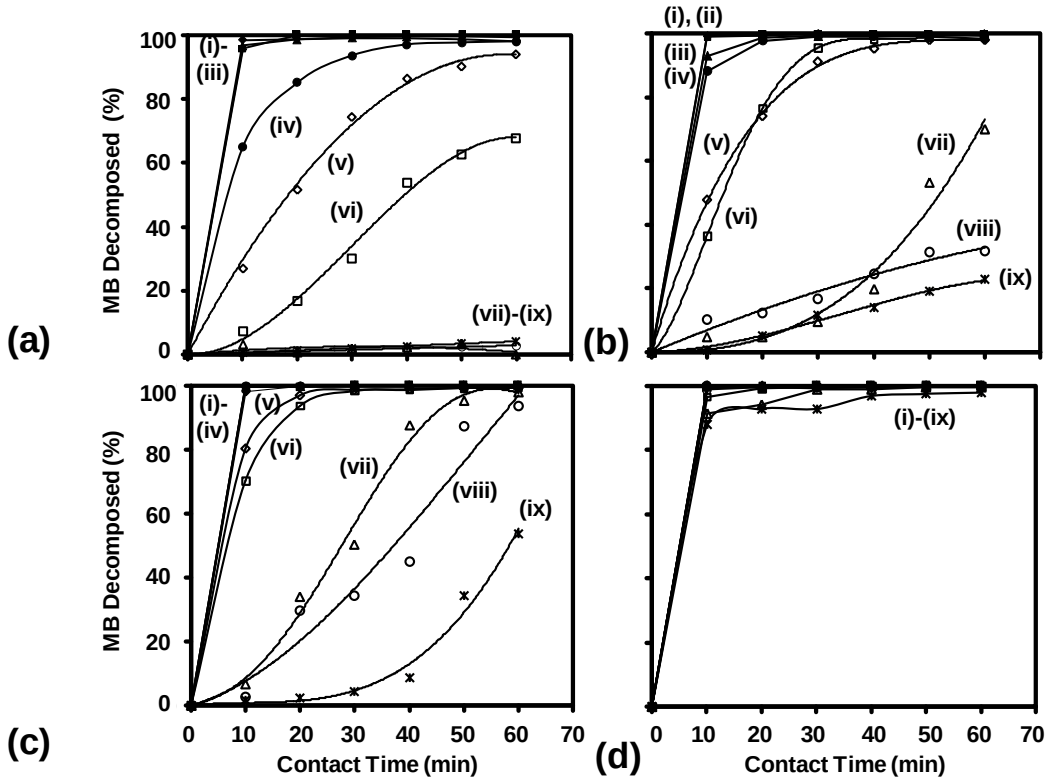

Fig. 4.12. Variation in the normalized concentration of MB decomposed in the dark as a function of contact time for the different initial H_2O_2 concentrations: 3 (a), 15 (b), 30 (c), and 50 wt% (d). The initial MB concentration is varied as 30 (i), 60 (ii), 90 (iii), 150 (iv), 200 (v), 250 (vi), 500 (vii), 750 (viii), and 1000 μM (ix).

As a result, in the present case, the consumption of H_2O_2 is due to the presence of a catalyst which generates the O_2^- and $^{\bullet}OH$ in the dark which in turn attack and decompose the dye adsorbed on the surface of nanotubes. It is believed that the consumption of H_2O_2 by the catalyst via Eqs. (4.3) and (4.4) would reduce the bleaching effect of H_2O_2 if the latter is present in the system. However, since the bleaching effect of H_2O_2 is not observed in the absence of catalyst, the dye-decomposition data presented in Fig. 4.4 is directly used to obtain the variation in the normalized MB concentration simultaneously adsorbed and decomposed in the dark, typically after 1 h of contact time, as a function of initial MB concentration, Fig. 4.13.

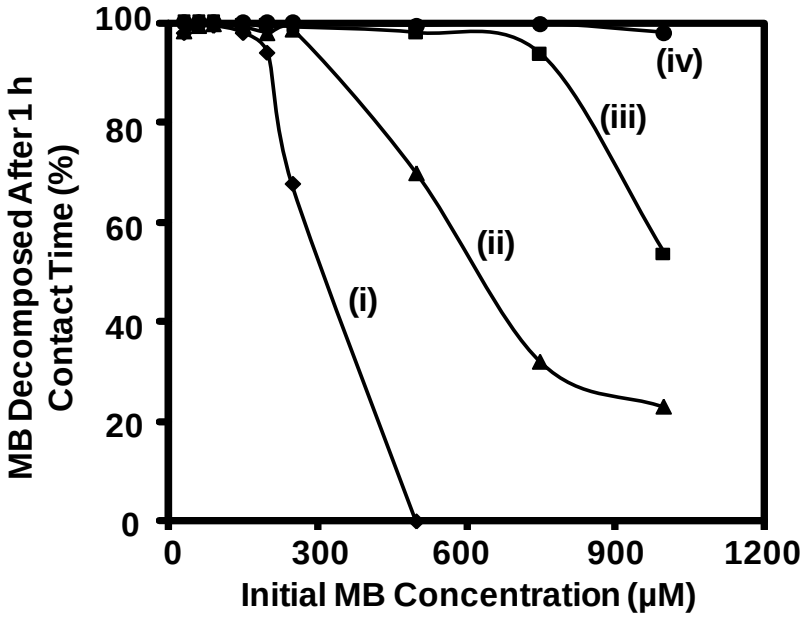

Fig. 4.13. Variation in the normalized concentration of MB decomposed after the contact time of 1 h as a function of initial MB concentration for the initial H_2O_2 concentration varying as: 3 (i), 15 (ii), 30 (iii), and 50 wt% (iv).

It is noted that the amount of MB decomposed in the dark after 1 h of contact time is 100% for lower range of initial MB concentration independent of initial H_2O_2 concentration. Although the former is noted to decrease below 100% typically in higher range of initial MB concentration for a given initial H_2O_2 concentration, the critical value of initial MB concentration at which the drop begins is noted to shift to higher values with the increasing initial H_2O_2 concentration. As a result, for the initial H_2O_2 concentration of 50 wt%, the MB decomposition is almost 100% for the entire initial MB concentration range investigated here. Hence, 50 wt% appears to be the most suitable initial H_2O_2 concentration for decomposing the MB, under the dark, in a highly concentrated aqueous dye-solution.

The data presented in Figs. 4.12 and 4.13 is further utilized to calculate the amount of MB simultaneously adsorbed and decomposed in the dark per unit mass of HTN per unit hour q' (mg g^{-1} h^{-1}) for a given initial H_2O_2 concentration, using the equation of form,

$$q' = \frac{(C_0 - C_t) \times V}{m_{HTN} \times t} \tag{4.5}$$

Where, C_t (mg l^{-1}) is the MB concentration within the solution at the contact time of t=1 h (Note: If the dye is decomposed completely in less than 1 h, then t corresponds to the contact time (in hours) at which 100% dye-decomposition is first observed), V (l) the initial volume of MB solution, and m_{HTN} (g) the amount of HTN used as a catalyst. The obtained variation in q' as a function of initial H_2O_2 concentration is presented in Fig. 4.14.

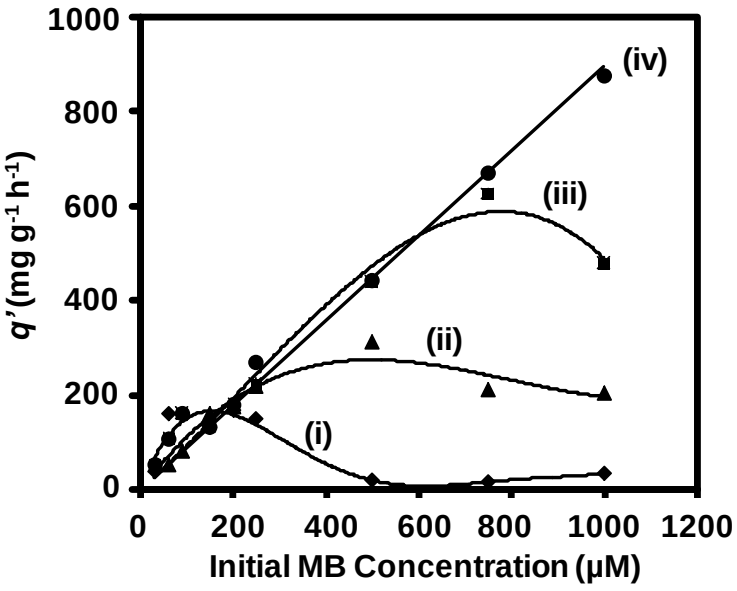

Fig. 4.14. Variation in q' as a function of initial MB concentration for the initial H_2O_2 concentration varying as: 3 (i), 15 (ii), 30 (iii), and 50 wt% (iv).

It is seen that, for a given initial H_2O_2 concentration, q' increases with the initial MB concentration, reaches a peak-value, and then decreases with further increase in the initial H_2O_2 concentration. The maximum value of q' (q'_m) and the corresponding initial MB

concentration both shift to higher values with the increasing initial H_2O_2 concentration. The obtained linear-variation in the q'_m as a function of initial H_2O_2 concentration is presented in Fig. 4.15.

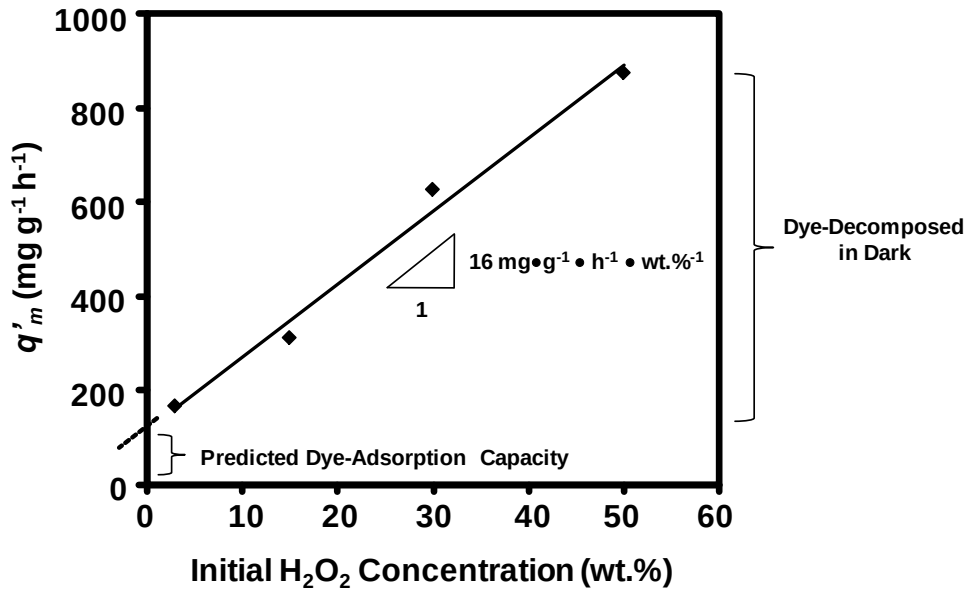

Fig. 4.15. Variation in q'_m as a function of initial H_2O_2 concentration.

It is noted that the best-fitted straight-line (regression correlation coefficient, $<r^2>$=0.987) does not pass through the origin. The extrapolation of this linear-variation gives the Y-intercept (corresponding to the initial H_2O_2 concentration of zero) equal to 114 mg g^{-1} h^{-1}. It is to be further noted that in the presence of H_2O_2 with the initial concentration varying in the range of 3-50 wt%, the dye-removal takes place via simultaneous dye-adsorption and dye-decomposition processes on the surface of catalyst. This mechanism primarily involves the generation of O_2^- and $^{\bullet}OH$ on the surface of HTN and their subsequent attack on the adsorbed MB dye molecules degrading them into the non-harmful species.[19] However, in the absence of H_2O_2 but in the presence of catalyst, the dye-removal essentially occurs only via surface-adsorption process.[30,68] As a result, the Y-intercept value of 114 mg g^{-1} h^{-1} must correspond to the dye-adsorption capacity (114 mg g^{-1}) of HTN since the dye-adsorption data obtained after the contact time of 1 h is used for the

calculation within the entire range of initial MB concentration investigated here. Thus, by utilizing the one-step dye-removal method of novel chemically-activated catalytic process conducted in the dark, the dye-adsorption capacity of HTN, processed via hydrothermal treatment of sol-gel derived nanocrystalline anatase-TiO_2, is estimated to be 114 mg g^{-1}.

In order to confirm the predicted value of dye-adsorption capacity, the dye-adsorption measurements, typically for 1 h duration of contact time at the initial solution-pH of ~10, were conducted via conventional approach involving the equilibrium adsorption / desorption of dye molecules on the surface of adsorbent.[30,68-69] (Note: the dye-adsorption capacity of HTN has been determined earlier by varying the initial solution-pH within the range of 2.5-11.[30] The maximum amount of dye-adsorbed on the surface of HTN varies as 11, 32, 105, 68 corresponding to the initial solution-pH of ~2.5 (acidic), 7.5 (neutral), 10 (basic), and 11 (basic). Thus, the predicted value (114 mg g^{-1}) of dye-adsorption capacity is comparable with that reported earlier at the initial solution-pH of ~10. Hence, in the present investigation, the dye-adsorption capacity has been determined for the present sample at the initial solution-pH of ~10.) The obtained variation in the normalized concentration of MB adsorbed on the surface of HTN as a function of contact time, as obtained for the different initial MB concentrations, is presented in Fig. 4.16. It is observed that the normalized concentration of MB adsorbed on the surface of HTN increases rapidly within first 10 min of contact time and then tends to attain an equilibrium with further increase in the contact time. The normalized concentration of MB adsorbed at equilibrium on the surface of HTN reaches almost 100% at lower initial MB concentrations and decreases with increase in the latter.

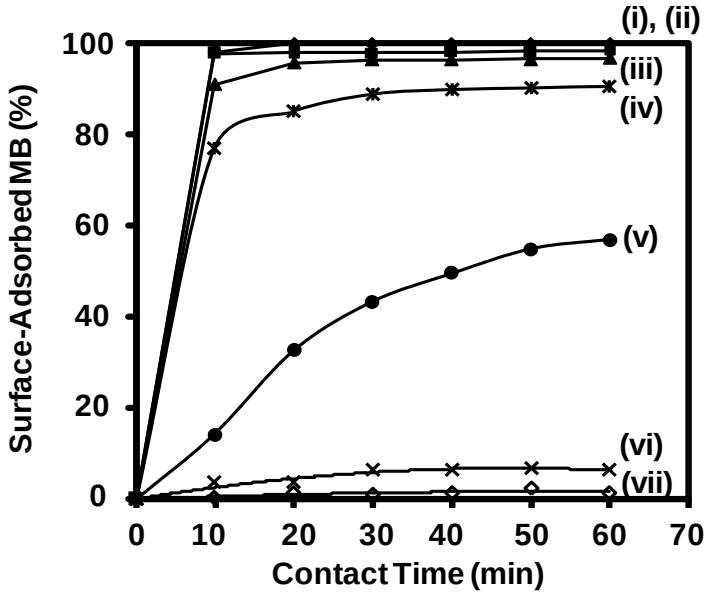

Fig. 4.16. Variation in the normalized concentration of surface-adsorbed MB as a function of contact time at the initial solution-pH of ~10. The initial MB concentration is varied as 7.5 (i), 60 (ii), 90 (iii), 150 (iv), 200 (v), 250 (vi), and 750 μM (vii).

The adsorption data presented in Fig. 4.16 is utilized to calculate the equilibrium amount of MB adsorbed on the surface per unit mass of HTN, q_e (mg g^{-1}), using the Eq. (3.5). The obtained variation in q_e as a function of initial MB concentration is presented in Fig. 4.17. It is noted that q_e increases gradually with the initial MB concentration, reaches a maximum value (q_m (mg g^{-1}), regarded here as the dye-adsorption capacity since the measurements are conducted at the initial solution-pH of ~10), and then decreases drastically with further increase in the initial MB concentration which has been explained in our earlier investigation.[30] The adsorption of MB dye molecules, which are cationic in an aqueous solution, on the surface of HTN is via an electrostatic attraction mechanism due to the negatively-charged surface of HTN at the initial solution-pH of ~10. When the initial MB concentration within the solution is very high, their strong interaction with the OH^- ions already present within the solution restricts the amount of latter adsorbed on the surface of HTN.

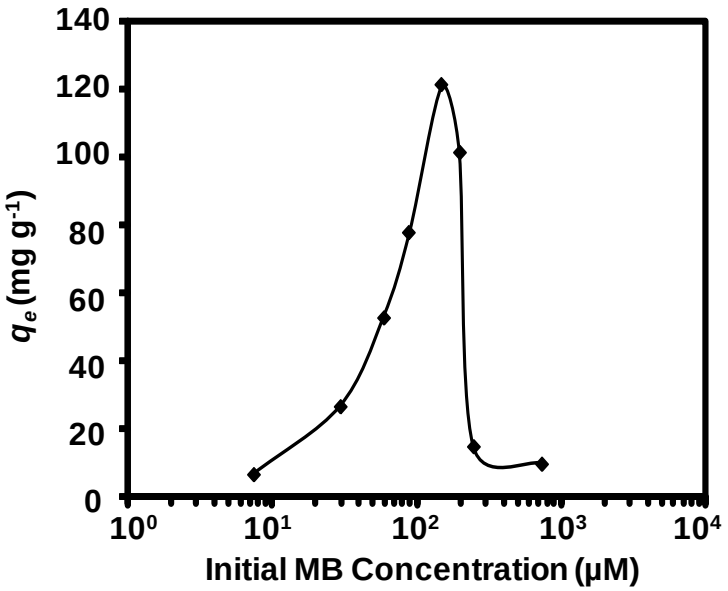

Fig. 4.17. Variation in q_e as a function of initial MB concentration at the initial solution-pH of ~10.

This in turn reduces the amount of negative surface-charge developed, and hence, the amount of surface-adsorbed MB. The dye-adsorption capacity of HTN is thus observed to be 121 mg g^{-1}. As per the earlier investigation, the dye-adsorption capacity of 105 mg g^{-1} has been reported for HTN processed using the commercially available nanocrystalline anatase-TiO_2 as a precursor for the hydrothermal treatment.[30] As a result, the predicted value of dye-adsorption capacity (114 mg g^{-1}) appears to fall well within the range (105-121 mg g^{-1}) as observed for the conventional method considering the different nature of precursors used during the hydrothermal treatment. Thus, it is confirmed that the dye-adsorption capacity of HTN can be precisely predicted via one-step dye-removal method of novel chemically-activated catalytic process conducted in the dark even though the dye-adsorption and dye-decomposition occur simultaneously under this test-condition.

4.3.3. Determination of equilibrium adsorption isotherm and kinetics models for HTN

The equilibrium adsorption data, derived using Fig. 4.16, is fitted using the Langmuir, Freundlich, and DKR isotherms.[30,68-72] The values of different parameters of three isotherm models obtained from the slopes and intercepts of the best-fitted straight lines, Fig. 4.18a-c, as well as the calculated values of E, ΔG^0, and R_L are tabulated in Table 4.2. It is noted that the $<r^2>$ values are the highest and closest to 1 for the Langmuir and Freundlich isotherms. The $<r^2>$ values as observed for these two models are also comparable. The value of q_m (125 mg g^{-1}) estimated using the former model is equivalent to the experimentally determined value of q_m (121 mg g^{-1}). Moreover, the value of R_L which is in between 0 and 1 and the negative ΔG^0 value further support the Langmuir model which in turn suggests the maximum coverage via monolayer adsorption of MB on the surface of HTN.[30] Also, the value of $1/n$ (0.276) which is in between 0 and 1 strongly favors the Freundlich model which in turn suggests the presence of heterogeneity on the surface of catalyst and the significance of pores in the catalyst during the dye-adsorption process.[72-73] Hence, the equilibrium adsorption of MB on the surface of HTN follows both the Langmuir and Freundlich isotherms which is in accordance with the earlier report considering the initial solution-pH of ~10 at which the dye-adsorption capacity is determined.[30]

Table 4.2. Values of equilibrium isotherm related parameters for the MB adsorption on the surface of HTN.

pH	q_m (EXP)	Langmuir					Freundlich			DKR			
		q_m	K_L	r^2	R_L	ΔG^0	n	K_F	r^2	q_m	B	r^2	E
10	121	125	8	0.984	0.006-0.106	-39.4	3.62	78	0.997	86.3	-1×10^{-8}	0.817	7.1

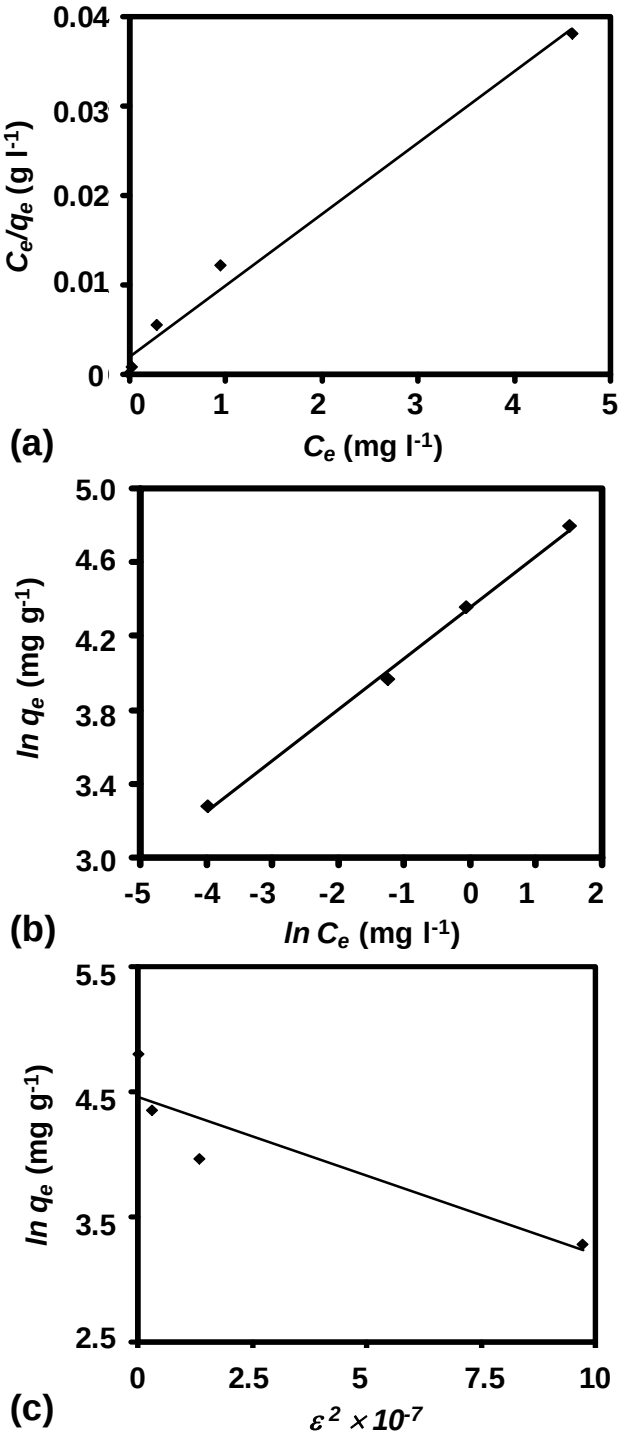

Fig. 4.18. Langmuir (a), Freundlich (b), and DKR (c) isotherm plots at the initial solution-pH of ~10.

The rate at which MB is adsorbed from an aqueous solution on the surface of HTN is analyzed using three different kinetics models: Lagergren pseudo-first-order, pseudo-second-order, and intra-particle diffusion.[72,74]

The equilibrium adsorption data presented in Fig. 4.16 is further utilized to fit the above kinetics models and the values of different parameters derived from the slopes and intercepts of the best-fitted straight-lines, Fig. 4.19, are tabulated in Table 4.3. It is noted that the $<r^2>$ values are the highest and closest to 1 only for the pseudo-second-order kinetics model. Moreover, the values of q_e estimated using this model are comparable with the experimentally determined values of q_e (specifically for lower range (7.5-150 μM) of intial MB concentration). The model predicts the dye-adsorption capacity of HTN to be 125 mg g^{-1} which is also comparable with the experimentally determined value. Hence, it appears that the equilibrium adsorption of MB on the surface of HTN follows the pseudo-second-order kinetics in agreement with the earlier report.[30]

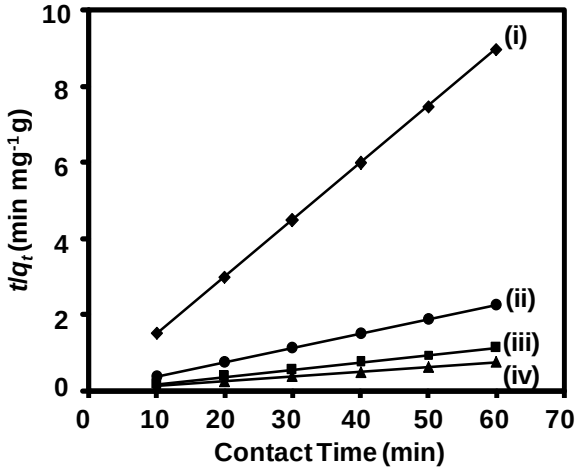

Fig. 4.19. Typical pseudo-second-order kinetics plots at the initial solution-pH of ~10. The initial MB concentration is varied as 7.5 (i), 30 (ii), 60 (iii), and 150 μM (iv).

The maximum fraction of surface-area of HTN covered by MB dye, at equilibrium, is calculated using the following equation,[30]

$$Coverage(\%) = \frac{q_m \times N_{AV} \times SA_{MB}}{MW_{MB} \times S_{HTN} \times 10} \quad (4.6)$$

where, N_{AV} is the Avogadro's number (6.023×10^{23} molecules $mole^{-1}$), MW_{MB} the molecular weight of MB dye (319.85 g $mole^{-1}$), SA_{MB} and S_{HTN} the surface-area (m^2) of a single MB dye molecule (8.723×10^{-19} m^2; dimensions: 1.43 nm × 0.61 nm × 0.4 nm)[30,75] and the specific surface-area (288 m^2 g^{-1}) of HTN (Note: In Eq. (4.6), q_m has the value of 121 mg g^{-1}). It is noted that the MB dye covers 70% of surface-area of HTN at the initial solution-pH of ~10. Hence, the possibility of excess MB adsorption is ruled out in the present case which also supports the monolayer adsorption of dye-molecules in accordance with the Langmuir model. Hence, it appears that the amount of surface-coverage by MB dye favors the Langmuir isotherm over the Freundlich isotherm.

Table 4.3. Values of kinetics constants for MB dye adsorption on the surface of HTN.

[MB] (μM)	q_e (Exp)	Pseudo-First-Order Kinetics			Pseudo-Second-Order Kinetics			Intra-Particle Diffusion Kinetics		
		q_e	k_1	r^2	q_e	k_2	r^2	k_{id}	C	r^2
7.5	6.7	6.7	0.396	1	6.7	1.17	1	0.028	6.515	0.603
30	26.6	4.8	0.085	1	27	0.114	1	0.098	25.75	0.959
60	52.7	6.3	0.02	0.607	55.6	0.162	1	0.086	52.01	0.915
90	77.7	26.8	0.129	0.909	83.3	0.024	1	0.871	71.7	0.675
150	121	84.3	0.117	0.986	125	0.0043	0.999	3.767	94.82	0.833
200	101.5	136	0.0645	0.948	166.7	0.0002	0.99	16.65	-20.3	0.958
500	14.7	28.4	0.147	0.877	17.5	0.0062	0.985	1.73	2.541	0.759
750	9.7	10.5	0.039	0.969	23.8	0.0007	0.369	0.044	2.502	0.369

4.3.4. Validation of method of prediction of dye-adsorption capacity using HP-HTN

4.3.4.1. Dye-adsorption characteristics of HP-HTN

The adsorption properties of HP-HTN are studied using the cationic MB dye by varying the contact time, initial MB dye concentration, and initial solution-pH. The variation in the normalized concentration of MB dye adsorbed on the surface of HP-HTN as a function of contact time, as obtained for the different initial MB dye concentration and initial solution-pH values varying in the range of 7.5-500 μM and 2.5-10 respectively, is presented in Fig. 4.20. It is observed that the normalized concentration of MB dye adsorbed on the surface of HP-HTN increases rapidly within the first 10 min of contact time and then it tends to attain equilibrium with further increase in the latter. At the lower initial MB dye concentrations, almost 100% MB dye is adsorbed on the surface of HP-HTN which decreases with further increase in the initial MB concentration. This variation is consistent with the variation reported earlier for the pure HTN by Narayani et al.,[30] except for the highest initial solution-pH of 11. Under the latter condition, the equilibrium amount of MB dye adsorbed on the surface of pure HTN has been reported to increase first in the lower range of initial MB dye concentration (~15-100 μM) which is not observed here for the HP-HTN, Fig. 4.20d. Bavykin et al.[76] suggested that the electrostatic attraction between the positively charged MB dye molecules and the negatively charged surface of HTN is responsible for the adsorption of former on the surface of latter. Although in a neutral aqueous suspension, the nanotubular titanates tend to develop a negative surface potential due to the dissociation of titanic acid,[76] at the initial solution-pH of 11, the negative charge on the surface of pure HTN is predominantly governed by the adsorption of OH^- ions; while, in the case of HP-HTN, it is additionally contributed by the presence of HPO_4^{2-} anions on the surface. According to

Narayani et al.,[30] at the initial solution-pH of 11, the strong interaction between the positively charged MB molecules with the excess OH^- ions remaining in the solution delays the adsorption of former on the surface of pure HTN. However, due to their higher ionic strength than that of OH^- ions, the presence of HPO_4^{2-} anions can nullify this effect and may allow the cationic MB dye molecules to be readily adsorbed on the surface of HP-HTN. Such interaction in turn causes the equilibrium amount of MB adsorbed to remain maximum at the lower initial MB concentrations and then to decrease continuously with the increase in the latter, Fig. 4.20d. Thus, the effect of higher concentration of OH^- ions in the solution having the initial solution-pH of 11 appears to be nullified due to the presence of HPO_4^{2-} anions on the surface of HP-HTN.

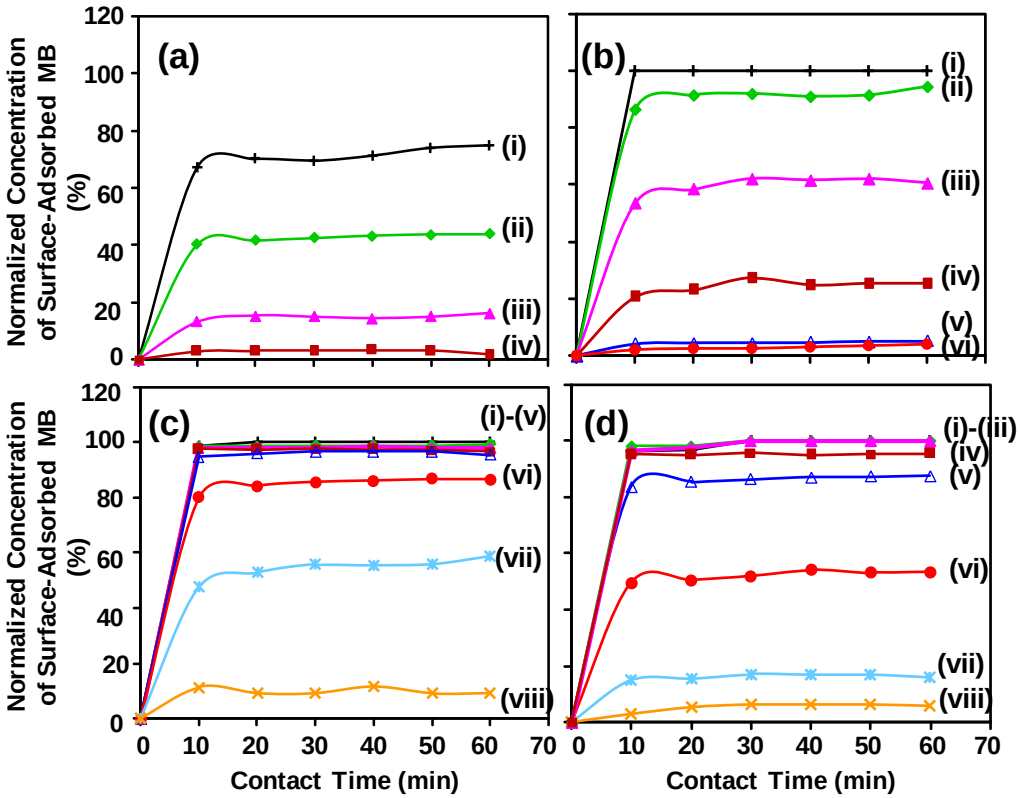

Fig. 4.20. Variation in the normalized concentration of surface-adsorbed MB as a function of contact time as obtained using HP-HTN for different initial solution-pH values: 2.5 (a), 7.5 (b), 10 (c), and 11 (d). The initial MB dye concentration is varied as 7.5 (i), 30 (ii), 60 (iii), 90 (iv), 150 (v), 200 (vi), 250 (vii), and 500 μM (viii).

The adsorption data is utilized to calculate the amount of MB dye adsorbed on the surface at equilibrium per unit mass of HP-HTN, q_e (mg g^{-1}), using the Eq. (3.9). The obtained variation in q_e as a function of initial MB dye concentration is presented in Fig. 4.21a. It is noted that q_e increases initially with the initial MB dye concentration and reaches a maximum value q_m (mg g^{-1}); then, it decreases with further increase in the initial MB dye concentration. The initial rise in q_e is attributed to a greater driving force for the gradual consumption of more number of active surface-sites available on the surface of HP-HTN for the MB adsorption. The decrease in q_e values at higher initial MB concentration is ascribed to the decrease in the negative charge present on the surface of HP-HTN as a result of reduced adsorption of OH^- ions on their surfaces due to the strong interaction of latter with the cationic MB dye molecules within the solution.[9,30,43] This may also be contributed by the presence of HPO_4^{2-} anions on the surface of HP-HTN. The variation in q_m as a function of initial solution-pH is plotted in Fig. 4.21b. The MB dye adsorption capacity of HP-HTN is thus estimated to be 139 mg g^{-1} at the initial solution-pH of 10 which appears to be larger than that (105 and 121 mg g^{-1}) reported earlier for pure HTN.[30,43]

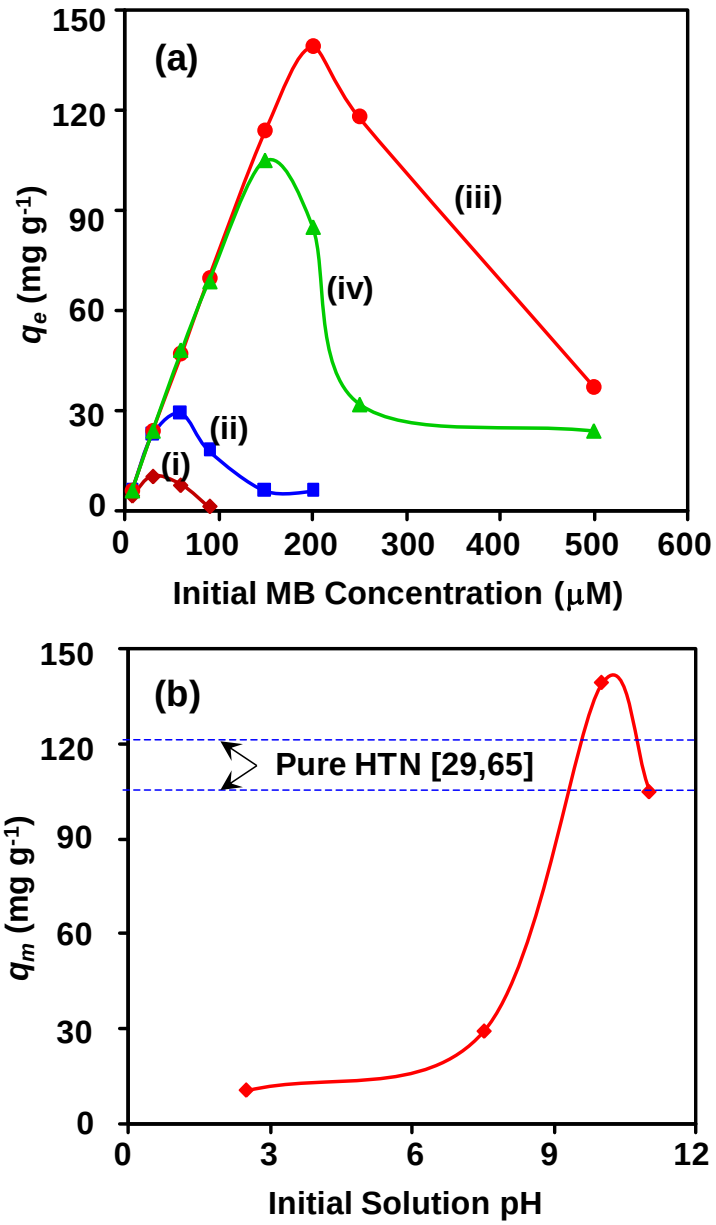

Fig. 4.21. (a) Variation in q_e as a function of initial MB concentration as obtained using the HP-HTN at the different initial solution-pH values: 2.5 (i), 7.5 (ii), 10 (iii), and 11 (iv). (b) Variation in q_m as a function of initial solution-pH as obtained using HP-HTN. For comparison, the MB dye-adsorption capacity values reported earlier for HTN are shown using the dotted lines.[30,43]

The higher MB adsorption capacity of HP-HTN relative to that of pure HTN is attributed here to the presence of HPO_4^{2-} anions on their surfaces which not only provide more active sites for the dye adsorption by enhancing the specific surface-area and pore

volume, Table 4.1, but also increase the negative surface-potential due to their higher ionic strength. The obtained variation in the zeta-potential of pure HTN and HP-HTN is shown in Fig. 4.22. The point-of-zero-charge for the two samples has been determined to be 2.8 and 3.2 respectively. Thus, the point-of-zero-charge of HP-HTN is noted to be higher than that of pure HTN which is in agreement with that reported earlier by Kim et al..[77] Higher negative surface-potential of HP-HTN than that of pure HTN as observed below the point-of-zero-charge near and within the basic region is due to the presence of HPO_4^{2-} anions on their surfaces which strongly supports higher MB adsorption capacity of former than that of latter.

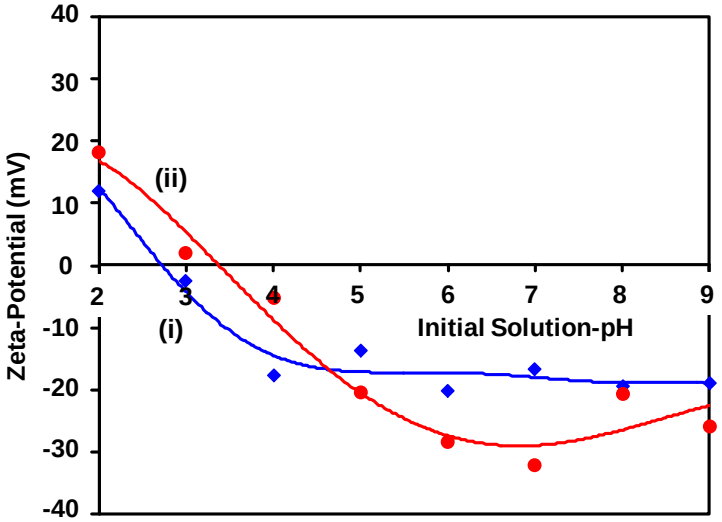

Fig. 4.22. Variation in the zeta-potential of pure HTN (i) and HP-HTN (ii) as a function of initial solution-pH.

The equilibrium dye-adsorption data, presented in Fig. 4.20, is fitted using the Langmuir and DKR isotherm models. The values of different parameters of Langmuir isotherm model obtained from the slopes and intercepts of the best-fitted straight-lines, Fig. 4.23 as well as those of R_L and ΔG^0 are tabulated in Table 4.4. It is noted that the experimentally determined values of q_m are well predicted by Langmuir isotherm model with the

regression correlation coefficient, $<r^2>$, values close to 1. Moreover, R_L and ΔG^0 values are calculated to be within the range of 0.002 to 0.25 and -41 to -34 kJ mol^{-1} respectively, which indicate that the adsorption process is highly favorable and spontaneous in nature. Hence, the Langmuir isotherm model appears to satisfactorily describe MB adsorption on the surface of HP-HTN within the initial solution-pH range of 2.5-11 suggesting a monolayer adsorption of MB dye molecules on the surface of latter. As per the procedure described elsewhere,[43] the maximum surface-coverage by MB dye molecules on the surface of HP-HTN is calculated to be 66% which is comparable with that (52-70%) reported earlier for pure HTN,[30,43] which also supports the monolayer adsorption of MB dye molecules on the surface of HP-HTN.

Table 4.4. Values of parameters of Langmuir isotherm model and related parameters as obtained for HP-HTN.

Initial Solution-pH	q_m	q_m	Δq_m	Δq_m	K_L	R_L	ΔG^0	r^2
2.5	10.5	12.6	-2.1	-20	0.93	0.1-0.3	-34	1
7.5	29.1	29.4	-0.3	-1	17	0.003-0.02	-41	0.999
10	139	167	-28	-20	1.2	0.013-0.25	-35	0.998
11	105	111	-6	-5.7	9	0.002-0.04	-40	0.985

(Note: Δq_m (mg g^{-1}) and Δq_m (%) represent the standard and normalized standard deviations respectively).

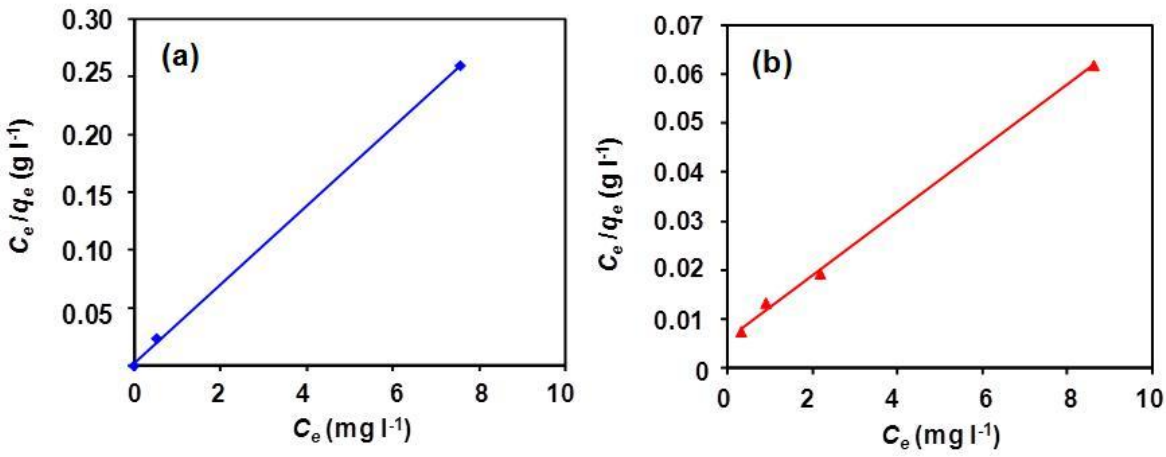

Fig. 4.23. Langmuir isotherm plots at the initial solution-pH of 7.5 (a) and 10 (b) as obtained for HP-HTN.

The values of different parameters of DKR isotherm model obtained from the slopes and intercepts of the best-fitted straight-lines, Fig. 4.24 as well as that of *E* are tabulated in Table 4.5 typically at the initial solution-pH of 10. It is noted that the dye-adsorption capacity of 139 mg g^{-1} is precisely predicted by this model with the $<r^2>$ value of 0.997. Moreover, the *E* value of 1.6 kJ mol^{-1} supports the fact that the adsorption of MB on the surface of HP-HTN is via electrostatic force of attraction mechanism instead of ion-exchange mechanism.[9,30] It is thus noted that, at the initial solution-pH of 10, the equilibrium MB adsorption data obtained for HP-HTN follows both the Langmuir and DKR isotherm models.

Table 4.5. Values of parameters of DKR isotherm model and related parameters at the initial solution-pH of 10 as obtained for HP-HTN.

Initial Solution- pH	q_m *(Exp)*	q_m	β	*E*	r^2
10	139	139	2×10^{-7}	1.6	0.997

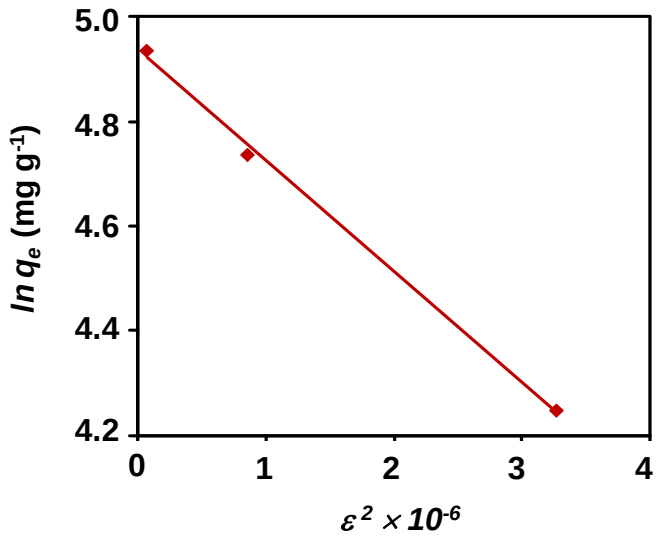

Fig. 4.24. DKR isotherm plot at the initial solution-pH of 10 as obtained for HP-HTN.

Narayani et al.[30] reported that the equilibrium MB adsorption on the surface of pure HTN follows the Langmuir and DKR models at the initial solution-pH of 2.5 and 11 respectively; while, a transition from Langmuir to DKR model is observed at the intermediate initial solution-pH values. In the present investigation, Langmuir model is predominantly obeyed within the entire investigated range (2.5-11) of initial solution-pH. Thus, the initial solution-pH range over which Langmuir model is obeyed appears to be extended for HP-HTN relative to that (2.5-7.5) reported earlier for the pure HTN.[30] Padinhattayil et al.[78] and Jose et al.[79] demonstrated that the initial solution-pH range over which Langmuir model is obeyed is dependent on the specific surface-area and dye-adsorption capacity of hydrothermal derived adsorbents. Hence, the observed dependence of Langmuir model within the investigated range of initial solution-pH is attributed here to the higher specific surface-area, Table 4.1, and higher dye-adsorption capacity, Fig. 4.21b, of HP-HTN relative to those of pure HTN.[30,79] The kinetics of MB dye adsorption from an aqueous solution on the surface of HP-HTN is analyzed using the pseudo-second-order model. The graphs presented in Fig. 4.25 are fitted using the above kinetics model and the values of different parameters derived from the slopes and

intercepts of the best-fitted straight-lines, Fig. 4.25 are tabulated in Table 4.6. It is noted that the experimentally determined values of q_e are well predicted by this model with the $<r^2>$ values close to 1. Hence, the adsorption of MB dye on the surface of HP-HTN follows the pseudo-second-order kinetics which is in agreement with that reported earlier for the pure HTN by Lee et al..[68]

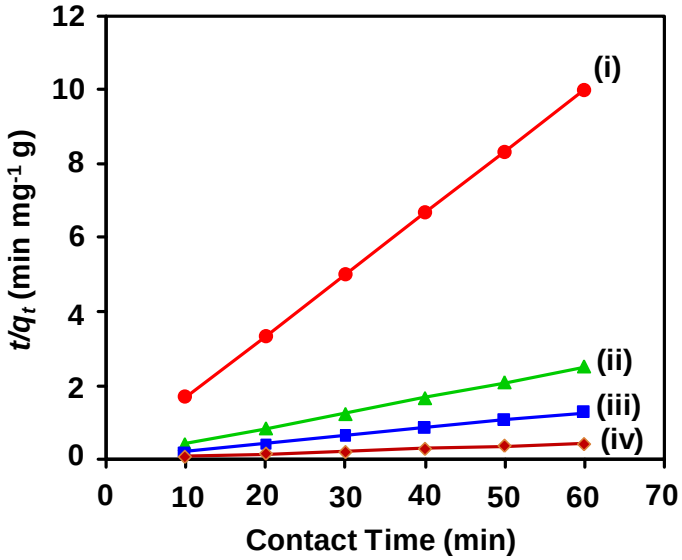

Fig. 4.25. Typical pseudo-second-order kinetics plots at the initial solution-pH of 10 as obtained for HP-HTN for the different initial MB dye concentrations: 7.5 (i), 30 (ii), 60 (iii), and 200 μM (iv).

Table 4.6. Values of parameters of pseudo-second-order kinetics model as obtained for HP-HTN.

Initial Solution pH	[MB]	q_e *(Exp)*	q_e	Δq_e	Δq_e	k_2	r^2
2.5	7.5	4.5	4.6	-0.1	-2.2	0.108	0.998
	30	10.5	10.9	-0.4	-3.8	0.064	0.999
	90	1.2	2.2	-1	-83.3	2.43	0.994
7.5	30	22.7	22.7	0	0	0.042	0.999
	60	29.1	30.3	-1.2	-4.1	0.027	0.998
	150	6.1	6.4	-0.3	-4.9	0.035	0.996
10	7.5	6	6	0	0	2.31	1
	200	139	143	-4	-2.9	0.008	1
	250	118	125	-7	-5.9	0.003	0.997
11	7.5	6	6.1	-0.1	-1.7	0.292	0.999
	150	105	111	-6	-5.7	0.016	1
	500	24	30.3	-6.3	-26.2	0.003	0.961

(Note: Δq_e (mg g^{-1}) and Δq_e (%) represent the standard and normalized standard deviations respectively).

4.3.4.2. Validating the new method of predicting dye-adsorption capacity

In order to recycle the adsorbent in the adsorption experiments as a catalyst, it is essential to decompose the previously adsorbed dye by a suitable technique. As demonstrated by Babitha et al.[19] and Jose et al.[43] and reviewed recently by Shukla and Oturan,[80] the MB dye adsorbed on the surface of pure HTN can be decomposed in another aqueous solution via chemically-activated catalytic process conducted in the dark involving the activation

of H_2O_2 (also called as the dark-catalysis process) in the presence of pure HTN. The MB degradation via the proposed mechanism involves the generation of ROS such as the $O_2^{\bullet-}$ and $^{\bullet}OH$ which subsequently attack and decompose the surface-adsorbed dye molecules. This also suggests that the amount of surface-adsorbed dye is one of the significant parameters in determining the kinetics of dye-degradation via the activation of H_2O_2. Using the EPR analysis, Lorencon et al.[81] confirmed that $O_2^{\bullet-}$, generated via reactions presented in Eqs. (4.7) and (4.8), are the dominant species in the decomposition of MB dye, Eq. (4.9), via H_2O_2 activation using pure HTN.

$$H_2O_2 \xrightarrow{HTN} O_2^{\bullet-} + 2H^+ + e^- \tag{4.7}$$

$$O_2 + e^- \xrightarrow{HTN} O_2^{\bullet-} \tag{4.8}$$

$$2C_{16}H_{18}N_3S^+ + 51O_2^{\bullet-} \xrightarrow{HTN} 32CO_2 + 6NO_3^- + 2SO_4^{2-} + 12H^+ + 12H_2O + 102e^- \tag{4.9}$$

As a result, the H_2O_2 activation offers an easy method for the surface-cleaning treatment of pure HTN (and HP-HTN as well as demonstrated in Fig. 4.26) to recycle them for the next cycle of dye-adsorption without the involvement of any external radiation or power source. As shown in Fig. 4.11, 97% of MB dye is adsorbed in the cycle-1 which reduces to 5% for the cycle-2. The HP-HTN with surface-adsorbed MB is then surface-cleaned by dispersing it in 30 wt% H_2O_2 solution under the continuous stirring which decomposes MB dye adsorbed on the surface of HP-HTN. The surface-cleaned HP-HTN exhibits enhanced MB adsorption (92%) in the cycle-3 which is comparable with that observed for the cycle-1. (Note: The minor difference in the amount of dye-adsorbed as observed for the cycles-1 and 3 is contributed by some loss of catalyst-powder during the solid-liquid separation obtained via centrifuging). This clearly demonstrates that HP-HTN can be regenerated and reused for the successive dye-adsorption cycles.

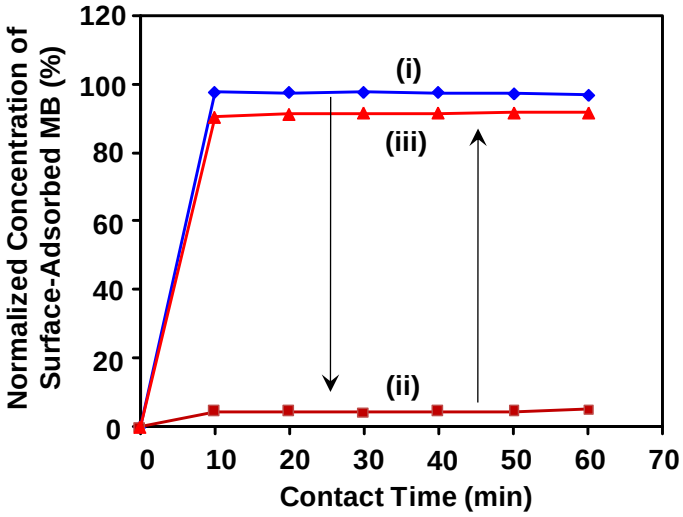

Fig. 4.26. Variation in the normalized concentration of MB dye adsorbed as a function of contact time as obtained for HP-HTN under the different test conditions. The successive dye-adsorption cycles, cycles-1, 2 (i, ii) and cycle-3 (iii), are conducted before and after the surface-cleaning treatment performed in H_2O_2 solution. For each dye-adsorption cycle, the initial MB dye concentration is 90 μM.

Babitha et al.[19] and Jose et al.[43] further revealed that the dye-adsorption and dye-decomposition processes can be combined in a one-step dye-removal process. Jose et al.[43] further examined the effect of initial H_2O_2 concentration (3-50 wt%) on q'_m using the one-step method of chemically-activated process conducted in the dark. It is demonstrated that the Y-intercept of graph of q'_m plotted as a function of initial H_2O_2 concentration provides the predicted value of dye-adsorption capacity of pure HTN which can also be measured experimentally via conventional equilibrium adsorption / desorption experiments. Inversely, based on the new method of prediction of dye-adsorption capacity as demonstrated by Jose et al.,[43] it is postulated here that the enhanced value of dye-adsorption capacity of HP-HTN (139 mg g^{-1}) as measured in the previous section when combined with q'_m values measured for any two initial H_2O_2

concentrations (for example, 3 and 15 wt%) should constitute a linear graph which would confirm the new method of prediction of dye-adsorption capacity.

To verify the above hypothesis, in the present investigation, the rate of MB decomposition in an aqueous solution is measured via the activation of H_2O_2 in the presence of HP-HTN for the initial H_2O_2 concentrations of 3 and 15 wt%. The obtained variation in the normalized concentration of MB dye decomposed in the dark as a function of contact time at the initial H_2O_2 concentration of 3 wt%, as obtained for the different initial MB concentrations, is presented in Fig. 4.27.

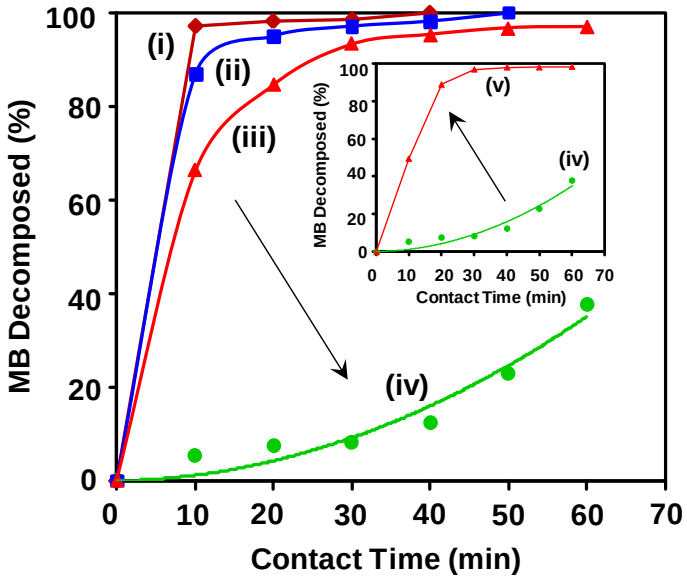

Fig. 4.27. Variation in the normalized concentration of MB decomposed in the dark as a function of contact time as obtained using HP-HTN at the initial H_2O_2 concentration of 3 wt%. The initial MB concentration is varied as 150 (i), 200 (ii), 250 (iii), and 500 μM (iv). The inset shows the comparison between the similar variation at the initial H_2O_2 concentrations of 3 (iv) and 15 wt% (v) for the constant initial MB concentration of 500 μM.

Higher MB degradation kinetics is observed at lower initial MB concentrations and the former is noted to decrease with increase in the latter. As shown in the inset, the higher the initial H_2O_2 concentration (15 wt%), the higher the MB degradation kinetics which is typically demonstrated here for the initial MB concentration of 500 μM. The amount of MB dye simultaneously adsorbed and decomposed at equilibrium in the dark per unit mass of HP-HTN per unit hour, q' (mg g^{-1} h^{-1}), is calculated as per the procedure described by Jose et al.[43] and plotted as a function of initial MB concentration, Fig. 4.28a. (Note: for comparison, such variation obtained for pure HTN, as reported earlier by Jose et al.,[43] is also shown in Fig. 4.28a). It is noted that the MB decomposition kinetics is higher for HP-HTN than that for pure HTN within the entire range of initial MB concentration investigated here which is attributed to higher MB adsorption capacity of HP-HTN than that of pure HTN, and Eq. (4.9). The q'_m value is calculated to be 194 mg g^{-1} h^{-1} for HP-HTN at the initial H_2O_2 concentration of 3 wt% which is higher than that (167 mg g^{-1} h^{-1}) reported earlier for pure HTN.[43] It is also noted that the q'_m values obtained for HP-HTN and pure HTN appear at almost comparable values of initial MB concentrations (~200-250 μM).

Jose et al.[43] reported q'_m value of 312 mg g^{-1} h^{-1} for pure HTN at the initial H_2O_2 concentration of 15 wt% which is observed at the initial MB concentration of 500 μM. As demonstrated in the inset of Fig. 4.27, the dye decomposition rate-capacity under the similar test conditions is enhanced to 393 mg g^{-1} h^{-1} for HP-HTN. Since q'_m values estimated at the initial H_2O_2 concentration of 3 and 50 wt% are higher for HP-HTN than those of pure HTN, it is evident that the surface-cleaning treatment via the activation of H_2O_2 would be more effective for the latter than that for pure HTN.

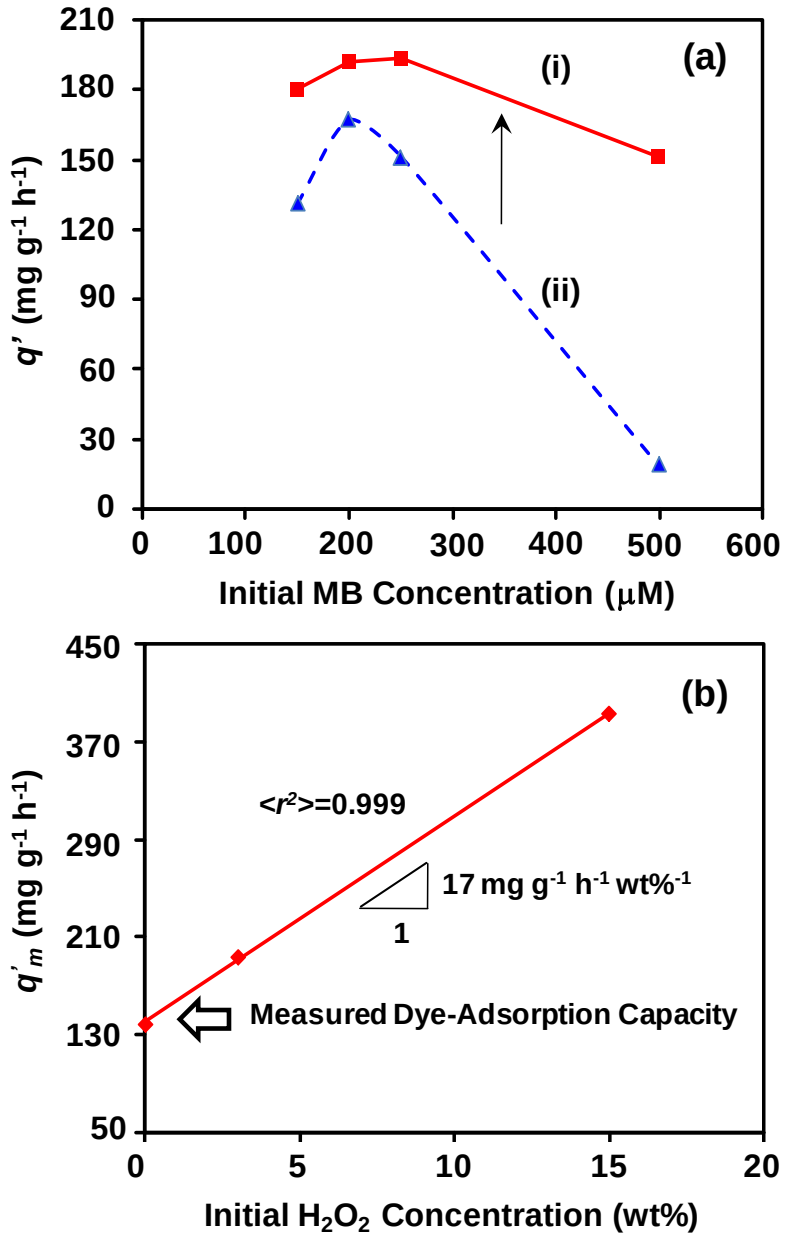

Fig. 4.28. (a) Variation in q' as a function of initial MB concentration as obtained for HP-HTN (i). For comparison, similar variation obtained for pure HTN (ii), as reported earlier elsewhere,[43] is also included. (b) The linear relationship between q'_m as a function of initial H_2O_2 concentration as obtained for HP-HTN.

The maximum dye-removal rate-capacity values of 139, 194, and 393 mg g^{-1} h^{-1} are, thus, obtained for HP-HTN at the initial H_2O_2 concentration of 0, 3, and 15 wt% respectively. (Note: since the dye-adsorption capacity of 139 mg g^{-1} is measured using the equilibrium

adsorption / desorption measurements conducted for 1 h, Figs. 4.20 and 4.21, it is reasonable to assume the value of dye-removal rate-capacity at the initial H_2O_2 concentration of zero is 139 mg g^{-1} h^{-1}). As seen in Fig. 4.28b, the variation in the obtained values of q'_m as a function of initial H_2O_2 concentration (within the range of 0-15 wt%) is a perfect straight line having the slope equal to 17 mg g^{-1} h^{-1} $wt\%^{-1}$ and $<r^2>$ value of 0.999. These values are closer to those (16 mg g^{-1} h^{-1} $wt\%^{-1}$ and 0.987) reported earlier for pure HTN by Jose et al..[43] Hence, the present analysis of the data obtained for HP-HTN strongly supports the method of prediction of dye-adsorption capacity of pure HTN using the one-step dye-removal method of chemically-activated catalytic process conducted in dark as reported earlier by Jose et al..[43]

To confirm the mechanism of MB dye-decomposition via chemical reactions presented in the Eqs. (4.7)-(4.9), $O_2^{\bullet-}$ trapping experiments are conducted. The qualitative variation in the concentration of $O_2^{\bullet-}$ produced after 5 min of contact time in 3 and 15 wt% H_2O_2 solution are presented and compared in Fig. 4.29a and b for HP-HTN and pure HTN respectively. The broad PL peaks located within the wavelength range of 426-473 nm confirm the generation of $O_2^{\bullet-}$ via activation of H_2O_2 using HP-HTN and pure HTN and further justify the mechanism of MB degradation via reactions presented in the Eqs. (4.7)-(4.9). As observed in Fig. 4.29a, the concentration of $O_2^{\bullet-}$ produced by HP-HTN in 15 wt% H_2O_2 solution is higher than that produced in 3 wt% H_2O_2 solution which strongly supports the enhanced value of q'_m under the former test condition as seen in Figs. 4.27 (inset) and 4.28b.

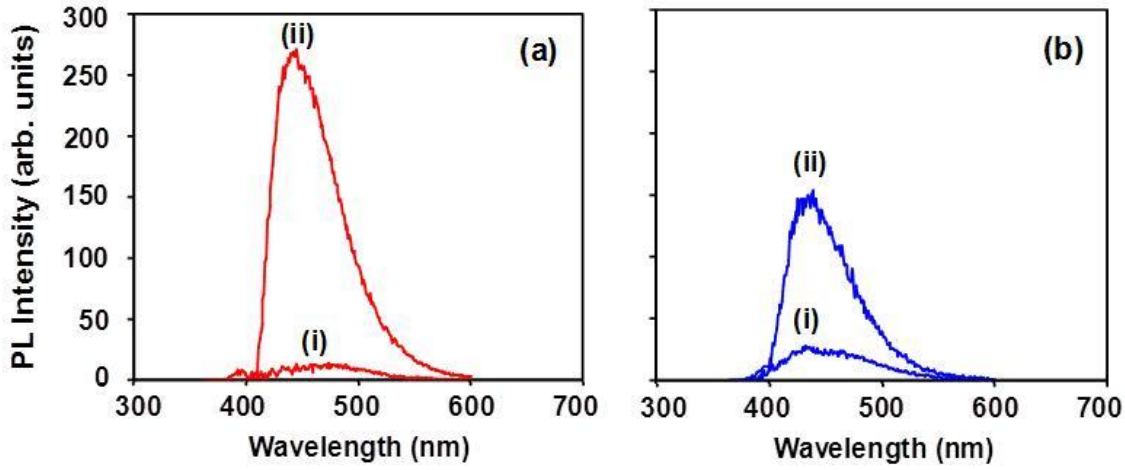

Fig. 4.29. Variation in the PL intensity as a function of wavelength associated with the formation of 3-aminophthalate obtained using HP-HTN (a) and pure HTN (b) in an aqueous solution containing 3 (i) and 15 wt% (ii) H_2O_2 after the constant contact time of 5 min. The excitation wavelength is 350 nm.

As noted in Fig. 4.29b, pure HTN also exhibits higher concentration of $O_2^{\bullet-}$ produced in 15 wt% H_2O_2 solution than that produced in 3 wt% H_2O_2 solution which also supports the enhanced value of q'_m under the former test condition as reported earlier in our previous investigation.[43] Moreover, the comparison of Fig. 4.29(a) and (b) shows that the concentration of $O_2^{\bullet-}$ produced in 15 wt% H_2O_2 solution by HP-HTN is higher than that produced by pure HTN which is attributed to the relatively larger concentration of $O_2^{\bullet-}$ already adsorbed on the surface of HP-HTN relative to that adsorbed on the surface of pure HTN which is the result of the chemical reaction presented in the Eq. (4.1) and their higher specific surface-area, Table 4.1, which may favor the chemical reactions presented in the Eqs. (4.7) and (4.8). This also justifies higher q'_m value observed for HP-HTN (393 mg g^{-1} h^{-1}) than that (312 mg g^{-1} h^{-1}) reported earlier for pure HTN in 15 wt% H_2O_2 solution.[43] Higher q'_m value is also observed for HP-HTN (194 mg g^{-1} h^{-1}) than that (167 mg g^{-1} h^{-1}) reported earlier for pure HTN in 3 wt% H_2O_2 solution.[43] However, this difference cannot be satisfactorily explained based on the difference the concentration of

$O_2^{\bullet-}$ produced by HP-HTN and HTN in 3 wt% H_2O_2 solution, Fig. 4.29. This strongly suggests that some other parameter plays a significant role in enhancing the q'_m value for HP-HTN relative to that of pure HTN in 3 wt% H_2O_2 solution. It appears that it is the higher MB dye-adsorption capacity of HP-HTN than that of pure HTN which has its own contribution in enhancing q'_m value for the former typically in 3 wt% H_2O_2 solution. As a result, the difference in both the MB dye-adsorption capacity and the concentration of $O_2^{\bullet-}$ produced are the dominating factors for the observed difference in q'_m values of HP-HTN and pure HTN typically at relatively higher (15 wt%) initial H_2O_2 concentration. However, for the lower initial H_2O_2 concentration (3 wt%), the difference in q'_m values is determined primarily by the difference in MB dye-adsorption capacity only.

4.4. Conclusions

Pure and HPO_4^{2-} anions modified HTN have been successfully synthesized via hydrothermal treatment of pure sol-gel derived nanocrystalline anatase-titania and TiP_2O_7/ PO_4^{3-} ions modified nanocrystalline anatase-titania respectively. HP-HTN exhibits higher MB adsorption capacity (139 mg g^{-1}) than that of pure HTN (105-121 mg g^{-1}). It is observed that HP-HTN exhibit higher dye-decomposition rate-capacity compared with that of pure-HTN. For HP-HTN, the maximum MB dye-removal rate-capacity of 194 and 393 mg g^{-1} h^{-1} has been determined at the initial H_2O_2 concentration of 3 and 15 wt%. A new method for predicting the adsorption capacity via one-step dye-removal method of chemically-activated catalytic process conducted in the dark has been demonstrated for pure HTN. The validity of new method for predicting the adsorption capacity is confirmed by applying it to HP-HTN.

References

(1) Ohtani, B. *J.Photochem. Photobiol. C* **2010**, *11*, 157.

(2) Kumar, S. G.; Devi, L. G. *J. Phys. Chem. A* **2011**, *115*, 13211.

(3) Gupta, V. *J. Environ. Manage.* **2009**, *90*, 2313.

(4) Crini, G. *Bioresour. Technol.* **2006**, *97*, 1061.

(5) Rafatullah, M.; Sulaiman, O.; Hashim, R.; Ahmad, A. *J. Hazard. Mater.* **2010**, *177*, 70.

(6) Kasuga, T.; Hiramatsu, M.; Hoson, A.; Sekino, T.; Niihara, K. *Adv. Mater.* **1999**, *11*, 1307.

(7) Lee, C.-K.; Liu, S.-S.; Juang, L.-C.; Wang, C.-C.; Lyu, M.-D.; Hung, S.-H. *J. Hazard. Mater.* **2007**, *148*, 756.

(8) Baiju, K. V.; Shukla, S.; Biju, S.; Reddy, M. L. P.; Warrier, K. G. K. *Mater. Lett.* **2009**, *63*, 923.

(9) Harsha, N.; Krishna, K. S.; Renuka, N. K.; Shukla, S. *RSC Adv.* **2015**, *5*, 30354.

(10) Bavykin, D. V.; Walsh, F. C. Eur. *J. Inorg. Chem.* **2009**, *2009*, 977.

(11) Tan, A.; Pingguan-Murphy, B.; Ahmad, R.; Akbar, S. *Ceram. Int.* **2012**, *38*, 4421.

(12) Lee, K.; Mazare, A.; Schmuki, P. *Chem. Rev.* **2014**, *114*, 9385.

(13) Ou, H.-H.; Lo, S.-L. *Sep. Purif. Technol.* **2007**, *58*, 179.

(14) Wong, C. L.; Tan, Y. N.; Mohamed, A. R. *J. Environ. Manage.* **2011**, *92*, 1669.

(15) Jang, J. S.; Choi, S. H.; Kim, D. H.; Jang, J. W.; Lee, K. S.; Lee, J. S. *J. Phys. Chem. C* **2009**, *113*, 8990.

(16) Thorne, A.; Kruth, A.; Tunstall, D.; Irvine, J. T.; Zhou, W. *J. Phys. Chem. B* **2005**, *109*, 5439.

(17) Chang, Z.; Liu, J.; Sun, X.; Liu, *J. Front. Chem. China* **2010**, *5*, 71.

(18) Sikhwivhilu, L. M.; Mpelane, S.; Mwakikunga, B. W.; Sinha Ray, S. *ACS Appl. Mater. Interfaces* **2012**, *4*, 1656.

(19) Babitha, K.B.; Warrier, K. G.; Shukla, S. *Adv. Sci. Eng. Med.* **2014**, *6*, 173.

(20) Baiju, K.; Shukla, S.; Sandhya, K.; James, J.; Warrier, K. *J. Phys. Chem. C* **2007**, *111*, 7612.

(21) Priya, R.; Baiju, K.; Shukla, S.; Biju, S.; Reddy, M.; Patil, K.; Warrier, K. *Catal. Lett.* **2009**, *128*, 137.

(22) Baiju, K.; Shukla, S.; Sandhya, K.; James, J.; Warrier, K. *J. Sol-Gel Sci. Technol.* **2008**, *45*, 165.

(23) Chatterjee, D.; Mahata, A. *J. Photochem. Photobiol. A* **2004**, *165*, 19.

(24) Nosaka, Y.; Yamashita, Y.; Fukuyama, H. *J. Phys. Chem. B* **1997**, *101*, 5822.

(25) Mao, Y.; Kanungo, M.; Hemraj-Benny, T.; Wong, S. S. *J. Phys. Chem. B* **2006**, *110*, 702.

(26) Priya, R.; Baiju, K.; Shukla, S.; Biju, S.; Reddy, M.; Patil, K.; Warrier, K. *J. Phys. Chem. C* **2009**, *113*, 6243.

(27) Chen, Q.; Du, G.; Zhang, S.; Peng, L.-M. *Acta Cryst. B* **2002**, *58*, 587.

(28) *Wu, D.; Liu, J.; Zhao, X.; Li, A.; Chen, Y.; Ming, N. Chem. Mater.* ***2006****, 18, 547.*

(29) Du, W. L.; Xu, Z. R.; Han, X. Y.; Xu, Y. L.; Miao, Z. G. *J. Hazard. Mater.* **2008**, *153*, 152.

(30) Narayani, H.; Kunniveetil, S. P.; Shukla, S. *Adv. Sci. Eng. Med.* **2013**, *5*, 63.

(31) An, Y.; Li, Z.; Wang, D.; Shen, *Phys. Status Solidi B* **2013**, *250*, 1592.

(32) Bavykin, D. V.; Parmon, V. N.; Lapkin, A. A.; Walsh, F. C. *J. Mater. Chem.* **2004**, *14*, 3370.

(33) Cao, G.; Li, H.; Zhang, X. *Micro Nano Lett.* **2011**, *6*, 98.

(34) Cesano, F.; Bertarione, S.; Uddin, M. J.; Agostini, G.; Scarano, D.; Zecchina, A.

J. Phys. Chem. C **2009**, *114*, 169.

(35) Ma, R.; Bando, Y.; Sasaki, T. Chem. *Phys. Lett.* **2003**, *380*, 577.

(36) Wu, F.; Wang, Z.; Li, X.; Guo, H. *J. Mater. Chem.* **2011**, *21*, 12675.

(37) Zhang, M.; Jin, Z.; Zhang, J.; Guo, X.; Yang, J.; Li, W.; Wang, X.; Zhang, Z. *J. Mol. Catal. A* **2004**, *217*, 203.

(38) Zhang, S.; Li, W.; Jin, Z.; Yang, J.; Zhang, J.; Du, Z.; Zhang, Z. *J. Solid State Chem.* **2004**, *177*, 1365.

(39) Guo, G.-S.; He, C.-N.; Wang, Z.-H.; Gu, F.-B.; Han, D.-M. *Talanta* **2007**, *72*, 1687.

(40) Chen, Q.; Zhou, W.; Du, G.; Peng, L.-M. *Adv. Mater.* **2002**, *14*, 1208.

(41) Tsai, C.-C.; Teng, H. *Chem. Mater.* **2006**, *18*, 367.

(42) Nakahira, A.; Kubo, T.; Numako, C. *Inorg. Chem.* **2010**, *49*, 5845.

(43) Jose, M.; Haridas, M. P.; Shukla, S. *J. Environ. Chem. Eng.* **2014**, *2*, 1980.

(44) Lapina, A.; Chatzichristodoulou, C.; Hallinder, J.; Holtappels, P.; Mogensen, M. *J. Solid State Electrochem.* **2014**, *18*, 39.

(45) Körösi, L.; Papp, S.; Bertóti, I.; Dékány, I. *Chem. Mater.* **2007**, *19*, 4811.

(46) Norberg, S. T.; Svensson, G.; Albertsson, *J. Acta Cryst. C* **2001**, *57*, 225.

(47) Yu, H.-F. *J. Phys. Chem. Solids* **2007**, *68*, 600.

(48) Li, F.; Jiang, Y.; Xia, M.; Sun, M.; Xue, B.; Liu, D.; Zhang, X. *J. Phys. Chem. C* **2009**, *113*, 18134.

(49) Jose, M.; Narayani, H.; Kumar, J.; Shukla, S. *Sci. Adv. Mater.* **2015**, *7*, 729.

(50) Lipinska-Kalita, K.; Kruger, M.; Carlson, S.; Andersen, A. K. *Physica B* **2003**, *337*, 221.

(51) Kuo, C.-Y.; Wu, C.-H.; Wu, J.-T.; Chen, Y.-R. *Reac. Kinet. Mech. Cat.* **2015**, *114*, 753.

(52) Liang, W.-J.; Hsieh, S.-J.; Hsu, C.-Y.; Chen, W.-F.; Kuo, P.-L. *J. Polym. Sci. Part B: Polym. Phys.* **2006**, *44*, 2135.

(53) Sing, K.S.W.; Everett, D.H.; Haul, R.; Moscou, L.; Pierotti, R.A.; Rouquerol, J.; Siemieniewska, T. *Pure Appl. Chem.* **1982**, *54*, 2201.

(54) Hsieh, C.-T.; Fan, W.-S.; Chen, W.-Y.; Lin, J.-Y. *Sep. Purif. Technol.* **2009**, *67*, 312.

(55) Yu, J.; Yu, H.; Cheng, B.; Trapalis, C. *J. Mol. Catal. A* **2006**, *249*, 135.

(56) Chang, F.; Wang, G.; Xie, Y.; Zhang, M.; Zhang, J.; Yang, H.-J.; Hu, X. *Ceram. Int.* **2013**, *39*, 3823.

(57) Yu, J.; Wang, W.; Cheng, B.; Su, B.-L. *J. Phys. Chem. C* **2009**, *113*, 6743.

(58) Lim, S. H.; Luo, J.; Zhong, Z.; Ji, W.; Lin, *J. Inorg. Chem.***2005**, *44*, 4124.

(59) Kubo, T.; Nakahira, A. *J. Phys. Chem. C* **2008**, *112*, 1658.

(60) Asapu, R.; Palla, V. M.; Wang, B.; Guo, Z.; Sadu, R.; Chen, D. H. *J. Photochem. Photobiol. A* **2011**, *225*, 81.

(61) Lin, L.; Lin, W.; Xie, J.; Zhu, Y.; Zhao, B.; Xie, Y. *Appl. Catal. B* **2007**, *75*, 52.

(62) Yu, J. C.; Zhang, L.; Zheng, Z.; Zhao, J. *Chem. Mater.* **2003**, *15*, 2280.

(63) Gopal, N. O.; Lo, H.-H.; Ke, T.-F.; Lee, C.-H.; Chou, C.-C.; Wu, J.-D.; Sheu, S.-C.; Ke, S.-C. *J. Phys. Chem. C* **2012**, *116*, 16191.

(64) Neville, E. M.; MacElroy, J. D.; Thampi, K. R.; Sullivan, J. A. J. Photochem. Photobiol. A **2013**, *267*, 17.

(65) Bokare, A. D.; Choi, W. *J. Hazard. Mater.* **2014**, *275*, 121.

(66) Inchaurrondo, N.; Massa, P.; Fenoglio, R.; Font, J.; Haure, P. *Chem. Eng. J.* **2012**, *198*, 426.

(67) Liu, W.; Andrews, S. A.; Stefan, M. I.; Bolton, J. R. *Water Res.* **2003**, *37*, 3697.

(68) Lee, C.-K.; Lin, K.-S.; Wu, C.-F.; Lyu, M.-D.; Lo, C.-C. *J. Hazard. Mater.* **2008**, *150*, 494.

(69) Erdem, E.; Karapinar, N.; Donat, R. *J. Colloid Interface Sci.* **2004**, *280*, 309.

(70) Wang, S.; Boyjoo, Y.; Choueib, A.; Zhu, Z. *Water Res.* **2005**, *39*, 129.

(71) Xiong, L.; Yang, Y.; Mai, J.; Sun, W.; Zhang, C.; Wei, D.; Chen, Q.; Ni, J. *Chem. Eng. J.* **2010**, *156*, 313.

(72) Matheswaran, M.; Karunanithi, T. *J. Hazard. Mater.* **2007**, *145*, 154.

(73) Eren, Z.; Acar, F. N. *J. Hazard. Mater.* **2007**, *143*, 226.

(74) Kumar, K. V.; Ramamurthi, V.; Sivanesan, S. *J. Colloid Interface Sci.* **2005**, *284*, 14.

(75) Pelekani, C.; Snoeyink, V. L. *Carbon* **2000**, *38*, 1423.

(76) Bavykin, D. V.; Redmond, K. E.; Nias, B. P.; Kulak, A. N.; Walsh, F. C. *Aust. J. Chem.* **2010**, *63*, 270.

(77) Kim, S.; Kim, M.; Hwang, S.-H.; Lim, S. K. *Appl. Catal. B* **2012**, *123*, 391.

(78) Padinhattayil, H.; Augustine, R.; Shukla, S. *J. Nanosci. Nanotechnol* **2013**, *13*, 3035.

(79) Jose, M.; Kumari, M.; Karunakaran, R.; Shukla, S. *J Sol-Gel Sci. Technol.* **2015**, *75*, 541.

(80) Shukla, S.; Oturan, M. A. *Environ. Chem. Lett.* **2015**, *13*, 157.

(81) Lorençon, E.; Brandão, F. D.; Krambrock, K.; Alves, D. C.; Silva, J. C.; Ferlauto, A. S.; Lago, R. M. *J. Mol. Catal. A* **2014**, *394*, 316.

Chapter 5

Ion-Exchange Bonded $H_2Ti_3O_7$ Nanosheets-Based Magnetic Nanocomposite for Dye Removal via Adsorption and Its Regeneration via Synergistic Activation of Persulfate

Graphical Abstract

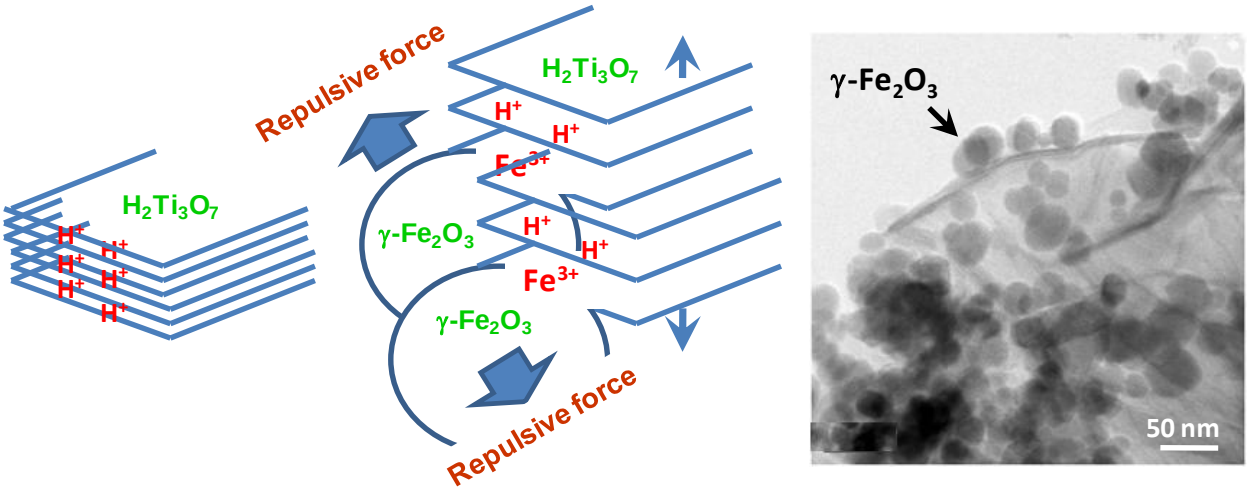

Highlights

- HTNSF magnetic nanocomposites are synthesized with varying weight-fraction of γ-Fe_2O_3 nanoparticles (5-25 wt%).
- A new model has been proposed to explain the formation mechanism of HTNSF magnetic nanocomposite.
- Dye-adsorption properties of HTNSF magnetic nanocomposites have been investigated using the cationic MB dye.
- Regeneration and reuse of HTNSF magnetic nanocomposites is demonstrated via synergistic activation of $S_2O_8^{2-}$ in aqueous solution.

Abstract

The magnetic nanocomposites (HTNSF) consisting of HTNS and maghemite (γ-Fe_2O_3) nanoparticles with varying weight-fraction (5-25 wt%) of latter have been successfully synthesized by simple mechanical mixing of precursors in an aqueous solution having neutral solution-pH. A new model has been proposed to explain the typical attachment of γ-Fe_2O_3 nanoparticles to the edges of HTNS via an ion-exchange bond formation. The dye-adsorption properties of HTNSF magnetic nanocomposites have been investigated using the cationic MB dye. The new model satisfactorily explains a strong dependence of positive deviation (relative to the variation governed by the law-of-mixture) observed in the variation of dye-adsorption capacity on the similar variation observed in the pore volume of HTNSF magnetic nanocomposite as a function of weight-fraction of γ-Fe_2O_3 nanoparticles. The maximum MB adsorption capacity of 76 mg g^{-1} is exhibited by HTNSF-10 sample which is higher than that (67 mg g^{-1}) of HTNS sample. The MB adsorption on the surface of HTNSF magnetic nanocomposite follows pseudo-second-order kinetics and Langmuir and DKR isotherm models. The variation in the regression correlation coefficient ($<r^2>$) values as a function of initial MB concentration strongly supports the Azizian analysis. The HTNSF-5 magnetic nanocomposite which contains the lowest weight-fraction (5 wt%) of γ-Fe_2O_3 nanoparticles shows the effective magnetic separation from the aqueous solution in 5 min. The reuse of HTNSF-5 magnetic nanocomposite has been successfully achieved through its regeneration via the activation of $S_2O_8^{2-}$ in an aqueous solution involving the synergy effect in between thermal activation and that by the constituents of HTNSF-5 magnetic nanocomposite.

5.1. Introduction

Two dimensional hydrogen titanate nanosheets (HTNS) are of major significance as the result of their novel physicochemical properties, such as ultrathin thickness, large specific surface-area, and the quantum confinement effect resulting in their suitability in diverse applications including photonic structures, lithium ion batteries, photocatalysis, and catalysis.[1-13] Different research groups have synthesized HTNS with different chemical and crystal structures intended for the different applications. Gateshki et al.[1] first reported the preparation of hydrogen titanate ($H_{0.67}Ti_{1.83}O_4 \bullet H_2O$) nanosheets by exfoliation of $Cs_{0.67}Ti_{1.83}O_4 \bullet H_2O$ through intercalation of tetrabutylammonium (TBA). Wu and Xu et al.[2] synthesized hydrogen titanate nanosheets via hydrothermal treatment of anatase-TiO_2 under highly alkaline conditions followed by washing of hydrothermal product using HCl typically under the supersonic irradiation condition. These nanosheets were subsequently used for deriving the nanosheets of monoclinic TiO_2. Takezawa and Imai[3] described a new bottom-up route for the preparation of layered hydrogen titanate ($H_2Ti_3O_7$) nanosheets using agar gel containing a titanium precursor and ammonium ions. Antonello et al.[4] synthesized titanate nanosheets using the titanium(IV) iso-propoxide ($Ti(OC_3H_7)_4$) precursor under the reflux and vacuum conditions. The method was claimed as a novel strategy in the fabrication of optically active photonic structures. Zhao et al.,[5] Lin et al.,[6] Wu et al.,[7] and Sutradhar et al.[8] synthesized organic-stabilizer free layered protonic $H_2Ti_2O_5 \cdot H_2O$ nanosheets via hydrothermal treatment and utilized them for the removal of Pb^{2+} cations and ciprofloxacin (CIP) from the aqueous solutions. Wang et al.[9] reported the synthesis of $H_2Ti_3O_7$ nanosheets on Ti foil via hydrothermal method and topotactically transformed them to a novel anatase/TiO_2(B) heterostructured nanosheet array which exhibited superior photocatalytic activity in the removal of Rhodamine B (RhB) dye from aqueous solution. Hareesh et al.[10] processed flyash

stabilized $H_2Ti_3O_7$ nanosheets via hydrothermal method for the removal of MB dye from an aqueous solution via adsorption mechanism. Luan and Wang[11] synthesized $H_2Ti_3O_7$ nanosheets by exfoliation of a layered precursor via interacting TBA cations, followed by ion-exchange with Na^+ ions and washing with water. 2D graphene/hydrogen titanate hybrid nanosheets were fabricated for application as anode materials in lithium-ion batteries. Zhou et al.[12] synthesized hydrogen titanate nanosheets by the soft-chemical delamination of layered protonic titanates (LPT) using ethylamine and used them as non-light driven catalyst for the degradation of RhB dye via H_2O_2 activation. Kim et al.[13] synthesized (3-aminopropyl)triethoxysilane (APTES) anchored $H_{0.67}Ti_{1.83}O_4 \bullet H_2O$ nanosheets as a stable nanocontainer for DNA.

It appears that there are only few reports available in the literature which have attempted to use HTNS for the removal of synthetic-dyes from the aqueous solutions either via adsorption or photocatalysis mechanism.[9-10,12] Surprisingly, all of the layered titanate nanosheets utilized for various applications (including the dye-removal) are non-magnetic in nature. No attempt has been made to convert the non-magnetic titanate nanosheets to magnetic nanosheets for any of the above applications. It is realized that, in the dye-removal application, the magnetic nanocomposites provide ease of solid-liquid separation via the use of an external magnetic field which offer large benefits over the several issues associated with the separation of non-magnetic counterparts.[14] In view of this, the first major objective of this investigation has been set to synthesize, for the first time, the magnetic nanocomposites (HTNSF) based on the HTNS and γ-Fe_2O_3 nanoparticles via a novel ion-exchange mechanism.[15] The second major objective has been set to use this magnetic nanocomposite, for the first time, for the removal of cationic MB dye from the aqueous solutions via adsorption mechanism and investigate the effect of weight-fraction of γ-Fe_2O_3 on the variation in the MB adsorption capacity of

magnetic nanocomposite. MB dye has been utilized for different industrial applications such as the medical photodynamical therapy, chromoendoscopy, textile industries, analytical chemistry, and sensitizer in the solar energy conversion.[16] All these applications, however, generate MB-charged effluents that may have carcinogenic and mutagenic properties towards the aquatic organisms. This is a serious cause of risk to the human life and eco-environment. Hence, the development of novel technology for the effective removal of MB dye from the aqueous solutions is of significance. The third major objective of present investigation has been set to demonstrate, for the first time, the magnetic separation of HTNSF nanocomposite using an external magnetic field followed by its regeneration and reuse via the non-light driven synergistic activation of persulfate.[16]

It is to be noted that in comparison with the conventional dye-removal technologies such as the photocatalysis[9] and electro-chemical oxidation,[17] the proposed dye-removal technology can be conducted in the dark without the use of any external radiation (such as the UV, solar, visible, and infrared) and power sources (such as the voltage, sonicator, and microwave generator) which is suggests considerable cost-saving in the dye-removal process. Moreover, further cost saving is achievable by the successful regeneration of catalyst via the activation of cheaper persulfate than that of costlier H_2O_2.

5.2. Experimental

5.2.1. Synthesis of HTNS

The spherical flyash (FA) particles (1-5 μM in size) were obtained from the National Thermal Power Corporation (NTPC), Ramagundam, India. The as-received FA particles were first surface-coated with anatase-TiO_2 via sol-gel method. For this, 5 g of as-received FA particles were suspended under the continuous stirring, using an overhead

stirrer (IKA Eurostar Digital, Germany), in 125 ml solution of 0.1 M (final concentration) $Ti(OC_3H_7)_4$, (98%, Sigma-Aldrich, India) dissolved completely in 2-propanol (>99.5%, Sigma-Aldrich, India). To this suspension, a clear solution of distilled water dissolved in 125 ml of 2-propanol was added dropwise under the continuous stirring. The *R*-value of 5 (defined as the ratio of molar concentration of water to that of $Ti(OC_3H_7)_4$ precursor) was selected for obtaining TiO_2-coating on the surface of FA particles via hydrolysis and condensation of precursor. The TiO_2-coated FA particles were separated from the solution using a centrifuge (R23, Remi Instruments Ltd., Mumbai, India) and dried in an oven at 80 ^oC overnight. The amorphous-TiO_2 coated FA particles were then calcined in a furnace at 600 ^oC for 2 h at the heating rate of 3 ^oC min^{-1} to obtain the anatase-TiO_2 coated FA particles. With this procedure, the FA-anatase-TiO_2 composite particles containing ~30 wt% anatase-TiO_2 was obtained.

5 g of anatase-TiO_2 coated FA particles were treated hydrothermally to obtain HTNS. The detailed procedure for hydrothermal processing is described in third chapter (section 3.2.3.).

5.2.2. Synthesis of HTNSF magnetic nanocomposites

The HTNSF magnetic nanocomposites having varying weight-fractions (5, 10, and 25 wt%) of γ-Fe_2O_3 nanoparticles (Aldrich Chemicals, Bengaluru, India) were synthesized via simple mechanical mixing involving an ion-exchange mechanism. In this method, appropriate quantities of γ-Fe_2O_3 nanoparticles and HTNS were dispersed separately in equal quantities of two different aqueous solutions at neutral solution-pH (~6.5) using an ultrasonication bath (Bandelin Sonorex Super with Built-In Heating, Aldrich Labware, Bengaluru, India). The two suspensions were then mixed to form total 1 g of solid particles suspended in 125 ml aqueous solution at neutral solution-pH which was stirred

vigorously using an overhead stirrer for 8 h at 600 rpm. The brownish product formed was separated using an external magnetic field provided by a small bar magnet and dried in an oven at 80 ^oC overnight to obtain HTNSF magnetic nanocomposites.

5.2.3. Characterization of HTNS and HTNSF magnetic nanocomposites

The morphology and average size of different samples were determined using TEM operated at 300 kV. (Note: the samples were ultrasonically dispersed in 30 ml acetone for 20 min in which the carbon-coated Cu-grid (Ted Pella, Inc., U.S.A.) of 3 mm diameter was dipped for the TEM sample preparation). The nanocrystalline nature of samples and different phases present were confirmed via obtaining the SAED patterns. The crystalline phases present were also determined using XRD. The broad-scan analysis was typically conducted within the 2θ range of 5-80^o using the Cu$K\alpha$ (λ_{Cu}=1.542 Å) X-radiation. The specific surface-area and pore-size distribution were measured using BET surface-area measurement technique via N_2 adsorption using the multi-point method after degassing the samples in flowing N_2 at 200 °C for 2 h. The magnetic properties of different samples were measured using a vibrating sample magnetometer (VSM) attached to a Physical Property Measurement System (PPMS, Quantum Design, Dynacool, U.S.A.). The pristine samples were subjected to different magnetic field strengths (H) and the induced magnetization (M) was measured at 298 K. The external magnetic field was reversed on saturation and the hysteresis loop was traced. The zeta potential measurements were performed using the electrophoretic light scattering in the pH range of 1-10. The band-gap energy (E_{BG}) measurements were conducted by obtaining the absorption spectra using the UV–visible spectrophotometer, operated in the DR mode, for the wavelengths within the range of 200–800 nm.

5.2.4. Dye-adsorption measurements using HTNS and HTNSF magnetic nanocomposites

The MB dye-adsorption experiments in the dark were carried out via the procedure already described in the third chapter (section 3.2.5).

5.2.5. Regeneration and reuse of HTNSF-5 magnetic nanocomposite in the dye-removal application

0.4 g l^{-1} of HTNSF-5 magnetic nanocomposite was added to 125 ml aqueous solution of MB dye having the initial concentration of 90 µM at the initial solution-pH of 10 under the ambient temperature (30 ^{o}C) condition. The dye-adsorption measurements were then conducted using procedure similar to the one described in the previous section. The HTNSF-5 sample with the surface-adsorbed MB dye, after separation from the aqueous solution using an external magnetic field provided by a small bar magnet and subsequent drying in an oven at 80 ^{o}C overnight, was utilized for the second-cycle of dye-adsorption measurement conducted under the similar test-conditions. Total three successive cycles of dye-adsorption measurements were conducted. The HTNSF-5 sample, with 107 mg g^{-1} of MB dye adsorbed on its surface, was utilized for the regeneration experiments. For this purpose, the former was added to 100 ml of 30 wt% H_2O_2 solution at room temperature (30 ^{o}C) and stirred continuously using an overhead stirrer for 3 h. The powder was separated from the aqueous solution using an external magnetic field provided by a small bar magnet, and after drying in an oven at 80 ^{o}C overnight, it was recycled for the fourth-cycle of dye-adsorption. Similar experiments were repeated for the demonstration of regeneration and reuse of HTNF-5 magnetic nanocomposite using the potassium persulfate (KPS, $K_2S_2O_8$, 99%, S.D. Fine-Chem Ltd., Mumbai, India) solution. The concentration of KPS solution used was changed to 0.1 M (~3 wt%).

The regeneration and reuse of HTNSF-5 magnetic nanocomposite using KPS solution was also demonstrated at higher temperature (75 ^oC) where five consecutive cycles of adsorption and reuse were conducted without and with the involvement of intermediate regeneration step. The experimental conditions used were, however, different than those used under the ambient temperature (30 ^oC) condition. In the present case, during the adsorption part of experiment, total volume of the solution, initial dye and catalyst concentrations were changed to 3 ml, 60 μM, and 1.2 g l^{-1} respectively. After the first cycle of MB adsorption conducted for the contact time of 1 h, a bar magnet was placed outside the container to attract the magnetic nanocomposite on its walls and the treated solution was decanted. The bar magnet was removed and fresh 10 ml distilled H_2O was poured into the container to collect the magnetic nanocomposite sticking on the walls of container. The aqueous suspension of magnetic nanocomposite was then dried in an oven at 80 ^oC overnight and dried sample was utilized for the second-cycle of dye-adsorption measurement conducted under the similar test-conditions. Total five successive cycles of dye-adsorption measurements were conducted without the use of any intermediate regeneration step. Later, dye-adsorption experiments were repeated with the involvement of regeneration step which was conducted after the end of each cycle of dye-adsorption. In this case, the dried HTNSF-5 magnetic nanocomposite with MB dye adsorbed on its surface was dispersed in 3 ml of 2 mM (0.06 wt%) KPS solution (obtained via dilution method) maintained at 75 ^oC and stirred using an overhead stirrer for 1 h. The regenerated catalyst was separated from the aqueous solution using an external magnetic field provided by a small bar magnet; and after drying in an oven at 80 ^oC overnight, it was reused for the next-cycle of dye-adsorption. Total five successive cycles of adsorption were conducted with the involvement of intermediate regeneration step.

5.2.6. Trapping of free $^{\bullet}OH$

125 ml aqueous solution (or suspension) was prepared by completely dissolving 5×10^{-4} M of TA (98%) and 2×10^{-3} M of NaOH without and with suspending 0.4 g l^{-1} of HTNSF-5 magnetic nanocomposite. This was followed by the addition of 0.1 M (~3 wt%) of KPS under continuous overhead stirring at room temperature (30 ^{o}C) and 4 ml sample suspension was separated after each 20 min time interval for total 60 min. The catalyst powder was separated using a bar magnet and the filtrate was then utilized for obtaining the PL spectra. The trapping of free $^{\bullet}OH$ by TA results in the formation of 2-hydroxyterephthalic acid which exhibits a characteristic PL peak located at ~425 nm at an excitation wavelength of ~315 nm. The intensity of PL peak is regarded as a measure of the amount of free $^{\bullet}OH$, and hence, that of the $SO_4^{\bullet-}$ produced at a given time due to the activation of $S_2O_8^{2-}$. The intensity of PL peak from the solution, obtained without the addition of KPS, is regarded as a reference peak (that is, time t=0 min).

5.3. Results and discussions

5.3.1. Characteristics of HTNS and HTNSF magnetic nanocomposites

The TEM images of as-received magnetic nanoparticles at different magnifications are provided in Fig. 5.1. It is noted that the as-received magnetic nanoparticles are aggregated with the non-spherical aggregate size of 200-300 nm, Fig. 5.1a, and the nanocrystallite size in the range of 15-40 nm, Fig. 5.1b. The non-spherical aggregates with fine intra-aggregate porosity are further observed to form bigger agglomerates having relatively larger inter-aggregate pore size (100-300 nm). The continuous rings observed in the SAED pattern, Fig. 5.1c, confirm the nanocrystalline nature of as-received magnetic particles. Moreover, the obtained SAED pattern is very similar to that reported by Morjan et al.[18] and is indexed according to the face centered cubic (FCC)

structure of γ-Fe_2O_3 phase which is also in accordance with the XRD results obtained here.

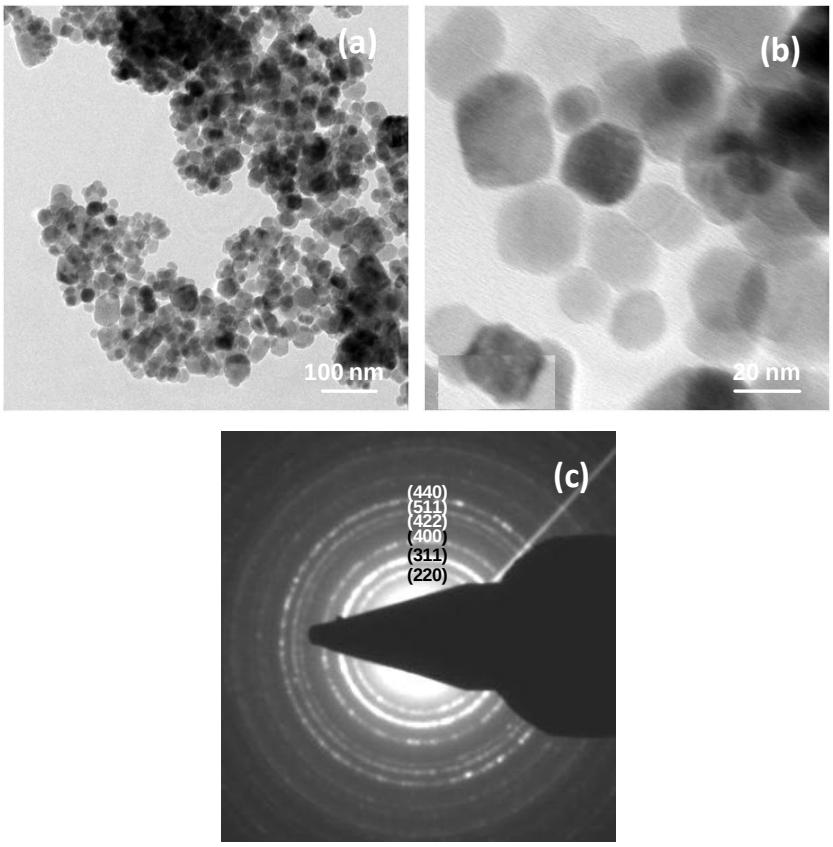

Fig. 5.1. TEM images of as-received γ-Fe_2O_3 nanoparticles at lower (a) and higher (b) magnifications. The corresponding SAED pattern is shown in (c).

The TEM images of HTNS and HTNSF magnetic nanocomposites are presented at lower and higher magnifications in Fig. 5.2 and Fig. 5.3 respectively. The corresponding SAED patterns are shown as an inset in the upper-left corners, Fig. 5.2.

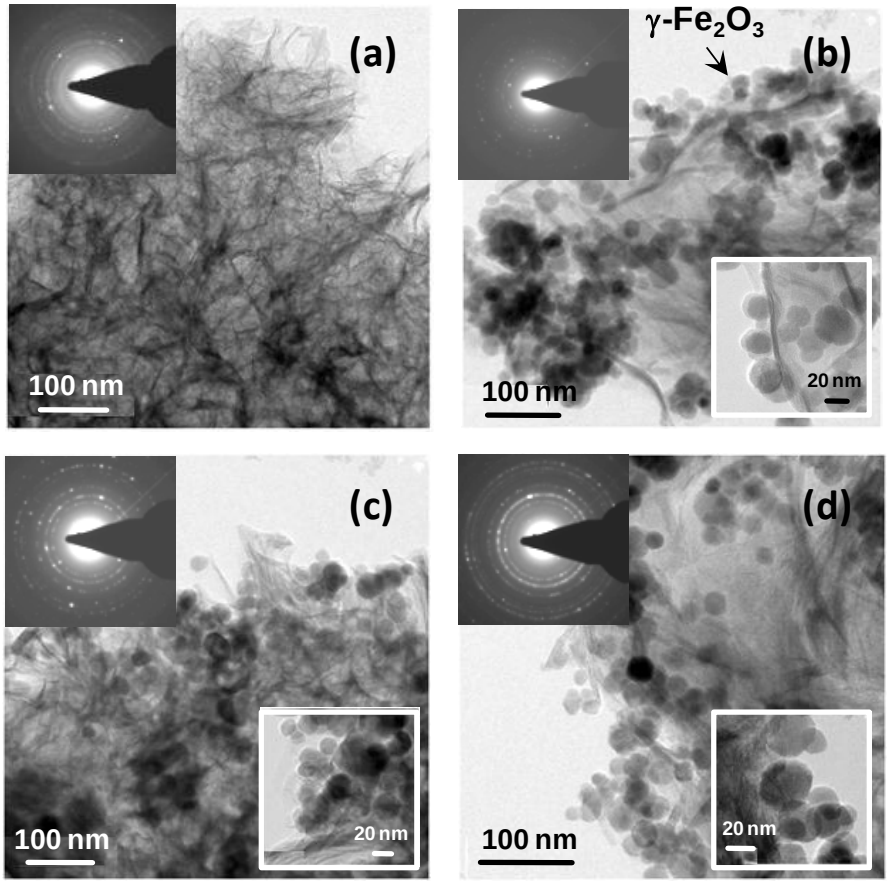

Fig. 5.2. TEM images of HTNS (a), HTNSF-5 (b), HTNSF-10 (c), and HTNSF-25 (d) magnetic nanocomposites. The insets in the upper-left and lower-right corners show the corresponding SAED patterns and the attachment of γ-Fe_2O_3 nanoparticles at the edges of nanosheets respectively.

The HTNS sample, Figs. 5.2a and 5.3a, clearly shows highly aggregated curled nanosheets having the average thickness of 5 nm. Surprisingly, two diffused concentric rings normally observed in the SAED pattern of hydrogen titanate which are indexed according to either monoclinic $H_2Ti_3O_7$ or orthorhombic protonic lepidocrocite titanate ($H_xTi_{2-x/4}\square_{x/4}O_4$, where x~0.7 and $\square$ is a vacancy),[19-20] are not observed in the SAED pattern presented in Fig. 5.2a. This is also consistent with the previous analysis reported by Hareesh et al..[10] The SAED pattern instead consists of large number (> 2) of closely spaced concentric rings which suggests the presence of unknown nanocrystalline phase in

addition to that of hydrogen titanate phase. Interestingly, the SAED patterns presented in Fig. 5.2b-d (see the insets in upper-left corners) also contain number of closely spaced concentric rings; however, they resemble that of γ-Fe_2O_3, Fig. 5.1c, instead of those of hydrogen titanate. This is a result of the formation of HTNSF magnetic nanocomposites consisting of hydrogen titanate having lower crystallinity and varying weight-fraction of highly crystalline γ-Fe_2O_3. Due to difference in the crystallinity of two phases, the HTNSF magnetic nanocomposites exhibit SAED pattern corresponding to that of γ-Fe_2O_3.

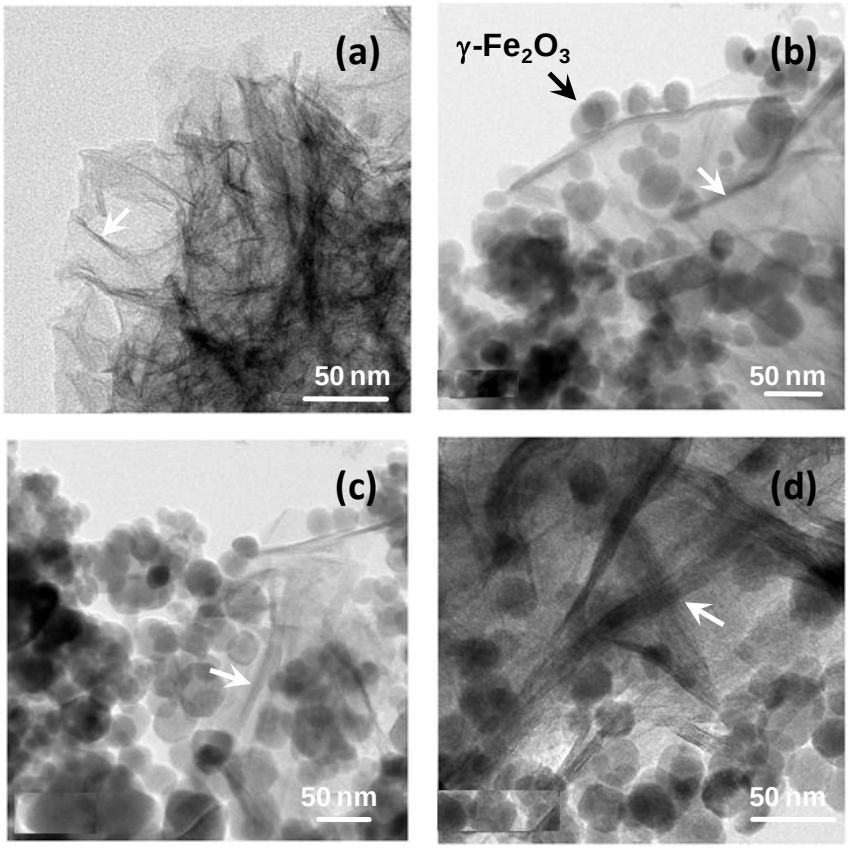

Fig. 5.3. High magnification TEM images of HTNS (a), HTNSF-5 (b), HTNSF-10 (c), and HTNSF-25 (d) magnetic nanocomposites. The white arrows indicate the thickness of stacked nanosheets within the aggregates.

As demonstrated in Fig. 5.3, the average thickness of curled aggregated nanosheets is noted to increase from 5 nm to 23 nm with the increasing weight-fraction of γ-Fe_2O_3 from 0 to 25 wt%. This possibly suggests that spacing between the stacked nanosheets within the aggregates increases with the weight-fraction of γ-Fe_2O_3 which is reflected in an increase in the average thickness of nanosheets. As demonstrated in the lower-right corner insets of Figs. 5.2b-d (and also in Fig. 5.3b-d), the magnetic γ-Fe_2O_3 nanoparticles are typically seen to be attached to the edges of nanosheets rather than on their surfaces.

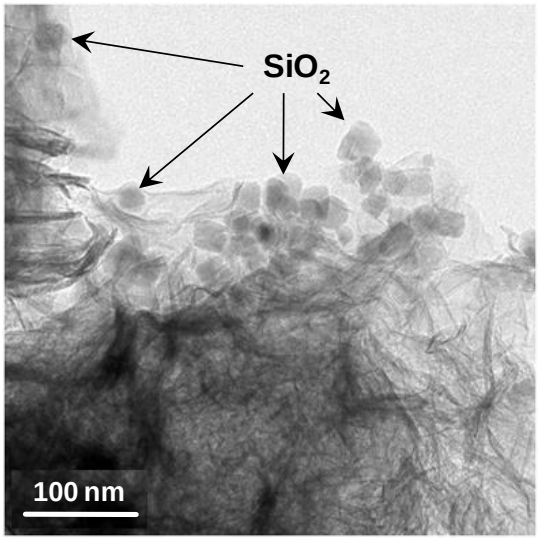

Fig. 5.4. TEM image showing attachment of SiO_2 nanoparticles at the edges of HTNS.

As shown in Fig. 5.4, the nanoparticles are also seen to be attached to the edges of HTNS which do not belong to those of γ-Fe_2O_3. However, in the latter case, these appear to be quartz (SiO_2) nanoparticles as per the EDX spectrum presented in Fig. 5.5a. The latter confirms the presence of Si in the HTNS in exceptionally large amount; while, all HTNSF magnetic nanocomposites, Figs. 5.5b-d show the presence of larger amount of Fe relative to that of Si in agreement with the TEM and SAED analyses. This also suggests that the SAED pattern presented in Fig. 5.2a predominantly belongs to that of SiO_2 nanoparticles rather than that of γ-Fe_2O_3 or hydrogen titanate. Moreover, the intense Si

peak as noted in Fig. 5.5a is also possibly contributed by the adsorption of silicate ions (SiO_4^{4-}) on the surface of HTNS. The attachment of SiO_2 nanoparticles to the edges of nanosheets of hydrogen titanate and the presence of SiO_4^{4-} ions on their surfaces are ascribed to the mechanism of formation of nanosheets during hydrothermal treatment of TiO_2-coated flyash particles and the subsequent washing of hydrothermal product as proposed earlier by Hareesh et al..[10]

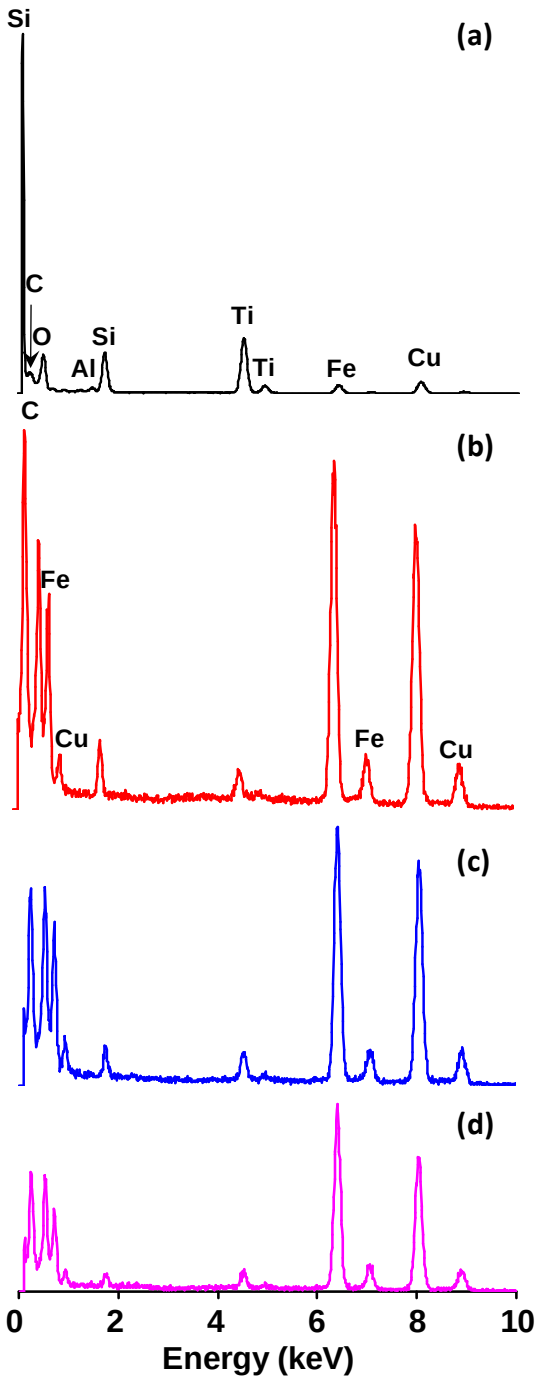

Fig. 5.5. EDX analyses of HTNS (a), HTNSF-5 (b), HTNSF-10 (c), and HTNSF-25 (d) magnetic nanocomposites. The Cu peak originates from the grid used for TEM analysis.

The powder XRD patterns of different samples are presented in Figs. 5.6 and 5.7; while, all identified phases, diffracting angles and planes, and the corresponding JCPDS card numbers are tabulated in the Table 5.1. It is noted that the as-received flyash particles

consists of SiO_2, mullite ($Al_6Si_2O_{13}$), and hematite (α-Fe_2O_3) having the weight-fraction of 69, 20, and 11 wt% respectively.

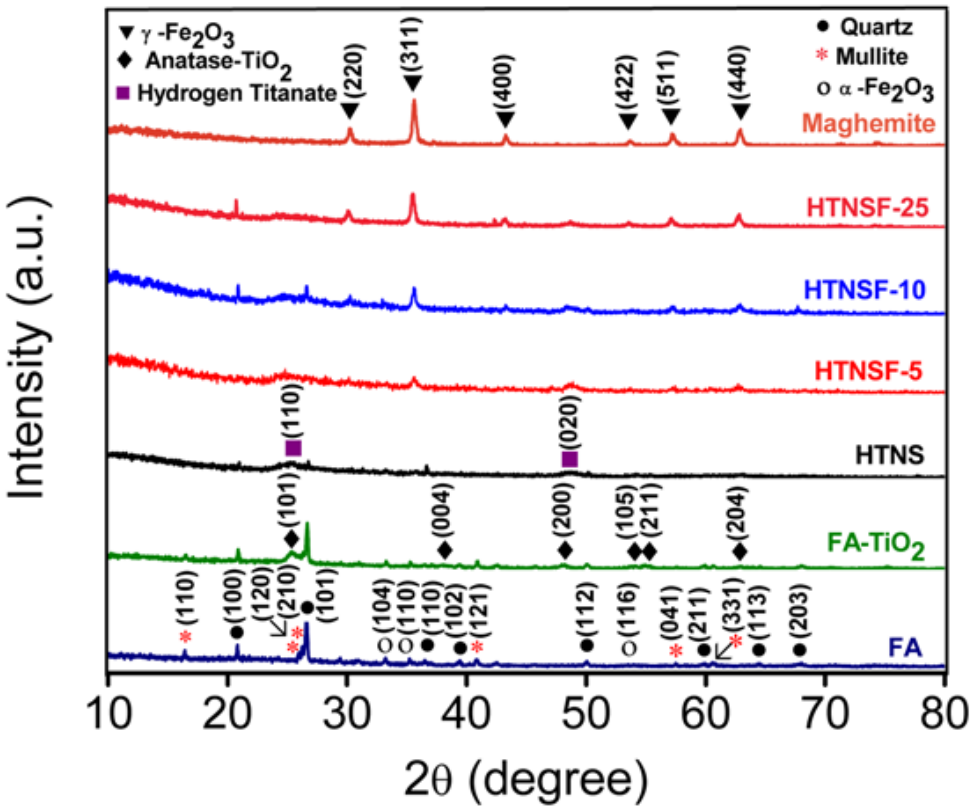

Fig. 5.6. XRD patterns as obtained for different samples.

The flyash-TiO_2 composite particles synthesized via sol-gel process show the successful deposition of anatase-TiO_2 on the surface of flyash particles. The product obtained after the hydrothermal treatment of flyash-TiO_2 core-shell composite particles exhibits two new broad peaks, which are identified as belonging to either monoclinic $H_2Ti_3O_7$ (with the interlayer spacing of 0.78 nm within the walls of nanotubes) or orthorhombic lepidocrocite-type or $H_2Ti_2O_4(OH)_2$-type hydrogen titanate structures, similar to the analysis presented earlier for the formation of nanotubes of hydrogen titanate via hydrothermal by Jose et al.[20] and others.[15,21]

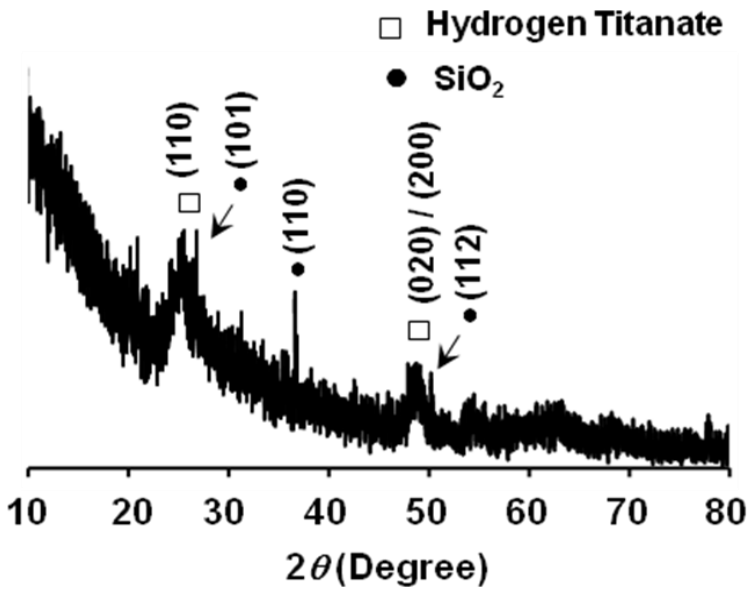

Fig. 5.7. Enlarged view of XRD pattern of HTNS showing the presence of SiO_2 phase along with that of hydrogen titanate phase.

The XRD patterns of HTNSF magnetic nanocomposites show a gradual increase in the intensity of main peak, (311), of γ-Fe_2O_3 which is in accordance with its increasing weight-fraction in these samples. It is to be noted that the XRD pattern of magnetic nanoparticles is ascribed to that of γ-Fe_2O_3 as per the JCPDS card number of 39-1346 rather than to Fe_3O_4 which has the XRD pattern almost similar to that of the former. Chen et al.[22], however, demonstrated that the XRD peaks of γ-Fe_2O_3 are slightly shifted to higher diffraction angles relative to those of Fe_3O_4. In consonance with this, in the present investigation it is noted that the obtained 2θ values for the magnetic nanoparticles, Table 5.1, are slightly larger than those listed in the JCPDS card numbers 19-0629, 75-0033, and 85-1436 for Fe_3O_4. In contrast to this, these 2θ values are closer to those reported by Barakat et al.[23] and also comparable with those listed in the JCPDS card number 39-1346 belonging to γ-Fe_2O_3. Moreover, the average lattice parameter of 0.8365 nm is calculated which is closer to that (0.835 nm) of γ-Fe_2O_3 than that (0.840

nm) of Fe_3O_4 as reported by Chen et al.[22] and Cai et al..[24] Hence, in this investigation, the structure of as-received magnetic nanoparticle is considered to be γ-Fe_2O_3.

Table 5.1. Identified phases, diffraction angles, and corresponding JCPDS card numbers (or the reference numbers) for the diffraction patterns presented in Figs. 5.6 and 5.7.

Identified Phase	Diffraction Angle 2θ (Degree) (Diffracting Plane)	JCPDS Card No. / [Reference]
SiO_2 (Quartz)	20.81 (100)	46-1015
	26.59 (101)	
	36.52 (110)	
	39.43 (102)	
	50.06 (112)	
	59.97 (211)	
	63.99 (113)	
	68.04 (203)	
$Al_6Si_2O_{13}$ (Mullite)	16.42 (110)	15-0776
	25.95 (120)	
	26.24 (210)	
	40.89 (121)	
	57.56 (041)	
	60.74 (331)	
α-Fe_2O_3 (Hematite)	33.16 (104)	33-0664
	35.21 (110)	
	53.97 (116)	
Anatase-TiO_2	25.36 (101)	21-1272
	37.85 (004)	
	48.19 (200)	
	54.09 (105)	
	55.16 (211)	
	62.83 (204)	
Hydrogen Titanate ($H_2Ti_3O_7$)	25.41 (110)	[19-20]
	48.52 (020) / (200)	
γ-Fe_2O_3 (Maghemite)	30.24 (220)	39-1346
	35.62 (311)	
	43.26 (400)	
	53.67 (422)	
	57.16 (511)	
	62.91 (440)	

It has been demonstrated that if the hydrothermal treatment is carried out by using pure anatase-TiO_2 precursor then nanosheets immediately roll to form nanotubes $H_2Ti_3O_7$ rather than the other types of structures with interlayer spacing of 0.78 nm within the walls of nanotubes.[15,21] Since, in the present investigation, the intermediate nanosheet morphology is stabilized by using the flyash-TiO_2 as precursor, it is assumed here that the structure of HTNS resembles that of $H_2Ti_3O_7$. According to the formation mechanism of nanosheets of $H_2Ti_3O_7$ as proposed by Hareesh et al.,[10] in highly alkaline aqueous solution under the hydrothermal conditions, anatase-TiO_2 coating on the surface of flyash tends to form large blocks of $Na_2Ti_3O_7$; while, the flyash particles become disintegrated and get dissolved in the surrounding alkaline medium. Large amount of SiO_4^{4-} and SiO_2 nanoparticles are released in this process from the flyash which may remain intercalated within and adsorbed on the surface of blocks of $Na_2Ti_3O_7$. During the subsequent washing in HCl solution and pure H_2O, an exfoliation of single nanosheets take place simultaneous with the operation of ion-exchange mechanism in which Na^+ ions are replaced with protons (H^+) forming $H_2Ti_3O_7$ phase. Due to the presence of large amount of surface-adsorbed SiO_4^{4-} ions, Fig. 5.5a, and SiO_2 nanoparticles attached to the edges of the nanosheets, Fig. 5.4, the rolling of latter to nanotube morphology is strongly prevented due to reduction in the number of dangling bonds on the surface of nanosheets. In support of this mechanism, the presence of SiO_2 nanoparticles is also detected in the XRD patterns of HTNS presented in Figs. 5.6 and 5.7.

The N_2 adsorption / desorption isotherms obtained using the different samples are presented in Fig. 5.8a; while, the corresponding pore size distribution graphs are shown in Fig. 5.8b. The values of specific surface-area and pore volume as obtained for the different samples are tabulated in the Table 5.2. According to the IUPAC classification,[25] the as-received flyash particles exhibit close to type I reversible isotherm with the

absence of any mesoporosity with the specific surface-area and pore volume as low as 2 m^2 g^{-1} and 0.008 cm^3 g^{-1}. The deposition of nanocrystalline anatase-TiO_2 via sol-gel method results in a change of the isotherm to type IV which is the characteristic feature of capillary condensation taking place in the mesopores. The flyash-TiO_2 composite particles exhibit the specific surface-area and pore volume of 21.5 m^2 g^{-1} and 0.08 cm^3 g^{-1} which are higher almost by 10 times than those of as-received flyash. This is in contrast to the observation made by Shi et al.[26] who deposited TiO_2 on the surface of flyash via sol-gel method; however, did not observe any significant increase in the specific surface-area and pore volume possibly due to the relatively larger concentration (250 g l^{-1}) of flyash used in their experiments which significantly reduced the amount of TiO_2 deposited over each individual flyash particle.

Table 5.2. Values of specific surface-area and pore volume as obtained for different samples.

Sample	Specific Surface-Area (m^2 g^{-1})	Pore Volume (cm^3 g^{-1})
Flyash	2.0	0.0086
Flyash-TiO_2	21.5	0.08
HTNS	334	0.45
HTNSF-5	334	0.51
HTNSF-10	346	0.495
HTNSF-25	269	0.448
γ-Fe_2O_3	37	0.263

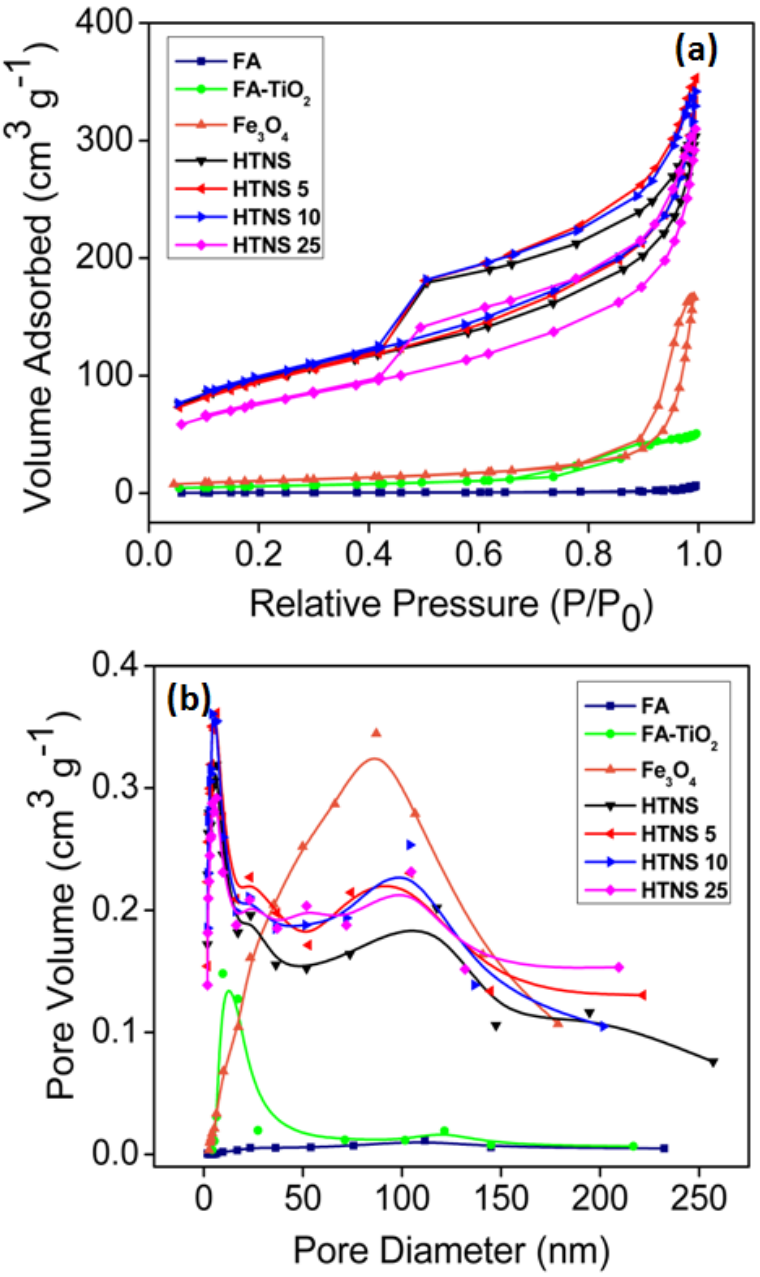

Fig. 5.8. N_2 adsorption / desorption isotherm curves (a) and the corresponding BJH pore-size distribution curves (b) as obtained for different samples.

In the present investigation, the increased specific surface-area and pore volume after the anatase-TiO_2 deposition on the surface of flyash is further supported by the presence of small hysteresis loop which is of type H2 which in turn suggests the presence of ink-bottle type mesopores in the nanocrystalline anatase-TiO_2 coating. The HTNS and HTNSF magnetic nanocomposites exhibit the isotherms of type II and the associated

hysteresis loop is of type H3 which strongly suggests the presence of aggregates of plate-like particles giving rise to slit-shaped pores. Comparison shows that the shape of isotherms and pore size distribution graphs as obtained for HTNS and HTNSF magnetic nanocomposites are similar to those reported recently for the magnetic nanocomposite consisting of molybdenum disulfide (MoS_2) nanosheets decorated with Fe_3O_4 nanoparticles by Song et al.[27] and for the layered protonated titanate nanosheets by Lin et al.[6] As seen in Fig. 5.8b, all the samples except as-received γ-Fe_2O_3 nanoparticles, show bimodal pore-size distribution and presence of large amount of mesopores within the structure in accordance with the BET analysis which appears to be the prominent features of HTNS and HTNSF magnetic nanocomposites. The peaks at the average pore size of 4.5-6 nm and 100 nm are possibly due to the intra- and inter-aggregate porosities in agreement with the TEM analysis.

The variation in the specific surface-area and pore volume as a function of weight-fraction of γ-Fe_2O_3 as obtained for HTNS and HTNSF magnetic nanocomposite samples is shown in Fig. 5.9. According to Lin et al.,[6] the specific surface-area for the layered protonic titanate nanosheets lies within the range of 96-350 $m^2\ g^{-1}$. The specific surface-area of HTNS (334 $m^2\ g^{-1}$), Fig. 5.9a, is within this reported range. (Note: the dotted lines are obtained by joining the values of specific surface-area and pore volume of HTNS with those associated with pure γ-Fe_2O_3 nanoparticles which follow the law-of-mixture of these two phases without any synergy effect in between them). It is clearly seen that the obtained variations in the specific surface-area and pore volume do not follow the law-of-mixture of two phases. The values of both of these parameters exhibit positive deviations from the law-of-mixture as a function of increasing weight-fraction of γ-Fe_2O_3. This clearly suggests the synergy effect in between the HTNS and γ-Fe_2O_3 nanoparticles which is described in the model presented in the Scheme 5.1. The latter also explains the

ion-exchange mechanism responsible for the formation of HTNSF magnetic nanocomposite. As shown in the Scheme 1a, H^+ ions are intercalated in between the $H_2Ti_3O_7$ nanosheets made up of TiO_6 octahedra; while, the as-received γ-Fe_2O_3 nanoparticles consist of Fe-O bonds on the surface with Fe having the oxidation state of +3. During the formation of HTNSF magnetic composite, the close approach of γ-Fe_2O_3 nanoparticles towards the aggregated $H_2Ti_3O_7$ nanosheets results in the ion-exchange reaction in between the Fe^{3+} cations and H^+ ions which replaces the intercalated H^+ ions with Fe^{3+} cations.

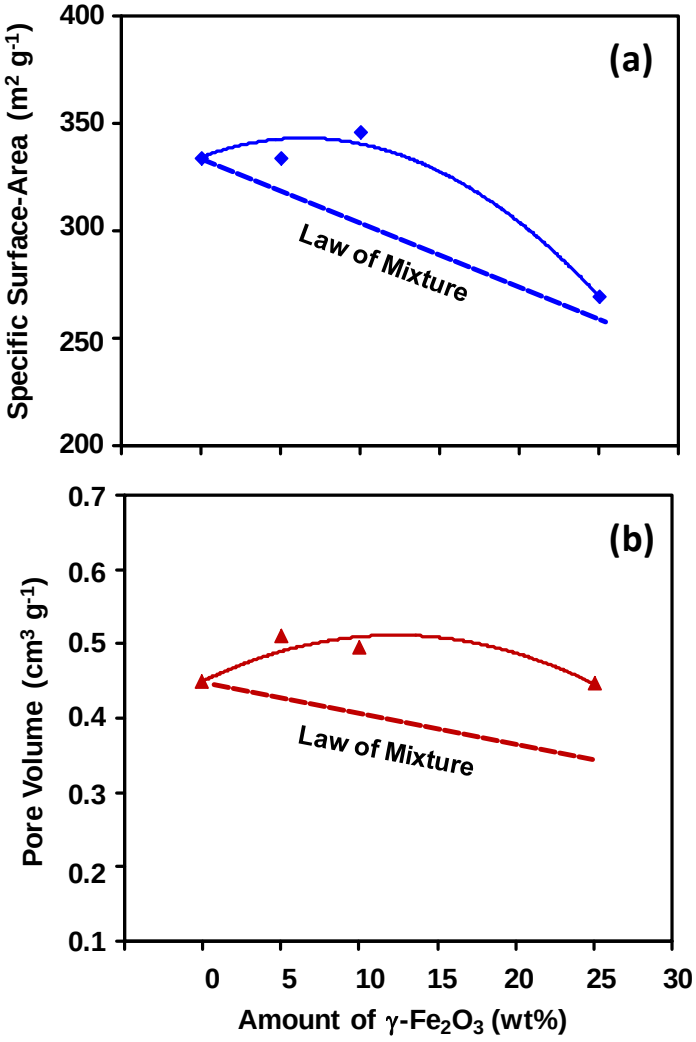

Fig. 5.9. Variation in specific surface-area (a) and pore-volume (b) as a function of weight-fraction of γ-Fe_2O_3 nanoparticles.

Since Fe^{3+} cations are already anchored to the surface of γ-Fe_2O_3 nanoparticles, the ion-exchange reaction results in the formation of ion-exchange bond at the interface of γ-Fe_2O_3 nanoparticles and aggregated $H_2Ti_3O_7$ nanosheets. Thus, the magnetic nanocomposite is formed in which the γ-Fe_2O_3 nanoparticles are attached to the aggregated $H_2Ti_3O_7$ nanosheets via ion-exchange bond typically at the edges of nanosheets where the ion-exchange reaction is highly likely to occur. This clearly explains the observation made in the TEM images, Figs. 5.2b-d (see lower-right corner insets) and 3b-d, where γ-Fe_2O_3 nanoparticles are seen to be attached to the aggregated $H_2Ti_3O_7$ nanosheets typically at the edges of nanosheets. In the Scheme 5.1b, the nanosheets are shown to be highly aggregated for HTNS. However, in the case of HTNSF magnetic nanocomposite, due to the existence of strong repulsive forces between the adjacent γ-Fe_2O_3 nanoparticles, the nanosheets tend to move apart from each other. This may reduce the aggregation tendency of nanosheets by increasing the average stacking distance in between the nanosheets. It appears that the magnitude of repulsive force increases with the weight-fraction of γ-Fe_2O_3 nanoparticles within the HTNSF magnetic nanocomposites. As a result, the average stacking distance between the aggregated nanosheets may increase with the weight-fraction of γ-Fe_2O_3 nanoparticles. This is strongly supported by an increase in the average thickness of aggregated nanosheets from 5 nm to 23 nm with the weight-fraction of γ-Fe_2O_3 nanoparticles, Fig. 5.3. Moreover, it is noted that an increase in the average stacking distance between the aggregated nanosheets as per the mechanism proposed in the Scheme 5.1b should also result in an increase in the volume of slit-shaped pores, and hence, in the specific surface-area. This satisfactorily explains the positive deviations in the values of these parameters from the variation governed by the law-of-mixture with the increasing weight-fraction of γ-Fe_2O_3 nanoparticles as observed in Fig. 5.9.

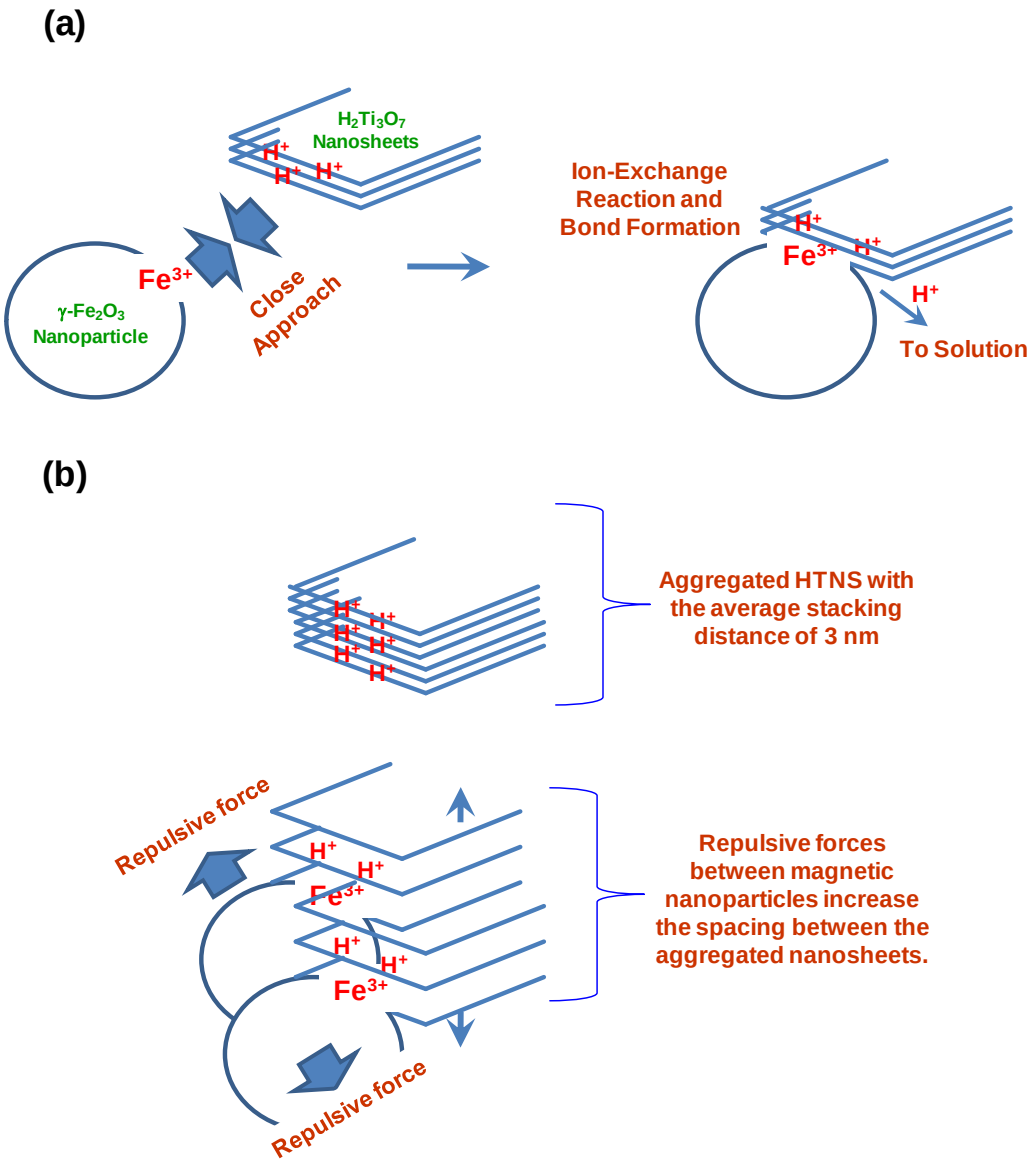

Scheme 5.1. Model describing the mechanism of formation of HTNSF magnetic nanocomposite via creation of an ion-exchange bond (a) and the mechanism of increase in pore volume and specific surface-area of HTNSF magnetic nanocomposite with the attachment of γ-Fe_2O_3 nanoparticles at the edges of nanosheets (b).

5.3.2. MB adsorption characteristics of HTNS and HTNSF magnetic nanocomposites

The variation in the normalized MB concentration adsorbed at equilibrium on the surface of HTNS and HTNSF magnetic nanocomposites is presented in Fig. 5.10 for the initial MB concentration range of 7.5-250 μM at the initial solution-pH of 10. The adsorption equilibrium is seen to be attained within the first 10 min of contact time. As demonstrated in Fig. 5.11, the point-of-zero charge for HTNS and HTNSF-5 magnetic nanocomposite is determined to be at the initial solution-pH of 2.0 and 3.0 respectively. As a result, the surface of HTNS and HTNSF magnetic nanocomposite is highly negatively charged at the initial solution-pH of 10 due to both the adsorption of large amount of OH^- ions from the surrounding aqueous solution and the prior presence of SiO_4^{4-} ions on their surfaces. This results in a strong electrostatic attraction between the positively charged cations of MB and negatively charged surface of HTNS. In Fig. 5.10, the normalized equilibrium concentration of MB adsorbed on the catalyst surface is noted to decrease with the increasing initial MB concentration. The equilibrium amount of MB adsorbed (q_e, mg g^{-1}) on the surface per unit weight of catalyst can be calculated using Eqs. (3.2) and (3.3).

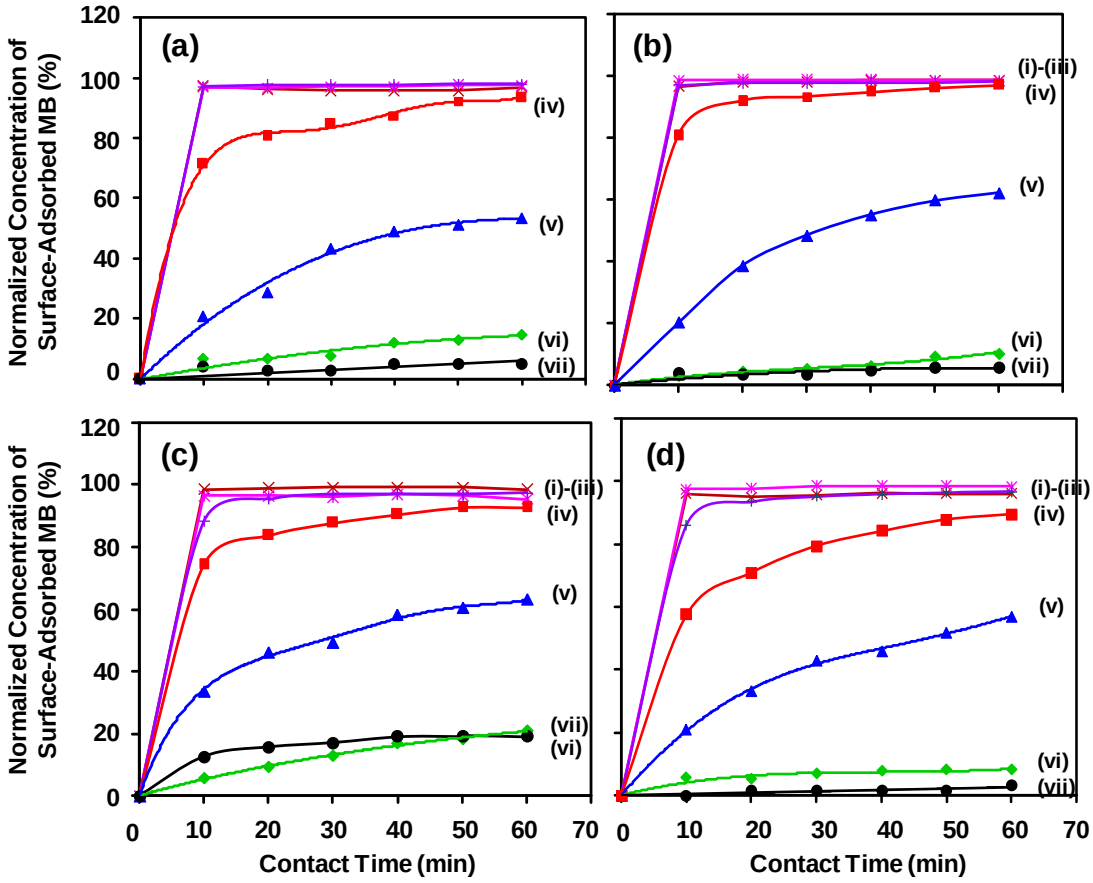

Fig. 5.10. Variation in the normalized concentration of surface-adsorbed MB as a function of contact time as obtained for HTNS (a), HTNSF-5 (b), HTNSF-10 (c), and HTNSF-25 (d) magnetic nanocomposites. The initial MB concentration is varied as 7.5 (i), 30 (ii), 60 (iii), 90 (iv), 150 (v), 200 (vi), and 250 μM (vii). The initial solution-pH is 10.

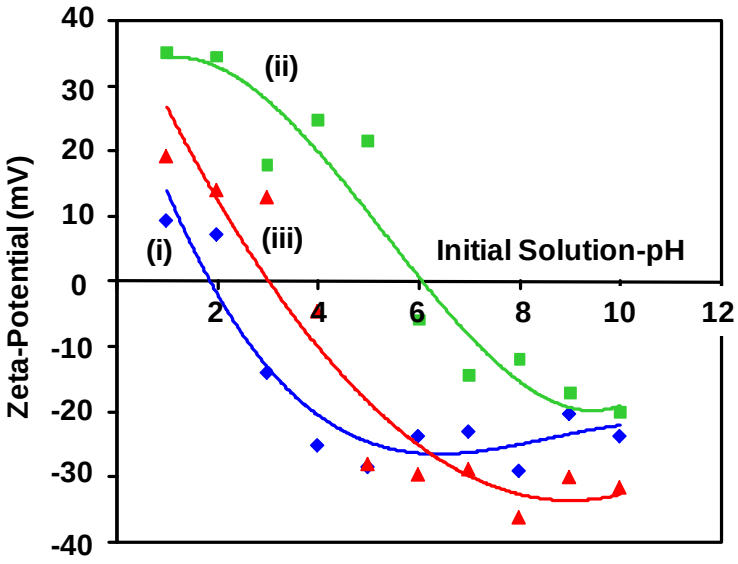

Fig. 5.11. Variation in the zeta-potential of HTNS (i), γ-Fe_2O_3 nanoparticles (ii), and HTNSF-5 magnetic nanocomposite (iii) as a function of initial solution-pH. The point-of-zero-charge is determined to be at the initial solution-pH of 2.0, 6.0, and 3.0 respectively.

The obtained variation in q_e as a function of initial MB concentration is presented in Fig. 5.12; while, the equilibrium adsorption isotherm curves are presented in Fig. 5.13. The q_e values are noted first to increase with the initial MB concentration, then to reach a maximum value (q_m, adsorption capacity) at the initial MB concentration of 100-150 μM, and then to decrease with further increase in the initial MB concentration. The increase in q_e values is attributed here to the greater driving force of MB to occupy potential adsorption sites on the surface of catalyst; while, the decrease is ascribed to decrease in the negative surface-charge on the surface of catalyst due to decrease in the adsorption of OH^- ions as a result of their strong interaction with the positively charged MB cations in the surrounding aqueous solution.

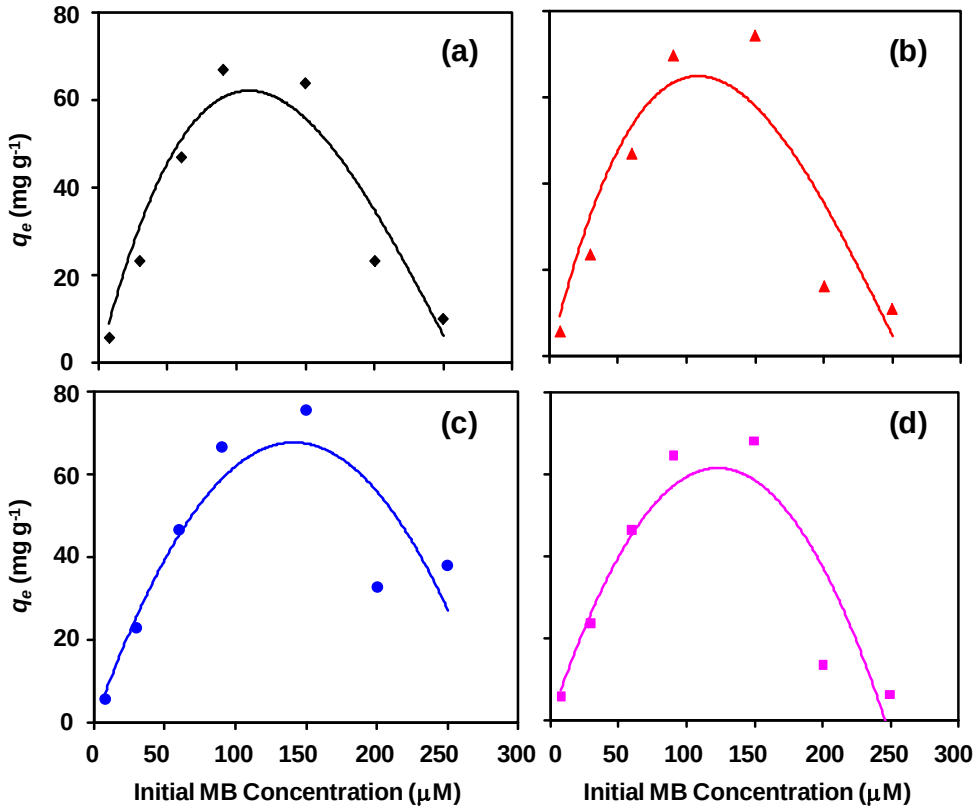

Fig. 5.12. Variation in q_e as a function of initial MB concentration as determined at the initial solution-pH value of 10 for different catalyst samples: HTNS (a), HTNSF-5 (b), HTNSF-10 (c), and HTNSF-25 (d).

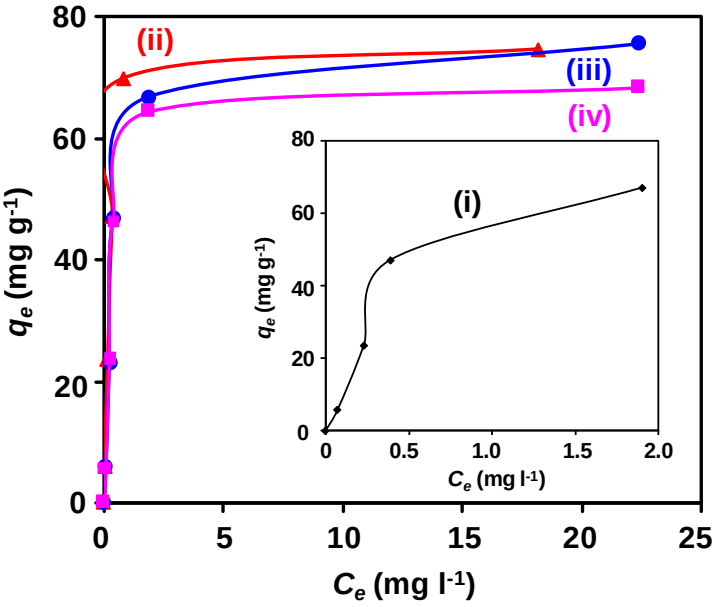

Fig. 5.13. Equilibrium adsorption isotherms for MB on different catalyst samples: HTNS (see the inset) (i), HTNSF-5 (ii), HTNSF-10 (iii), and HTNSF-25. (Note: data points above the peak values, Fig. 5.12, are not considered).

The obtained variation in q_m as a function of amount of γ-Fe_2O_3 is shown in Fig. 5.14. Relative to linear variation as governed by the law-of-mixture, a positive deviation in the variation of MB adsorption capacity as a function of amount of γ-Fe_2O_3 is observed. This clearly suggests a synergy effect in between the constituents of HTNSF magnetic nanocomposites in enhancing the MB adsorption capacity with the amount of γ-Fe_2O_3. The addition of magnetic component (γ-Fe_2O_3), having very low MB adsorption capacity (13 mg g^{-1}),[15] to $H_2Ti_3O_7$ nanosheets-based adsorbents should result in a decrease in the dye-adsorption capacity of magnetic nanocomposite relative to that of non-magnetic HTNS. This has been demonstrated earlier for Fe_3O_4-graphene magnetic nanocomposite by Yao et al.,[28] who reported the MB adsorption capacity of 70 mg g^{-1} and 45 mg g^{-1} for pure graphene and Fe_3O_4-graphene magnetic nanocomposite.

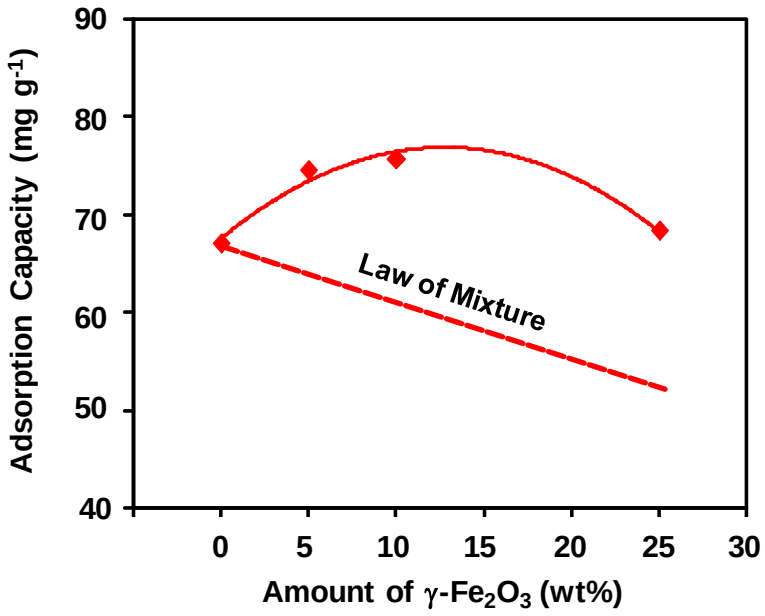

Fig. 5.14. Variation in MB adsorption capacity as a function of weight-fraction of γ-Fe_2O_3 nanoparticles. The initial solution-pH is 10.

Interestingly, in the present investigation, the nature of experimental variation in q_m follows the same trend as that of the pore volume and specific surface-area as noted in Fig. 5.9. Close inspection further reveals that the nature of experimental variation in q_m follows the same trend as that exhibited by pore volume rather than that shown by specific surface-area. This strongly suggests that the MB dye molecules preferentially occupy the potential adsorption sites available inside the volume of slit-type pores than those present on the surface of layered nanosheets. It is further noted that the HTNSF-10 magnetic nanocomposite possesses the maximum MB adsorption capacity of 76 mg g^{-1} which is higher than that (67 mg g^{-1}) of HTNS. This trend is exactly opposite to the one reported in the literature by Yao et al..[28] Secondly, the maximum MB adsorption capacity value obtained here is higher than those (25, 44-45, and 42 mg g^{-1}) reported (or reviewed) recently for the other types magnetic nanocomposites such as MoS_2-Fe_3O_4,[27] graphene nanosheets (GNS)-Fe_3O_4,[28-29] and multiwall carbon nanotubes (MWCNTs)-Fe_2O_3[30]

respectively. Moreover, the maximum MB adsorption capacity value obtained here is also higher than those (30 and 60 mg g^{-1}) reported for the MWCNTs-Fe_3O_4 and AC-Fe_3O_4 magnetic nanocomposites respectively as reported by Ai et al..[29] The MB adsorption capacity of CNTs and commercial adsorbent such as the activated carbon is reported to be 35-65 and 521 mg g^{-1}.[28,30] Thus, the MB adsorption capacity (67 mg g^{-1}) of HTNS as observed in this investigation is comparable with that of CNTs and graphene nanosheets[28] but lower than that of activated carbon. This is in agreement with the results obtained using the various carbon-based nanomaterials as sorbents as reported by Beless et al..[31] (Note: Li et al.,[32] however, demonstrated that activated carbon might exhibit lower MB adsorption capacity normalized by BET surface-area compared with that shown by the graphene oxide and CNTs. By using the organic pollutants other than MB, Apul et al.[33] and Ersan et al.[34] also showed that under certain test conditions granular activated carbon might exhibit lower adsorption capacity relative to that exhibited by other carbon-based adsorbents).

The time dependent MB adsorption on the surface of HTNS and HTNSF magnetic nanocomposites is analyzed using two different kinetics models – Lagergren pseudo-first-order and pseudo-second-order. The linear plots (see Fig. 5.15) with the regression correlation coefficient, $<r_2^2>$, approximately equal to one and q_e values approximately equal to that of experimentally observed values, q_e (Exp), (see the Table 5.3a) suggest that MB adsorption on the surface of HTNS and HTNSF magnetic nanocomposites follows the pseudo-second-order kinetics. In Table 5.3b, the values of parameters of pseudo-first-order kinetics model are tabulated typically for the lower and higher initial MB dye concentrations of 7.5 and 150 μM. It is noted that, for all samples, the lower the initial MB concentration, the lower the $<r_1^2>$ value and vice versa. As a result, the pseudo-first-order kinetics model which is not applicable for the lower initial MB

concentration, becomes applicable at higher value of latter. The comparison of $<r_2^2>$ values at the initial MB concentrations of 7.5 and 150 μM for all samples, Table 5.3a, suggests that the $<r_2^2>$ values slightly decrease at higher initial MB concentration. This suggests that the pseudo-second-order kinetics model which is applicable for the lower initial MB concentration, becomes inapplicable at higher value of latter.

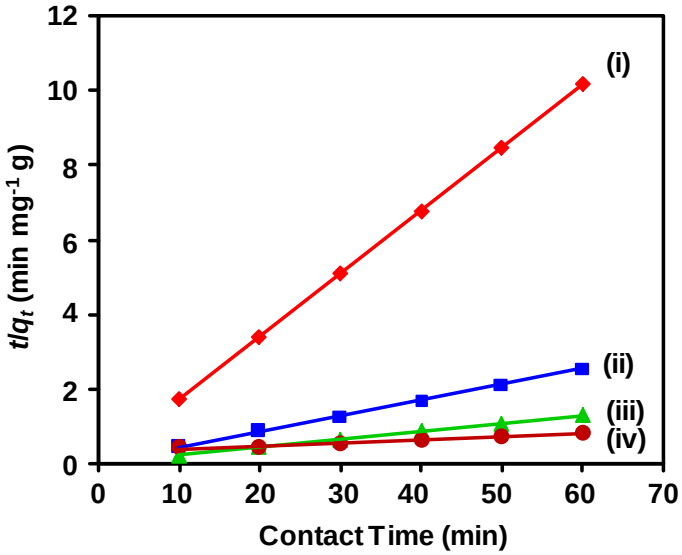

Fig. 5.15. Typical pseudo-second-order kinetics plots as obtained for HTNSF-5 sample for different initial MB concentrations: 7.5 (i), 30 (ii), 60 (iii), and 150 μM (iv).

Table 5.3. Values of parameters of pseudo-second-order (a) and Lagergren pseudo-first-order kinetics models (b) as obtained for different samples under the different test-conditions.

(a)

Sample	[MB]	q_e (Exp.)	q_e	k_2	$<r_2^2>$
HTNS	7.5	5.8	5.81	2.12	0.999
	60	47	47.6	0.44	1
	90	67	76.9	0.003	0.998
	150	64	100	0.0003	0.959
HTNSF-5	7.5	5.9	5.95	0.81	1
	60	47	47.6	0.15	1
	90	69.8	76.9	0.005	0.999
	150	74.5	125	0.0002	0.973
HTNSF-10	7.5	5.9	5.95	---	1
	60	46.7	47.6	0.023	0.999
	90	66.7	71.4	0.004	0.999
	150	75.6	91	0.0008	0.989
HTNSF-25	7.5	5.7	5.78	1.5	1
	60	46.3	47.6	0.016	0.999
	90	64.4	76.9	0.0015	0.999
	150	68.3	111	0.0003	0.992

(b)

Sample	[MB]	q_e (Exp.)	q_e	k_1	$<r_1^2>$
HTNS	7.5	5.8	1.47	0.083	0.597
HTNSF-5		5.9	2.5	0.19	0.822
HTNSF-10		5.9	--	--	--
HTNSF-25		5.7	4.86	0.193	0.978
HTNS	150	64	79.4	0.067	0.973
HTNSF-5		74.5	89.9	0.062	0.976
HTNSF-10		75.6	71	0.06	0.959
HTNSF-25		68.3	69.7	0.046	0.987

As demonstrated in Fig. 5.16, in the present investigation, this transition from the pseudo-second-order to Lagergren pseudo-first-order kinetics for HTNS typically occurs at the initial MB concentration of 150 μM which is highly consistent with the assumptions made in the theoretical derivations of these two kinetics models by Azizian.[35]

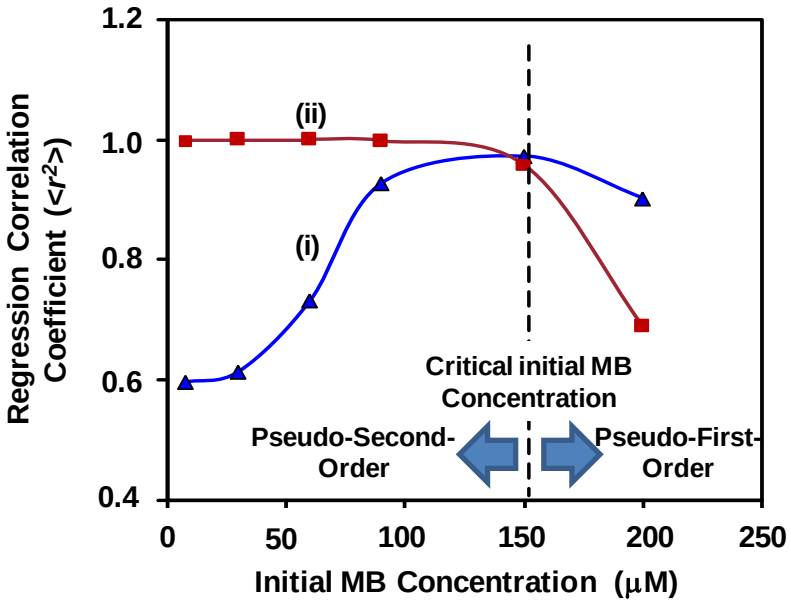

Fig. 5.16. Variation in the $<r^2>$ value as a function of initial MB concentration as obtained for HTNS using the Lagergren pseudo-first-order (i) and pseudo-second-order (ii) kinetics models.

The equilibrium adsorption of MB on the surface of HTNS and HTNSF magnetic nanocomposites is analyzed using three well known adsorption isotherm models - Langmuir, Freundlich, and DKR isotherm models and the corresponding plots for HTNSF-5 magnetic nanocomposite are presented in Fig. 5.17. The calculated values of different parameters of these equilibrium isotherm models are listed in Table 5.4. The q_m values as obtained via Langmuir and DKR models match with the experimentally observed values (q_m (Exp)), along with $<r^2>$ values which are close to unity. This strongly suggests a monolayer adsorption of MB on the surface of HTNS and HTNSF

magnetic nanocomposites. Moreover, R_L values (a dimensionless parameter) for the MB adsorption on the surface of both HTNS and HTNSF magnetic nanocomposites lies in between 0.004-0.17, Table 5.4., which indicates that the adsorption process is favorable.[15] In addition to this, both the negative values of ΔG^0 and E values less than 8 kJ mol^{-1}, Table 5.4., strongly suggest the spontaneous MB adsorption on the surface of HTNS and HTNSF magnetic nanocomposites via electrostatic attraction mechanism.[15,36]

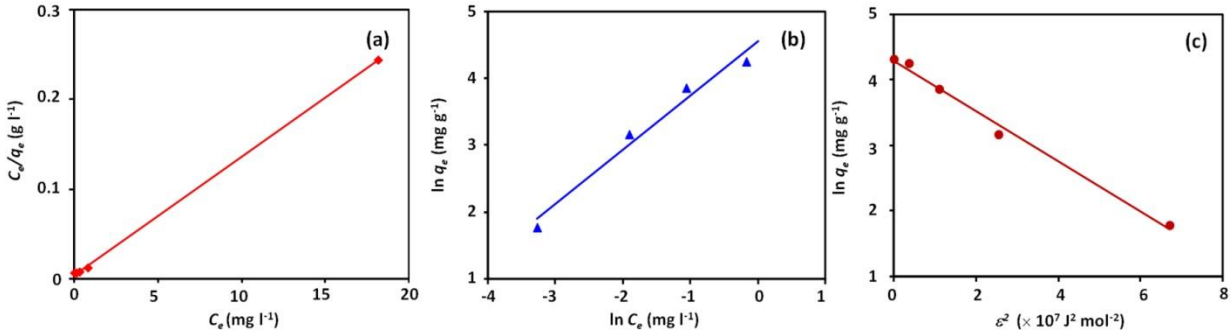

Fig. 5.17. Langmuir (a), Freundlich (b), and DKR (c) plots as obtained for HTNSF-5 magnetic nanocomposite.

Table 5.4. Values of parameters of different equilibrium adsorption isotherm models as obtained for different samples.

Sample	q_m (Exp.)	Langmuir				Freundlich				DKR			
		q_m	K_L	$<r>^2$	R_L	ΔG	n	K_F	$<r>^2$	q_m	β	$<r>^2$	E
HTNS	67	66.7	3.0	0.999	0.007-0.12	-37.0	1.35	57.4	0.851	69.7	6×10^{-8}	0.988	2.9
HTNSF-5	74.5	76.9	4.3	0.999	0.004-0.09	-38.0	1.23	94.6	0.974	73.2	4×10^{-8}	0.991	3.5
HTNSF-10	75.6	83.3	2.0	0.999	0.01-0.17	-36.0	1.36	56.9	0.856	73.3	6×10^{-8}	0.989	2.9
HTNSF-25	68.3	71.4	2.8	0.999	0.007-0.13	-37.0	1.40	55.9	0.842	70.3	6×10^{-8}	0.991	2.9

5.3.3. Magnetic separation, regeneration, and reuse of HTNSF magnetic nanocomposite

As reported earlier by Harsha et al.,[15] the as-received γ-Fe_2O_3 nanoparticles used in this investigation are superparamagnetic in nature and exhibit a small hysteresis loop with the saturation magnetization, remanent magnetization, and coercivity of 71 emu g^{-1}, 5.9 emu g^{-1} and 59 Oe respectively. The saturation magnetization value of 71 emu g^{-1} is comparable with that (76 emu g^{-1}) obtained for the bulk γ-Fe_2O_3 as reported by Millan et al..[37] Hence, with the attachment of γ-Fe_2O_3 nanoparticles to HTNS via the formation of an ion-exchange bond, Scheme 5.1b, it is possible to obtain HTNSF magnetic nanocomposites with varying weight-fractions of γ-Fe_2O_3 nanoparticles. The magnetization curves obtained for different HTNSF magnetic nanocomposites are presented in Fig. 5.18; while, the obtained values of various magnetic properties are tabulated in Table 5.5. Although the saturation magnetization is the smallest in the case of HTNSF-5 sample due to the lowest weight-fraction (5 wt%) of γ-Fe_2O_3 nanoparticles,[37] it could be separated from an aqueous solution using an external magnetic field in 5 min (see the inset located at lower-right corner of Fig. 5.18). Hence, the successful magnetic separation of HTNSF magnetic nanocomposite from the aqueous solution has been demonstrated in this investigation.

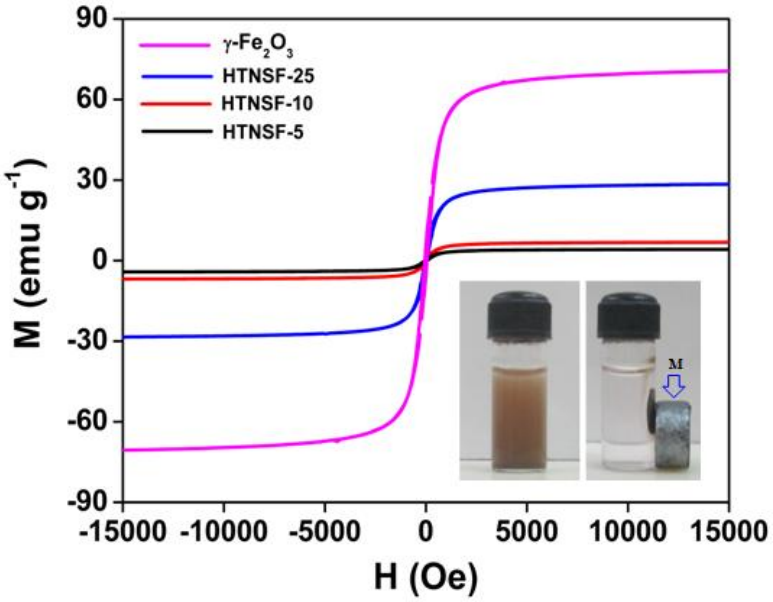

Fig. 5.18. Magnetization curves as obtained for different samples. The inset shows magnetic separation of HTNSF-5 nanocomposite from an aqueous solution. M represents an external magnet.

Table 5.5. Values of magnetic properties as obtained for different samples.

Sample	Saturation Magnetization (emu g^{-1})	Remanent Magnetization (emu g^{-1})	Coercive Field (Oe)
HTNS-5	4.3	0.40	-62.6
HTNSF-10	6.7	0.64	-58.2
HTNSF-25	29.0	2.96	-57.5
γ-Fe_2O_3	71.0	5.9	-58.7

After the magnetic separation of HTNSF magnetic nanocomposite form the treated aqueous solution, in order to reuse the catalyst for the next cycle of dye-adsorption, it is necessary to regenerate the catalyst either via desorption of previously adsorbed-dye or via completely decomposing the adsorbed-dye on the surface of catalyst. Since the first method merely transforms the adsorbed-dye from the solid phase to the liquid phase causing the secondary pollution,[38-39] in the present investigation, the second method of

catalyst regeneration has been attempted and compared for H_2O_2 and KPS activation techniques.[12,15,16]

The obtained variation in the normalized concentration of MB adsorbed as a function of contact time, at the initial MB concentration of 90 μM, is presented in Fig. 5.19a for three consecutive cycles of dye-adsorption. It is noted that the amount of MB adsorbed at the equilibrium decreases from 97% to 13% after three consecutive cycles of dye-adsorption which results in the total MB adsorption of 107 mg g^{-1} on the surface of HTNSF-5 magnetic nanocomposite. The regeneration of catalyst is then attempted using 30 wt% H_2O_2 solution to decompose MB dye which is adsorbed in the previous three cycles. However, as noted in Fig. 5.19a, only 8% of MB is adsorbed on the surface of HTNSF-5 magnetic nanocomposite in the fourth dye-adsorption cycle following its regeneration conducted using H_2O_2 solution. This strongly suggests that the regeneration treatment conducted using H_2O_2 solution could not decompose the previously adsorbed MB dye on the surface of HTNSF-5 magnetic nanocomposite. Surprisingly, Harsha et al.[15] successfully demonstrated that the H_2O_2 can be easily activated using the nanotubes of $H_2Ti_3O_7$ generating $O_2^{\bullet-}$ and $^{\bullet}OH$ which can attack and decompose the surface-adsorbed MB dye.

$$H_2O_2 \xrightarrow{H_2Ti_3O_7} O_2^- + 2H^+ + e^- \quad (5.1)$$

$$H_2O_2 + O_2^- \xrightarrow{H_2Ti_3O_7} {}^{\bullet}OH + OH^- + O_2 \quad (5.2)$$

Zhou et al.[12] also reported recently that the delaminated two-dimensional titanate nanosheets are superior non-light driven catalyst for the degradation of organic dyes (RhB) obtained through the generation of superoxide radical-ions via H_2O_2 activation. It is to be noted that, in the present investigation, the $H_2Ti_3O_7$ nanosheets are stabilized with SiO_4^{4-} ions and SiO_2 nanoparticles. Hence, there is a strong possibility that the potential

sites available on the surface and edges of HTNSF-5 magnetic nanocomposite are already occupied by the foreign species reducing the concentration of surface-adsorbed O_2^- ions and H_2O_2. As per the reaction shown in the Eq. (5.2), the adsorption of O_2^- ions and H_2O_2 in significant amount on the surface of HTNSF-5 magnetic nanocomposite appears to be an essential requirement in order to generate $^{\bullet}OH$ in large amount. This requirement is seriously hampered due to the prior presence of SiO_4^{4-} ions and SiO_2 nanoparticles on the surface and at the edges of HTNS nanosheets. In addition to this, it also appears that the activation of H_2O_2 via the visible-light induced photo-Fenton reaction[40-41] and direct photolysis[42] is also not possible in this investigation.

As an alternative to H_2O_2 activation, the regeneration treatment of HTNSF-5 magnetic nanocomposite after the third cycle of MB adsorption is conducted by replacing H_2O_2 solution with KPS solution at room temperature (30 ^oC). Surprisingly, it is noted that the fourth MB adsorption cycle conducted after the regeneration treatment in KPS solution results in a drastic increase in the adsorption capacity of HTNSF-5 magnetic nanocomposite from 13% to 90%, Fig. 5.19a. This successfully demonstrates that the regeneration treatment conducted in the KPS solution can decompose the previously adsorbed MB dye on the surface of HTNSF-5 magnetic nanocomposite. It is to be noted that persulfate ($S_2O_8^{-}$) is a strong oxidizing agent with the redox potential of 2.01 eV. Upon thermal, chemical, or photochemical activation, it is possible to generate $SO_4^{\bullet-}$ which are relatively stronger oxidizing species with the redox potential of 2.6 eV.[45] Moreover, $SO_4^{\bullet-}$ can further lead to the formation of $^{\bullet}OH$.

$$S_2O_8^{2-} \xrightarrow{\Delta} 2SO_4^{\bullet-} \tag{5.3}$$

$$SO_4^{\bullet-} + H_2O \rightarrow SO_4^{2-} + {}^{\bullet}OH + H^+ \tag{5.4}$$

These $SO_4^{\bullet-}$ and $^{\bullet}OH$ can then attack and degrade the surface-adsorbed cationic MB dye. In the present investigation, it appears that the thermal activation of $S_2O_8^{2-}$ has a major contribution in the successful regeneration of HTNSF-5 magnetic nanocomposite.[16]

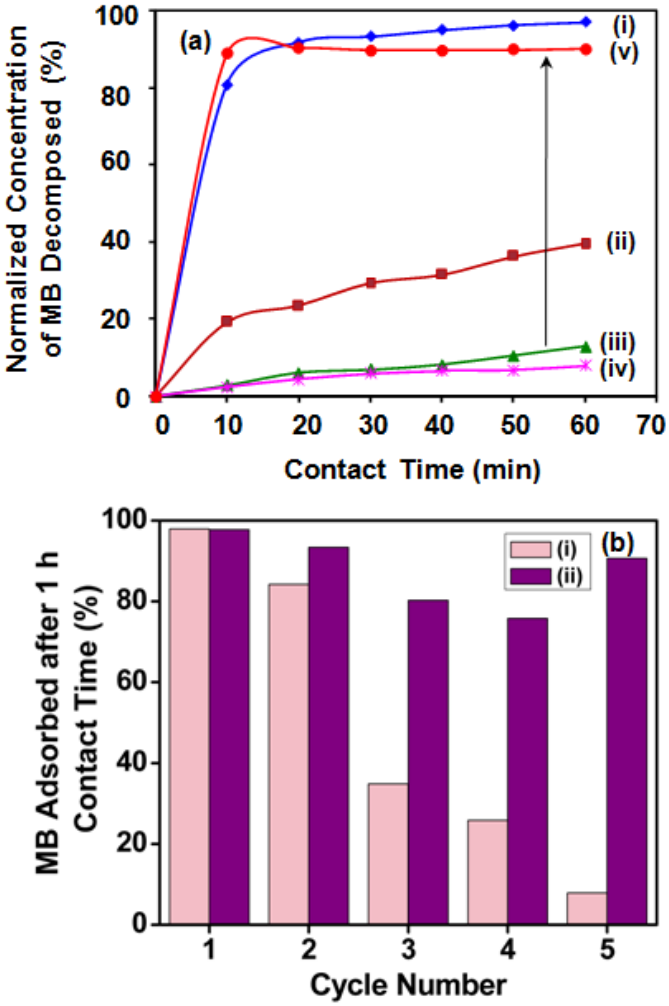

Fig. 5.19. (a) Variation in the normalized concentration of MB adsorbed as a function of contact time as obtained for HTNSF-5 magnetic nanocomposite under different test-conditions. The successive dye-adsorption cycles-1 to 3 (i–iii) are conducted before the regeneration treatment. The cycle-4 ((iv) and (v)) is carried out after the regeneration treatment conducted at room temperature (30 ^{o}C) in H_2O_2 (30 wt%) (iv) and KPS (0.1 M (~3 wt%)) (v) solutions respectively. For each dye-adsorption cycle, the initial MB concentration is 90 μM. (b) Variation in the normalized concentration of MB adsorbed

after 1 h of contact time as a function of dye-adsorption cycle number as obtained for HTNSF-5 magnetic nanocomposite without (i) and with (ii) the involvement of regeneration treatment in KPS solution conducted at 75 ^oC after each dye-adsorption cycle. The initial MB and KPS concentrations are 90 μM and 2 mM (0.06 wt%) respectively.

As demonstrated in Fig. 5.19b, the regeneration treatment conducted in KPS solution at slightly higher temperature (75 ^oC), after each single cycle of MB adsorption, also maintains the original MB adsorption capacity for the consecutive five adsorption cycles with the reduced time (1 h) required for the regeneration treatment. (Note: the regeneration time at the room temperature is 3 h). The oxidation of MB (30-70 ^oC)[17] and other organic pollutants in water such as sulfamonomethoxine (80 ^oC),[43] 1,1,1-Trichloroethane (20-50 ^oC),[44] and methyl *tert*-butyl ether (20-50 ^oC)[45] via thermal activation of $S_2O_8^{2-}$ is reported in the literature by others. The findings in these earlier reports suggest that the degradation of organic pollutants via thermal activation of $S_2O_8^{2-}$ is highly temperature dependent. In general, higher temperatures provide more energy to rupture O–O bonds of $S_2O_8^{2-}$ and more readily produce reactive species such as $SO_4^{\bullet-}$ and $^{\bullet}OH$, thereby leading to more rapid degradation of synthetic dyes in water. This is consistent with the results of $^{\bullet}OH$ trapping experiments conducted at 30 ^oC without and with the presence of HTNS-5 magnetic nanocomposite as presented in Fig. 5.20a and b respectively. Without the presence of latter, Fig. 5.20a, the concentration of $^{\bullet}OH$ produced is noted to increase continuously with the activation time (also see the inset in Fig. 5.20b). In view of the chemical reaction presented in the Eq. (5.4), this strongly suggests corresponding increase in the concentration of $SO_4^{\bullet-}$ with the activation time via chemical reaction presented in the Eq. (5.3). The inset in Fig. 5.20b shows that the concentration of $^{\bullet}OH$ produced within the first 20 min of activation time is larger in the

presence of HTNS-5 magnetic nanocomposite than that produced in the absence of latter. This strongly suggests a positive synergy effect between the thermal activation and that by the constituents of HTNSF-5 magnetic nanocomposite. It appears that in the presence of HTNS-5 magnetic nanocomposite, having relatively smaller quantity of γ-Fe_2O_3 nanoparticles with +3 oxidation state of Fe, the sulfate ions produced via chemical reaction presented in the Eq. (5.4) may react with Fe^{3+} ions present on the surface of γ-Fe_2O_3 nanoparticles producing Fe^{2+} and $SO_4^{\bullet-}$.[43]

$$Fe^{3+} + SO_4^{2-} \rightarrow Fe^{2+} + SO_4^{\bullet-} \tag{5.5}$$

Since the HTNSF-5 nanocomposite can absorb visible-light (see Fig. 5.21), the $O_2^{\bullet-}$ generated on the surface may also produce $SO_4^{\bullet-}$.

$$O_2 + e^- \rightarrow O_2^{\bullet-} \tag{5.6}$$

$$O_2^{\bullet-} + S_2O_8^{2-} \rightarrow SO_4^{\bullet-} + SO_4^{2-} + O_2 \tag{5.7}$$

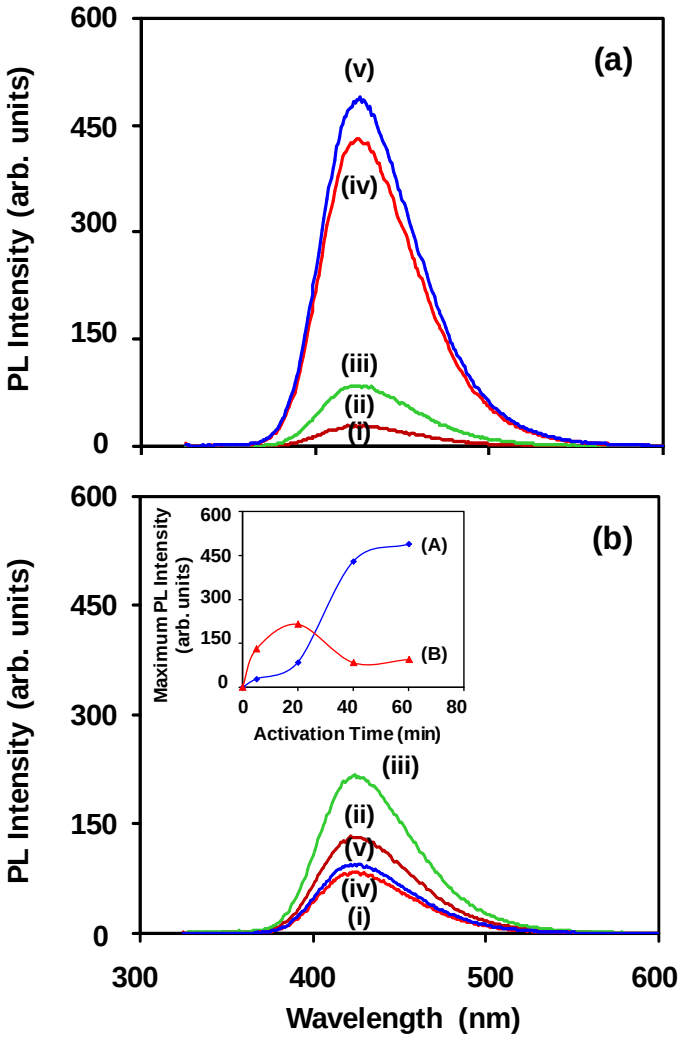

Fig. 5.20. Variation in PL intensity associated with the formation of 2-hydroxyterephthalic acid as a function of activation time of KPS in the absence (a) and presence (b) of HTNSF-5 magnetic nanocomposite. The activation time varies as 0 (i), 5 (ii), 20 (iii), 40 (iv), and 60 min (v). The inset in (b) shows variation in the maximum PL intensity as a function of activation time in the absence (A) and presence (B) of HTNSF-5 magnetic nanocomposite.

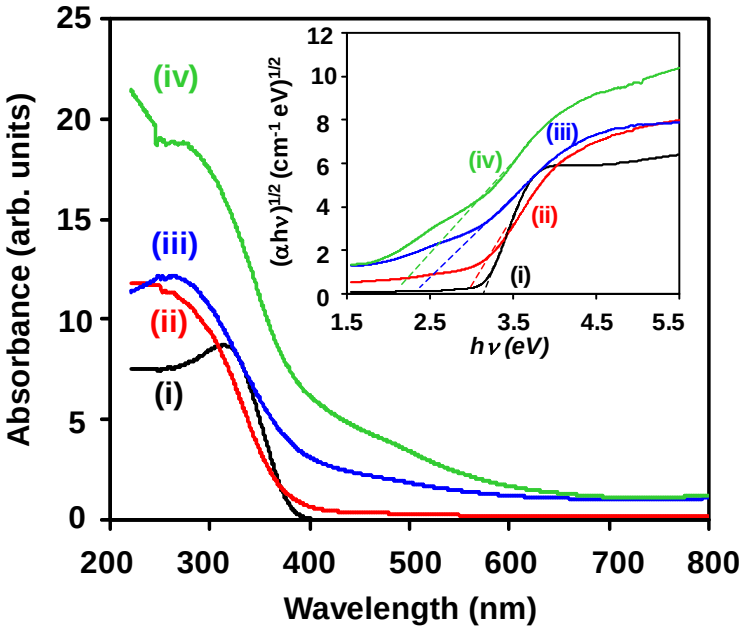

Fig. 5.21. UV-visible DR spectra obtained using different catalyst samples: anatase-TiO_2 (i), HTNS (ii), HTNSF-5 (iii), and HTNSF-10 (iv). The inset shows the corresponding plots of transformed Kubelka–Munk function versus energy of absorbed light.

The E_{BG} measurements show that anatase-TiO_2, HTNS, HTNSF-5, HTNSF-10, and γ-Fe_2O_3 nanoparticles (latter is not included in Fig. 5.21 for clarity) possess the E_{BG} values of 3.2, 2.9, 2.4, 2.1, and 1.97 eV respectively. Hence, it is clear that HTNS and HTNSF magnetic nanocomposites can easily absorb visible-light in solar-radiation under the normal ambient condition below the wavelength of 428 nm and 515-590 nm respectively which can generate the electron-hole pairs in the conduction and valence bands of HTNS. The visible-light induced electrons can then undergo photo-Fenton reaction generating $^{\bullet}OH$.[40]

$$H_2O_2 + e^- \rightarrow {}^{\bullet}OH + OH^- \qquad (5.8)$$

It, however, appears that the photo-Fenton reaction is hampered by lower amount of visible-light absorption by HNTS, poor adsorption of H_2O_2 their surfaces, and lack of effective interfacial charge transfer reaction which is attributed to the prior presence of

SiO_4^{4-} ions and SiO_2 nanoparticles on their surfaces and edges. In addition to this, the photo-Fenton reaction, Eq. (5.8), is also possible to occur via generation of visible-light induced electron-hole pairs within the γ-Fe_2O_3 nanoparticles since it can absorb visible-light below the wavelength of 629 nm.[43] However, their weight-fraction in HTNSF-5 magnetic nanocomposite is very low to cause any significant activation of H_2O_2. The direct photolysis of H_2O_2 using UV-radiations having wavelengths in the range of 200-280 nm is reported to generate $^{\bullet}OH$ in large amount.[42] However, such an intense UV-light is not present in solar-radiation under the normal ambient conditions. Hence, the possibility of direct photolysis of H_2O_2 to generate $^{\bullet}OH$ in large amount is also ruled out.

Overall, as a consequence of various factors discussed above, H_2O_2 is not successfully activated by HTNSF-5 magnetic nanocomposite to generate $^{\bullet}OH$ during the regeneration treatment. Hence, the successful regeneration and reuse of HTNSF-5 magnetic nanocomposite could not be achieved using H_2O_2 activation technique; although, such technique is successfully utilized in the case of delaminated two-dimensional titanate nanosheets[12] and magnetic nanocomposites based on $H_2Ti_3O_7$ nanotubes[15] due to the absence of foreign species such as SiO_4^{4-} ions and SiO_2 nanoparticles on their surfaces and at the edges.

The chemical reactions presented in the Eqs. (5.4), (5.5), and (5.7) satisfactorily explain the higher concentration of $^{\bullet}OH$ observed within the first 20 min of activation time in the presence of HTNSF-5 magnetic nanocomposite. As observed in the inset of Fig. 5.20b, the concentration of $^{\bullet}OH$ produced is noted to decrease and then to increase marginally with further increase in the activation time above 20 min. Such variation in the $^{\bullet}OH$ concentration, and possibly that of $SO_4^{\bullet-}$ concentration, is attributed to their consumption by Fe^{2+} ions[46] and $O_2^{\bullet-}$.

$$Fe^{2+} + {}^{\bullet}OH \rightarrow Fe^{3+} + OH^{-} \quad (5.9)$$

$$O_2^{\bullet-} + {}^{\bullet}OH \rightarrow OH^{-} + O_2 \quad (5.10)$$

$$Fe^{2+} + SO_4^{\bullet-} \rightarrow Fe^{3+} + SO_4^{2-} \quad (5.11)$$

$$O_2^{\bullet-} + SO_4^{\bullet-} \rightarrow SO_4^{2-} + O_2 \quad (5.12)$$

Nevertheless, above the activation time of 20 min, the combined concentration of $SO_4^{\bullet-}$ and $^{\bullet}OH$ appears to be sufficiently large enough to decompose MB adsorbed on the surface of HTNSF-5 magnetic nanocomposite, Fig. 5.19a. The comparison of Fig. 5.20a and b, thus, reflect a strong synergy effect in between the thermal activation and that by the constituents of HTNSF-5 magnetic nanocomposite in the generation of $SO_4^{\bullet-}$ and $^{\bullet}OH$. Overall, the magnetic separation of HTNSF-5 magnetic nanocomposite followed by its regeneration and reuse via synergistic activation of $S_2O_8^{2-}$ is successfully achieved in this investigation.

5.4. Conclusions

HTNSF magnetic nanocomposites are successfully synthesized with varying weight-fraction of γ-Fe_2O_3 nanoparticles and utilized for the removal of cationic MB dye from the aqueous solutions via adsorption mechanism. A new model has been proposed to explain the formation mechanism of HTNSF magnetic nanocomposite involving the development of an ion-exchange bond via exchange of Fe^{3+} ions in place of H^+ at the interface of constituents of magnetic nanocomposite. Moreover, the new model also explains the dependence of variation in the MB adsorption capacity of HTNSF magnetic nanocomposite on that of pore-volume and specific surface-area, as a function of increasing weight-fraction of γ-Fe_2O_3 nanoparticles, on the basis of repulsive forces created in between the adjacent γ-Fe_2O_3 nanoparticles. As a result, the HTNSF-10 magnetic nanocomposite possesses the maximum MB adsorption capacity of 76 mg g^{-1}

which is higher than that (67 mg g^{-1}) of HTNS. The MB adsorption on the surface of HTNS and HTNSF magnetic nanocomposites follows the pseudo-second-order kinetics and Langmuir and DKR isotherm models. The variation in $<r^2>$ values as a function of initial MB concentration strongly supports the Azizian analysis which suggests the applicability of pseudo-second-order and Lagergren pseudo-first-order kinetics models at lower (< 150 μm) and higher (> 150 μm) initial MB concentrations. The successful recycling of HTNSF-5 magnetic nanocomposite, containing the lowest amount of γ-Fe_2O_3 nanoparticles, is demonstrated via its magnetic separation in 5 min followed by its regeneration by decomposing the previously adsorbed MB dye using the synergistic activation of $S_2O_8^{2-}$ in an aqueous solution. A strong synergy effect is observed in between the thermal activation and that by the constituents of HTNSF-5 magnetic nanocomposite in the generation of $SO_4^{\bullet-}$ and $^{\bullet}OH$. The regeneration of HTNSF-5 magnetic nanocomposite using H_2O_2 solution, however, could not be achieved due to the attachment of SiO_2 nanoparticles to the edges of nanosheets of hydrogen titanate and the presence of SiO_4^{4-} ions on their surfaces. Overall, HTNSF magnetic nanocomposite provides an effective way for the removal of cationic MB dye involving the surface-adsorption of dye, its magnetic separation, followed by its regeneration and reuse via the synergistic activation of $S_2O_8^{2-}$ in an aqueous solution. The developed technology may be utilized in future for the removal of other types of synthetic-dyes from the aqueous solutions.

References

(1) Gateshki, M.; Hwang, S.-J.; Park, D. H.; Ren, Y.; Petkov, V. *Chem. Mater.* **2004**, *16*, 5153.

(2) Wu, Y.; Xu, B. *Chin. Sci. Bull.* **2005**, *50*, 2153.

(3) Takezawa, Y.; Imai, H. *Small* **2006**, *2*, 390.

(4) Antonello, A.; Guglielmi, M.; Bello, V.; Mattei, G.; Chiasera, A.; Ferrari, M.; Martucci, A. *J. Phys. Chem. C* **2010**, *114*, 18423.

(5) Zhao, B.; Chen, F.; Gu, X.; Zhang, J. *Chem. Asian J.* **2010**, *5*, 1546.

(6) Lin, C.-H.; Wong, D. S.-H.; Lu, S.-Y. *ACS Appl. Mater. Interfaces* **2014**, *6*, 16669.

(7) Wu, Q.; Yang, X.; Liu, J.; Nie, X.; Huang, Y.; Wen, Y.; Khan, J.; Khan, W. U.; Wu, M.; An, T. *ACS Appl. Mater. Interfaces* **2014**, *6*, 17730.

(8) Sutradhar, N.; Sinhamahapatra, A.; Pahari, S. K.; Bajaj, H. C.; Panda, A. B. *Chem. Commun.* **2011**, *47*, 7731.

(9) Wang, C.; Zhang, X.; Zhang, Y.; Jia, Y.; Yang, J.; Sun, P.; Liu, Y. *J. Phys. Chem. C* **2011**, *115*, 22276.

(10) Hareesh, P.; Babitha, K.; Shukla, S. *J. Hazard. Mater.***2012**, *229*, 177.

(11) Luan, X.; Wang, Y. *J. Mater. Sci. Technol.* **2014**, *30*, 839.

(12) Zhou, C.; Luo, J.; Chen, Q.; Jiang, Y.; Dong, X.; Cui, F. *Chem. Commun.* **2015**, *51*, 10847.

(13) Kim, T. W.; Kim, I. Y.; Park, D.-H.; Choy, J.-H.; Hwang, S.-J. *Sci. Rep.***2016**, *6*, 21993.

(14) Thazhe, L.; Shereef, A.; Shukla, S.; Reshmi, C. P; Varma, M. R.; Suresh, K. G.; Patil, K.; Warrier, K. G. K *J. Am. Ceram. Soc.* **2010**, *93*, 3642.

(15) Harsha, N.; Krishna, K. S.; Renuka, N. K.; Shukla, S. *RSC Adv.* **2015**, *5*, 30354.

(16) Ghauch, A.; Tuqan, A. M.; Kibbi, N.; Geryes, S. *Chem. Eng. J.***2012**, *213*, 259.

(17) Shukla, S.; Oturan, M. A. *Environ. Chem. Lett.* **2015**, *13*, 157.

(18) Morjan, I.; Dumitrache, F.; Alexandrescu, R.; Birjega, R.; Fleaca, C.; Voicu, I.;

Gavrila, L.; Soare, I.; Filoti, G.; Kuncser, V.; Prodan, G.; Ciupina, V.; Vekas, L. Nanotech-2007: Nano Science and Technology institute (NSTI) Conferenc and Expo, Sanata Clara, California, U.S.A. **2007**, 4, 234.

(19) Jose, M.; Haridas, M. P.; Shukla, S. *J. Environ. Chem. Eng.* **2014**, *2*, 1980.

(20) Jose, M.; Harsha, N.; Suhailath, K.; Mohamed, A. P.; Shukla, S. *J. Environ. Chem. Eng.* **2016**, *4*, 1295.

(21) Wu, D.; Liu, J.; Zhao, X.; Li, A.; Chen, Y.; Ming, N. *Chem. Mater.* **2006**, *18*, 547.

(22) Chen, T.; Xu, H.; Xie, Q.; Chen, J.; Ji, J.; Lu, H. *Earth Planet. Sci. Lett.* **2005**, *240*, 790.

(23) Barakat, N. A. *J. Mater. Sci.***2012**, *47*, 6237.

(24) Cai, W.; Wan, J. *J. Colloid Interface Sci.* **2007**, *305*, 366.

(25) Sing, K. S. W.; Everett, D. H.; Haul, R.; Moscou, L.; Pierotti, R. A.; Rouquerol, J.; Siemieniewska, T.; *Pure Appl. Chem.* **1982**, *54*, 2201.

(26) Shi, Z.; Yao, S.; Sui, C. *Catal. Sci. Technol*. **2011**, *1*, 817.

(27) Song, H. J.; You, S.; Jia, X. H.; Yang, J. *Ceram. Int.* **2015**, *41*, 13896.

(28) Yao, Y.; Miao, S.; Liu, S.; Ma, L. P.; Sun, H.; Wang, S. *Chem. Eng. J.* **2012**, *184*, 326.

(29) Ai, L.; Zhang, C.; Chen, Z. *J. Hazard. Mater.* **2011**, *192*, 1515.

(30) Namvari, M.; Namazi, H. *Int. J. Environ. Sci. Technol.* **2016**, *13*, 599.

(31) Beless, B.; Rifai, H. S.; Rodrigues, D. F. *Environ. Sci. Technol.***2014**, *48*, 10372.

(32) Li, Y.; Du, Q.; Liu, T.; Peng, X.; Wang, J.; Sun, J.; Wang, Y.; Wu, S.; Wang, Z.; Xia, Y. *Chem. Eng. Res. Des.***2013**, *91*, 361.

(33) Apul, O. G.; Wang, Q.; Zhou, Y.; Karanfil, T. *Water Res.* **2013**, *47*, 1648.

(34) Ersan, G.; Kaya, Y.; Apul, O. G.; Karanfil, T. *Sci. Total Environ.* **2016**, 565, 811.

(35) Azizian, S. *J. Colloid Interface Sci.* **2004**, *276*, 47.

(36) Lee, C.-K.; Lin, K.-S.; Wu, C.-F.; Lyu, M.-D.; Lo, C.-C. *J. Hazard. Mater.* **2008**, *150*, 494.

(37) Millan, A.; Urtizberea, A.; Silva, N. J. O.; Palacio, F.; Amaral, V.S.; Snoeck, E.; Serin, V. *J. Magn. Magn. Mater.***2007**, *312*, L5.

(38) Konicki, W.; Sibera, D.; Mijowska, E.; Lendzion-Bieluń, Z.; Narkiewicz, U. *J. Colloid Interface Sci.* **2013**, *398*, 152.

(39) Zhang, Y.-R.; Wang, S.-Q.; Shen, S.-L.; Zhao, B.-X. *Chem. Eng. J.* **2013**, *233*, 258.

(40) Chu, W.; Wong, C. *Water Res.* **2004**, *38*, 1037.

(41) Chan, J. Y. T.; Ang, S. Y.; Ye, E.; Sullivan, M.; Zhang, J.; Lin, M. *Phys. Chem. Chem. Phys.* **2015**, *17*, 25333.

(42) Lopez, A.; Bozzi, A.; Mascolo, G.; Kiwi, J. *J. Photochem. Photobiol. A* **2003**, *156*, 121.

(43) Ding, Y.; Zhu, L.; Yan, J.; Xiang, Q.; Tang, H. *J. Environ. Monit.* **2011**, *13*, 3057.

(44) Gu, X.; Lu, S.; Li, L.; Qiu, Z.; Sui, Q.; Lin, K.; Luo, Q. *Ind. Eng. Chem. Res.* **2011**, *50*, 11029.

(45) Huang, K.-C.; Couttenye, R. A.; Hoag, G. E. *Chemosphere* **2002**, *49*, 413.

(46) Narayani, H.; Arayapurath, H.; Shukla, S. *Catal. Lett.* **2013**, 143, 807.

Chapter 6

Synergistic Persulfate Activation as an Efficient and Cost-Effective Approach for Removal of Organic Synthetic-Dyes from Aqueous Solutions Using Magnetic Pd-Fe_3O_4-Flyash Composite Particles as Catalyst

Graphical Abstract

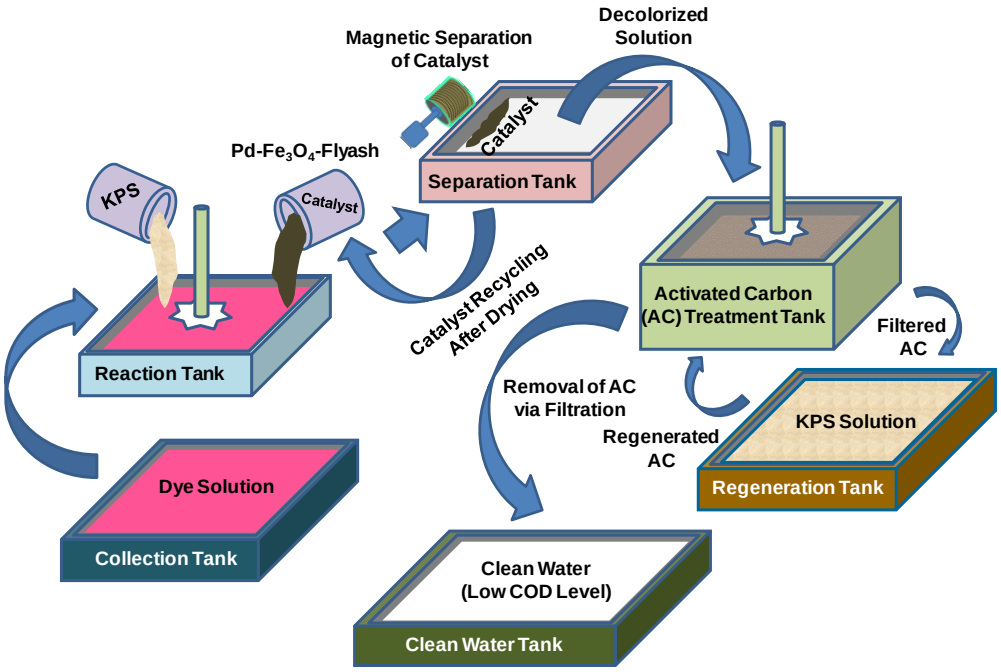

Highlights

- Magnetic Pd-Fe_3O_4-flyash composite particles are processed via wet-chemical route.
- Composite particles remove organic dye from aqueous solution via $S_2O_8^{2-}$ activation.
- COD is predominantly reduced via $S_2O_8^{2-}$ activation in one step catalytic process.
- Regeneration of AC is demonstrated via $S_2O_8^{2-}$ activation.
- $S_2O_8^{2-}$ activation is efficient, cost-effective, non-hazardous than H_2O_2 activation.

Abstract

Magnetic palladium (Pd)-Fe_3O_4-flyash composite particles have been recently utilized for the removal of industrial azo reactive dyes from the aqueous solutions. The mechanism of dye-removal involves AOPs such as the activation of costlier and hazardous oxidizer such as H_2O_2. The process also requires further backing-up with the adsorption treatment of AC to control the enhanced COD level of treated aqueous solution which not only increases the number of steps involved in the dye-removal process but also results in the generation of large amount of sludge. There is an urgent need to replace H_2O_2 with an efficient, cost-effective, and non-hazardous oxidizer which can resolve the aforementioned issues in the present dye-removal application. In this investigation, we utilize the magnetic Pd-Fe_3O_4-flyash composite particles for the decoloration of aqueous solutions containing industrial azo reactive dyes such as Corafix Red ME4B and Corazol Black BX via synergistic activation of $S_2O_8^{2-}$ involving the catalytic and thermal contributions. In contrast to the activation of H_2O_2, the synergistic activation of $S_2O_8^{2-}$ anions is noted to significantly reduce the COD level almost in a single step which reduces the dependency on the post adsorption treatment of AC. Moreover, the regeneration of AC in the present dye-removal application has also been demonstrated using the synergistic activation of $S_2O_8^{2-}$ anions. The latter, hence, appears to be an efficient, cost-effective, and non-hazardous approach for the removal of organic synthetic-dyes from aqueous solutions by using the magnetic Pd-Fe_3O_4-flyash composite particles as catalyst.

6.1. Introduction

Organic synthetic-dyes are recalcitrant organic compounds that are extensively used in various industries such as the textile, pulp and paper, leather tanning, food, agricultural research, hair colorings, and light-harvesting arrays. Even very small amount of synthetic dyes in water is highly visible, affecting the aesthetic merit, transparency, and gas solubility of water bodies. There are more than 100,000 commercially available dyes with over 7×10^5 ton of dye-stuff produced annually.[1] After the dyeing process, loss of colorants to the environment is approximately 10-50%. Many of these dyes are toxic and even carcinogenic which pose a serious hazard to the aquatic and human life.[1] In India alone, dyestuff industry produces around 60,000 metric tons of dyes, which is approximately 6.6% of total colorants used worldwide.[2] The increased color fastness, stability, and resistance of dyes to the degradation have made the color removal from industrial wastewaters progressively difficult.

Various wastewater treatment plants use the combination of chemical (such as the coagulation and flocculation[3-4]) and biological treatments (involving the bacterial processes[5]) which are backed-up with the pressurized sand and activated carbon filtration processes to generate clean water from the industry effluents containing organic synthetic-dyes. Such wastewater treatment plants generate large amount of sludge on a daily basis creating its storage, handling, regeneration, and reuse issues. As an alternative, a new dye-removal technology involving the use of AOPs has been recently suggested as the replacement to the combination of coagulation / flocculation and biological treatments.[6-7] In the former process, H_2O_2 which is a strong oxidizer is first activated using magnetic Pd-Fe_3O_4-flyash composite particles which provide several benefits in the dye-removal application.[6] First, the catalyst generates high concentration

of $^{\bullet}OH$ via activation of H_2O_2 which can attack and degrade the organic pollutants present in the aqueous solutions within a short duration of time creating no sludge issues. Secondly, the catalyst being magnetic in nature can be easily separated from the treated aqueous solution using an external magnetic field which results in no loss of catalyst while conducting the successive cycles of dye-degradation. Third, the AOP process which is further backed-up with the AC treatment generates clean water with very low level of COD since AC adsorbs both the intermediate products of dye-degradation and carbon leached into the aqueous solution from the catalyst-surface during the dye-degradation process.

Nevertheless, H_2O_2 based AOP process itself has three major drawbacks which need to be overcome to realize the commercial importance of proposed technology. First, H_2O_2 is a costlier and hazardous chemical. Hence, alternative cost-effective, efficient, and non-hazardous oxidizers are required to be developed as a replacement for H_2O_2. Secondly, the COD levels are known to increase initially simultaneously with the decoloration of aqueous solutions which demand the post-treatment of aqueous solution with AC. Third, after the prolong use of wastewater treatment plant, AC can lead to the generation of large amount of sludge causing the secondary pollution due to the adsorption of pollutants on its surface. The regeneration of AC using a suitable cost-effective technique is highly essential. There is an urgent need to resolve the above issues possibly with a unique solution which is currently lacking in the literature.

As far the AOPs are concerned, the degradation of organic synthetic-dyes in the aqueous solutions by using the thermal[8-9] and catalyst-driven[10-12] activation of $S_2O_8^{2-}$ and peroxymonosulfate (HSO_5^-) anions have been reported in the literature. It appears that the use of $S_2O_8^{2-}$ and HSO_5^- anions as strong oxidizers offer an efficient, cost-effective, and

non-hazardous approach for the removal of toxic organic synthetic-dyes from the aqueous solutions instead of H_2O_2. Although in the dye-removal application, Pd-catalyst has been utilized for the activation of H_2O_2,[6] its use for the removal of organic synthetic-dyes from the aqueous solution via the activation of $S_2O_8^{2-}$ and HSO_5^- anions has never been reported. Hence, the first major objective of present investigation is to replace H_2O_2 with the efficient, cost-effective, and non-hazardous $S_2O_8^{2-}$ anions to reduce the overall cost and steps involved in the proposed dye-removal process involving magnetic Pd-Fe_3O_4-flyash composite particles as catalyst.

In addition to this, in the literature, AC has also been utilized as a catalyst for the activation of $S_2O_8^{2-}$ and HSO_5^- anions to degrade the harmful organic synthetic-dyes in the aqueous solution.[13-14] Hence, it appears that, in the proposed dye removal process, the AC may be regenerated via the activation of cheaper oxidizer such as $S_2O_8^{2-}$ anions. Hence, the second major objective in the present investigation has been set to demonstrate the regeneration of AC using the synergistic activation of $S_2O_8^{2-}$ involving the contribution of both temperature and catalyst.

6.2. Experimental

6.2.1. Chemicals

Terephthalic acid (TA, 98%) was purchased from Sigma-Aldrich Chemicals, Bengaluru, India; KPS (99%, AR ACS), AC (AR grade, phosphorous free), MB dye ($C_{16}H_{18}ClN_3S$, 96%) from S.D. Fine-Chem Ltd., Mumbai, India; HCl (36 wt%) from Ranbaxy Fine-Chemicals; and NH_4OH solution (25% NH_3) from Qualigens Fine Chemicals Pvt. Ltd., Mumbai, India. Azo reactive dye in the powder form, such as Corafix Red ME4B, was received from Colourtex Industries Limited, Surat, India. The spherical flyash (FA) particles (1-5 μM in size) were obtained from the NTPC, Ramagundam, India. The

details of all other materials used in the present investigation are already provided in literature.[6]

6.2.2. Preparation of magnetic Pd-Fe_3O_4-flyash composite particles

Pd-Fe_3O_4-flyash composite particles having both magnetic and catalytic properties were prepared via the combination of electroless deposition and inverse co-precipitation techniques as per the procedure already described in literature.[6] In short, the magnetic coating of Fe_3O_4 nanoparticles was first deposited on the surface of as-received flyash particles via inverse-precipitation technique. This was followed by the electroless deposition of Pd nanoparticles on the surface of magnetic Fe_3O_4-flyash composite particles. As per the theoretical calculations, the final magnetic Pd-Fe_3O_4-flyash composite particles contain 1.44 wt% Pd and 19 wt% Fe_3O_4 with the balance weight of Sn-flyash particles (referred only as flyash particles in the following text).

6.2.3. Characterization of magnetic Pd-Fe_3O_4-flyash composite particles and as-received AC

The morphology, chemical constituents, specific surface-area, average pore size and its distribution, crystalline phases, surface-chemistry, and magnetic properties of Pd-Fe_3O_4-flyash composite particles and as-received AC have been analyzed using different analytical techniques such as TEM, EDX, BET surface-area measurement, XRD, FTIR, and PPMS techniques. The details of all characterization techniques have been already reported in literature.[6]

6.2.4. Dye-decoloration from aqueous solutions via activation of $S_2O_8^{2-}$ anions using magnetic Pd-Fe_3O_4-flyash composite particles as catalyst

The magnetic Pd-Fe_3O_4-flyash composite particles were utilized for the decomposition of industrial dyes (Corafix Red ME4B and Corazol Black BX) in an aqueous solution under the dark-condition at room temperature (30 ^oC) in the presence of a strong-oxidizer such as $S_2O_8^{2-}$ anions. In 100 ml aqueous solution, Corafix Red ME4B or Corazol Black BX dye of varying initial dye concentration (0.003, 0.03, and 0.3 g l^{-1}) was dissolved completely under the continuous overhead stirring. 100 g l^{-1} of magnetic composite particles were then dispersed in the above dye-solution followed by the addition of 10 mM KPS (equivalent of 0.27 wt%). The resulting suspension was stirred for 1 h in the dark-condition. 8 ml aliquots were collected after each 15 min time interval and catalyst particles were separated from the solution using a centrifuge operated at 3000 rpm. The solutions were then used for obtaining the UV-visible absorption spectra to determine the amount of dye decomposed at a given time calculated using the Eqs. (3.2) and (3.3). Two controlled experiments were conducted using Corafix Red ME4B dye for the total contact time of 1 h in the presence of KPS without the addition of any catalyst and with the addition of as-received flyash as a catalyst. In the third set of controlled experiment, the dye-removal test for the total contact time of 1 h was conducted in the absence of KPS with the addition of as-received flyash as a catalyst.

The cyclic-tests for the Corafix Red ME4B dye decomposition in the dark-condition were conducted for the consecutive 5 cycles at the initial Corafix Red ME4B dye concentration of 0.03 g l^{-1} and initial KPS concentration of 10 mM KPS using the magnetic Pd-Fe_3O_4-flyash composite particles (catalyst concentration of 100 g l^{-1}). After the completion of each cycle of dye-decomposition, the catalyst was separated from the

treated solution using either a centrifuge or a magnetic separator (Sigma-Aldrich Labware, Bengaluru, India) and then dried in an oven at 80 ^{o}C for 12 h. The dried-catalyst thus obtained was used for the next-cycle of MB degradation conducted in the dark-condition.

The $^{\bullet}$OH trapping experiments were typically performed using TA which were produced under the continuous overhead stirring in an aqueous solution due to the activation of $S_2O_8^{2-}$ anions.[6,15] These experiments were similar to the one described above for the dye-decomposition measurements conducted in the dark-condition for Corafix Red ME4B dye except that the dye was replaced with 5×10^{-4} M of TA and 2×10^{-3} M of NaOH. TA is a non-fluorescent molecule; however, the trapping of free $^{\bullet}$OH by TA results in the formation of 2-hydroxyterephthalic acid which is a highly fluorescent molecule. In the present investigation, the latter exhibits a characteristic PL peak located in between 425-428 nm at an excitation wavelength of 315 nm. The $^{\bullet}$OH trapping experiments were also conducted at room temperature (30 ^{o}C) without the addition of magnetic Pd-Fe_3O_4-flyash composite particles.

The COD levels were measured as per the procedure already described in the literature.[6] Typical dye-decomposition experiments were conducted at room temperature (30 ^{o}C) in 100 ml of 10 mM KPS solution using the initial Corafix Red ME4B dye concentration of 0.03 g l^{-1} in the presence of 100 g l^{-1} magnetic Pd-Fe_3O_4-flyash composite particles. The filtrate solutions obtained from these experiments after the contact time of 1 h were utilized for the measurement of COD level. In addition to this, the filtrate obtained was further treated with the adsorption treatment of AC. For the latter treatment, 50 g l^{-1} of AC was added to the total 100 ml of filtrate solution and the suspension was

mechanically stirred for the contact time of 5 h. The AC was separated from the treated solution via filtration method instead of using the centrifuge.

6.2.5. Adsorption characteristics of as-received AC

125 ml of aqueous suspension, with the initial solution-pH adjusted in between 2.5-11 using HCl and NH_4OH solution, was prepared at room temperature (30 ^oC) by dissolving 7.5-750 μM of MB dye and then dispersing 0.4 g l^{-1} of as-received AC. The suspension was stirred in the dark and 4 ml sample suspension was separated after each 10 or 30 min time interval for total 180 min. The catalyst powder was separated using a centrifuge operated at 3000 rpm. The filtrate was then utilized for obtaining the absorption spectra using the UV-visible absorption spectrophotometer to determine the amount of dye adsorbed at a given time which is calculated using the Eqs. (3.2) and (3.3).

6.2.6. Regeneration of AC via synergistic activation of $S_2O_8^{2-}$ anions

In these experiments, 0.4 g l^{-1} of as-received AC was added to 125 ml aqueous solution of MB dye having the initial concentration of 90 μM at the initial solution-pH of 11 adjusted using NH_4OH solution. The dye-adsorption measurement was then conducted using the procedure similar to the one described in the previous section. AC with the surface-adsorbed MB dye, after separation from the aqueous solution via filtration and subsequent drying in an oven at 80 ^oC overnight, was utilized for the second-cycle of dye-adsorption measurement conducted under the similar test-conditions. Total five successive cycles of dye-adsorption measurements were conducted. AC with 317 mg g^{-1} of MB dye adsorbed on its surface was utilized for the regeneration treatment. In this treatment, the latter was added to 100 ml of 10 mM KPS solution maintained at 75 ^oC and stirred continuously using an overhead stirrer for 3 h. The regenerated AC was

separated from the aqueous solution via filtration, and after drying in an oven at 80 ^{o}C overnight, it was recycled for the sixth-cycle of dye-adsorption.

6.3. Results and Discussion

6.3.1. Morphological, chemical, and structural analyses of magnetic Pd-Fe_3O_4-flyash composite particles and as-received AC

The results of TEM, EDX, XRD, BET, and PPMS analyses of magnetic Pd-Fe_3O_4-flyash composite particles and as-received AC are already described in literature.[6] Briefly, as per the EDX analysis, these particles contain O, Al, Si, Pd, Sn, Ca, and Fe having the atomic concentrations of 7, 40, 26, 5, 7, 3, and 12% respectively. Moreover, the magnetization curve obtained for these magnetic composite particles exhibits S-type magnetic hysteresis with very thin hysteresis loop having small value of saturation magnetization of ~1.0 emu g^{-1}. The latter appears to be sufficient for the solid-liquid separation (within 3-4 min) using an external bar magnet. The extremely smaller values of remanence magnetization (0.047 emu g^{-1}) and coercivity (42.5 Oe) are the characteristic features of superparamagnetic nanoparticles. Besides, AC exhibits plate-like nanoparticles of average size of 50 nm having mesoporous structure with the specific surface-area and pore volume of 1,012 m^2 g^{-1} and 0.528 cm^3 g^{-1} respectively and the oxygen containing surface groups such as the quinones, carboxylic acids, and carboxylic anhydrides.

6.3.2. Decoloration of aqueous solutions containing Corafix Red ME4B dye using KPS and as-received flyash

The results of controlled experiments conducted for the removal of Corafix Red ME4B dye from the aqueous solutions are presented in Fig. 6.1. It is observed that, when only KPS is used, Corafix Red ME4B dye can be removed significantly from the aqueous solution only at the lowest initial dye concentration of 0.003 g l^{-1}. The amount of dye-removed is the highest at the lowest initial dye-concentration and the former decreases with increasing latter. At the highest initial dye-concentration (0.3 g l^{-1}), no removal of Corafix Red ME4B dye is observed.

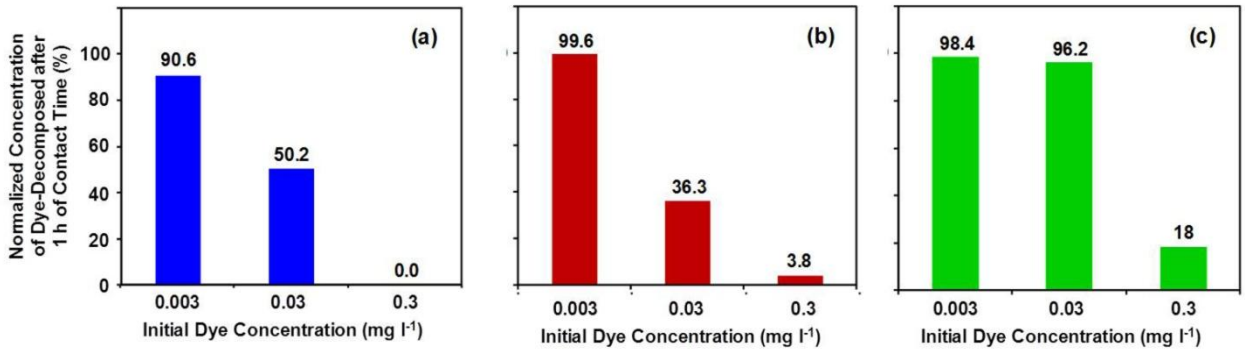

Fig. 6.1. Variation in the amount of Corafix Red ME4B dye decomposed after 1 h of contact time as measured under the different test-conditions involving the aqueous dye solution containing KPS (a), as-received flyash (b), and both KPS and as-received flyash (c). The concentrations of KPS and as-received flyash are 10 mM and 100 g l^{-1}.

As per the various reports, the thermal activation of $S_2O_8^{2-}$ anions can generate $SO_4^{\bullet-}$ and subsequently $^{\bullet}OH$ which can attack and degrade the dye molecules present in the surrounding aqueous solutions.[8-9,15-16]

$$S_2O_8^{2-} \xrightarrow{\Delta} 2SO_4^{\bullet-} \quad (6.1)$$

$$SO_4^{\bullet-} + H_2O \rightarrow SO_4^{2-} + {}^{\bullet}OH + H^+ \quad (6.2)$$

However, the present results show that this mechanism of dye decomposition is capable of removing the industrial azo reactive dye from the aqueous solutions in the lower concentration range. Similar to the previous case, as demonstrated in Fig. 6.1b, the use of as-received flyash (without KPS) also removes Corafix Red ME4B dye from the aqueous solution in significant amount at the lowest initial dye concentration of 0.003 g l^{-1} via adsorption mechanism.[17] This mechanism of dye-removal, however, is also not effective in removing the Corafix Red ME4B dye when the initial dye concentration is increased possibly due to the lower adsorption capacity of as-received flyash particles.[17] As noted in Fig. 6.1c, due to the cumulative effect of both the mechanisms, the dye-removal performance obtained by using the combination of flyash and KPS appears to be better than their individual effects. However, even in the latter case, the overall effect of initial dye-concentration on the amount of dye-removed appears to be similar to the previous two cases.

6.3.3. Decoloration of aqueous solutions containing Corafix Red ME4B and Corazol Black BX dye via synergistic activation of $S_2O_8^{2-}$ anions using magnetic Pd-Fe_3O_4-flyash composite particles

The variation in the color of dye-solutions, containing both KPS and magnetic Pd-Fe_3O_4-flyash composite particles, as a function of contact time as obtained for the varying initial dye concentration is presented in Fig. 6.2a-c. Within the investigated range, the decoloration of initial dye solution is clearly visible within the first 15-30 min of contact time for all initial dye concentrations. Typical variation in the intensity of absorbance-peak located at ~542 nm related to Corafix Red ME4B dye as observed with increasing contact time, for the different initial dye-concentrations, is presented in Fig. 6.2d-f. The decoloration of initial dye solutions within the first 15-30 min of contact time, as noted in Fig. 6.2a-c, is strongly supported by the sharp decrease in absorbance in the visible

region. It is, thus, successfully shown that the aqueous solutions containing Corafix Red ME4B dye, with initial concentration in the range of 0.003-0.3 g l^{-1}, can be completely decolorized by using the magnetic Pd-Fe_3O_4-flyash composite particles in combination with KPS. Comparison with the results of controlled experiments shows that the complete dye-removal within the investigated range of initial dye-concentration is the combined effect of surface-deposited nanoparticles of Pd / Fe_3O_4 and KPS. The magnetic separation of Pd-Fe_3O_4-flyash composite particles from the treated aqueous solution and their catalytic nature in the dye removal application have been demonstrated earlier by Narayani et al..[6]

According to Muhammad et al.[11] and Gokulakrishnan et al.[12], the activation of $S_2O_8^{2-}$ anions by metal ion catalysis occurs by an oxidation-reduction reaction in which lower valent metal ions act as electron donor. Accordingly, in the present system, the presence of Pd^0 and Fe^{2+} can lead to the activation of $S_2O_8^{2-}$ anions generating $SO_4^{\bullet-}$ and subsequently $^{\bullet}OH$.

$$Pd^0 + 2S_2O_8^{2-} \rightarrow Pd^{2+} + 2SO_4^{\bullet-} + 2SO_4^{2-} \quad (6.3)$$

$$Fe^{2+} + S_2O_8^{2-} \rightarrow Fe^{3+} + SO_4^{\bullet-} + SO_4^{2-} \quad (6.4)$$

The $SO_4^{\bullet-}$ produced via thermal activation of $S_2O_8^{2-}$ anions, Eq. (6.1), and activation by Pd^0 and Fe^{2+}, Eqs. (6.3) and (6.4), may generate $^{\bullet}OH$, Eq. (6.2), which can be effectively trapped.

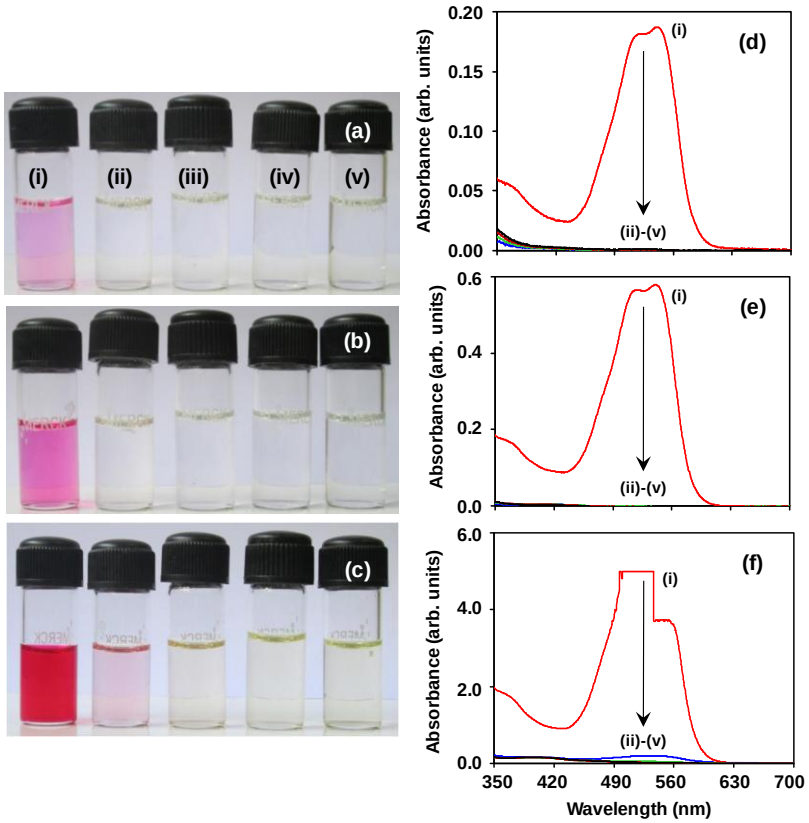

Fig. 6.2. Variation in the color of initial dye-solutions (a-c) and that in the intensity of absorbance-peak located at ~542 nm (d-f), as a function of contact time as obtained for Corafix Red ME4B dye by using the magnetic Pd-Fe_3O_4-flyash composite particles (100 g l^{-1}). The initial dye concentration varies as 0.003 (a,d), 0.03 (b,e), and 0.3 g l^{-1} (c,f). The contact time varies as 0 (i), 15 (ii), 30 (iii), 45 (iv), and 60 min (v). The initial KPS concentration is 10 mM.

The variation in the color of initial dye-solutions containing Corazol Black BX as a function of contact time, as obtained for the varying initial dye concentrations, is presented in Fig. 6.3 (a-c). Within the investigated range, the decolorization of initial dye solution is clearly visible within the first 15-30 min of contact time for all initial dye concentrations. Typical variation in the intensity of absorbance-peak located at ~600 nm related to the Corazol Black BX dye, as observed with the increasing contact time for the initial dye-concentrations of 0.003, 0.03 and 0.3 g l^{-1}, is presented in Fig. 6.3(d-f). The

decolorization of initial dye solutions within the first 15-30 min of contact time, as noted in Fig. 6.3(d-f), is strongly supported by the sharp decrease in the absorbance in the visible region.

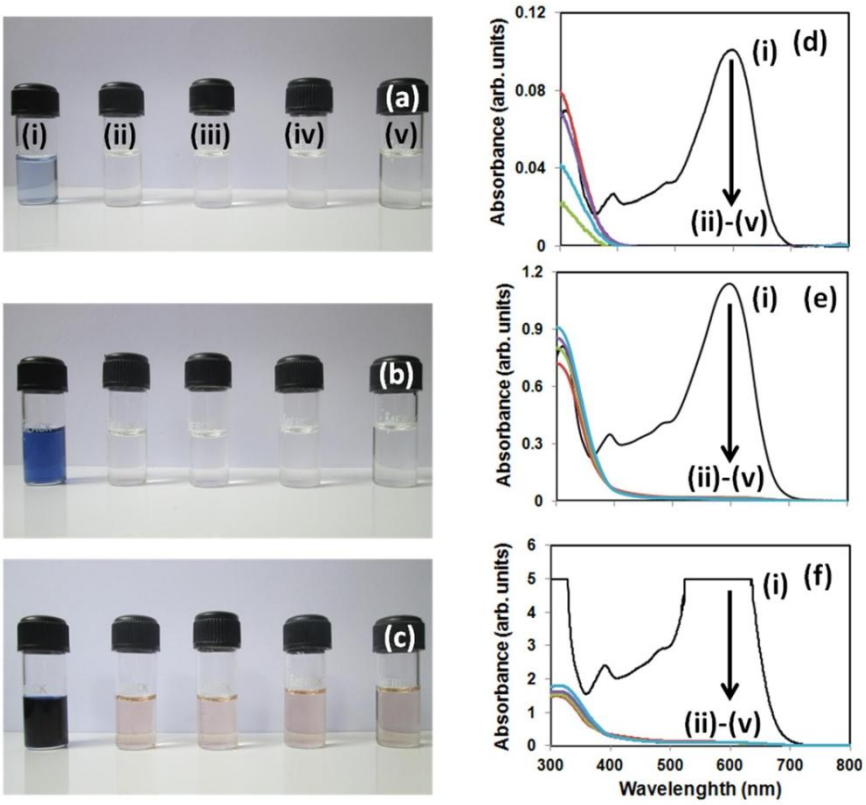

Fig. 6.3. Variation in the color of initial dye-solutions (a-c) and that in the intensity of absorbance-peak located at ~600 nm (d-f), as a function of contact time as obtained for Corazol Black BX dye by using the magnetic Pd-Fe_3O_4-flyash composite particles (100 g l^{-1}). The initial dye concentration varies as 0.003 (a,d), 0.03 (b,e), and 0.3 g l^{-1} (c,f). The contact time varies as 0 (i), 15 (ii), 30 (iii), 45 (iv), and 60 min (v). The initial KPS concentration is 10 mM.

The recyclability of magnetic Pd-Fe_3O_4-flyash composite catalyst was examined using Corafix Red ME4B with the initial concentration of 0.03 g l^{-1} and presented in Fig. 6.4. The magnetic Pd-Fe_3O_4-flyash composite particles are tested for five successive dye-degradation cycles to study their stability and regenerability. In each cycle, the catalyst

was tested for 60 min, separated by using the magnetic separation, dried and then used for the next cycle of dye degradation. Almost 100% dye degradation is achieved in all five cycles which strongly supports the catalytic nature of magnetic Pd-Fe_3O_4-flyash composite particles.

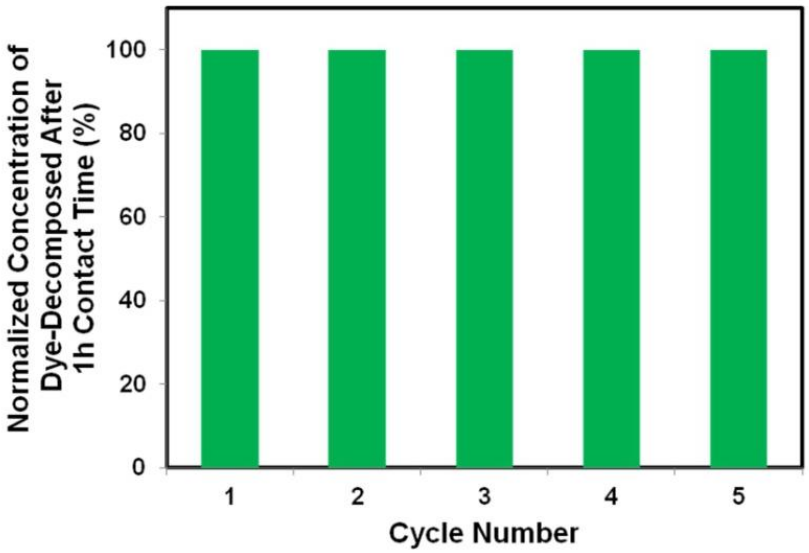

Fig. 6.4. Variation in the normalized concentration of Corafix Red ME4B dye degraded after 1 h of contact time as a function of dye-degradation cycle number. The initial dye (Corafix Red ME4B), KPS, and catalyst (magnetic Pd-Fe_3O_4-flyash composite particles) concentrations are 0.03 g l^{-1}, 10 mM, and 100 g l^{-1}.

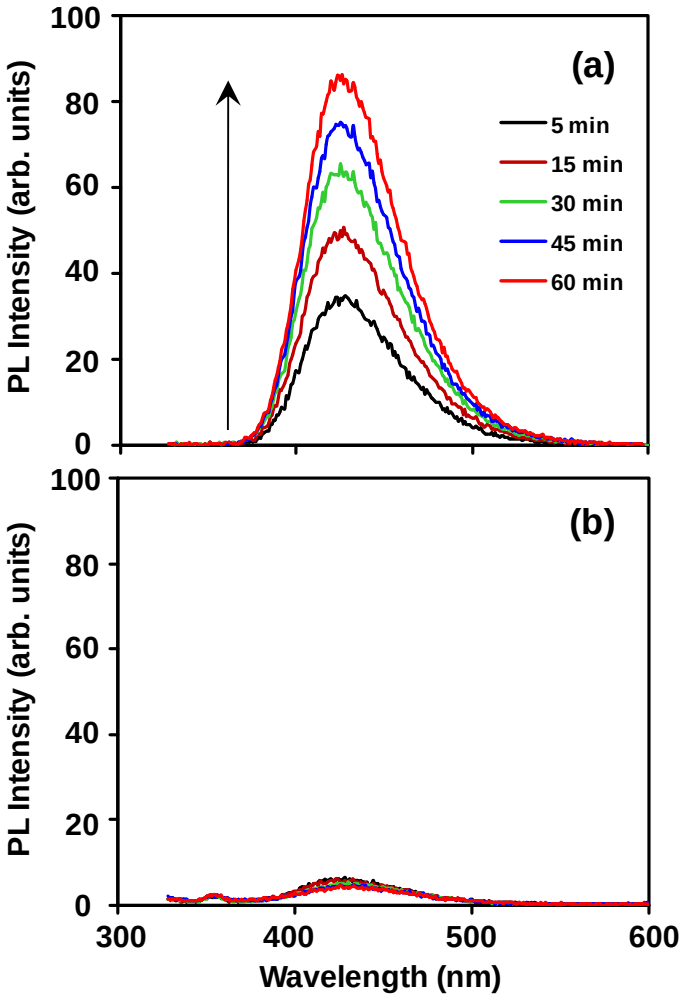

Fig. 6.5. Variation in the PL intensity associated with the formation of 2-hydroxyterpthalic acid for varying contact time as obtained without (a) and with (b) the addition (100 g l^{-1}) of magnetic Pd-Fe_3O_4-flyash composite particles in 10 mM KPS solution at room temperature (30 ^oC). The excitation wavelength is 315 nm.

In Fig. 6.5a, qualitative variation in the concentration of $^{\bullet}OH$ is presented as a function of activation time of $S_2O_8^{2-}$ anions. It is noted that the concentration of $^{\bullet}OH$ increases systematically with the time of thermal activation, which suggests that $SO_4^{\bullet-}$ too are gradually produced via proposed mechanism, Eq. (6.1). Surprisingly, in the presence of magnetic Pd-Fe_3O_4-flyash composite particles, the concentration of $^{\bullet}OH$ is noted to decrease drastically. This strongly suggests that Pd^{2+} and Fe^{3+} ions have scavenging

effect on the generated $^{\bullet}OH$, Eqs. (6.5) and (6.6), which possibly regenerate the catalyst nanoparticles allowing further generation of $SO_4^{\bullet-}$, Eqs. (6.3) and (6.4).

$$Pd^{2+} + 2^{\bullet}OH \rightarrow Pd^{0} + O_2 + 2H^{+} \quad (6.5)$$

$$Fe^{3+} + 2^{\bullet}OH \rightarrow Fe^{2+} + {}^{\bullet}OOH + H^{+} \quad (6.6)$$

The degradation of Corafix Red ME4B dye as observed in Fig. 6.2 under the simultaneous presence of KPS and magnetic Pd-Fe_3O_4-flyash composite particles is, hence, attributed to the attack of $SO_4^{\bullet-}$; while, $^{\bullet}OH$ produced play the role of regenerating the catalyst nanoparticles.

The measured variation in the COD levels under different test conditions are presented in Fig. 6.6. The COD level of initial aqueous solution containing Corafix Red ME4B dye is as high as 240 mg l^{-1}. By using the combined treatment of KPS and magnetic Pd-Fe_3O_4-flyash composite particles significant reduction in the COD level up to 60 mg l^{-1} is noted, which is further reduced marginally to 40 mg l^{-1} by the post adsorption treatment of AC. Narayani et al. recently reported that the COD level may increase substantially simultaneously with the decoloration of aqueous solution if the magnetic Pd-Fe_3O_4-flyash composite particles are used to activate H_2O_2 which is a strong oxidizer.[6] This is attributed to the leaching of carbon already present on the surface of flyash particles and the presence of intermediate products of dye degradation. The present results, however, show that the replacement of H_2O_2 with KPS is beneficial not only for completely avoiding the initial rise in the COD level but also in reducing the number steps involved in the dye-removal process due to less dependency on the post adsorption treatment of AC. Such a replacement has made it possible to decolorize the aqueous dye solution simultaneously with significant decrease in the COD level via one step catalytic process.

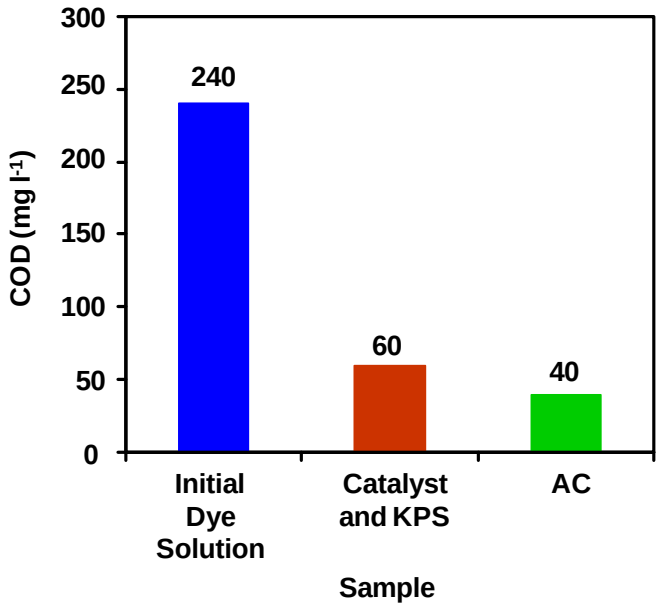

Fig. 6.6. Comparison of final COD levels obtained under the different conditions used in the dye-removal tests which are conducted at room temperature (30 ^{o}C) for the total contact time of 1 h. The initial dye (Corafix Red ME4B), KPS, and catalyst (magnetic Pd-Fe_3O_4-flyash composite particles) concentrations are 0.03 g l^{-1}, 10 mM, and 100 g l^{-1}. The adsorption treatment of AC is conducted following the combined treatment of catalyst and KPS using the AC concentration of 50 g l^{-1} and total contact time of 5 h.

Thus, it is successfully shown that the combination of magnetic Pd-Fe_3O_4-flyash composite particles and KPS provide an efficient, cost-effective, and non-hazardous approach for the removal of organic synthetic-dye from the aqueous solutions compared with the combination of magnetic Pd-Fe_3O_4-flyash composite particles and H_2O_2. (Note: see the Table 6.1 for the comparison of present magnetic catalyst with other non-magnetic and magnetic based activators as reported in the literature for the removal of various organic pollutants from the aqueous solutions and industry wastewaters via activation of $S_2O_8^{2-}$ anions.)

Table 6.1. Brief summary of data reported in the literature on the removal of various organic pollutants from aqueous solutions and industry wastewaters via activation of $S_2O_8^{2-}$ anions using different non-magnetic (i) and magnetic (ii) activators.

(i)

Catalyst	**Target pollutant**	**Optimum reactant concentrations ($g\ l^{-1}$)**	**Result**	**Reference**
Activated carbon	Fulvic acid (FAc)	[FAc]=0.4 [Catalyst]=0.75 [KPS]=0.81 Temperature= 150 ^oC O_2 Pressure= 0.5 Ma	100% degradation in 4 h	[13]
Fe^{2+} H_2O_2 OH^-	Levofloxacin (LFX)	[LFX]=0.027 LFX:$S_2O_8^{2-}$:Fe^{2+} (m:m:m)=1:10:1	The order of performance Fe^{2+}> H_2O_2>OH^-	[18]
Combination of either ozone or ultrasound	Polychlorinated biphenyls-contaminated soil	Soil:$S_2O_8^{2-}$ (w/w)= 1:0.0005	Sonication accelerates the chemical oxidation process	[19]
Fe-based MOFs	Acid orange 7 (AO)	[AO]=0.08 [Catalyst]= 0.2 [KPS]=4.06	97% removal in 240 min	[20]
Flyash	Pharmaceutical effluent	Effluent=250 ml [Catalyst]= 4 [KPS]=0.595	At 75 ^oC, 94.25% of COD reduction is achieved in 3 h	[21]
N-doped graphene	Sulfamethoxazole (SMX)	[SMX]=0.005 [Catalyst]= 0.05 [KPS]= 0.27	99.9% removal in 3 h	[22]

Nanodiamond	Phenol	[Phenol]=0.02 [Catalyst]= 0.2 [KPS]=1.76	100% phenol oxidation in 2 h	[23]
Citric acid (CA) chelated -Fe(II)	Trichloroethylene (TCE)	[TCE]=0.019 [Fe(II)]= 0.3 mM [CA]=0.15 mM [KPS]= 0.61	100% degradation in 60 min	[24]
Nano-Co_3O_4	Orange G (OG)	[OG]=0.045 [Catalyst]=0.5 [KPS]= 0.54	90.7% removal in 3 h	[25]
Fe/S modified carbon nanotubes	2,4-Dichlorophenol (DCP)	[DCP]=0.005 [Catalyst]=0.1 [KPS]:[Catalyst]=1:1	94.8% degradation in 30 min	[26]
Polyhydroquinone-coated Fe_3O_4@ MWCNT	Flumequine (FQ)	[FQ]=0.12 [Catalyst]=0.12 [KPS]= 20.64	78% removal in 6 h	[27]
$LiFePO_4$	Orange G (OG)	[OG]=0.09 [Catalyst]= 0.2 [KPS]=0.54	93.6% removal after 10 min	[28]
α-MnO_2 nanowires	2,4-Dichlorophenol (DCP)	[DCP]=0.1 [Catalyst]=0.2 [KPS]=5.4	90.2% degradation in 180 min	[29]
SWCNTs rGO mesoporous carbon Activated carbon	Phenol	[Phenol]=0.02 [Catalyst]=0.2 [KPS]=1.75	Carbocatalysts show higher activity than metal oxides	[23]

(ii)

Catalysts	**Target pollutant**	**Optimum reactant concentrations ($g\ l^{-1}$)**	**Result**	**Reference**
Iron-modified diatomite	Perfluorooctanoic acid (PFOA)	[PFOA]=0.01 [Catalyst]= 8.3 [KPS]= 81.1	50% removal in 6 h	[30]

Fe@rGO	Trichloroethylene (TCE)	[TCE]=0.02 [Catalyst]= 1 [KPS]= 4.06	Higher removal in the acidic medium	[31]
Peanut shell magnetic carbon	MB	[MB]=0.04 [Catalyst]= 0.06 [KPS]= 0.5	90% removal in 30 min	[32]
Fe_3O_4 nanoparticles	Sulfamonomethoxine (SMM)	[SMM]=0.017 [Catalyst]=0.56 [KPS]= 0.32	100% removal in 15 min	[33]
AC@Fe_3O_4	Tetracycline (TC)	[TC]=0.01 [Catalyst]= 0.4 [KPS]= 10.81	99.8% removal in 180 min	[34]
CuO@Fe_3O_4	Phenol	[Phenol]=0.0094 [Catalyst]=0.3 [KPS]=1.35	100% mineralization in 120 min	[35]
Core-shell Fe^0@Fe_3O_4	Dibutyl phthalate (DBT)	[DBT]=0.005 [Catalyst]=0.5 [KPS]= 0.5	94.7% degradation in 180 min	[36]
CuO@Fe_3O_4	2,4-Dichlorophenol (DCP)	[DCP]=0.1 [Catalyst]= 0.624 [KPS]=2.7	96.9% degradation in 180 min	[37]
Ascorbic acid-coated Fe_3O_4	2,4-Dichlorophenol (DCP)	[DCP]=0.1 [Catalyst]= 2 [KPS]=8.1	98.5% degradation in 150 min	[38]
nFe_3O_4@rGO	Trichloroethylene (TCE)	[TCE]=0.02 [Catalyst]= 6.9 [KPS]=0.81	98.6% degradation in 5 min	[39]
$CuFe_2O_4$@MWCNTs	Diethyl phthalate (DEP)	[DEP]= 0.005 [Catalyst]=0.1 [DEP]:[KPS]=1:200	100% degradation in 30 min	[40]

Pd-Fe_3O_4-flyash	Corafix Red ME4B	[Red ME4B]= 0.3 [Catalyst]=100 [Pd]=1.44 [KPS]=2.7	100% degradation in less than 60 min	Present work

(Note: KPS: potassium persulfate, MWCNT: multi-walled carbon nanotubes, SWCNT: single-walled carbon nanotubes, MOF: metal organic framework, rGO: reduced graphene oxide)

In the present investigation, magnetic Pd-Fe_3O_4-flyash composite particles have been utilized as activator for the removal of Corafix Red ME4B and Corazol Black BX dye (industrial azo reactive dye) from the aqueous solutions via AOPs involving the activation of $S_2O_8^{2-}$ anions. Being magnetic in nature, the present catalyst primarily resolves the major solid-liquid separation issue associated, on the industrial scale, compared with all non-magnetic activators reported in the literature, Table 6.1. Moreover, further comparison with the non-magnetic / magnetic-based catalysts suggests that the choice of flyash as a support for the top magnetic Fe_3O_4 and catalytic Pd layers is a cost-effective approach for the preparation of composite catalyst compared with that of graphene, reduced graphene oxide, and single- / multiwall-carbon nanotubes as support material. It also appears that the magnetic Pd-Fe_3O_4-flyash composite particles have never been utilized for the removal of organic synthetic-dye such as Corafix Red ME4B and Corazol Black BX from the aqueous solutions via activation of $S_2O_8^{2-}$ anions. The utilization of $S_2O_8^{2-}$ anions as activator is also a cost-effective technique in the removal Corafix Red ME4B and Corazol Black BX from the aqueous solutions compared with the use of H_2O_2 as an oxidizer[6] (see the cost-analysis provided in the Appendix 6.1). Thus, the comparison with the data presented in the Table 6.1 strongly justifies the aforementioned novelties of present work relative to the existing literature.

6.3.4. MB dye removal from aqueous solutions using AC via adsorption mechanism and its regeneration through synergistic activation of $S_2O_8^{2-}$ anions

The obtained variation in the normalized equilibrium concentration of MB dye adsorbed on the surface of AC at different initial solution-pH values is presented in Fig. 6.7. It is noted that the normalized equilibrium concentration of MB adsorbed on the surface of AC decreases with increasing initial MB concentration.

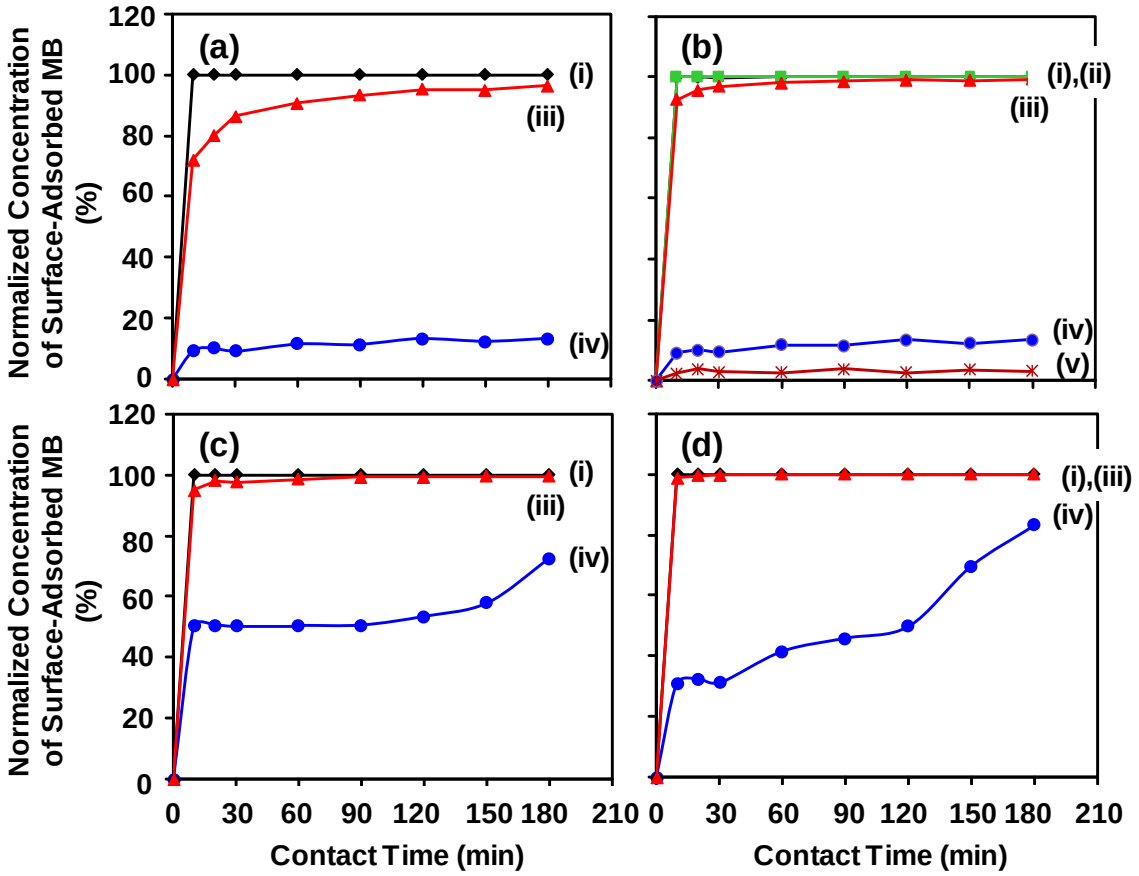

Fig. 6.7. Variation in the normalized concentration of surface-adsorbed MB as a function of contact time as obtained for as-received AC at different initial solution-pH values: 2.5 (a), 7.5 (b), 10 (c), and 11 (d). The initial MB dye concentration varies as 60 (i), 100 (ii), 250 (iii), 500 (iv), and 750 (v).

The equilibrium adsorption data is used to calculate the equilibrium amount of MB adsorbed (q_e, mg g^{-1}) on the surface per unit weight of catalyst,[15] The adsorption isotherms are presented in Fig. 6.8; while, the variation in q_e as a function of initial MB concentration as obtained for the different initial solution-pH values is presented in Fig. 6.9. The initial rise in q_e value with the initial MB concentration is due to increased driving force for the MB adsorption on the surface of AC. As mentioned earlier, using the FTIR analysis, Narayani et al. demonstrated that the surface of as-received AC contains various oxygen containing groups such as lactones, quinones, carboxylic acids, and carboxylic anhydrides.[6] According to Purkait et al., these oxygen containing groups become anionic in the aqueous solution providing negative charge to the surface of AC.[41] As a result, the adsorption of MB dye, which is cationic in an aqueous solution, appears to be due to the electrostatic attraction between the adsorbent surface and adsorbate. (Note: the point-of-zero charge (pH_{pzc}) for AC is reported to be in between 3-7 (see the Table 6.2). This also explains the gradual increase in q_m (defined as the maximum q_e value obtained at different initial solution-pH values) with the initial solution-pH as observed in the inset of Fig. 6.9d which is in agreement with the results reported by El Qada et al..[42]

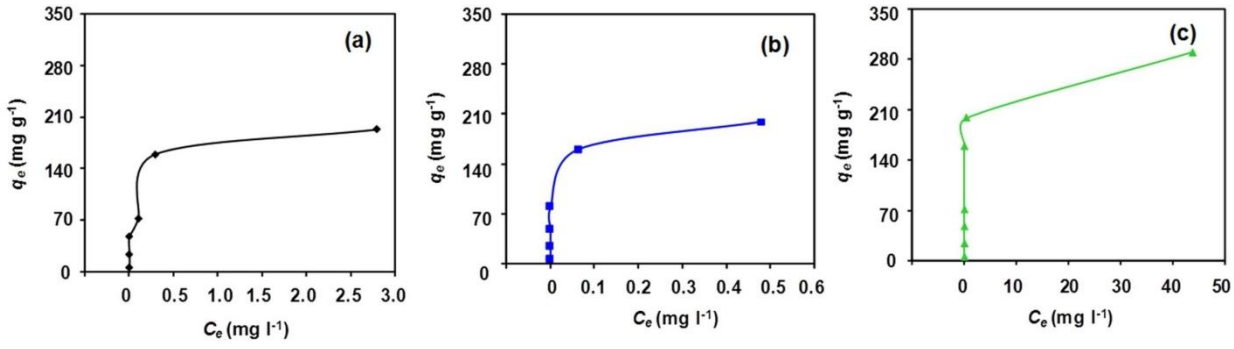

Fig. 6.8. Equilibrium adsorption isotherms for MB on as-received AC for different initial solution-pH values: 2.5 (a), 7.5 (b), and 10 (c).

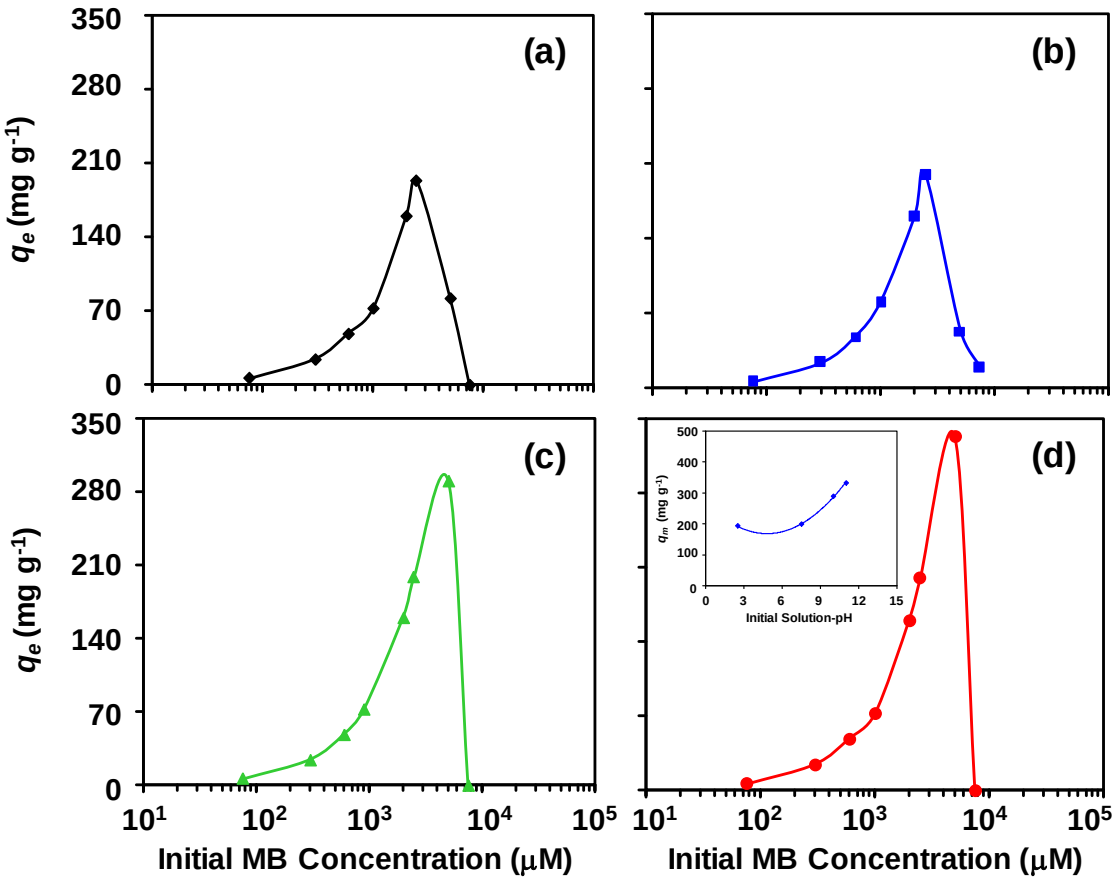

Fig. 6.9. Variation in q_e as a function of initial MB concentration as obtained for the as-received AC at different initial solution-pH values: 2.5 (i), 7.5 (ii), 10 (iii), and 11 (iv). The inset in (d) shows the variation in q_m as a function of initial solution-pH.

Within the investigated range of initial solution-pH, the dye-adsorption capacity of AC is noted to be 333 mg g^{-1} at the initial solution-pH of 11 which appears to be within the range (10-970 mg g^{-1}) as reported in the literature (see the Table 6.2). The decrease in q_e value as observed in Fig. 6.9 typically at higher initial MB concentrations is ascribed to decrease in the negative charge on the surface of AC caused by the increased interaction between positively charged MB molecules and negatively charged OH^- present in the solution.[15] The q_m value, however, is not observed to be decreased at the highest initial solution-pH of 11 possibly as a result of the effect of very high BET specific surface-area (1,012 m^2 g^{-1}) and pore volume (0.528 cm^3 g^{-1}) of as-received AC which allow relatively

large concentration of OH^- to be adsorbed on its surface; thus, reducing the interaction between the positively charged MB molecules and negatively charged OH^- present in the solution.

Table 6.2. Characteristics of MB adsorption on various types of AC as reported in the literature.

Source of Activated Carbon	**Activating Agent**	**Adsorption Capacity (mg g^{-1})**	**Specific Surface-Area (m^2 g^{-1})**	**pH**	**Point of Zero Charge (pH_{pzc})**	**Reference**
Bituminous coal	Steam	580	857.1	11	6.3	[42]
Cashew nut shell	KOH	68.7 (Langmuir)	984	10	-	[43]
Rice straw	H_2SO_4	62.5 (Langmuir)	-	7	-	[44]
Commercial sucrose	KOH	709.4	1534	-	3	[45]
Fox nutshell	$ZnCl_2$	968.7	2869	11	-	[46]
Posidonia oceanica (L.) dead leaves	$ZnCl_2$	285.7	1483	6.5	-	[47]
Flamboyant pods	NaOH	890	2854	6.5	-	[48]
Oil palm fibre	KOH	277.8	1354	6.5	-	[49]
Coconut shell	NaOH	955.2	2825	-	-	[50]
Poly(vinyl alcohol) microspheres	H_2SO_4	602.4	-	-	-	[51]
Walnut shells	$ZnCl_2$	315	1800	7	-	[52]
Watermelon rind	$ZnCl_2$	231.48	1156	-	5.4	[53]
Oil palm woods	Physical activation	90.9	1084	-	-	[54]
Cotton stalk	$ZnCl_2$	193.5	794.8	9-10	5.9	[55]

Bamboo	Microwave	291.6	1335	-	3.7	[56]
Vetiver roots	H_3PO_4	423 (Langmuir)	1004	5	3.4	[57]
Jute fiber	H_3PO_4	225.64	-	5–10	4.6	[58]
Artichoke leaves	H_3PO_4	790	2038	9	6	[59]
Rattan sawdust	KOH	294.1 (Langmuir)	1083	-	-	[60]
Oil palm fiber	KOH-microwave	382.3	1223	12	7.0	[61]
Finger-citron-residue	KOH	581.4 (Langmuir)	2887	7	-	[62]
Sewage sludge	Calcium sulfate	131.8 (Langmuir)	14.3	12	5.5	[63]
Rice husk	Physical	9.7	180.5	-	6.1	[64]
Hazelnut husk	$ZnCl_2$	476.2	1369	7	5.5	[65]
Buriti shells	$ZnCl_2$	274.6 (Langmuir)	843	7	-	[66]

The MB adsorption on the surface of AC is further analyzed using different kinetics and equilibrium isotherm models.[15] It appears that the adsorption of MB on the surface of AC follows the pseudo-second-order kinetics, Table 6.3. (Note: considering the respective $<r^2>$ values, the Lagergren pseudo-first-order and intraparticle diffusion kinetics models are found to be invalid; hence, they are not presented here).

Table 6.3. Values of parameters of pseudo-second-order kinetics model as obtained at the different initial solution-pH values.

pH	[MB]	q_e (Exp.)	q_e	k_2	r^2
2.5	60	48	50	---	1
	200	159	167	0.012	1
	250	193	200	0.001	0.999
	500	82	83	0.012	0.987
7.5	60	48	50	---	1
	200	160	167	0.037	1
	250	199	200	0.006	1
	500	53	55	0.002	0.992
10	60	48	50	---	1
	200	160	167	---	1
	250	199	200	0.0125	1
	500	290	250	0.001	0.992
11	60	48	50	---	1
	200	160	167	---	1
	250	200	200	---	1
	500	333	250	0.001	0.984

Moreover, the comparison of values of different parameters as obtained for different isotherm models, Table 6.4, suggests that the Langmuir model shows the best fit which indicates monolayer adsorption of MB on the surface of AC via electrostatic force of attraction.

Table 6.4. Values of parameters of different equilibrium adsorption isotherm models as obtained at different initial solution-pH values.

pH	q_m (Exp.)	Langmuir					Freundlich			DKR			
		q_m	K_L	r^2	R_L	ΔG	n	K_F	r^2	q_m	β	r^2	E
2.5	193	200	---	0.997	---	---	3.7	162	0.741	210	3×10^{-8}	0.966	4.1
7.5	199	200	250	0.998	0.002	-48	---	---	---	---	---	---	---
10	290	200	---	1	----	---	---	---	---	---	---	---	---

Although the AC treatment can adsorb the organic dye and intermediate products of dye degradation to control the final COD levels, Fig. 6.6, the long term utilization of AC in the dye removal process can generate sludge issues causing the secondary pollution. Hence, it is necessary to demonstrate the regeneration of AC possibly using the same technique as used for the dye degradation process. For this purpose, the MB dye is first adsorbed on the surface of AC via five successive dye-adsorption cycles as shown in Fig. 6.10a. AC with 317 mg g^{-1} of MB dye adsorbed on its surface is utilized for the regeneration treatment in an aqueous solution containing KPS and maintained at 75 ^{o}C. Drastic improvement in the amount of MB dye adsorbed is clearly noted after the regeneration treatment, Fig. 6.10b, which strongly suggests that the previously adsorbed MB dye is completely decomposed on the surface of AC. The latter is the result of synergistic activation of $S_2O_8^{2-}$ anions by temperature, Eqs. (6.1) and (6.2), and AC itself, Eqs. (6.7) and (6.8),[13-14] resulting in the generation of $SO_4^{\bullet-}$ and $^{\bullet}OH$ which attack and degrade the MB dye molecules.

$$AC-OOH + S_2O_8^{2-} \rightarrow SO_4^{\bullet-} + AC-OO^{\bullet} + HSO_4^{-} \quad (6.7)$$

$$AC-OH + S_2O_8^{2-} \rightarrow SO_4^{\bullet-} + AC-O^{\bullet} + HSO_4^{-} \quad (6.8)$$

According to Purkait et al.,[41] the well-established methods for the regeneration of spent AC can be classified in three broad groups such as thermal, chemical, and biological regeneration which are associated with several major drawbacks which include the involvement of very high temperatures (1100 K), loss of carbon, need for purification of solvents used for desorption of adsorbates, slower kinetics and lower regeneration efficiencies, and large capital investment in high pressure equipment. In comparison with the reported methods, it appears that the present method of regeneration of AC provides

several benefits which include the involvement of very lower temperature, fast kinetics, higher efficiencies, and lower capital investment.

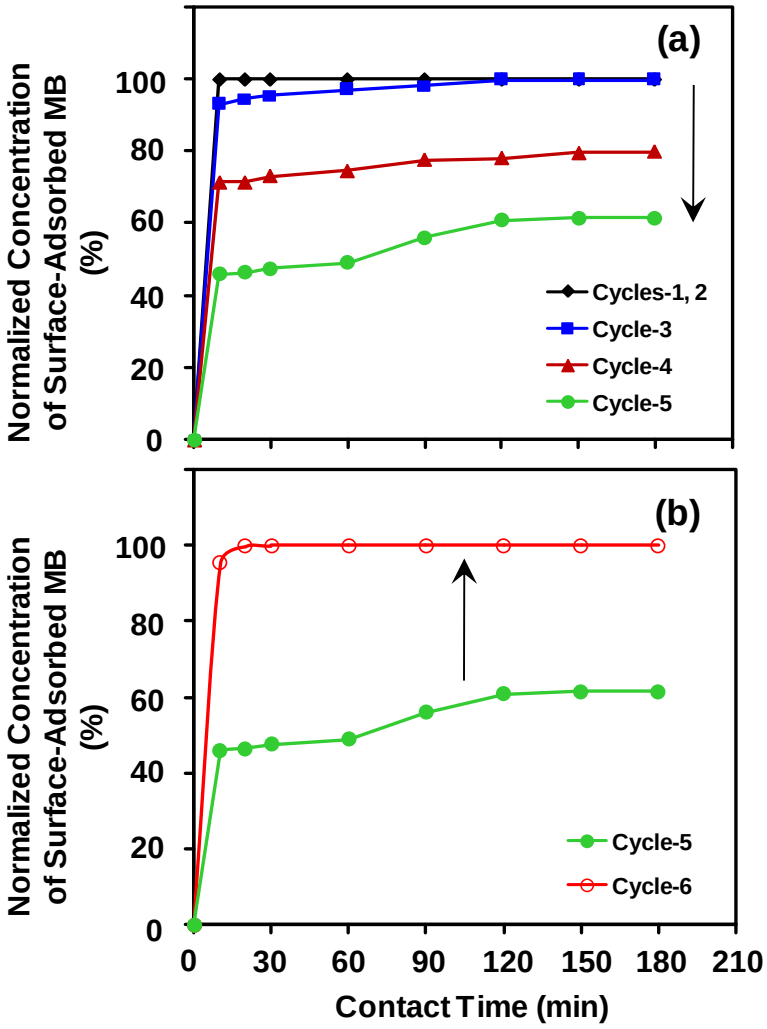

Fig. 6.10. Variation in the normalized concentration of MB adsorbed as a function of contact time as obtained for as-received AC (0.4 g l^{-1}) involving the successive dye adsorption cycles-1 to 5 (a) and 6 (b) conducted before and after the regeneration treatment of AC respectively. The initial MB concentration and initial solution-pH are 90 µM and 11. The regeneration treatment of AC is conducted using 10 mM KPS solution (equivalent of 0.27 wt%) at 75 ^{o}C for the total contact time of 3 h.

6.3.5. Efficient, cost-effective, and non-hazardous dye-removal technology based on magnetic Pd-Fe_3O_4-flyash composite particles

It appears that the magnetic Pd-Fe_3O_4-flyash composite particles can decompose organic synthetic-dye in an aqueous solution via synergistic activation of $S_2O_8^{2-}$ anions. In our previous investigation,[6] these composite particles were utilized to activate H_2O_2 which is highly costlier and hazardous oxidizer (see the cost-analysis provided in the Appendix 6.1). As a result, the use of KPS as demonstrated in this investigation offers an efficient, cost-effective, and non-hazardous approach for the removal of organic synthetic-dye from the aqueous solutions. In addition to this, in the previous investigation, the enhanced COD level of catalyst treated aqueous solution was controlled by using the post adsorption treatment of AC.[6] Moreover, no regeneration of AC was demonstrated to avoid the secondary pollution. In the present investigation, the COD level is demonstrated to be reduced significantly via single step involving the synergistic activation of $S_2O_8^{2-}$ anions; thus, reducing the dependency on the post adsorption treatment of AC. The synergistic activation of $S_2O_8^{2-}$ anions is also shown to be useful to regenerate the surface of as-received AC. Overall, based on the results obtained in this investigation, the dye-removal technology involving the use of magnetic Pd-Fe_3O_4-flyash composite particles as catalyst, as proposed in our earlier investigation,[6] is modified and summarized in the Scheme 6.1.

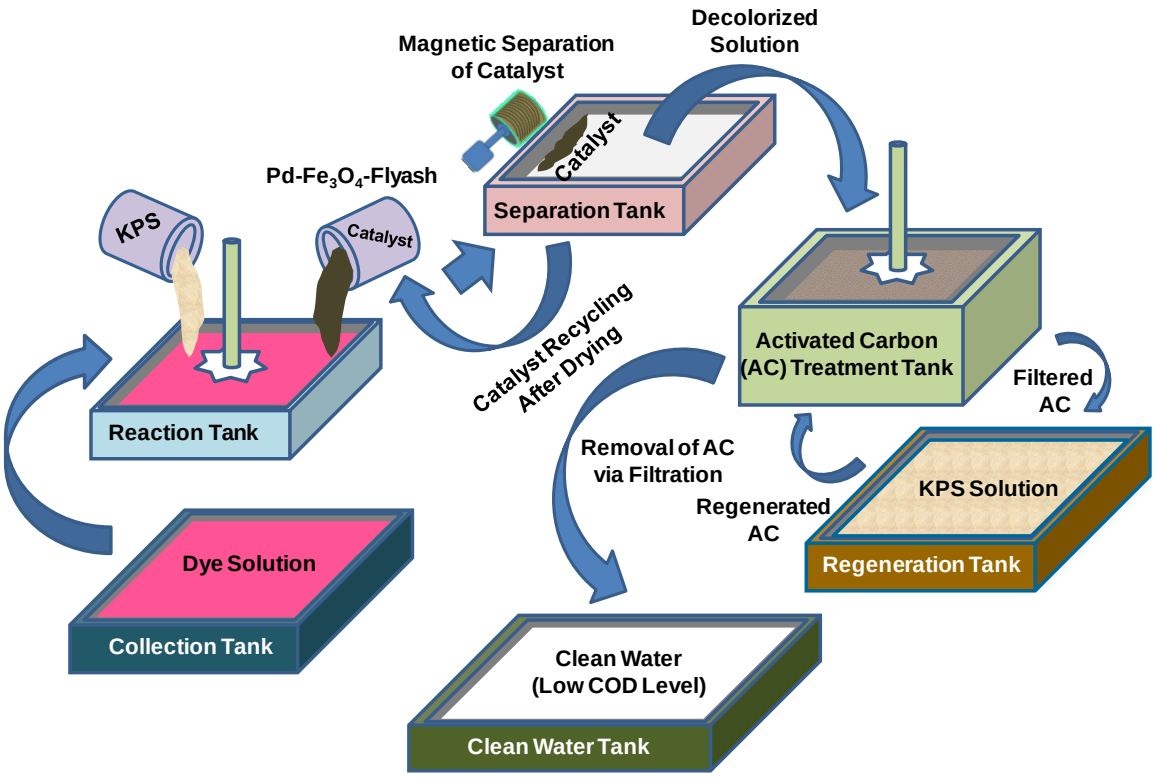

Scheme 6.1. Modified dye-removal technology based on the magnetic Pd-Fe_3O_4-flyash composite particles as catalyst and KPS as an efficient, cost-effective, and non-hazardous oxidizer.

4. Conclusions

The magnetic Pd-Fe_3O_4-flyash composite particles, synthesized via combination of inverse co-precipitation and electroless techniques, are successfully utilized for the removal of Corafix Red ME4B and Corazol Black BX dyes from the aqueous solution using KPS as an oxidizer. The mechanism of dye-removal involves the attack of $SO_4^{\bullet-}$ and $^{\bullet}OH$ generated via synergistic activation of $S_2O_8^{2-}$ anions involving the catalytic and thermal contributions. The actual dye degradation and regeneration of catalyst nanoparticles appear to be predominantly due to $SO_4^{\bullet-}$ and $^{\bullet}OH$ respectively. Substantial reduction in the COD level is achieved through a single step catalytic process which could be further reduced marginally using the post adsorption treatment of AC. The

regeneration of AC has been demonstrated by decomposing the previously adsorbed cationic MB dye on its surface via synergistic activation of $S_2O_8^{2-}$ anions. The latter technique, hence, appears to be an efficient, cost-effective, and non-hazardous approach for the removal of organic synthetic-dyes from aqueous solutions by using the magnetic Pd-Fe_3O_4-flyash composite particles as catalyst. The present technology can be utilized in future for the removal other organic-synthetic dyes from the aqueous solutions and industry effluents.

Appendix 6.1

It is to be noted that, in the present investigation, the choice of oxidant is the most critical parameter which primarily governs the cost of dye-removal process. In our previous investigation,[6] H_2O_2 is used as a strong oxidizer. As per the Catalog (2016) of S.D Fine-Chem Ltd., Mumbai, India, the cost of 500 ml of 50 wt% H_2O_2 is approximately Indian Rupees (IND Rs.) 500.00 (1 U.S. Dollar = 68 IND Rs.). For the removal of 0.3 g l^{-1} of Corafix Red ME4B dye, dissolved in 1 L of 50 wt% H_2O_2, by using 100 g l^{-1} of Pd-Fe_3O_4-flyash magnetic composite particles, the cost of oxidizer utilized is calculated to be IND Rs. 1000.00 per liter.

In the present investigation, the costlier H_2O_2 solution is replaced with KPS solution. As per the Catalog (2016) of S.D Fine-Chem Ltd., Mumbai, India, the cost of 500 g of KPS is approximately IND Rs. 845.00. For the removal of 0.3 g l^{-1} of dye, dissolved in 1 L of distilled H_2O, by using 100 g l^{-1} of Pd-Fe_3O_4-flyash magnetic composite particles to activate 10 mM of KPS, the cost of oxidizer utilized is calculated to be IND Rs. 5.00 per liter. Thus, it is clearly noted that the cost of oxidizer in the current dye-removal process is significantly reduced by a factor of 200 by replacing H_2O_2 solution with KPS solution without affecting the performance of dye-removal process.

References

(1) Crini, G. *Bioresour. Technol.* **2006**, *97*, 1061.

(2) Singh, K.; Arora, S. *Crit. Rev. Env. Sci. Technol.* **2011**, *41*, 807.

(3) Zahrim, A.; Hilal, N. *Water Resour. Ind.* **2013**, *3*, 23.

(4) Chethana, M.; Sorokhaibam, L. G.; Bhandari, V. M.; Raja, S.; Ranade, V. V. *ACS Sustainable Chem. Eng.* **2016**, *4*, 2495.

(5) Saratale, R. G.; Saratale, G.; Chang, J.; Govindwar, S. *J. Taiwan Inst. Chem. Eng.* **2011**, *42*, 138.

(6) Narayani, H.; Augustine, R.; Sumi, S.; Jose, M.; Nair, K. D.; Samsuddin, M.; Prakash, H.; Shukla, S. *Sep. Purif. Technol.* **2017**, *172*, 338.

(7) Soon, A. N.; Hameed, B. *Desalination* **2011**, *269*, 1.

(8) Gu, X.; Lu, S.; Li, L.; Qiu, Z.; Sui, Q.; Lin, K.; Luo, Q. *Ind. Eng. Chem. Res.* **2011**, *50*, 11029.

(9) Huang, K.-C.; Couttenye, R. A.; Hoag, G. E. *Chemosphere* **2002**, *49*, 413.

(10) Zhang, T.; Zhu, H.; Croué, J.-P. *Environ. Sci. Technol.* **2013**, *47*, 2784.

(11) Muhammad, S.; Saputra, E.; Sun, H.; Izidoro, J. d. C.; Fungaro, D. A.; Ang, H. M.; Tadé, M. O.; Wang, S. *RSC Adv.* **2012**, *2*, 5645.

(12) Gokulakrishnan, S.; Parakh, P.; Prakash, H. *J. Hazard. Mater.* **2012**, *213*, 19.

(13) Xu, X.-Y.; Zeng, G.-M.; Peng, Y.-R.; Zeng, Z. *Chem. Eng. J.* **2012**, *200*, 25.

(14) Saputra, E.; Muhammad, S.; Sun, H.; Wang, S. *RSC Adv.* **2013**, *3*, 21905.

(15) Jose, M.; Aswathi, P.; Sriram, K.; Parakh, P.; Prakash, H.; Shukla, S. *RSC Adv.* **2016**, *6*, 80133.

(16) Ghauch, A.; Tuqan, A. M.; Kibbi, N.; Geryes, S. *Chem. Eng. J.* **2012**, *213*, 259.

(17) Babu, B. K.; Purayil, J. V.; Padinhattayil, H.; Shukla, S.; Warrier, K. G. *Int. J. Appl. Ceram. Technol.* **2013**, *10*, 186.

(18) Epold, I.; Dulova, N. *J. Environ. Chem. Eng.* **2015**, *3*, 1207.

(19) Goi, A.; Viisimaa, M. *J. Environ. Chem. Eng.* **2015**, *3*, 2839.

(20) Li, X.; Guo, W.; Liu, Z.; Wang, R.; Liu, H. *Applied Surface Science* **2016**, *369*, 130.

(21) Nachiappan, S.; Gopinath, K. P. *Journal of Environmental Chemical Engineering* **2015**, *3*, 2229.

(22) Chen, H.; Carroll, K. C. *Environ. Pollut.* **2016**, *215*, 96.

(23) Duan, X.; Sun, H.; Kang, J.; Wang, Y.; Indrawirawan, S.; Wang, S. *ACS Catal.* **2015**, *5*, 4629.

(24) Wu, X.; Gu, X.; Lu, S.; Xu, M.; Zang, X.; Miao, Z.; Qiu, Z.; Sui, Q. *Chem. Eng. J.* **2014**, *255*, 585.

(25) Zhang, J.; Chen, M.; Zhu, L. *RSC Adv.* **2016**, *6*, 758.

(26) Cheng, X.; Guo, H.; Zhang, Y.; Liu, Y.; Liu, H.; Yang, Y. *J. Colloid Interface Sci.* **2016**, *469*, 277.

(27) Feng, M.; Qu, R.; Zhang, X.; Sun, P.; Sui, Y.; Wang, L.; Wang, Z. *Water Res.* **2015**, *85*, 1.

(28) Lin, X.-m.; Ma, Y.-w.; Wang, Y.; Wan, J.-q.; Guan, Z.-y. *RSC Adv.* **2015**, *5*, 94694.

(29) Zhao, Y.; Zhao, Y.; Zhou, R.; Mao, Y.; Tang, W.; Ren, H. *RSC Adv.* **2016**, *6*, 35441.

(30) da Silva-Rackov, C. K. O.; Lawal, W. A.; Nfodzo, P. A.; Vianna, M. M. G. R.; do Nascimento, C. A. O.; Choi, H. *Appl. Catal. B* **2016**, *192*, 253.

(31) Ahmad, A.; Gu, X.; Li, L.; Lv, S.; Xu, Y.; Guo, X. *Environ. Sci. Pollut. Res.* **2015**, *22*, 17876.

(32) Zhou, L.; Ma, J.; Zhang, H.; Shao, Y.; Li, Y. *Appl. Surf. Sci.* **2015**, *324*, 490.

(33) Yan, J.; Lei, M.; Zhu, L.; Anjum, M. N.; Zou, J.; Tang, H. *J. Hazard. Mater.* **2011**, *186*, 1398.

(34) Jonidi Jafari, A.; Kakavandi, B.; Jaafarzadeh, N.; Rezaei Kalantary, R.; Ahmadi, M.; Akbar Babaei, A. *J. Ind. Eng. Chem.* **2017**, 45, 323.

(35) Lei, Y.; Chen, C.-S.; Tu, Y.-J.; Huang, Y.-H.; Zhang, H. *Environ. Sci. Technol.***2015**, *49*, 6838.

(36) Li, H.; Wan, J.; Ma, Y.; Wang, Y. *Chem. Eng. J.* **2016**, *301*, 315.

(37) Sun, C.; Zhou, R.; E, J.; Sun, J.; Ren, H. *RSC Adv.* **2015**, *5*, 57058.

(38) Sun, C.; Zhou, R.; Jianan, E.; Sun, J.; Su, Y.; Ren, H. *RSC Adv.* **2016**, *6*, 10633.

(39) Yan, J.; Gao, W.; Dong, M.; Han, L.; Qian, L.; Nathanail, C. P.; Chen, M. *Chem. Eng. J.* **2016**, *295*, 309.

(40) Zhang, X.; Feng, M.; Qu, R.; Liu, H.; Wang, L.; Wang, Z. *Chem. Eng. J.* **2016**, *301*, 1.

(41) Purkait, M.; Maiti, A.; DasGupta, S.; De, S. *J. Hazard. Mater.* **2007**, *145*, 287.

(42) El Qada, E. N.; Allen, S. J.; Walker, G. M. *Chem. Eng. J.* **2006**, *124*, 103.

(43) Kumar, P. S.; Ramalingam, S.; Sathishkumar, K. *Korean J. Chem. Eng.* **2011**, *28*, 149.

(44) Mashhadi, S.; Javadian, H.; Ghasemi, M.; Saleh, T. A.; Gupta, V. K. *Desalin. Water Treat.* **2016**, 57, 21091.

(45) Bedin, K. C.; Martins, A. C.; Cazetta, A. L.; Pezoti, O.; Almeida, V. C. *Chem. Eng. J.* **2016**, *286*, 476.

(46) Kumar, A.; Jena, H. M. *J. Cleaner Prod.* **2016**, *137*, 1246.

(47) Dural, M. U.; Cavas, L.; Papageorgiou, S. K.; Katsaros, F. K. *Chem. Eng. J.* **2011**, *168*, 77.

(48) Vargas, A. M.; Cazetta, A. L.; Kunita, M. H.; Silva, T. L.; Almeida, V. C. *Chem. Eng. J.* **2011**, *168*, 722.

(49) Tan, I.; Hameed, B.; Ahmad, A. *Chem. Eng. J.* **2007**, *127*, 111.

(50) Cazetta, A. L.; Vargas, A. M.; Nogami, E. M.; Kunita, M. H.; Guilherme, M. R.; Martins, A. C.; Silva, T. L.; Moraes, J. C.; Almeida, V. C. *Chem. Eng. J.* **2011**, *174*, 117.

(51) Jia, Z.; Li, Z.; Li, S.; Li, Y.; Zhu, R. *J. Mol. Liq.* **2016**, *220*, 56.

(52) Yang, J.; Qiu, K. *Chem. Eng. J.* **2010**, *165*, 209.

(53) Üner, O.; Geçgel, Ü.; Bayrak, Y. *Water Air Soil Pollut.* **2016**, *227*, 1.

(54) Ahmad, A.; Loh, M.; Aziz, J. *Dyes Pigm.* **2007**, *75*, 263.

(55) Deng, H.; Yang, L.; Tao, G.; Dai, J. *J. Hazard. Mater.* **2009**, *166*, 1514.

(56) Liu, Q.-S.; Zheng, T.; Li, N.; Wang, P.; Abulikemu, G. *Appl. Surf. Sci.* **2010**, *256*, 3309.

(57) Altenor, S.; Carene, B.; Emmanuel, E.; Lambert, J.; Ehrhardt, J.-J.; Gaspard, S. *J. Hazard. Mater.* **2009**, *165*, 1029.

(58) Senthilkumaar, S.; Varadarajan, P.; Porkodi, K.; Subbhuraam, C. *J. Colloid Interface Sci.* **2005**, *284*, 78.

(59) Benadjemia, M.; Millière, L.; Reinert, L.; Benderdouche, N.; Duclaux, L. *Fuel Process. Technol.* **2011**, *92*, 1203.

(60) Hameed, B.; Ahmad, A.; Latiff, K. *Dyes Pigm.* **2007**, *75*, 143.

(61) Foo, K.; Hameed, B. *Fuel Process. Technol.* **2012**, *99*, 103.

(62) Gong, R.; Ye, J.; Dai, W.; Yan, X.; Hu, J.; Hu, X.; Li, S.; Huang, H. *Ind. Eng. Chem. Res.* **2013**, *52*, 14297.

(63) Liu, L.; Lin, Y.; Liu, Y.; Zhu, H.; He, Q. *J. Chem. Eng. Data* **2013**, *58*, 2248.

(64) Sharma, Y.; Upadhyay, S. *Can. J. Chem. Eng.* **2011**, *89*, 377.

(65) Karaçetin, G.; Sivrikaya, S.; Imamoğlu, M. *J. Anal. Appl. Pyrolysis* **2014**, *110*, 270.

(66) Pezoti, O.; Cazetta, A. L.; Souza, I. P.; Bedin, K. C.; Martins, A. C.; Silva, T. L.; Almeida, V. C. *J. Ind. Eng. Chem.* **2014**, *20*, 4401.

Chapter 7

Summary and Suggestions for the Future Work

7.1. Summary

The present study involves the utilization of titania, titanate, and flyash-based nanostructures (such as the nanoparticles, nanotubes, nanoplates, and nanosheets) and nanocomposites for the removal of organic synthetic-dyes from the aqueous solutions using three different dye-removal mechanisms such as the photocatalysis, adsorption, and AOPs. The basic and industrial azo reactive dyes are used for this purpose. Various synthesis methods such as the sol-gel, hydrothermal, ion-exchange, inverse co-precipitation, electroless deposition, and their combination are developed for the processing of aforementioned nanostructures and nanocomposites. Attention is paid to utilize the developed nanostructures and nanocomposites for resolving some of the pending issues associated with the three dye-removal mechanisms to make them suitable for commercialization in the near-future.

1. Nanocrystalline TiO_2 with pure-anatase and mixed anatase-rutile structures is processed using the conventional and acid-catalyst-modified sol-gel methods. Among the three different acid-catalysts investigated, CH_3COOH and H_3PO_4 are observed to stabilize the nanocrystalline TiO_2 in the anatase phase; while, HNO_3 results in a considerable anatase-to-rutile phase transformation. The samples are utilized for the degradation of cationic MB dye in an aqueous solution under the UV-radiation exposure. The maximum photocatalytic activity (k_{app}=0.55 min^{-1}) is exhibited by the sample processed using H_3PO_4 as an acid-catalyst. This is attributed to higher MB adsorption (30%) on its surface due to its maximum specific surface-area (144 m^2 g^{-1}) and relatively higher negative surface-charge (-

23.2 mV) which are the result of strong binding of PO_4^{3-} anions on the surface of nanocrystalline anatase-TiO_2. Interestingly, the same sample possess the lowest crystallinity and lowest concentration of $^{\bullet}OH$ produced under the UV-radiation exposure which do not support the maximum photocatalytic activity exhibited by this sample. Nevertheless, the involvement of PO_4^{3-} anions in the degradation of MB dye under the UV-radiation exposure is confirmed via FTIR analysis. The obtained results, thus, strongly support the dual-role of PO_4^{3-} anions in enhancing the photocatalytic activity of nanocrystalline anatase-TiO_2 which is comparable with that (k_{app}=0.57 min^{-1}) of commercial Degusa-P25. The lowest crystallinity of this sample appears to be compensated by the dual-role of PO_4^{3-} anions. However, it appears that, maintaining higher photocatalytic activity for large number of successive dye-degradation cycles, typically at higher initial dye-concentrations, is a major issue to be addressed with the developed photocatalyst. Considering the limitations of present sol-gel derived nanostructures and the photocatalysis mechanism, it is realized that there is an urgent need to explore further the possibility of using the sol-gel derived products for deriving 1-deminsional nanostructures, having higher specific surface-area, which can remove the organic synthetic-dye from an aqueous solution via other effective mechanism such as the adsorption.

2. Pure and Ag-doped nanoparticles of anatase-TiO_2 synthesized using CH_3COOH-modified sol-gel process are, hence, utilized as precursors for the processing of highly crystalline and high aspect-ratio nanotubes / nanoplates of pure and Ag-doped anatase-TiO_2 via modified hydrothermal method. It is observed that the hydrothermal treatment of pure and Ag-doped nanocrystalline anatase-TiO_2 precursors and the subsequent washing of hydrothermal products result in the

formation of nanotubes / nanoplates of pure and Ag-doped anatase-TiO_2 instead of the nanotubes of hydrogen titanate which are invariably obtained with the use of unmodified anatase-TiO_2 as a precursor. It is proposed that the formation of nanotubes / nanoplates of pure and Ag-doped anatase-TiO_2 via modified hydrothermal method, without the involvement of thermal treatment, is due to the operation of double ion-exchange mechanism which is in contrast to that of conventional single ion-exchange mechanism responsible for the formation of nanotubes of hydrogen titanate. Pure and Ag-doped nanotubes / nanoplates of anatase-TiO_2 are utilized for the removal of cationic MB dye from the aqueous solutions via adsorption mechanism. Within the investigated initial solution pH range of 2.5-11, the maximum MB adsorption capacity of nanotubes of undoped anatase-TiO_2 is determined to be 32 mg g^{-1} at the initial solution-pH of 10. The MB adsorption capacity of Ag-doped nanotubes / nanoplates of anatase-TiO_2 (Ag/Ti ratio of 0.01 and 0.05) is determined to be 39 and 34 mg g^{-1} at the initial solution-pH of 10. Thus, the largest MB adsorption capacity is exhibited by Ag-doped nanotubes of anatase-TiO_2 having Ag/Ti ratio of 0.01. The amount of MB adsorption on the surface of nanotubes of anatase-TiO_2 is, thus, shown to be enhanced by controlling the initial solution pH and amount of Ag-doping. The MB adsorption on the surface of undoped and Ag-doped nanotubes of anatase-TiO_2 follows the pseudo-second-order kinetics and equilibrium adsorption predominantly follows the Langmuir model within the investigated range of initial solution pH and Ag/Ti ratio.

3. Pure and TiP_2O_7 / PO_4^{3-} ions modified nanocrystalline anatase-TiO_2 synthesized using the conventional and H_3PO_4-modified sol-gel processes are, then, utilized as precursors for the processing of pure and HPO_4^{2-} anions modified nanotubes of

$H_2Ti_3O_7$ via modified hydrothermal method. HTN and HP-HTN are utilized for the removal of MB dye from the aqueous solutions via adsorption mechanism. The MB adsorption capacity of HP-HTN is determined to be 139 mg g^{-1} which is higher than that (105-121 mg g^{-1}) of pure HTN. The latter is also utilized for the removal of cationic MB dye from the aqueous solutions via one-step method of chemically-activated catalytic process conducted in the dark. The Fenton-like AOP process involves the activation of strong oxidizer such as H_2O_2 using HTN which decomposes MB in the dark-condition (also known as dark-catalysis) via the generation and attack of radical-ions ($^{\bullet}OH$ and $O_2^{\bullet-}$). The maximum MB degradation rate-capacity (mg g^{-1} h^{-1}) for the one-step method of dark-catalysis process is measured by varying the initial MB and H_2O_2 concentrations. It is demonstrated that the plot of variation in the maximum MB degradation rate-capacity as a function of initial H_2O_2 concentration can precisely predict the MB adsorption capacity of HTN. The validity of new method of predicting the MB adsorption capacity is confirmed by obtaining similar plots for HP-HTN. However, being non-magnetic in nature, both HTN and HP-HTN could not be separated from the treated aqueous solution using an external magnetic field. Hence, the need for the development of magnetic nanocomposite is realized which would provide the benefit of ease of magnetic separation in the dye-removal application. It is also recognized that the demonstration of regeneration and reuse of nanostructured / nanocomposite based adsorbent in the dye-removal application is essential.

4. As a result, the nanosheets of $H_2Ti_3O_7$ are synthesized via hydrothermal treatment of sol-gel derived nanocrystalline anatase-TiO_2 coated on the surface of flyash particles. Magnetic nanocomposites consisting of $H_2Ti_3O_7$ nanosheets and γ-Fe_2O_3 nanoparticles are further processed via ion-exchange mechanism by using a simple

mechanical mixing of two precursors in an aqueous solution having neutral solution-pH. A new model is proposed to explain the typical attachment of γ-Fe_2O_3 nanoparticles to the edges of HTNS via an ion-exchange bond formation. HTNSF magnetic nanocomposites are utilized for the removal of cationic MB dye from the aqueous solutions via adsorption mechanism. Interestingly, the attachment of γ-Fe_2O_3 nanoparticles is observed to enhance the MB adsorption capacity of HTNS instead of decreasing it. A new model is proposed which satisfactorily explains the strong dependence dye-adsorption capacity on the pore volume and specific surface-area of HTNSF magnetic nanocomposite. The latter shows the effective magnetic separation from an aqueous solution in few minutes using an external magnetic field provided by a bar magnet. The reuse of HTNSF-5 magnetic nanocomposite for five successive cycles of dye-adsorption is successfully achieved through its regeneration via the activation of $S_2O_8^{2-}$ anions in an aqueous solution involving the synergy effect in between thermal activation and that by the constituents of HTNSF-5 magnetic nanocomposite. It appears that the combination of adsorption and AOP is very effective not only for the removal of organic synthetic-dye from an aqueous solution but also to regenerate the adsorbent for conducting the subsequent dye-adsorption cycles. It is realized that the AOP process conducted without the prior adsorption process would possibly minimize the total time required for the dye-removal from an aqueous solution making the process more suitable for the actual commercial application.

5. Consequently, magnetic Pd-Fe_3O_4-flyash composite particles, synthesized via combination of inverse co-precipitation and electroless techniques, are successfully utilized for the removal of industrial azo reactive dyes such as the Corafix Red ME4B and Corazol Black BX dyes from the aqueous solutions using KPS as a

cheap and strong oxidizer as a replacement for costlier and hazardous H_2O_2. The mechanism of dye-removal involves the attack of $SO_4^{\bullet-}$ and $^{\bullet}OH$ generated via synergistic activation of $S_2O_8^{2-}$ anions involving the catalytic and thermal contributions. In contrast to the activation of H_2O_2, the synergistic activation of $S_2O_8^{2-}$ anions is noted to significantly reduce the COD level almost in a single step which reduces the dependency on the post adsorption treatment of AC. Moreover, the regeneration of AC is also demonstrated using the synergistic activation of $S_2O_8^{2-}$ anions. Hence, AOP based on the activation of $S_2O_8^{2-}$ anions using the magnetically separable Pd-Fe_3O_4-flyash composite particles appears to be an efficient, cost-effective, and non-hazardous approach for the removal of organic synthetic-dyes from the aqueous solutions.

6. Finally, within the limits of investigated mechanisms of dye-removal, synthesized nanostructures and nanocomposites, and the range of values of different test-parameters, it is proposed that the dye-removal mechanism involving AOPs based on the activation of $S_2O_8^{2-}$ anions is suitable for the faster, cheaper, and efficient removal of organic synthetic-dyes from the aqueous solutions.

7.2. Suggestions for the future work

The following are the recommendations proposed for the future work.

1. Predicting the dye-adsorption capacity of pure and Ag-doped nanotubes of anatase-TiO_2 processed via conventional and H_3PO_4-modified hydrothermal method using the one-step method of chemically-activated catalytic process conducted in the dark.

2. Synthesis of magnetic Fe_3O_4-AC and Pd-Fe_3O_4-AC nanocomposites via the combination of electroless and inverse co-precipitation techniques and their utilization for the removal of industrial azo reactive dyes via synergistic activation of $S_2O_8^{2-}$ anions.

Output

List of Patents

1. Shukla, S. V.; Padinhattayil, H.; Narayani, H.; **Jose, M.**; Karunakaran, R., "Semiconductor-oxides nanotubes-based composite particles useful for dye-removal and processes thereof", Notice of Grant Issued for Chinese Patent Application No. 201480002356.7 (3-March-2017, Filed on 11-March-2015); Taiwan Patent No. I542564 (Granted on 21-July-2016).

List of Publications

1. **Jose, M.**; Sriram, K.; Reshma, R.; Vidya, U. V.; Shukla, S., "Synergistic persulfate activation as an efficient and cost-effective approach for removal of organic synthetic-dyes from aqueous solutions using magnetic Pd-Fe_3O_4-flyash composite particles as catalyst", *J. Environ. Chem. Eng.* **2017**, doi: 10.1016/j.jece.2016.12.027
2. **Jose, M.**; Aswathi, P. T.; Sriram, K.; Parakh, P.; Prakash, H.; Shukla, S., "Ion-exchange bonded $H_2Ti_3O_7$ nanosheets-based magnetic nanocomposite for dye removal via adsorption and its regeneration via synergistic activation of persulfate", *RSC Adv.* **2016**, *6*, 80133-80144.
3. **Jose, M.**; Harsha, N.; Suhailath, K.; Mohamed, A. P.; Shukla, S., "Hydrogen phosphate anions modified hydrogen titanate nanotubes for methylene blue adsorption from aqueous solution: validating novel method of predicting adsorption capacity", *J. Environ. Chem. Eng.* **2016**, *4*, 1295-1307.
4. **Jose, M.**; Kumari, M.; Karunakaran, R.; Shukla, S., "Methylene blue adsorption from aqueous solutions using undoped and silver-doped nanotubes of anatase-titania

synthesized via modified hydrothermal method", *J. Sol-Gel Sci. Technol.* **2015**, *75*, 541-550.

5. **Jose, M.**; Kumari, M.; Karunakaran, R.; Shukla, S., "Hydrothermal synthesis of highly crystalline nanotubes/nanoplates of pure and silver-doped anatase-titania using acid-catalyst-modified sol–gel precursors", *J. Sol-Gel Sci. Technol.* **2015**, *73*, 38-47.
6. **Jose, M.**; Narayani, H.; Kumar, J.; Shukla, S., "Photocatalytic activity of acid-catalyst-modified sol–gel processed nanocrystalline titania: on dual-role of active surface-sites", *Sci. Adv. Mater.* **2015**, *7*, 729-745.
7. **Jose, M.**; Haridas, M. P.; Shukla, S., "Predicting dye-adsorption capacity of hydrogen titanate nanotubes via one-step dye-removal method of novel chemically-activated catalytic process conducted in dark", *J. Environ. Chem. Eng.* **2014**, *2*, 1980-1988.
8. **Jose, M.**; Kumar, J.; Shukla, S., "Highest photocatalytic activity observed for nanocrystalline anatase-titania having lowest crystallinity", *Nano Bulletin* **2013**, *2*, 130104.

List of Conference Presentations

1. **Jose, M.**; Sriram, K.; Shukla, S., "Ion-exchange bonded $H_2Ti_3O_7$ nanosheets-based magnetic nanocomposite for dye removal via adsorption and its regeneration via synergistic activation of persulfate" (Oral Presentation) In: Research Scholars Symposium on Materials Science and Engineering, organized by the Indian Institute of Metals (IIM), Trivandrum chapter, CSIR-NIIST, Thiruvananthapuram, Kerala, India, 20-December-2016.
2. **Jose, M.**; Narayani, H,; Sriram, K.; Shukla, S. "$H_2Ti_3O_7/\gamma$-Fe_2O_3 magnetic nanocomposites for organic dye removal from aqueous solutions via adsorption and

activation of strong oxidizers", (Invited Oral Presentation) In: 2nd International Conference on Harnessing Engineering Technology and Innovation for Sustainable Growth (HETIS-2016), Organized by Dr. S. S. Bhatnagar University Institute of Chemical Engineering and Technology (Dr. SSBUICET), Panjab University, Chandigarh, Panjab, India, 30-October-2016 to 1-November-2016.

3. **Jose, M.**; Shukla, S., "Predicting dye-adsorption capacity of hydrogen titanate nanotubes via one-step dye-removal method of novel dark-catalysis process", (Poster Presentation) In: International Conference on Advanced Functional Materials (ICAFM), Organized by the National Institute for Interdisciplinary Science and Technology (CSIR-NIIST), Materials Research Society of India (MRSI), Indian Ceramic Society (InCerS), Indian Institute of Metals (IIM), and Society for Polymer Science (SPS, India), Thiruvananthapuram, Kerala, 19-21 February 2014.
4. **Jose, M.**; Shukla, S., "Effect of precursor-functionalization on the structure and dye-adsorption capacity of hydrothermally processed nanotubes", (Poster Presentation) In: International Symposium for Research Scholars (ISRS) on Metallurgy, Materials Science and Engineering, IIT-Chennai, Tamilnadu, India, 13–15 December 2012.
5. **Jose, M.**; Remya, K.; Shukla, S., "Effect of silver-doping on dye-adsorption capacity of hydrothermally synthesized anatase-titania", (Poster Presentation) In: Second International Conference on Advanced Oxidation Processes (AOP- 2012), M.G. University, Kottayam, Kerala, India, 6–8 October 2012.
6. **Jose, M.**; Remya, K.; Harsha, N.; Shukla, S., "Effect of acid-catalyst on visible and ultraviolet photocatalytic activity of sol-gel derived silver-doped nanocrystalline anatase-titania", (Poster presentation) In: National Seminar on Current Trends in Chemistry (CTriC-2012), Department of Applied Chemistry, Cochin University of Science and Technology (CUSAT), Cochin, Kerala, India, 20-21 January 2012.

7. **Jose, M.**; Remya, K.; Shukla, S., “Processing Ag-doped hydrogen titanate nanotubes and their dye-adsorption capacity”, (Poster Presentation) In: Platinum Jubilee Session of Indian Ceramic Society (InCerS), Agra, Uttar Pradesh, India, 20-22 December 2011.